CHAPTER 4 - REACTOR

TABLE OF CONTENTS

TABLE OF CONTENTS (CoNT'd)

TABLE OF CONTENTS (CONT'd)

TABLE OF CONTENTS (Cont'd)

TABLE OF CONTENTS (Cont'd)

TABLE OF CONTENTS (Cont'd)

TABLE OF CONTENTS (Cont'd)

TABLE OF CONTENTS (Cont'd)

CHAPTER 4 - REACTOR

LIST OF TABLES

CHAPTER 4 - REACTOR

LIST OF FIGURES

LIST OF FIGURES (Cont'd)

LIST OF FIGURES (Cont'd)

LIST OF FIGURES (Cont'd)

CHAPTER 4 - REACTOR

4.1 SUMMARY DESCRIPTION

The reactor is of the pressurized water type using two reactor coolant loops. A vertical cross section of the reactor is shown in Figure 4.1-1. The reactor core is composed of 177 fuel assemblies and 73 control element assemblies (CEAs). The fuel assemblies are arranged to approximate a right circular cylinder with an equivalent diameter of 123 inches (3.12 meters) and an active length of 150 inches (3.81 meters). The fuel assembly, which provides for 236 fuel rod positions (16 x 16 array), consists of five guide tubes welded to spacer grids and is closed at the top and bottom by end fittings. The guide tubes each displace four fuel rod positions and provide channels which guide the CEAs over their entire length of travel. Incore instrumentation is installed in the central guide tube of selected fuel assemblies. The incore instrumentation is routed into the bottom of the fuel assemblies through the bottom head of the reactor vessel. Figure 4.1-2 shows the reactor core cross section and dimensional relations between fuel assemblies, fuel rods, and CEA guide tubes.

The fuel is low-enrichment UO_2 in the form of ceramic pellets and is encapsulated in prepressurized Zircaloy tubes which form a hermetic enclosure.

The reactor coolant enters the inlet nozzles of the reactor vessel, flows downward between the reactor vessel wall and the core barrel, and passes through the flow skirt section, where the flow distribution is equalized, and into the lower plenum. The coolant then flows upward through the core removing heat from the fuel rods. The heated coolant enters the core outlet region where the coolant flows around the outside of control element assembly shroud tubes to the reactor vessel outlet nozzles. The control element assembly shroud tubes protect the individual neutron absorber elements of the CEAs from the effects of coolant cross-flow above the core.

The reactor internals support and orient the fuel assemblies, control element assemblies, and incore instrumentation, and guide the reactor coolant through the reactor vessel. They also absorb static and dynamic loads and transmit the loads to the reactor vessel flange. They will safely perform their functions during normal operating, upset, and faulted conditions. The internals are designed to safely withstand forces due to dead weight, handling, temperature and pressure differentials, flow impingement, vibration, and seismic acceleration. All reactor components are considered Category I for seismic design. The design of the reactor internals limits deflection where required by function. The stress values of all structural members under normal operating and expected transient conditions are not greater than those established by Section III of the ASME Code. The effect of neutron irradiation on the materials concerned is included in the design evaluation. The effect of accident loadings on the internals is included in the design analysis.

Reactivity control is provided by two independent systems: the control element drive system and the chemical and volume control system. The control element drive system controls short-term reactivity changes and is used for rapid shutdown. The chemical and volume control system is used to compensate for long-term reactivity changes and can make the reactor subcritical without the benefit of the control element drive system. The design of the core and the reactor protection system prevents fuel damage limits from being exceeded for any single malfunction in either of the reactivity control systems.

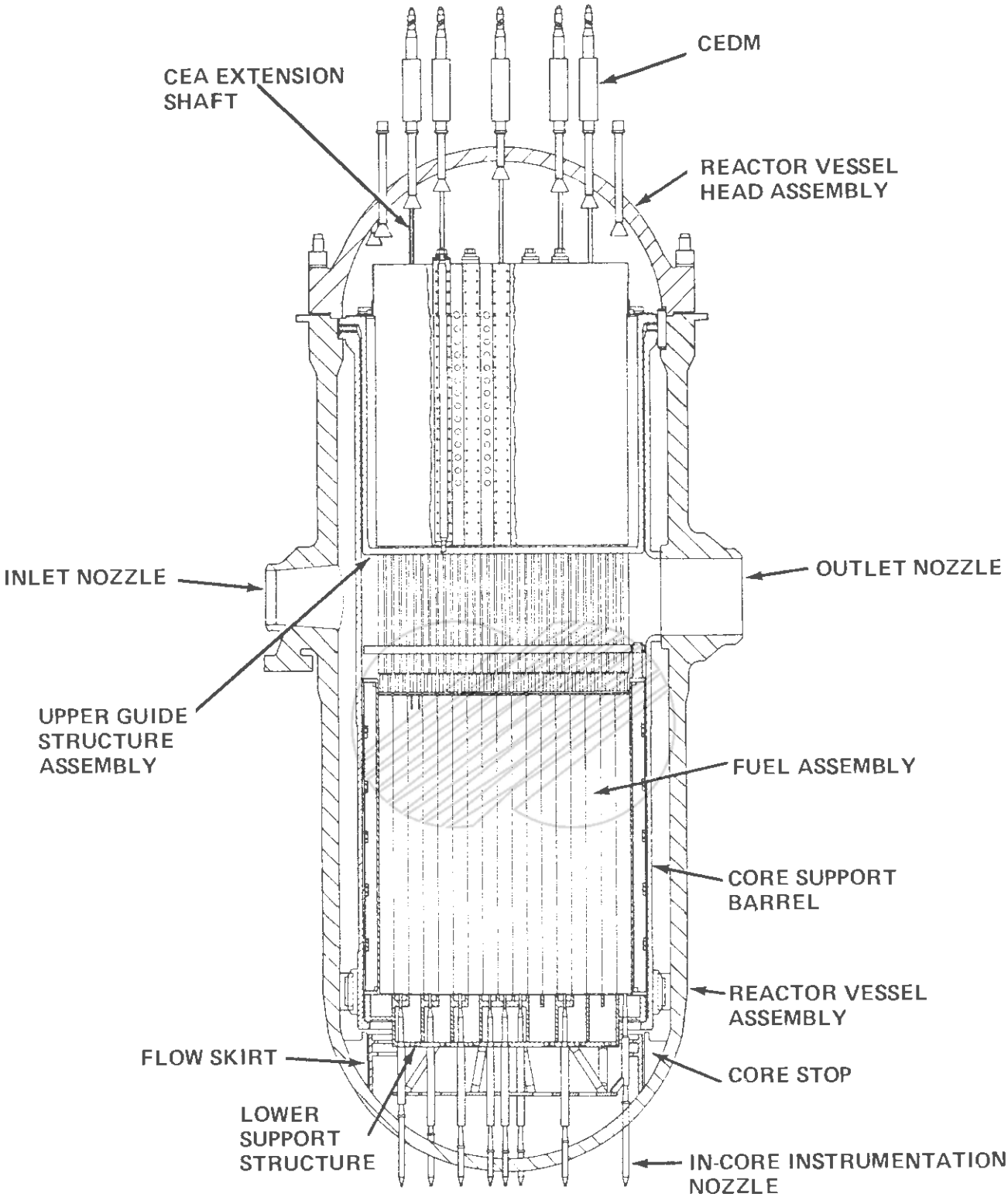

KOREA ELECTRIC POWER CORPORATION
YONGGWANG 3 & 4
FSAR

REACTOR VERTICAL ARRANGEMENT

Figure 4.1-1

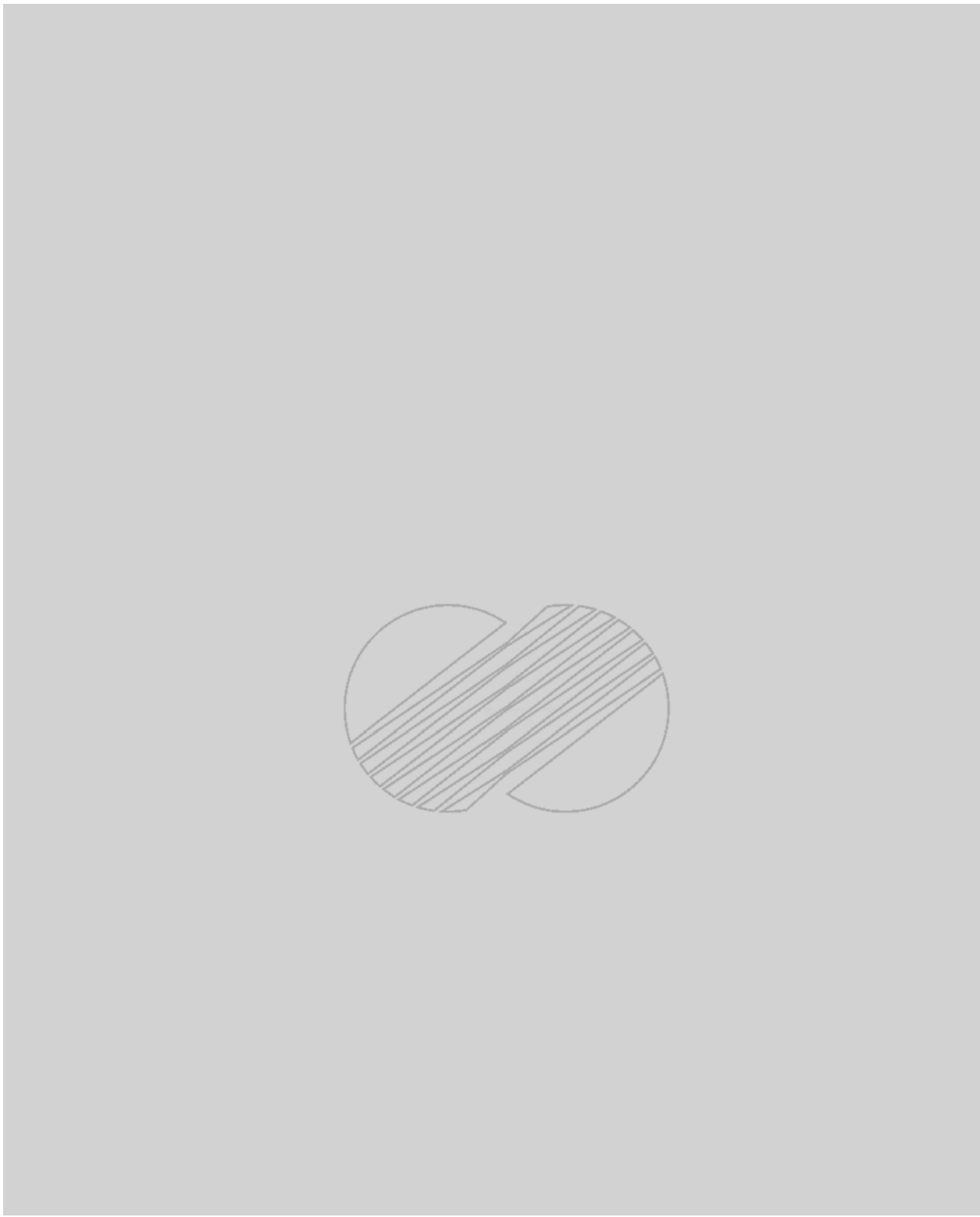

KOREA ELECTRIC POWER CORPORATION
YONGGWANG 3 & 4
FSAR

REACTOR CORE CROSS SECTION

Figure 4.1-2

4.2 FUEL SYSTEM DESIGN

4.2.1 Design Bases

4.2.1.1 Fuel Assembly

The fuel assemblies are required to meet design criteria for each design condition listed below to ensure that the functional requirements are met. Except where specifically noted, the design bases presented in this section are consistent with those used for previous Westinghouse Electronic Company(WEC) 16 x 16 fuel assembly designs.

a. Nonoperation and Normal Operation (Condition I)

Condition I situations are those which are planned or expected to occur in the course of handling, initial shipping, storage, reactor servicing, and power operation (including maneuvering of the plant). Condition I situations must be accommodated without fuel assembly failure and without any effect which would lead to a restriction on subsequent operation of the fuel assembly. The guidelines stated below are used to determine loads during Condition I situations:

1. Handling and Shipping

Loads correspond to the maximum possible axial and lateral loads and accelerations imposed on the fuel assembly by shipping and handling equipment during these periods, assuming that there is no abnormal contact between the fuel assembly and any surface and that there is no equipment malfunction. Irradiation effects on material properties are considered when analyzing the effects of handling loads that occur during refueling. Additional

information regarding shipping and handling loads is contained in Subsection 4.2.3.1.5.

2. Storage

Loads on both new and irradiated fuel assemblies reflect storage conditions of temperature, chemistry, means of support, and duration of storage.

3. Reactor Servicing

Loads on the fuel assembly reflect those encountered during refueling and reconstitution.

4. Power Operation

Loads are derived from conditions encountered during transient and steady-state operation in the design power range. (Hot operational testing, system startup, hot standby, operator-controlled transients within specified rate limits, and system shutdown are included in this category.)

5. Reactor Trip

Loads correspond to those produced in the fuel assembly by control element assembly (CEA) motion and deceleration.

b. Upset Conditions (Condition II)

Condition II situations are unplanned occurrences and operating basis earthquake (OBE) which may occur with moderate frequency during the life of the plant. The fuel assembly design should have the capa-

bility to withstand any upset condition with margin to mechanical failure and with no permanent effects that would prevent continued normal operation. Events classified as upset conditions are listed below:

1. Operating basis earthquake (OBE)

2. Uncontrolled CEA withdrawal

3. Uncontrolled boron dilution

4. Partial loss-of-coolant flow

5. Idle loop startup (in violation of established operating procedures)

6. Loss of load (reactor-turbine load mismatch)

7. Loss of normal feedwater

8. Loss of offsite power

9. Excessive heat removal (feedwater system malfunction)

10. CEA drop

11. Accidental depressurization of the reactor coolant system (RCS)

c. Emergency Conditions (Condition III)

Condition III situations are unplanned incidents which might occur infrequently during plant life. Rod mechanical failure must be

prevented for any Condition III situation in any area not subject to extreme local conditions (e.g., in any rod not immediately adjacent to the impact surface during fuel handling accident). Incidents classified as emergency conditions are listed below:

1. Complete loss or interruption of primary coolant flow at 100% power, excluding reactor coolant pump locked rotor

2. Steam bypass malfunction

3. Minor fuel handling accident (fuel assembly and grapple remain connected)

4. Inadvertent loading of fuel assembly into improper position.

d. Faulted Conditions (Condition IV)

Condition IV situations are postulated accidents (as discussed in Chapter 15) and the safe shutdown earthquake (SSE), LOCA (mechanical excitation only), combined SSE and LOCA, and major fuel handling accident whose consequences are such that integrity and operability of the nuclear energy system may be impaired. Mechanical fuel failures are permitted, but they must not impair the operation of the engineered safety features (ESF) systems to mitigate the consequences of the postulated accident. Accidents classified as faulted conditions are listed below:

1. Safe shutdown earthquake (SSE)

2. Loss-of-coolant accident (LOCA)

3. Locked reactor coolant pump rotor

4. Major secondary system pipe rupture

5. CEA ejection

6. Major fuel handling accident (fuel assembly and grapple are disengaged)

4.2.1.1.1 Fuel Assembly Structural Integrity Criteria

For each of the design conditions, there are criteria which apply to the fuel assembly and components with the exception of fuel rods. These criteria are listed below and give the allowable stresses and functional requirements for each design condition. Criteria for fuel rods are discussed separately in Subsection 4.2.1.2.

a. Design Conditions I and II

$$P_m \leq S_m \qquad (4.2\text{-}1)$$

$$P_m + P_b \leq F_s S_m \qquad (4.2\text{-}2)$$

where P_m, S_m, P_b, and F_s are as defined in d. below.

Under cyclic loading conditions, stresses must be such that the cumulative fatigue damage factor does not exceed 0.8. Cumulative fatigue damage factor is defined as the sum of the ratios of the number of cycles at a given cyclic stress (or strain) condition to the maximum number permitted for that condition. The selected limit of 0.8 is used in place of 1.0 (which would correspond to the absolute maximum fatigue damage factor permitted) to provide additional margin in the design.

During the OBE, fuel assembly deflections must be such that permanent deformations are limited to a value allowing the CEAs to scram.

b. Design Condition III

$$P_m \leq 1.5\ S_m \qquad (4.2\text{-}3)$$

$$P_m + P_b \leq 1.5\ F_s S_m \qquad (4.2\text{-}4)$$

where P_m, S_m, P_b, and F_s are as defined in d. below.

c. Design Condition IV

$$P_m \leq S'_m \qquad (4.2\text{-}5)$$

$$P_m + P_b \leq F_s S'_m \qquad (4.2\text{-}6)$$

where the symbols are as defined in d. below and

S'_m = smaller value of 2.4 S_m or 0.7 S_u.

1. For small pipe break LOCA in which the break equivalent diameter is less than 0.5 ft^2 (0.046 m^2), the fuel assembly deformation shall be limited to a value not exceeding the deformation that would preclude satisfactory insertion of the CEAs. For the small break cold leg LOCA event, CEAs shall be capable of scramming within the 90% insertion time limit.

2. For large pipe break LOCA in which the break equivalent diameter is greater than 0.5 ft^2 (0.046 m^2), deformation of structural components is limited to maintain the fuel in a coolable array. CEA insertion is not required for these events as the appropriate safety analyses do not take credit for CEA insertion.

3. For the upper end fitting holddown springs, calculated shear stress must not exceed the minimum yield stress in shear.

4. For the spacer grids, the predicted impact loads must be less than the tested grid capability, as defined in Reference 46.

5. During the SSE, fuel assembly deflections must be such that permanent deformations are limited to a value allowing the CEAs to scram.

d. Nomenclature

The symbols used in defining the allowable stress levels are as follows:

P_m = Calculated general primary membrane stress*

P_b = Calculated primary bending stress*

S_m = Design stress intensity value as defined by Section III, ASME Boiler and Pressure Vessel Code**

---

* P_m and P_b are defined by Section III, ASME Boiler and Pressure Vessel Code.

** With the exception of zirconium base alloys, the design stress intensity values, S_m, of materials not tabulated by the Code are determined in the same manner as the Code. The design stress intensity of zirconium base alloys shall not exceed two-thirds of the unirradiated minimum yield strength at temperature. Basing the design stress intensity on the unirradiated yield strength is conservative because the yield strength of zircaloy increases with irradiation. The use of the two-thirds factor ensures 50% margin to component yielding in response to primary stresses. This 50% margin, together with its application to the minimum unirradiated properties and the general conservatism applied in the establishment of design conditions, is sufficient to ensure an adequate design.

S_u = Minimum unirradiated ultimate tensile strength

F_s = Shape factor corresponding to the particular cross section being analyzed*

S'_m = Design stress intensity value for faulted conditions

The definition of S'_m as the lesser value of 2.4 S_m and 0.7 S_u is contained in the ASME Boiler and Pressure Vessel Code, Section III.

4.2.1.1.2 Material Selection

The GUARDIAN fuel assembly grid cage structure consists of 10 Zircaloy-4 spacer grids, 1 Inconel 625 GUARDIAN spacer grid (at the lower end), 5 Zircaloy-4 guide tubes, 2 stainless steel end fittings, and 4 Inconel X-750 coil springs. ZIRLO and M5 selected for fuel rod cladding and Zircaloy-4 selected for guide tubes, and spacer grids, have a low neutron absorption cross section and high corrosion resistance to reactor coolant environment. ZIRLO and M5 selected for fuel rod cladding, has a superior corrosion resistance and lower in-reactor irradiation growth. Also, there is little reaction between the cladding and fuel or fission products. As described in Subsection 4.2.3, ZIRLO and M5 as cladding, Zircaloy-4 as a CEA guide tubes, fuel rod endplug, and spacer grids have demonstrated their ability.

The bottom spacer grid of the GUARDIAN fuel assembly is Inconel 625 and is welded to the lower end fitting. In this region of local inlet turbulence, Inconel 625 was selected rather than Zircaloy-4 to provide additional strength and relaxation resistance. Inconel 625 is a very strong material with good ductility, corrosion resistance and stability under irradiation at temperatures below 1000 °F (537.8 °C).

---

* The shape factor, Fs, is defined as the ratio of the "plastic" moment (all fibers just at the yield stress) to the initial yield amount (extreme fiber at the yield stress and all other fibers stressed in proportion to their distance from the neutral axis). The capability of cross sections loaded in bending to sustain moments considerably in excess of that required to yield the outermost fibers is discussed in Timoshenko (Reference 1).

The materials used in the components of PLUS7 fuel assembly is very similar to those of GUARDIAN fuel assembly. But there is a little difference in the materials of spacer grid, guide tubes and Inconel components. PLUS7 fuel assembly skeleton consists of nine ZIRLO spacer grids, three Inconel-718 spacer grids(top, bottom and protective grid), five ZIRLO guide tubes, 304 stainless steel lower and upper end fittings and four Inconel-718 coil prings. The top and bottom grids are connected to guide tubes by sleeves and protective grid is fixed between guide tubes endplug and the top of Lower end fitting using the washers welded at intersection of grid strips,

The fuel assembly upper and lower end fittings are of cast Type 304 stainless steel, and the upper and lower end fitting posts are Type 304 stainless steel machined components. This material was selected based on considerations of adequate strength and high corrosion resistance. Also, Type 304 stainless steel has been used successfully in almost all pressurized water reactor environments, including all currently operating WEC reactors.

4.2.1.1.3 Control Element Assembly Guide Tubes

All CEA guide tubes are manufactured in accordance with ASTM B353, "Wrought Zirconium and Zirconium Alloy Seamless and Welded Tubes for Nuclear Service," with the following exceptions and/or additions:

a. Chemical Properties

Additional limits for Zircaloy-4 are placed on oxygen, carbon, and silicon. Additional limits for ZIRLO are placed on alloying element of niobium, tin, iron, oxygen, and impurities. 733

b. Mechanical Properties

Minimum values are specified for the tensile strength, yield strength, and total elongation at room temperature and high temperature.

"Delete"

4.2.1.1.4 Zircaloy-4 Bar Stock

All Zircaloy-4 bar stock is fabricated in accordance with Grade R60804, ASTM B351, "Hot-Rolled and Cold-Finished Zirconium and Zirconium Alloy Bars, Rod and Wire for Nuclear Application," with the following exceptions and/or additions:

a. Chemical Properties

Additional limits are placed on alloying element of tin, oxygen, and impurities. 733

b. Metallurgical Properties

The maximum average grain size is restricted.

4.2.1.1.5 Zircaloy-4 and ZIRLO Strip Stock

All Zircaloy-4 and ZIRLO strip stock is fabricated in accordance with ASTM B352, "Zirconium and Zirconium Alloy Sheet, Strip and Plate for Nuclear Application," with the following exceptions and/or additions:

a. Chemical Properties

Zircaloy-4 strip stock restricts the content of tin, iron, chromium, and oxygen. Some limits are placed on impurities. ZIRLO strip stock restricts the content of tin, iron, oxygen and niobium and some limits are placed on impurities.

"Delete"

b. Mechanical Properties

The minimum values of yield strength, tensile strength and total elongation at room temperature are specified. A bending test is performed to ensure adequate formability.

4.2.1.1.6 Stainless Steel Castings

All stainless steel castings are fabricated in accordance with Grade CF-8, ASTM A744, with the following addition:

Heat treatment is specified to meet designated cooling rate and the acceptable level delta ferrite.

The stainless steel precision casting for PLUS7 fabricated in accordance with Grade CF3 are inspected by tensile test at room temperature, liquid penetration test and radiographic test.

4.2.1.1.7 Stainless Steel Tubing

All stainless steel tubing is fabricated in accordance with ASTM A269, with the following addition:

Carbon content is limited on tubing to be welded.

The stainless steel tubing for PLUS7 fabricated in accordance with Grade 304 or 304 L is additionally controlled for cobalt content.

4.2.1.1.8 Inconel Compression Springs

All Inconel springs are fabricated in accordance with AMS 5699, with the following additions:

a. Specific lubrication coating is specified to avoid copper contamination.
b. Microstructures are examined to ensuree limination of process related surface defects.

All Inconel wires for PLUS7 fabricated in accordance with Grade Inconel 718 are inspected for alloy composition, grain size, tensile properties at room temperature and eddy current test, The compression springs are inspected by the penetration test.

4.2.1.1.9 Inconel Bottom Spacer Grid Strip Material

Inconel spacer grid strip material is procured in accordance with the specification for nickel-chromium-molybdenum-columbium alloy plate, sheet, and strip, Specification ASTM B443, with the following additional requirements:

"Delete"

The Inconel strips for PLUS7 fabricated in accordance with Inconel 718 are inspected for alloy composition, hardness, bending properties, microstructure including grain size, and tensile properties at room temperature.

4.2.1.2 Fuel Rods

4.2.1.2.1 Fuel Cladding Design Limits

The fuel cladding is designed to sustain the effects of steady-state and expected transient operating conditions without exceeding acceptable levels of stress and strain. Except where specifically noted, the design bases presented in this section are consistent with those used for previous WEC and KNFC core designs. The fuel rod design accounts for cladding irradiation growth, external pressure, differential expansion of fuel and clad, fuel swelling,

densification, clad creep, fission and other gas releases, initial internal helium pressure, thermal stress, pressure and temperature cycling, and flow-induced vibrations. The structural criteria discussed below are based on the following for the normal, upset, and emergency loading combinations identified in Subsection 4.2.1.1. For a discussion of the thermal/hydraulic criteria, see Subsection 4.4.1.

a. During normal operating and upset conditions, the maximum primary tensile stress in the clad shall not exceed two-thirds of the minimum unirradiated yield strength of the material at the applicable temperature. The corresponding limit under emergency conditions is the material yield strength and the limit for faulted conditions is the smaller value of 1.6 times the yield strength or 0.7 times the ultimate strength. The use of the unirradiated material yield strength as the basis for allowable stress is conservative because the yield strength of clad increases with irradiation. The use of the two-thirds factor ensures 50% margin to component yielding in response to primary stresses. This 50% margin, together with its application to the minimum unirradiated properties and the general conservatism applied in the establishment of design conditions, is sufficient to ensure an adequate design.

b. Net unrecoverable circumferential strain shall not exceed 1% as predicted by computations considering clad creep and fuel-clad interaction effects.

"Delete"

The acceptability of this design limit is demonstrated by the fact that the ductility of ZIRLO and M5 clad is similar to that of Zircaloy(Reference 69, 73 and Table 4.2-3) and also, the ductility of Zircaloy is enough for the design limit based on the collected data until now. 733

"Delete"

c. The clad is initially pressurized with helium to an amount sufficient to prevent gross clad deformation under the combined effects of external pressure and long-term creep. For conservatism, the clad design does not rely on the support of the holddown spring in the plenum region.

d. Cumulative fatigue damage factor, defined as the sum of the ratios of the number of cycles in a given effective strain range ($\triangle\varepsilon$)to the permitted number (N) at that range, as taken from Figure 4.2-2, will not exceed 0.8.

"Delete"

"Delete"

For the cycle strain limit design curve, O'Donnell and Langer curve(Reference 13) is used considering a minimum safety factor of 2 on the stress amplitude or a minimum safety factor of 20 on the number of cycles, whichever is more conservative(Reference 69).

As discussed in Subsection 4.2.1.2.5, the fatigue calculation method includes the effect of clad creep to reduce the pellet-to-clad diametral gap during that portion of operation when the pellet and clad are not in contact. The same model is used for predicting clad fatigue as is used for predicting clad strain. Therefore, the effects of creep and fatigue loadings are considered together in determining end-of-life clad strain. From the calculated strain and the cyclic strain limit design curve, the permitted number of cycles and thus the cumulative strain cycling usage defined as above is evaluated.

e. There is no specific limit on lateral fuel rod deflection for structural integrity considerations except that which is brought about through application of cladding stress criteria. The absence of a specific limit on rod deflection is justified because it is the fuel assembly structure and not the individual fuel rod that is the limiting factor for fuel assembly lateral deflection.

f. The fuel rod internal pressure increases with increasing burnup, and toward end-of-life, the total internal pressure, due to the combined effects of the initial helium fill gas and the released fission gas, can approach values comparable to the external primary coolant pressure. The maximum predicted fuel rod internal pressure is consistent with the following criteria:

1. The primary stress in the cladding resulting from differential pressure does not exceed the stress limits specified earlier in this section.

2. The internal pressure does not cause the clad to creep outward from the fuel pellet surface while operating at the design peak linear heat rate for normal operation. In determining compliance with this criterion, internal pressure is calculated for the peak power rod in the reactor, including accounting for the maximum computed fission gas release. In addition, the pellet swelling rate (to which the calculated clad creep rate is compared) is based on the observed swelling rate of "restrained" pellets (i.e., pellets in contact with clad), rather than on the greater observed swelling behavior of pellets which are free to expand.

   The criteria discussed above do not limit fuel rod internal pressure to values less than the primary coolant pressure, and the occurrence of positive differential pressures would not adversely affect normal operation if appropriate criteria for cladding stress, strain, and strain rate were satisfied.

g. The design limits of the fuel rod cladding, with respect to vibration considerations, are incorporated within the fuel assembly design. It is a requirement that the spacer grid intervals, in conjunction with the fuel rod stiffness, be such that fuel rod vibration, as a result of mechanical or flow induced excitation, does not result in excessive wear of the fuel rod cladding at the spacer grid contact areas.

h. The cladding tubes undergo at slow rates in reactor operation. This causes tinning of the cladding tubes walls and impairs heat transfer to the coolant. The burnup extension of fuel rod causes the increase of the corrosion and the resultant enhanced corrosion can impair mechanical integrity of fuel rods. An extensive corrosion and high burnup program showed that PWR fuel rods retain their mechanical integrity during normal operation and handling up to a corrosion layer thickness of 100 ㎛ with sufficient safety margin against failure. Therefore, as a proper restricted value, a circumferential averaged corrosion layer thickness of 100㎛ is specified for design limit.

4.2.1.2.2 Fuel Rod Cladding Properties

4.2.1.2.2.1 Mechanical Properties

a. Modulus of Elasticity

Young's Modulus is as follows.

$E(psi) = 1.685x10^{7}-7.5x10^{3}xT$ (T:°F) (ZIRLO)
$E(MPa) = 1.0606x10^{5}-47.64xT$ (T: K) (M5)

b. Poisson's Ratio

Poisson's Ratio is as follows.

$\nu = 0.3699 - 4.092x10^{-5}xT$ (T: °F) (ZIRLO)
$\nu = 0.37$ (M5)

c. Thermal Coefficient of Expansion

Thermal coefficient of expansion in the diametral direction is as follows.

$\Delta R/R = 3.22x10^{-6}x(T-70)$ (T: °F) (ZIRLO)
$\Delta R/R = 8.31x10^{-6}x(T-20)$ (T: °C) (M5)

d. Yield Strength

Yield strength is as follows.

ZIRLO: 531 MPa
M5: 250 MPa

e. Ultimate Strength

Ultimate tensile strength is as follows.

ZIRLO: 710 MPa
M5: 400 MPa

f. Uniform Tensile Strain

Uniform tensile strain is as follows.

ZIRLO: 1 %
M5: 1 %

"Delete" 733

4.2.1.2.2.2 Dimensional Requirements

a. Tube straightness is limited to 0.010 in/ft, and inside diameter and wall thickness are tightly controlled.

b. Ovality is measured as the difference between maximum and minimum inside diameters and is acceptable if within the diameter tolerances.

c. Outside diameter is specified as 0.382 inch for GUARDIAN fuel and 0.374 inch for PLUS7 fuel.

d. Inside diameter is specified as 0.332 inch for GUARDIAN fuel and 0.329 inch for PLUS7 fuel.

"Delete" 733

e. Wall thickness is specified as 0.023 inch minimum for GUARDIAN fuel and 0.0207 inch minimum for PLUS7 fuel. 733

4.2.1.2.2.3 Metallurgical Properties

A restriction is placed on the hydride orientation factor for any third wall thickness of the tube cross section (inside, middle, or outside). The hydride orientation factor, defined as the ratio of the number of radially oriented hydride platelets to the total number of hydride platelets, shall not exceed 0.3. The independent evaluation of three portions of the cross section is included to allow for the possibility that hydride orientation may not be uniform across the entire cross section.

4.2.1.2.2.4 Chemical Properties

All fuel rod cladding is manufactured in accordance with ASM B811, "Standard Specification for Wrought Zirconium Alloy Seamless Tubes for Nuclear Reactor Fuel Cladding," except additional limits for ZIRLO cladding are placed on tin, oxygen, niobium, iron and impurities. Additional limits for M5 cladding are placed on niobium, oxygen, sulfur and impurities. 733

4.2.1.2.3 Fuel Rod Component Properties

4.2.1.2.3.1 Zircaloy-4 Bar Stock

All Zircaloy-4 bar stock is fabricated in accordance with ASTM B351, "Hot-Rolled and Cold-Finished Zirconium and Zirconium Alloy Bars, Rod and Wire for Nuclear Application," with the following exceptions and additions:

a. Chemical Properties

Additional limits are placed on alloying element of tin, oxygen, and impurities. 733

b. Metallurgical Properties

The maximum average grain size is restricted.

c. Nondestructive Testing

Ultrasonic inspection is required.

4.2.1.2.3.2 Stainless Steel Compression Springs

All stainless steel springs are fabricated from 302 stainless steel wire manufactured in accordance with "Delete" ASTM A313. 733

4.2.1.2.4 UO_2 Fuel Pellet Properties

4.2.1.2.4.1 Chemical Composition

Salient points regarding the structure, composition, and properties of the UO_2 fuel pellets are discussed in the following subsections. Where the effect of irradiation on a specific item is considered to be of sufficient importance to warrant reflection in the design or analyses, that effect is also discussed.

a. Chemical analyses are performed for the constituents specified in the material specification.

"Delete"

b. The oxygen-to-uranium ratio is maintained between 1.99 and 2.01.

c. The sum of the cross sections of impurities shall not exceed a equivalent thermal neutron capture cross section of natural boron specified in material specification.

d. The total hydrogen content of finished ground pellets is restricted.

e. The nominal enrichment of the fuel pellets is specified and shall be held within ±0.05 wt.% U-235.

4.2.1.2.4.2 Microstructure

a. The pellet fabrication process maximizes the pore content of pellets in a specified range. Acceptable porosity distribution is determined by comparison of approved visual standards with photo-micrographs from each pellet lot.

b. The average grain size shall exceed a specified minimum size.

4.2.1.2.4.3 Density

a. The density of the sintered pellet after grinding shall be between [redacted] and [redacted] of theoretical density (TD), based on a UO_2 theoretical density of 10.96 g/cm^3.

b. The in-pile stability of the fuel is ensured by the use of an NRC-approved out-of-pile test during production. The details of this test, and the associated rationale, are presented in References 15, 63 64 and 67. | 109

c. The effects of irradiation on the density of sintered UO_2 pellets are treated in compliance with Regulatory Guide 1.126, Revision 1, by virtue of the NRC approved model for fuel evaluation presented in References 15, 63, 64 and 67. | 109

4.2.1.2.4.4 Thermal Properties

a. Thermal Expansion

The thermal expansion of UO_2 is described by the following temperature-dependent equations (References 16, 17):

$$\% \text{ Linear Expansion} = (-1.723 \times 10^{-2}) + (6.797 \times 10^{-4}\ T) + (2.896 \times 10^{-7}\ T^2) \quad \text{from } 25°C \text{ to } 2200°C \qquad (4.2\text{-}7)$$

$$\% \text{ Linear Expansion} = 0.204 + (3 \times 10^{-4} T) + (2 \times 10^{-7}\ T^2) + (10^{-10}\ T^3) \quad \text{above } 2200°C. \qquad (4.2\text{-}8)$$

where T = temperature (°C).

b. Thermal Emissivity

A value of 0.85 is used for the thermal emissivity of UO_2 pellets over the temperature range 800 to 2600 K (References 18 , 19, and 20).

c. Melting Point and Thermal Conductivity

The variation of melting point and thermal conductivity with burnup is discussed in Reference 15.

d. Specific Heat of UO_2

The specific heat of UO_2 is described by the following temperature-dependent equations (Reference 21):

$T < 2240°F$

$$C_p = 49.67 + 2.2784 \times 10^{-3}T - \frac{3.2432 \times 10^6}{(T + 460)^2} \qquad (4.2\text{-}9)$$

$T \geq 2240°F$

$$C_p = -126.07 + 0.2621T - 1.399 \times 10^{-4}T^2 + 3.1786 \times 10^{-8}T^3 - 2.483 \times 10^{-12}T^4 \qquad (4.2\text{-}10)$$

where:

C_p = specific heat ($Btu/ft^3\text{-}°F$)

T = temperature ($°F$)

4.2.1.2.4.5 Mechanical Properties

a. Young's Modulus of Elasticity

The static modulus of elasticity of unirradiated fuel of 97% TD and deformed under a strain rate of 0.097 (hr^{-1}) is given by (Reference 22):

$$E = 14.22\ (1.6715 \times 10^6 - 924.4T) \qquad (4.2\text{-}11)$$

at $1000°C \leq T \leq 1700°C$

where:

E = modulus of elasticity in psi,

T = temperature in °C

b. Poisson's Ratio

The Poisson's Ratio of polycrystalline UO_2 has a value of 0.32 at 25°C based on Reference 23. The same reference notes a 10% decrease in value over the range of 25 °C to 1800 °C. Assuming the decrease is linear, the temperature dependence of the Poisson's Ratio (υ) is given by the following equation:

$$\upsilon = 0.32 - (T-25) \times (1.8 \times 10^{-5}) \quad (4.2\text{-}12)$$
$$\text{at } 25\ ^{\circ}C \leq T \leq 1800^{\circ}C$$

where:

υ = Poisson's Ratio
T = temperature in °C

At temperature above 1800 °C, a constant value of 0.29 is used for Poisson's Ratio.

"Delete"

4.2.1.2.5 Fuel Rod Pressurization

Fuel rods are initially pressurized with helium for two reasons:

a. To preclude clad collapse during the design life of the fuel. Internal pressurization, by reducing stresses from differential pressure, extends the time required to produce creep collapse beyond the required service life of the fuel.

b. To improve the thermal conductivity of the pellet-to-clad gap within the fuel rod. Helium has a higher coefficient of thermal conductivity than the gaseous fission products.

In unpressurized fuel, the initially good helium conductivity is eventually degraded through the addition of the fission product gases released from the pellets. The initial helium pressurization results in a high helium-to-fission products ratio over the design life of the fuel with a corresponding increase in the gap conductivity and heat transfer. The effect of fuel rod power level and pin burnup on fuel rod internal pressure has been studied parametrically.

The initial helium fill pressure is [redacted] for GUARDIAN fuel and [redacted] for PLUS7 fuel. This initial fill pressure is sufficient to prevent clad collapse discussed in Subsection 4.2.3.2.7 and produce a maximum EOL internal pressure consistent with the criteria of Subsection 4.2.1.2.1. The calculational methods employed to generate internal pressure histories are discussed in References 15, 63, and 64.

4.2.1.2.5.1 Capacity for Fission Gas Inventory

The greater portion of the gaseous fission products remain either within the lattice or the microporosity of the UO_2 fuel pellets and do not contribute to the fuel rod internal pressure. However, a fraction of the fission gas is released from the pellets by diffusion and pore migration and thereafter contributes to the internal pressure.

The determination of the effect of fission gas generated in and released from the pellet column is discussed in Subsection 4.2.3.2.2. The rod pressure increase, which results from the release of a given quantity of gas from the fuel pellets, depends upon the amount of open void volume available within the fuel rod and the temperatures associated with the various void volumes. In

the fuel rod design, the following void volumes are considered in computing internal pressure:

a. Fuel rod upper end plenum

b. Fuel clad annulus

c. Fuel pellet end dishes and chamfers

d. Fuel pellet open porosity

e. Fuel crack volume

These volumes are not constant during the life of the fuel. The model used for computing the available volume as a function of burnup and power level accounts for the effects of fuel and clad thermal expansion, fuel pellet densification, clad creep, clad growth, and irradiation-induced swelling of the fuel pellets.

4.2.1.2.5.2 Fuel Rod Plenum Design

The fuel rod upper end plenum is required to serve the following functions:

a. Provide space for axial thermal expansion and burnup swelling of the pellet column.

b. Contain the pellet column holddown spring.

c. Act as a plenum region to ensure an acceptable range of fuel rod internal pressure.

Of these functions, Item c is the most limiting constraint on plenum length selection, since the range of temperatures in the fuel rod, together with the effects of swelling, thermal expansion, and fission gas release, produce a wide range of internal pressure during the life of the fuel. The fuel rod plenum pressure is consistent with the pressurization and clad collapse criteria specified in Subsection 4.2.1.2.1.

4.2.1.2.5.3 Outline of Procedure Used to Size the Fuel Rod Plenum

a. A parametric study of the effects of plenum length on maximum and minimum rod internal pressure is performed. Because the criteria pertaining to maximum and minimum rod internal pressure differ, the study is divided into two sections:

1. Maximum Internal Pressure Calculation

Maximum rod pressure is limited by the criteria specified in Subsection 4.2.1.2. Maximum end-of-life pressure is determined for each plenum length by including the fission gas released, selecting conservative values for component dimensions and properties, and accounting for burnup effects on component dimensions. The primary cladding stress produced by each maximum pressure is then compared with the stress limits to find the margin available with each plenum length. Stress limits are listed in Subsection 4.2.1.2.1.

2. Minimum Internal Pressure/Collapse Calculation

Minimum rod pressure is limited by the criterion that no rod will be subject to collapse during the design lifetime. The minimum pressure history for each plenum length is determined by neglecting fission gas release, selecting a conservative combination

of component dimensions and properties, and accounting for dimension changes during irradiation, including the effects of cladding creep, cladding growth, pellet densification, pellet swelling, and thermal expansion. Each minimum pressure history is inputted to the cladding collapse model (References 26 and 65) to establish the acceptability of the associated plenum length.

b. For each plenum length, there is a resultant range of acceptable initial fill pressures. The optimum plenum length is generally considered to be the shortest, which satisfies all criteria related to maximum and minimum rod internal pressure including a range sufficient to accommodate a reasonable manufacturing tolerance on initial fill pressure.

c. Additional information on those factors that have a bearing on determination of the plenum length are discussed below:

1. Creep and dimensional stability of the fuel rod assembly influence the fission gas release model and internal pressure calculations, and are accounted for in the procedure of sizing the fuel rod plenum length. Creep in the cladding is accounted for in a change in clad inside diameter, which in turn influences the fuel/clad gap. The gap change varies the gap conductance in the FATES computer code (References 15, 63, 64, 69 and 73) with resulting change in annulus temperature, internal pressure, and fission gas release. In addition, the change in clad inside diameter causes a change in the internal volume, with its resulting effect on temperature and pressure. Dimensional stability considerations affect the internal volume of the fuel rod, causing changes in internal pressure and temperature. Fuel pellet densification reduces the stack height and pellet diameter. Irradiation-induced radial and axial swelling of the fuel pellets decreases the internal

volumewithin the fuel rod. In-pile growth of the fuel rod cladding contributes to the internal volume. Axial and radial elastic deformation calculations for the cladding are based on the differential pressure the cladding is exposed to, resulting in internal volume changes. Thermal relocation, as well as differential thermal expansion of the fuel rod materials, also affects the internal volume of the fuel rods.

2. The maximum expected fission gas release in the peak power rod is calculated using the FATES computer code. Rod power history input to the code is consistent with the design limit peak linear heat rate set by LOCA considerations, and therefore, the gas release used to size the plenum represents an upper limit.

Because of time-varying gap conductance, fuel temperature and depletion,and expected fuel management, the release rate varies as a function of burnup.

4.2.1.2.6 Fuel Rod Performance

Steady-state fuel temperatures are determined by the FATES computer program. The calculational procedure considers the effect of linear heat rate, fuel relocation, fuel swelling, densification, thermal expansion, fission gas release, and clad deformations. The model for predicting fuel thermal performance, including the specific effects of fuel densification on increased LHGR and stored energy, is discussed in References 15, 63, 64, 69 and 73.

Significant parameters such as cold pellet and clad diameters, gas pressure and composition, burnup, and void volumes are calculated and used as initial conditions for subsequent calculations for stored energy during the ECCS analysis. The coupling mechanism between FATES calculations and the ECCS analysis is described in detail in Reference 27.

Discussions of uncertainties associated with the model and of comparative analytical and experimental results are also included in References 15, 63, 64 67 and 68.

4.2.1.3 Burnable Poison Rods

4.2.1.3.1 Burnable Poison Rod Cladding Design Limits

The burnable poison rod design, similar to the fuel rod design, accounts for external pressure, differential expansion of pellets and clad, pellet swelling, clad creep, fission gas release, initial internal helium pressure, thermal stress, and flow-induced vibrations. Except where specifically noted, the design bases presented in this section are consistent with those used for the fuel rod design. The structural criteria for the normal, upset, and emergency loading combinations are identified in Subsections 4.2.1.1 and 4.2.1.2 and are highlighted as follows:

a. During normal operating and upset conditions, the maximum primary tensile stress in the clad shall not exceed two-thirds of the minimum unirradiated yield strength of the material at the applicable temperature. The corresponding limit under emergency conditions is the material yield strength and the limit for faulted conditions is the smaller value of 1.6 times the yield strength or 0.7 times the ultimate strength.

b. Net unrecoverable circumferential clad strain shall not exceed 1% as predicted by computations considering clad creep and poison pellet swelling effects.

c. The clad is initially pressurized with helium to an amount sufficient to prevent gross clad deformation under the combined effects of external pressure and long-term creep. For conservatism, the clad

design does not rely on the support of the holddown spring in the plenum region.

4.2.1.3.2 Burnable Poison Rod Cladding Properties

Cladding tubes for burnable poison rods are purchased under the specification for fuel rod cladding tubes. Therefore, the mechanical, metallurgical, chemical, and dimensional properties of the cladding are as discussed in Subsection 4.2.1.2.2.

4.2.1.3.3 Gd_2O_3-UO_2 Burnable Poison Pellet Properties

4.2.1.3.3.1 Thermal-Physical Properties

This section describes evaluations of gadolinia-urania properties and of thermal conductivity and melting temperature correlations appropriate for gadolinia-urania compositions of interest in PWR applications of Gd_2O_3-UO_2 burnable absorbers.

The material properties that influence the thermal performance of gadolinia-urania fuel have been reviewed to ascertain how UO_2 properties are influenced by the addition of gadolinia. These include the thermal conductivity, solidus temperature, specific heat, and the coefficient of thermal expansion. The effects of gadolinium addition on these properties are discussed in detail in Reference 28.

4.2.1.3.3.1.1 Thermal Conductivity

The thermal conductivity (k) is calculated as the product of the measured thermal diffusivity (ㅓ), density (½), and specific heat (C_p) according to the following relation:

$$k = ㅓ \ ½ \ C_p \qquad (4.2\text{-}13)$$

The effects that Gd_2O_3 addition have on the corresponding UO_2 material properties for each of these three properties are discussed as follows:

a. Density

When a solid solution of Gd_2O_3-UO_2 is formed, gadolinium atoms replace some of the uranium atoms in the UO_2 crystalline lattice. This substitution by lighter gadolinium atoms causes a reduction in the theoretical density of UO_2 and in the lattice spacing. Combining the effects of reduced atomic weight in the unit cell, due to the lighter gadolinium atoms, and reduced unit cell volume, due to changes in lattice spacing, yields the following correlation for the theoretical density of Gd_2O_3-UO_2 solid solutions:

$$\rho_{th} = 10.96 - 0.033x \qquad (4.2\text{-}14)$$

where:

ρ_{th} = the theoretical density of Gd_2O_3-UO_2 solid solution in gm/cm^3

x = the weight percent of Gd_2O_3

b. Specific Heat

The relatively recent work of B&W (Reference 29), although limited to temperatures below 1800℃, shows that the specific heat of gadolinia-urania mixtures of up to 8 wt.% Gd_2O_3 does not differ significantly from that of pure UO_2. Within the temperature range of 900℃ to 1800℃, the reported specific heat of the mixture is slightly higher than that of pure UO_2. Determination of the specific heat of gadolinia-urania mixtures in the temperature and composition ranges

of interest in PWR application is included in the workscope of a research program for the determination of the properties of gadolinia-urania sponsored by the Nuclear Fuel Industry Research Group (NFIR).

"Delete"

Based on the existing information, and considering that the Gd_2O_3 content is not likely to exceed 12 wt.%, the specific heat of gadolinia-urania solid solutions can be conservatively assumed to be identical to that of pure UO_2. This assumption is conservative because the measured specific heat of either form of pure gadolinium is higher than that of UO_2 within the measured range of temperatures. Thus, the use of UO_2 specific heat will result in a low value for gadolinia-urania conductivity.

c. Thermal Diffusivity

A review of the literature reveals that five separate experimental studies have been done on the thermal diffusivity of sintered gadolinia-urania solid solutions (References 29, 30, 31, 32, and 33). The early work of Lee and Kim (Reference 33) was not used in this evaluation because no information was given on characterization of the fuel except for its composition. The remaining data sets were utilized to quantify the influence of gadolinium addition on the thermal diffusivity of gadoliniam-urania fuel.

A problem was noted, however, in that while the individual experimental data are internally consistent (i.e., diffusivities decrease with increasing Gd_2O_3 additions and high temperature mixture diffusivities approach pure UO_2 values), absolute values of diffusivities at common compositions and temperatures vary between experiments.

Experimental parameters that might contribute to inconsistencies, such as sample preparation techniques, specimen densities, specimen stoichiometry, specimen homogeneity, and measurement techniques, were apparently similar among the experiments. Therefore, the reason(s) for this variation has not been determined.

In order to utilize the data in a consistent manner, and to smooth out variations among experiments, a normalization procedure was developed. This enabled development of the needed correlations of the variation in properties with gadolinia content. For a given experiment, each individual diffusivity value was normalized to the pure UO_2 diffusivity measured by that experiment at the same (or an interpolated) temperature. These "normalized" diffusivities, which provide the ensitivity of diffusivity to Gd_2O_3 concentration, were used with the WEC expression for pure UO_2 conductivity to derive a conductivity expression for gadolinia-urania fuel.

d. Thermal Conductivity

The values of Gd_2O_3-UO_2 conductivity were generated using above mentioned data with the expression for UO_2 conductivity. A least-squares analysis was performed with these data and a modified form of the CE conductivity expression for pure UO_2 to obtain the following relation for the conductivity of 95% dense gadolinia-urania fuel.

The specific equation that defines the thermal conductivity of the Gd_2O_3-UO_2 mixture is contained in Reference 28. At 0 wt.% Gd_2O_3, this equation reduces to the conductivity for pure UO_2 given in Reference 15. For bulk densities other than 95% of theoretical density, conductivity given by the equation is adjusted by the Maxwell-Eucken correction (References 15 and 34) used for pure UO_2.

4.2.1.3.3.1.2 Solidus Temperature

The most recent study of the gadolinia-urania solidus temperature is being conducted by Battelle Northwest Laboratory under the sponsorship of NFIR (Reference 30). Although this investigation is incomplete, the preliminary results indicate that within the accuracy of the measuring technique (~10℃), the addition of 4 wt.% Gd_2O_3 produces no measurable decrease in solidus temperature from that of pure UO_2.

Based on existing data in the literature, the best estimate of the solidus line in the dilute solid solutions of gadolinia-urania is that supported by the data of Wada et al. (Reference 35) and Newman et al. (Reference 29). Specific data points which support a linear decrease in solidus temperature with increasing Gd_2O_3 content are shown in Reference 28.

"Delete"

4.2.1.3.3.1.3 Specific Heat

As discussed in Subsection 4.2.1.3.3.1.1, the available data on the specific heat of gadolinia-urania, although limited, do not suggest that any significant difference exists between the specific heat of uranium and gadolinia-urania up to 8 wt.% Gd_2O_3. Based on these data, the specific heat of pure UO_2 is used in modeling the thermal performance of gadolinia-urania solid solutions.

4.2.1.3.3.1.4 Coefficient of Thermal Expansion

Data presented by Newman et al. (Reference 29) indicate that up to at least 1600℃ (i.e., the upper limit of their data) the Gd_2O_3 content has very little effect on the linear thermal expansion of Gd_2O_3-UO_2 solid solutions. It is reasonable to assume (see Reference 35) that the thermal expansion correlation for pure UO_2 can be used for dilute solid solutions of Gd_2O_3-UO_2 beyond the

1600°C upper limit of the B&W data base. Hence, the thermal expansion of Gd_2O_3-UO_2 solid solutions up to 12 wt.% Gd_2O_3 is assumed to be the same as pure UO_2.

4.2.1.4 Control Element Assemblies

Except where specifically noted, the design bases presented in this section are consistent with those used for previous designs.

The mechanical design of the control element assemblies (CEAs) is based on compliance with the following functional requirements and criteria:

a. Short-term reactivity control is provided for or initiated under all normal and adverse conditions experienced during reactor startup, normal operation, shutdown, and accident conditions.

b. Mechanical clearances of the CEAs within the fuel and reactor internals are such that the requirements for CEA positioning and reactor trip are attained under the most adverse accumulation of tolerances.

c. Structural material characteristics are such that radiation-induced changes to the CEA materials will not impair the functions of the reactivity control system.

4.2.1.4.1 Thermal and Physical Properties of Absorber Material

The primary control element absorber materials consist of boron carbide (B_4C) pellets. Inconel Alloy 625 is used as the absorber material for the part strength control elements. Refer to Figures 4.2-3, 4.2-4, and 4.2-5 for the specific application and orientation of the absorber materials. The significant thermal and physical properties used in mechanical analysis of the

absorber materials are listed in Table 4.2-1.

4.2.1.4.2 Compatibility of Absorber and Cladding Materials

The cladding material used for the control elements is Inconel Alloy 625. The selection of this material for cladding is based on a consideration of strength, creep resistance, corrosion resistance, and dimensional stability under irradiation and also upon the acceptable performance of this material for this application in other WEC reactors currently in operation.

a. B_4C/Inconel 625 Compatibility

Studies have been conducted by HEDL(Reference 36) on the capability of Type 316 stainless steel with B_4C under irradiation for thousands of hours at temperatures between 1300 °F (704.4℃) and 1600 °F (871.1 ℃). Carbide formation to a depth of about 0.004 inch (0.1 mm) in the Type 316 stainless steel was measured after 4400 hours at 1300 °F (704.4℃). Similar compound formation depths were observed after ex-reactor bench testing. After testing at 1000 °F (537.8 ℃), only 0.001 in/yr of penetration was measured. Since Inconel 625 is more resistant to carbide formation than Type 316 stainless steel, and the expected pellet/clad interfacial temperature in the standard design is below 800°F (426.7℃), it is concluded that B4C is compatible with Inconel 625.

4.2.1.4.3 Cladding Stress-Strain Limits

The stress limits for the Inconel Alloy 625 cladding are as follows:

a. Nonoperation, normal operation, and upset conditions:

$$P_m \leq S_m$$
$$P_m + P_b \leq F_s S_m$$

The net unrecoverable circumferential strain shall not exceed 1% on the cladding diameter, considering the effects of pellet swelling and cladding creep.

b. Emergency conditions

$P_m \leq 1.5\ S_m$

$P_m + P_b \leq 1.5\ F_s S_m$

c. Faulted conditions

$P_m \leq S'_m$

$P_m + P_b \leq F_s S'_m$

where S'_m is the smaller of $2.4\ S_m$ or $0.7\ S_u$

For definitions of P_m, P_b, S_m, S'_m, S_u, and F_s, see Subsection 4.2.1.1.1. For the Inconel 625 CEA cladding, the value of S_m is two-thirds of the minimum specified yield strength at temperature.

For Inconel 625, the specified minimum yield strength is 65,000 lb/in^2 (4570 kg/cm^2) at 650°F (343.3°C).

F_s = Mp/My where Mp is the bending moment required to produce a fully plastic section and My is the bending moment that first produces yielding at the extreme fibers of the cross section. The capability of cross sections loaded in bending to sustain moments considerably in excess of that required to yield the outermost fiber is discussed in Reference 1. For the CEA cladding dimensions, F_s = 1.33.

The values of uniform and total elongation of Inconel Alloy 625 cladding are estimated to be as follows:

Fluence (E > 1 MeV), (nvt)	1×10^{22}	3×10^{22}
Uniform elongation (%)	3	1
Total elongation (%)	6	3

4.2.1.4.4 Irradiation Behavior of Absorber Materials

a. Boron Carbide

1. Swelling

The linear swelling of B_4C increases with burnup according to the relationship:

$$\% \ L = (0.1) \text{ B-10 Burnup, a/o}$$

This relationship was obtained from experimental irradiations on high density (>90% theoretical density (TD)) wafers (Reference 37) and pellets with densities ranging between 71% and 98% TD (References 36 and 38). Dimensional changes were measured as a function of burnup, after irradiating at temperatures expected in the design.

2. Thermal Conductivity

The thermal conductivity of unirradiated 73% dense B_4C decreases linearly with temperatures from 300°F (148.9°C) to 1600°F (871.1°C), according to the following relationship:

$$\lambda = \frac{1 \text{ cal/cm-K-sec}}{2.17\ (6.87 + 0.017\ T)} \qquad (4.2\text{-}15)$$

where T = temperature (K)

This relationship was obtained from measurements performed on pellets ranging from 70% to 98% TD (Reference 39).

The relationship between the thermal conductivity of irradiated 73% TD B_4C pellets and temperature given below was derived from measured values (Reference 39) on higher density pellets irradiated to fluences out to 3×10^{22} nvt (E > 1 MeV).

$$\lambda = \frac{1 \text{ cal/cm-K-sec}}{2.17\ (38 + 0.025\ T)} \qquad (4.2\text{-}16)$$

where T = temperature (K)

Thermal conductivity measurements of seventeen B_4C specimens with densities ranging from 83% to 98% TD, irradiated at temperatures from 930°F (498.9°C) to 1600°F (871.1°C) showed that thermal conductivity decreased significantly after irradiation. The rate of decrease is high at the lower irradiation temperatures, but saturates rapidly with exposure.

3. Helium Release

Helium is formed in B_4C as B-10 burnup progresses. The fraction of helium released from the pellets is important for determining rod internal gas pressure. The relationship between helium release and irradiation temperature given below was developed at ORNL (Reference 40) to fit experimental data obtained from thermal reactor irradiations.

$$\% \text{ He release} = e^{(C-1.85D)}\ e^{-Q/RT} \qquad (4.2\text{-}17)$$

where:

C = Constant (6.69 for pellets)

D = Fractional density (0.73 for CE pellets)

Q = Activation energy constant (3600 cal/mole)

R = Gas Constant (1.98 cal/mole - K)

T = Pellet temperature (K)

This expression becomes

$$\% \text{ He release} = 208\ e^{(-1820/T)} + 5$$

when the above parameters are substituted. In this form, design values for helium release as a function of temperature are generated. The 5% helium release allowance (the last term in the expression) was added to ensure that design values lie above all reported helium release data. Calculated values of helium release obtained from the recommended design expression lie above all experimental data points (References 36, 41, and 42) obtained on B_4C pellet specimens irradiated in thermal reactors.

4. Pellet Porosity

Experimental evidence is available(Reference 43) which shows that for pellet densities below 90%, essentially all porosity is open at beginning-of-life. Irradiation-induced swelling does not change the characteristics of the porosity, but only changes the bulk volume of the specimens. Therefore, the amount of porosity available at end-of-life is the same as that present at beginning-of-life.

b. Inconel 625

1. Swelling

Available information indicates that Inconel 625 is highly resistant to radiation swelling. Exposure of Inconel 625 to a fluence of 3×10^{22} nvt (E > 1 MeV) at a temperature of 400℃ (725°F)showed no visible cavities in metallographic examinations (Reference 44) so that swelling, if any, would be very minor. Direct measurements made after exposure of Inconel 625 to a fluence 5×10^{22} nvt (E > 1 MeV) as LMFBR conditions showed no evidence of swelling (Reference 45). Further exposure to 6×10^{22} nvt (E > 1 MeV) at 500℃ (932°F) showed essentially no swelling as measured by immersion density, but did show small cavities. Thus, Inconel 625 is not cted to swell below fluences of 3×10^{22} nvt (E > 1 MeV).

2. Ductility

The ductility of Inconel 625 decreases after irradiation. Extrapolation of lower fluence data on Inconel 625 and 500 indicates that the values of uniform and total elongation of Inconel 625

after 1 x 10^{22} nvt (E > 1 MeV) are 3% and 6%, respectively.

3. Strength

The value of yield strength of Inconel 625 increases after irradiation in the manner typical for metals. However, no credit is taken for increases in yield strength in the design analyses above the value initially specified.

4.2.1.5 Surveillance Program

4.2.1.5.1 Requirements for Surveillance and Testing of Irradiated Fuel Rods

The surveillance program for ZIRLO clad has been performed in the North Anna-1. The program included a poolside examination campaign after first and second operational cycles. The examinations include visual inspection for overall performance, dimensional measurements and cladding oxide measurements to track corrosion behavior of ZIRLO material. Results after the first and second cycle operations indicated the fuel behaved as expected with no indications that would alter the planned fuel management scheme for the WEC fuel.

The surveillance program has been performed in the YGN Unit 4 to observe the spacer grid-to-rod fretting wear performance of the ZIRLO fuel cladding in the GUARDIAN grid fuel assembly. The results showed that the grid-to-rod fretting wear depths were less than the design limit and would not be a concern in the GUARDIAN grid fuel assembly.

An irradiation program for the PLUS7 fuel assemblies are being performed in the UCN Unit 3. Four PLUS7 fuel assemblies were loaded from the cycle 5 and will be operating for the following two cycles. In particular, based on the third cycle irradiation performance results, one fuel assembly will be loaded again for fourth cycle operation for evaluating the high burnup fuel performance. The poolside examinations include visual inspections for overall performance, dimensional measurements to characterize growth behavior, and cladding oxide measurements to track corrosion behavior of the ZIRLO material. Results after the first and second cycle operations indicated the fuel behaved as expected with no indications that would alter the planned fuel management scheme of the PLUS7 fuel. The same examination will be done for the third cycle irradiated fuels. Also hot cell examinations by non-destructive and destructive tests are planned for the third or fourth cycle irradiated PLUS7 fuels.

4.2.2 Description and Design Drawings

This subsection summarizes the mechanical design characteristics of the fuel

system and discusses the design parameters that are of significance to the performance of the reactor. A summary of mechanical design parameters is presented in Table 4.2-2. These data are intended to be descriptive of the design; limiting values of these and other parameters will be discussed in the appropriate sections.

4.2.2.1 Fuel Assembly

a. GUARDIAN Fuel Assembly

The fuel assembly (Figure 4.2-6) consists of 236 fuel and gadolinium (poison) rods, 5 guide tubes, 11 fuel rod spacer grids, upper and lower end fittings, and a holddown device. The outer guide tubes, spacer grids, and end fittings form the structural frame of the assembly.

The fuel spacer grids (Figure 4.2-7) maintain the fuel rod array by providing positive lateral restraint to the fuel rod but only frictional restraint to axial fuel rod motion. The grids are fabricated from preformed Zircaloy or Inconel strips (the bottom spacer grid material is Inconel) interlocked in an egg crate fashion and welded together. Each cell of the spacer grid contains two leaf springs and four arches. The leaf springs press the rod against the arches to restrict relative motion between the grids and the fuel rods. The perimeter strips contain features designed to prevent hangup of grids during a refueling operation.

The ten Zircaloy-4 spacer grids are fastened to the Zircaloy-4 guide tubes by welding, and each grid is welded to each guide tube at eight locations, four on the upper face of the grid and four on the lower face of the grid, where the spacer strips contact the guide tube surface. The lowest spacer grid (Inconel) is not welded to the guide tubes due to material differences. It is supported by an Inconel 625 skirt, which is welded to the spacer grid and to welded to the perimeter of the lower end fitting.

The upper end fitting is an assembly consisting of two cast Type 304 stainless steel plates, five machined posts, and four helical Inconel X-750 springs. The upper end fitting attaches to the guide tubes to serve as an alignment and locating device for each fuel assembly and has features to permit lifting of the fuel assembly. The lower cast plate locates the top ends of the guide tubes and is designed to prevent excessive axial motion of the fuel rods.

The Inconel X-750 springs are of conventional coil design having a mean diameter of 1.859 in (47.2 mm), a wire diameter of 0.319 in (8.10 mm), and approximately 16 active coils. Inconel X-750 was selected for this application because of its previous use for coil springs and good resistance to relaxation during operation.

The upper cast plate of the assembly, called the holddown plate, together with the helical compression springs, comprise the holddown device. The holddown plate is movable, acts on the underside of the extended tube of the upper guide structure, and is loaded by the compression springs. Since the springs are located at the upper end of the assembly, the spring load combines with the fuel assembly weight to counteract upward hydraulic forces. The determination of upward hydraulic forces includes factors accounting for flow maldistribution, fuel assembly component tolerances, crud buildup, drag coefficient, and bypass flow. The springs are sized and the spring preload is selected such that a net downward force will be maintained for all normal and anticipated transient flow and temperature conditions. The design criteria limit the maximum stress under the most adverse tolerance conditions to below the yield strength of the spring material. The maximum stress occurs during cold conditions and decreases as the reactor heats up. The reduction in stress is due to a decrease in spring deflection resulting from differential thermal expansion between the Zircaloy fuel assemblies and the stainless steel internals.

During normal operation, a spring will never be compressed to its solid height. However, if the fuel assembly were loaded in an abnormal manner such that a spring were compressed to its solid height, the spring would continue to serve its function when the loading condition returned to normal.

The lower end fitting is a simple stainless steel casting consisting of a plate with flow holes and a support leg at each corner (total of four legs) that aligns the lower end of the fuel assembly with the core support structure's alignment pins. Each alignment pin is required to position the corners of four lower end fittings.

The four outer guide tubes have a widened region at the upper end which contains an internal thread. Connection with the upper end fitting is made by passing the externally threaded end of the guide posts through holes in the lower cast flow plate and into the guide tubes. When assembled, the flow plate is secured between flanges on the guide tubes and on the guide posts. The connection with the upper end fitting is locked with a mechanical crimp. Each outer guide tube has, at its lower end, a welded Zircaloy-4 fitting. This fitting has a threaded portion which passes through a hole in the fuel assembly lower end fitting and is secured by a Zircaloy-4 nut. This joint is secured with a stainless steel locking disc tack welded to the lower end fitting in four places.

The center instrumentation guide tube inserts into a socket and slot in the upper and lower end fittings, respectively, and is thus retained laterally by the relatively small clearance at these locations. The upper end fitting socket is created by the center guide tube post which is threaded into the lower cast flow plate and tack welded in four places. There is no positive axial connection between the center guide tube and the end fittings.

The five guide tubes have the effect of ensuring that bowing or excessive swelling of the adjacent fuel rods cannot result in obstruction of the control element pathway. This is so for two reasons:

1) There is sufficient clearance between the fuel rods and the guide tube surface to allow an adjacent fuel rod to reach rupture strain due to excessive swelling without contacting the guide tube surface.

2) The guide tube, having considerably greater diameter and wall thickness (and also, being at a lower temperature) than the fuel rod, is considerably stiffer than the fuel rods and would, therefore, remain straight, rather than be deflected by contact with the surface of an adjacent bowed fuel rod.

Therefore, the bowing or swelling of fuel rods would not result in obstruction of the control element channels such as could hinder CEA movement.

The fuel assembly design enables reconstitution, i.e., removal and replacement of fuel and poison rods, of an irradiated fuel assembly. The fuel and poison rod lower end caps are conically shaped to ensure proper insertion within the fuel assembly grid cage structure; the upper end caps are designed to enable grappling of the fuel and poison rod for removal and handling. Threaded joints that mechanically attach the upper end fitting to the control element guide tubes will be properly torqued and locked during service, but may be removed to provide access to the fuel and poison rods.

Loading and movement of the fuel assemblies is conducted in accordance with strictly monitored administrative procedures and, at the completion of fuel loading, an independent check as to the location and orientation of each fuel assembly in the core is required.

The serial number provided on the fuel assembly upper end fitting enables verification of fuel enrichment and orientation of the fuel assembly. The serial number is also provided on the lower end fitting to ensure preservation of fuel assembly identity in the event of upper end fitting removal. Additional markings are provided on the fuel rod upper end caps as a secondary check to distinguish between fuel enrichments and burnable poison rods, if present.

During the manufacturing process, the lower end cap of each rod is marked to provide a means of identifying the pellet enrichment, pellet lot, and fuel stack weight. In addition, a quality control program requires that measures be established for the identification and control of materials, components, and partially fabricated subassemblies. These means provide assurance that only acceptable items are used and also provide a method of relating an item or assembly from initial receipt through fabrication, installation, repair, or modification to an applicable drawing, specification, or other pertinent technical document.

b. PLUS7 fuel assembly

The PLUS7 fuel assembly(Figure 4.2-6a) consists of 236 fuel and gadolinium(poison) rods, 5 guide tubes, 12 fuel rod spacer grids, upper and lower end fittings and a holddown device. The outer guide tubes, spacer grids, and end fittings form the structural frame of the assembly.

The twelve spacer grids such as Figure 4.2-6a consist of nine ZIRLO mid spacer grids, one Inconel top and bottom grids, and one Inconel protective grid (Figure 4.2-7a)and maintain the fuel rod array by providing positive lateral restraint to the fuel rod but only frictional restraint to axial fuel rod motion. The grids are fabricated from preformed ZIRLO or Inconel strips interlocked in an egg crate fashion and welded together.

Each cell of the ZIRLO spacer grid contains 2 contoured springs and 4 contoured dimples. The mid grids have the mixing vane to improve the thermal performance by enhancing the coolant mixing ability. Inconel top and bottom

grid consist of 2 springs and 4 dimples. Inconel top grid is designed to have reduced spring force to minimize the potential for fuel rod bow, whereas Inconel bottom grid has a high spring force that is capable of providing fuel rod support up to design burnup. Inconel protective grid contains compliant dimples that provide a coplanar four point contact with fuel rod in each grid cell. With small holed nozzle and fuel rod solid endplug, Inconel grid is designed to trap and filter foreign materials. Outer strap of grid has a design characters to prevent the hang-up on grid of adjacent fuel assembly during the reloading operation

Using mid grid sleeve that is attached to mid grid by welding, ZIRLO mid grids are welded to guide tubes and instrument tube to fix their axial position in fuel assembly. Inconel top and bottom grids are fixed through the sleeves which are wleded to guide tube and instrument tube.

The upper end fitting is an assembly consisting of two cast type 304 stainless steel plates, four machined outer posts, and four helical Inconel springs. The upper end fitting is attached to the guide tube assembly using inner extension inserted into outer guide post to serve as an alignment and locating device for each fuel assembly and has features to permit lifting of the fuel assembly. The lower cast plate, called flow plate, located at the top ends of the guide tubes and is designed to prevent excessive axial motion of the fuel rods.

The Inconel 718 was selected for hold down spring application not only because of its previous use for coil spring but also good resistance to relaxation during operation. The design requirements and function of PLUS7 holddown spring and holddown plate are same as those of Guardian's.

The lower end fitting is consisting of a plate with flow holes, a support leg at each corner(total of four legs), a skirt plate and a cylinderical instrument guide. The flow plate is machined and has functions to filter the foreign materials with Inconel protective gird. The support leg aligns the lower end of the fuel assembly with the core support structure's alignment pins. Each alignment pin is required to position the corners of four lower end fittings.

The four outer guide tubes are welded to the internally threaded flange at the upper end. Connection with the upper end fitting is made by passing the externally threaded end of the inner extension into the outer guide post and guide tube flange and the inner extension is threaded into guide tube flange and the upper head of inner extension crimped to prevent un-torqueing at the upper portion of outer guide post. Each outer guide tubes is, at its lower end, welded to the internally threaded endplug. The lower end fitting is attached to the guide tube endplug by thimble screws which penetrate through the flow plate of lower end fitting and protective grid washer. The screws are locked in place by expanding a thin walled section of the screw cap into cutout in the underside of the plate.

PLUS7 fuel assembly have the same functional and design requirements of GUARDIAN fuel assembly except for above features

4.2.2.2 Fuel Rods

The fuel rods consist of slightly enriched UO_2 cylindrical ceramic pellets, a round wire Type 302 stainless steel compression spring, and bottom alumina spacer disc (for GUARDIAN) all encapsulated within a clad tube seal welded with Zircaloy-4 end caps. The fuel rods are internally pressurized with helium during assembly. Figure 4.2-8 and Figure 4.2-8a depict the GUARDIAN fuel rod and PLUS7 fuel rod design, respectively. PLUS7 fuel rod uses axial balnket(low enriched UO_2 pellet) to reduce axial neutron leakage in the top and the bottom of fuel rod stacked region in UO_2 fuel rod.

Each fuel rod includes both a serial number and a visual identification mark. The serial number ensures traceability of the fabrication history of each fuel rod component. The identification mark provides a visual check on pellet enrichment batch during fuel fabrication.

The fuel cladding is cold-worked and stress-relief-annealed ZIRLO and recrystallized M5 tube. The actual tube forming process consists of a series of cold working and annealing operations, the details of which are selected to provide the combination of properties discussed in Subsection 4.2.1.2.2.

The UO_2 pellets are dished at both ends in order to better accommodate thermal expansion and fuel swelling. The density of the UO_2 in the pellets is 10.44 g/cm^3, which corresponds to 95.25% of the 10.96 g/cm^3 theoretical density (TD) of UO_2. However, because of the volume of the pellet dishes and chamfers, the average density of the pellet stack is reduced to 10.114 g/cm^3 for GUARDIAN fuel and 10.313 g/cm^3 for PLUS7 fuel, respectively. This number is referred to as the "stack density."

The compression spring located at the top of the fuel pellet column maintains the column in its proper position during handling and shipping. The alumina spacer disc at the lower end of the GUARDIAN fuel rod reduces the lower end cap temperature. The fuel rod plenum, which is located above the pellet column, provides space for axial thermal differential expansion of the fuel column and accommodates the initial helium loading and evolved fission gases (see Subsections 4.2.1.2.5.1 and 4.2.1.2.5.2). The specific manner in which these factors are taken into account, including the calculation of temperatures for the gas contained within the various types of rod internal void volume, is discussed in References 15 and 63.

4.2.2.3 Burnable Poison Rods

The burnable absorber (poison) rods are included in selected fuel assemblies to reduce the beginning-of-life moderator coefficient. They replace fuel rods at selected locations. The poison rods (Figure 4.2-9 and 4.2-9a) are mechanically similar to fuel rods, but GUARDIAN fuel rods consist of Gd_2O_3 admixed in natural UO_2 in the

central rod portion of the effective fuel region and natural UO_2 at the top and bottom portions of the effective fuel region. PLUS7 fuel rods consist of Gd_2O_3 admixed in low enriched UO_2 in the central rod portion of the effective fuel region and low enriched UO_2 at the top and bottom portion of the effective fuel region. The total column length is the same as the column length in the fuel rods.

Each poison rod assembly includes a serial number and visual identification mark. The serial number is used to record fabrication information for each component in the rod assembly. The identification mark is unique to poison rods and provides a visual check on the pellet gadolinium content during fuel bundle fabrication.

4.2.2.4 Control Element Assemblies

The control element assemblies (CEAs) consist of both four and twelve neutron absorber elements arranged to engage the peripheral guide tubes of fuel assemblies. The neutron absorber elements are connected by a spider structure which couples to the control element drive mechanism (CEDM) drive shaft extension. The neutron absorber elements of a four-element CEA engage the four corner guide tubes in a single fuel assembly. The four-element CEAs are used for control of power distribution and core reactivity in the power operating range. The twelve-element CEAs engage the four corner guide tubes in one fuel assembly and the two nearest corner guide tubes in adjacent fuel assemblies. The twelve-element CEAs make up the balance of the control groups of CEAs and provide a bank of strong shutdown rods. The control element assemblies are shown in Figures 4.2-3, 4.2-4, and 4.2-5. The pattern of CEAs (total of 73) is shown in Figure 4.2-10. Note that up to eight additional CEAs may be installed if desired for additional flexibility or future use.

Part-strength CEAs are differentiated from full-strength CEAs by using alpha-numeric serialization instead of the numerical system used on the full-strength CEAs.

The control elements of a full-strength CEA consist of an Inconel 625 tube loaded with a stack of cylindrical absorber pellets. The absorber material

consists of 73% TD boron carbide (B_4C) pellets, with the exception of the lower portion of the elements, which contain reduced-diameter B_4C pellets wrapped in a sleeve of Type 347 stainless steel felt metal.

The design objective realized by the use of felt metal and reduced-diameter B_4C pellets in the element tip zones is that as the B_4C pellets swell due to irradiation, the felt-metal sleeve compresses as a result of the applied loading. This compression limits the amount of induced strain in the cladding. Therefore, suitable buffering of the CEA following scram, which occurs when the element tips enter a reduced diameter portion of the fuel assembly guide tubes, is not affected with long-term exposure of the CEA to reactor operating conditions. | 164

During normal powered operation, most of the CEAs are expected to be in the fully withdrawn position. Thus, the local B-10 burnup progresses at a lower rate, and CEA life is prolonged.

Above the poison column is a plenum which provides expansion volume for helium released from the B_4C. The plenum volume contains a Type 302 stainless steel holddown spring, which restrains the absorber material against longitudinal shifting with respect to the clad while allowing for differential expansion between the absorber and the clad. The spring develops a load sufficient to maintain the position of the absorber material during shipping and handling.

Each full-strength control element is sealed by welds which join the tube to an Inconel 625 nose cap at the bottom and an Inconel 625 connector at the top which makes up part of the end fitting at the top. The end fittings, in turn, are threaded and crimped in place by a locking nut to the spider structure, which provides rigid lateral and axial support for the control elements. The spider hub bore is specially machined to provide a point of attachment for the CEA extension shaft.

Eight of the 73 CEAs are part-strength CEAs. The control elements of a part-strength CEA consist of Inconel 625 slugs over the entire active length.

Each full-strength or part-strength CEA is positioned by a magnetic jack control element drive mechanism (CEDM) mounted on the reactor vessel closure head. The extension shaft joins with the CEA spider and connects the CEA to the CEDM. Full- and part-strength CEAs may be connected to any extension shaft depending on control requirements. Mechanical reactivity control is achieved by positioning groups of CEAs by the CEDMs.

In the outlet plenum region, all CEAs are enclosed in CEA shrouds, which provide guidance and protect the CEA and extension shaft from primary coolant cross flow. Within the core, each element travels in a Zircaloy guide tube. The guide tubes are part of the fuel assembly structure and ensure proper orientation of the control elements with respect to the fuel rods.

When the extension shaft is released by the CEDM, the combined weight of the shaft and CEA causes the CEA to insert into the fuel assembly.

The lower ends of the four outer fuel assembly guide tubes are tapered gradually to form a region of reduced diameter which, in conjunction with the control element on the CEA, constitutes an effective hydraulic buffer for reducing the deceleration loads at the end of a trip stroke. This purely hydraulic damping action is augmented by a spring and plunger arrangement on the CEA spider. When fully inserted, the CEAs rest on the upper guide structure support plate.

The capability of the CEAs to scram within the allowable time is demonstrated as part of the flow testing discussed in Subsection 4.2.4.4.

4.2.2.5 Neutron Source Assemblies

The function of the neutron source assembly, shown in Figure 4.2-11, is to provide a base neutron flux level such that required monitoring of neutron flux level can be accomplished during fuel loading, refueling, and shutdown conditions.
However, in case that the irradiated fuel assemblies provide at least 0.5 counts per second on the source range detectors, the neutron source assemblies can be removed from the reactor core.

4.2.3. Design Evaluation

4.2.3.1 Fuel Assembly

4.2.3.1.1 Vibration Analyses

Four of external excitation are recognized in evaluating the fuel assembly susceptibility to vibration damage. These sources are as follows:

a. Reactor Coolant Pump Blade Passing Frequency

Comprehensive vibration assessment programs on previous WEC reactors indicate that peak pressure pulses are expected at the pump blade passing frequency (120 Hz), with a lesser but still pronounced peak at twice this frequency.

b. Lower Support Structure Motion

Random lateral motion between the fuel assembly and the lower support structure is expected to occur with an amplitude similar to that of other CE reactors in the frequency range of between 2 and 10Hz.

c. Flow Induced Fuel Rod Vibration Resulting from Coolant Flow Through the Fuel Assembly

The expected amplitude of such vibration is 0.004 inches(0.1016 mm)or less.

d. Flow-Induced Control Element Assembly Vibration

YGN 3&4 incorporates design features that minimize possible CEA vibration so that no significant wear is produced in the guide tubes.

These sources of potential excitation are not expected to have an adverse effect on the performance of the YGN 3&4 fuel assembly.

The capability of the YGN 3&4 fuel assembly to sustain the effects of flow-induced vibration without adverse effects has been demonstrated in the dynamic flow tests as reported in Appendix 4B1.

4.2.3.1.2 CEA Guide Tubes

The CEA guide tubes were evaluated for structural adequacy using the criteria given in Subsection 4.2.1.1 in the following areas:

a. Steady axial load due to the combined effects of axial hydraulic forces and upper end fitting holddown forces.

For normal operating conditions, the resultant guide tube stress levels are significantly less than the design limits.

b. Short-term axial load due to the impact of the spring loaded CEA spider against the upper guide structure support plates at the end of a CEA trip.

For trips occurring during normal power operation, solid impact is not predicted to occur because the kinetic energy of the CEA is dissipated in the hydraulic buffer and because of the CEA spring.

c. Short-term differential pressure load occurring in the hydraulic buffer regions of the outer guide tubes at the end of each trip stroke.

The buffer region slows the CEA during the last few inches of the trip stroke. The resultant differential pressure across the guide tube in this region gives rise to circumferential stresses that are significantly less than the design limits. The trip is assumed to be repeated daily. However, the resultant stress is too small to have a significant effect on fatigue usage.

For conditions other than normal operation, the additional mechanical loads imposed on the fuel assembly by an OBE (equivalent to one-half SSE), SSE, and large-break LOCA and their resultant effects on the control element guide tubes are discussed in the following subsection.

4.2.3.1.2.1 Operating Basis Earthquake (OBE)

During the postulated OBE, the fuel assembly is subjected to lateral and axial accelerations which, in turn, cause the fuel assembly to deflect from its normal shape. The method of calculating these deflections is described in Subsection 3.7.3.14. The magnitude of the lateral deflections and resultant stresses are evaluated for acceptability. The method for calculating stresses from deflected shapes is described in Reference 46. The fuel assembly is designed to be capable of withstanding the axial loads without buckling and without sustaining excessive stresses.

4.2.3.1.2.2 Safe Shutdown Earthquake (SSE)

The axial and lateral loads and deformation sustained by the fuel assembly during a postulated SSE have the same origin as those discussed above for the OBE, but they arise from initial ground accelerations twice those assumed for the OBE. The analytical methods used for the SSE are identical to those used for the OBE.

4.2.3.1.2.3 Loss-of-Coolant Accident (LOCA)

In the event of a large-break LOCA, there will occur rapid changes in pressure and flow within the reactor vessel. Associated with the transient are relatively large axial and lateral loads on the fuel assemblies. The response of a fuel assembly to the mechanical loads produced by a LOCA is considered acceptable if the fuel assemblies are maintained in a coolable array, i.e., acceptably lower grid crushing.

4.2.3.1.2.4 Combined SSE and LOCA

For demonstrating margin in the design, the maximum stress intensities for each individual event are combined by a square-root-of-sum-of-the-squares (SRSS) method. This is performed as a function of fuel assembly elevation and position, e.g., the maximum stress intensities for the center guide tube at the upper grid elevation (as determined in the analysis discussed in the above paragraphs for SSE and LOCA) are combined by the SRSS method. Additional details regarding the method of analysis for combining seismic and LOCA loads and stresses are described in Reference 46. The results of the YGN 3&4 analysis demonstrate that the allowable stresses described in Subsection 4.2.1.1 are not exceeded for any position along the fuel assembly even under the added conservatism provided by this load combination.

To qualify the complete fuel assembly, full-scale hot-loop testing has been conducted. These tests evaluated fretting and wear of components, refueling procedures, fuel assembly uplift forces, holddown performance and compatibility of the fuel assembly with interfacing reactor internals, CEAs and CEDMs under conditions of reactor water chemistry, flow velocity, temperature, and pressure. The details of the hot loop testing are reported in Appendix 4B1.

4.2.3.1.3 Spacer Grid Evaluation

The function of the spacer grids is to provide lateral support to fuel and poison rods in such a manner that the axial forces are not sufficient to buckle or bow the rods and that the wear resulting at the grid-to-clad contact points is limited to acceptably small amounts. It is also a criterion that the grid be capable of withstanding the lateral loads imposed during the postulated seismic and LOCA events.

Fuel assemblies are designed such that the combination of fuel rod rigidity, grid spacing, and grid preload will not result in significant fuel rod deformation under axial loads, and the long-term effects of clad creep (reduction in clad OD), the reduction of grid stiffness with temperature and the partial relaxation of the grid material during operation ensure that this criterion is also satisfied during all operating conditions. Moreover, inspection of irradiated fuel assemblies from previous WEC plants -- Maine Yankee (14 x 14), Calvert Cliffs (14 x 14), Palisades (15 x 15), Fort Calhoun (14 x 14), and ANO-2(16 X16) reactors -- has not shown significant bowing of the fuel rods. Also in case of PLUS7 fuel, Inconel top grid has a low spring force than Inconel bottom grid to prevent fuel rod bowing.

In view of these factors and the similarity of these designs to the YGN 3&4 designs, it is concluded that the axial forces applied by the grids on the cladding will not result in a significant degree of fuel rod bow. The influence of fuel rod lateral deflection is discussed further in Subsection 4.2.3.2.6. Additional discussion of the causes for and effects of fuel rod bowing are contained in Subsection 4.2.3.2.5 and in Reference 47, 69 and 73.

The capability of the grids to support the clad without excessive clad wear is demonstrated by out-of-pile flow testing on the Standard System 80 assembly and PLUS7 assembly design and by the results of postirradiation examination of grid-to-clad contact points in Maine Yankee fuel assemblies, which showed only negligible clad wear (Reference 69).

The capability of the grid to withstand the lateral loads produced during the postulated seismic and LOCA events is demonstrated by impact testing of the reference grid design, and comparing the test results with the analytical predictions of the seismic and LOCA loads.

The Zircaloy-4 and ZIRLO spacer grid material is of the almost same composition as the fuel rods and grid tubes with which it is in contact, thereby eliminating any problem of chemical incompatibility with those components. For the same reason, adequate resistance to corrosion from the primary coolant is assured (see Subsection 4.2.3.2.3, item a, for additional information relative to the corrosion resistance of Zircaloy-4 in the primary coolant environment).

The Inconel material used for the lowest spacer grid in GUARDIAN fuel and for the top, bottom and protective spacer grids in PLUS7 is in contact with the coolant, the Type 304 stainless steel lower end fitting (to which it is welded), the fuel rods, the poison rods, and the guide tubes. The mutual chemical compatibility of these materials in a reactor environment has been demonstrated by WEC's use of these materials in fuel assemblies that have been operated in other WEC reactors and for which post-irradiation examination has yielded no evidence of chemical reaction between these components. In addition, experiments have also been performed at WEC on Inconel-type alloys and Zircaloy-4 which showed that eutectic reactions did not occur below 2200°F (1204 ℃), a temperature far in excess of that anticipated at the lower grid location in the event of a LOCA.

4.2.3.1.4 Dimensional Stability of Zircaloy Alloys

Zircaloy and ZIRLO components are designed to allow for dimensional changes resulting from irradiation-induced growth. Extensive analyses of in-pile growth data have been performed to formulate a comprehensive model of in-pile growth (Reference 3 and 70). The in-pile growth equations are used to determine the minimum axial differential growth allowance which must be included in the axial gap between the fuel rods and the upper end fitting. For determining the gap between the fuel rods and the upper end fitting, the growth correlations for fuel rod and guide tube growth are combined statistically such that the minimum initial gap is adequate to accommodate the upper 95% probability level of differential growth between fuel rods and guide tubes in the peak burnup fuel assembly. For predicting axial and lateral growth of the fuel assembly structure (thereby establishing the minimum initial clearance with interfacing components), the equations are used conservatively to ensure adequate margins to interference are maintained. The manner in which the in-pile growth equations are used in design is described in References 4, 49, 69, and 73.

4.2.3.1.5 Fuel Handling and Shipping Design Loads

Three specific design bases have been established for shipping and handling loads:

a. When the fuel assembly supported in the new fuel shipping container, the GUARDIAN fuel assembly shall be capable of sustaining the effect of 5g axial, lateral, or vertical acceleration and the PLUS7 fuel assembly shall be capable of sustaining the effect of 4g axial, 6g lateral or vertical acceleration without sustaining stress levels in excess of those allowed for normal operation. The criterion was originally established experimentally, and its adequacy is continually confirmed by the presence of impact recorders, as discussed in the following paragraph.

Impact recorders are included with each shipment which indicate if loadings in excess of shipping load criteria are sustained. A record of shipping loads in excess of shipping load criteria indicates an unusual shipping occurrence, in which case the fuel assembly is inspected for damage before releasing it for use.

The axial shipping load path is through either end fitting to the guide tubes. A axial shipping load produces a compressive stress level in the guide tubes less than the two-thirds yield stress limit that is allowed for normal condition events. The fuel assembly is prevented from buckling by being clamped at grid locations. For lateral or vertical shipping loads, the grid spring tabs have an initial preload which exceeds shipping load times the fuel rod weight. Therefore, the spring tabs see no additional deflection as a result of shipping load of the shipping container. In addition, the side load on the grid faces produced by the shipping load is less than the measured impact strength of the grids.

b. The fuel assembly shall be capable of sustaining a 5000-pound (2268-kg) axial load applied at the upper end fitting by the refueling grapple (and resisted by an equal load at the lower end fitting) without sustaining stress levels in excess of those allowed for normal operation. The 5000-pound (2268-kg) load was chosen in order to provide adequate lift capability should an assembly become lodged. This load criterion is greater than any lift load that has been encountered in service.

c. The fuel assembly shall be capable of withstanding a 0.125-inch (3.175-mm) deflection in any direction whenever the fuel assembly is raised or lowered from or to a horizontal position without sustaining a permanent deformation beyond the fuel assembly inspection envelope.

Fuel handling procedures require the use of a strongback to limit the fuel assembly deflection to a maximum of 0.125 inch(3.175 mm) in any direction whenever the fuel assembly is raised or lowered from or to a horizontal position. This limits the stress and strain imposed upon the fuel assembly to values well below the limits set for normal operating conditions. The adequacy of the 0.125-inch(3.175 mm) criterion is based on the inclusion of this limitation in specifications and procedures for fuel handling equipment, which is thereby constrained to provide support such that lateral deflection is limited to 0.125 inch(3.175 mm).

4.2.3.1.6 Fuel Assembly Analysis Results

The results of the fuel assembly analysis confirm that the design criteria of Subsection 4.2.1.1, regarding stress, strain, and fatigue, are satisfied including seismic and LOCA conditions.

4.2.3.1.7 Fuel Assembly Liftoff Analysis

The results of the analysis confirm that the fuel assembly will not lift off during reactor operation. This analysis considers the appropriate combination of forces as described in Subsection 4.2.2.1.

4.2.3.2 Fuel Rods

The evaluations discussed in this section are based on assumed fuel rod operation within certain linear heat rate limits related to avoiding excessive fuel and clad temperatures. Information concerning the bases for these limits is contained in Section 4.4.
The results of fuel rod analysis confirm that fuel rod integrity is maintained up to rod average burnup of 60,000 MWD/MTU in the reference 69, 72, and 73.

4.2.3.2.1 Results of Vibration Analyses

Three sources of external excitation are recognized in evaluating the fuel rod susceptibility to vibration damage. These sources are described in Subsection 4.2.3.1.1.

These sources of external excitation are not expected to have an adverse effect on the performance of the fuel rod. Subsection 4.2.3.2.4 includes additional information on fuel rod response to the sources.

4.2.3.2.2 Fuel Rod Internal Pressure and Stress Analysis

A fuel rod cladding stress analysis is conducted to determine the circumferential stress and strain resulting from normal, upset, and emergency conditions. The analysis includes the calculation of cladding temperatures and rod internal pressures during each of the occurrences listed in Subsection 4.2.1.1. The design criteria to be used to evaluate the analytical results are specified in Subsection 4.2.1.2.1. Fuel rod stresses resulting from seismic events are calculated using the methodology described in Reference 46.

The results of the fuel rod analyses confirm that the design criteria of Subsection 4.2.1.2.1 regarding rod internal pressure, stress, strain and strain fatigue are satisfied, including seismic and LOCA conditions. Seismic and LOCA analyses have been performed using the methodology described in Reference 46. The results of the analysis are within the acceptable limits.

4.2.3.2.3 Potential for Chemical Reaction

a. Corrosion

The clad corrosion is mainly affected by cycle length, local heat flux, coolant temperature and coolant chemistry condition. The analysis result with the corrosion evaluation model(reference 69 and 73) confirm that the design limit of section 4.2.1.2.1 regarding cladding corrosion is satisfied for the rod average burnup of up to 60,000 MWD/MTU.

"Delete"

Coolant chemistry parameters have been specified that minimize corrosion product release rates and their mobility in the primary system. Specifically, the precore hot functional environment is controlled (pH and oxygen) to provide a thin, tenacious, adherent, Protective oxide film. This approach minimizes corrosion product release and associated inventory on initial startup and subsequent operation. During operation, the recommended lithium concentration range (0.2-3.5 ppm) effects a chemical potential gradient or driving force between hotter and cooler surfaces (fuel cladding and steam generator tubing, respectively) such that soluble iron and nickel species will preferentially deposit on the steam generator surfaces. The associated pH also minimizes general corrosion product release rates from primary system surfaces. Moreover, the specified hydrogen concentration range ensures reducing conditions in the core, thereby avoiding low solubility Fe^{3+}. Additionally, dissolved hydrogen promotes rapid recombination of oxidizing species. (Recall that oxidizing species and a fast neutron flux are synergistic prerequisites to accelerated corrosion.)

During operation, lithium, dissolved oxygen, and dissolved hydrogen are monitored at a frequency consistent with maintaining these parameters within their specifications.

Postoperational examinations of fuel cladding that has operated within these specifications have shown no significant chemical or corrosive attack of the cladding. Therefore, fuel cladding corrosion does not limit the anticipated performance.

b. External Hydriding

During operation of the reactor with exposure to high-temperature and high-pressure water, cladding reacts to form a protective oxide film in accordance with the following equation:

$$Zr + 2H_2O \rightarrow ZrO_2 + 2H_2$$

[redacted] are absorbed by the ZIRLO and M5, respectively. The analysis result shows that the content of the absorbed hydrogen is less than 400 ppm and will not prove deteriorative to the cladding integrity.

"Delete"

c. Internal Hydriding

A number of reported fuel rod failures have resulted from excessive moisture available in the fuel. Under operation, this moisture oxidizes the cladding. A fraction of the hydrogen, which is generated during normal oxidation, is then absorbed into the cladding.

This localized hydrogen absorption by the cladding results in a localized fuel rod failure. Work performed at the Institute for Atomenergi, Halden Norway, of which WEC is a member, demonstrated that a threshold value of water moisture is required for hydride sunbursts to occur (Reference 51). Through a series of in-pile experiments, the level of this threshold value was established. The allowable hydrogen limit in the fuel complies with this requirement, ensuring that hydride sunbursts will not occur in the fuel rods with the cladding tubes.

d. Crud

Crud layers on zirconium oxide films are usually porous and noninsulating. As an example, heavy, but noninsulating, crud layers have been found in Yankee Rowe (WCAP-3317-6094, Yankee Core Evaluation Program, Final Report, 1971). With porous crud, water is free to flow through the crud and provides heat transfer by convection. Under these conditions, crud-enhanced corrosion should not occur.

Because of rigorous water chemistry monitoring, heavy buildup of crud has not occurred in WEC reactors which are reference model. Water chemistry monitoring is a continuous process and should ensure no dense crud buildup.

e. Fuel-Cladding Chemical Reaction

An in-depth postirradiation examination has been conducted wherein fuel-cladding chemical reactions were among those items studied (Reference 52). This study concluded that early unpressurized elements containing unstable fuel were more susceptible to stress corrosion attack than are the current elements that utilize stable fuel and pressurized cladding. By carefully monitoring the primary coolant activity of operating reactors, it has been concluded that the current fuel designs are not susceptible to stress corrosion cracking during normal plant operation.

Since stress corrosion attack is the result of a combination of stress imposed by the fuel on the cladding and the corrosive chemical species available to the cladding, irradiation programs have been pursued to define the conditions under which pellet-clad interaction will damage the cladding. These programs have been conducted at Halden, at Petten in the Netherlands, and at Studsvik in Sweden, and have confirmed that current fuel designs are not susceptible to failure by stress corrosion cracking during normal plant operation.

4.2.3.2.4 Fretting Corrosion

"Delete"

Since irradiation-induced stress relaxation causes a reduction in grid spring load, spacer grids must be designed for end-of-life conditions as well as beginning-of-life conditions to prevent fretting caused by flow-induced tube vibrations.

"Delete"

The fretting wear in the clad supported by spacer grids is evaluated in Reference 69 and 73. The results show that the clad integrity is not impaired by the spacer grid-to-rod fretting-wear.

4.2.3.2.5 Fuel Rod Bowing

Experience has proved that any specific criterion on allowable deflections (bowing), with respect to the effects which such deflections might have on thermal-hydraulic performance, is not necessary beyond the initial fuel rod positioning requirements of the grids. This variation in spacing is accounted for in the thermal-hydraulic analysis through the introduction of hot channel factors in calculating the maximum enthalpy rise in calculating DNBR.

This adjustment is called the pitch, bowing, and clad diameter enthalpy rise factor, which is conservatively applied to simulate a reduced flow area along the entire channel length. The value of this factor is given in Table 4.4-1 and its application is discussed in Section 4.4.

"Delete"

The subject of fuel rod bowing is discussed in Reference 47, 69 and 73.

4.2.3.2.6 Irradiation Stability of Fuel Rod Cladding

The combined effects of fast flux and cladding temperature are considered in three ways as discussed below:

a. Cladding Creep Rate

The in-pile creep performance of clad is dependent upon both the local material temperature and the local fast neutron flux. The functional form of the dependencies is presented in Reference 15, 26, 65, 69, and 73.

b. Cladding Mechanical Properties

The yield strength, ultimate strength, and ductility of clad are dependent upon temperature and accumulated fast neutron fluence. The temperature and fluence dependence is discussed in Subsection 4.2.1.2.2.1. Unirradiated properties were used depending upon which is more restrictive for the phenomenon evaluated.

c. Irradiation Induced Dimensional Changes

Clad has been shown to sustain dimensional changes (in the unstressed condition)as a function of the accumulated fast fluence.

These changes are considered in the appropriate clearances between the various core components. The irradiation induced growth correlation method is discussed in Reference 3 , 69 and 73.

"Delete"

4.2.3.2.7 Cladding Collapse Analysis

A cladding collapse analysis is performed to ensure that no fuel rod in the core will collapse during its design lifetime. The clad collapse calculation method (References 26 and 65) itself does not include arbitrary safety factors. However, the calculation inputs are deliberately selected to produce a conservative result. For example, the clad dimensional data are chosen to be worst-case combinations based either upon drawing tolerances or 95% confidence limits on as-built dimensions; the internal pressure history is based on minimum fill pressure with no assistance from released fission gas; and the flux and temperature histories are based on conservative assumptions. The result of the analysis confirms that cladding collapse does not occur.

4.2.3.2.8 Fuel Dimension Stability

Fuel swelling due to irradiation (accumulation of solid and gaseous fission products) and thermal expansion results in an increase in the fuel pellet diameter. The design makes provision for accommodating both forms of pellet

growth. The fuel-clad diametral gap is sufficient to accommodate the thermal expansion of the fuel. To accommodate irradiation-induced swelling, it is conservatively assumed that the fuel-clad gap is used up by the thermal expansion and that only the fuel porosity and the dishes on each end of the pellets are available. Thermal- and irradiation-induced creep of the restrained fuel results in redistribution of fuel so that the swelling due to irradiation is accommodated by the free volume. "Delete"

For such restrained pellets, and at a total fission-product-induced swelling rate of [redacted] △v/v per 10^{20} fissions/cm^3, [redacted] would be accommodated by the fuel porosity and dishes through fuel creep, and [redacted] would increase the fuel diameter. Assuming peak burnup,

when these numbers were compared to the minimum available volume and the maximum allowable strain, it was concluded that sufficient accommodation volume has been provided even under the most adverse burnup and tolerance conditions.

Early work on the swelling rates for UO_2 is described in References 8 and 53 through 56. These experiments were conducted using fuel materials made prior to the discovery of densification and would be appropriate for some of WEC's early production. The incorporation of performances that provide more representative fuel microstructures makes a more recent set of data from a WEC-conducted program more appropriate for swelling values.

Fuel pellets were fabricated by WEC and irradiated in Calvert Cliffs for four cycles to burnup levels up to 50 GWd/MTU (Reference 25) and Fort Calhoun for six-cycles to a local burnup of 63.3 GWd/MTU (Reference 68). Immersion density measurements taken from pellets of various burnups were plotted to determine the rate of volume increase with burnup. The rate derived from these measurements was [redacted] △v/v for 10 GWd/MTU in the Calvert Cliffs and [redacted] △v/v for 10 GWd/MTU in the Fort Clahoun. The results show that the fuel swelling rate of [redacted] △v/v for 10 GWd/MTU is valid for fuel burnups to 60 GWd/MTU. Since the levels of burnup were after cladding contact, the swelling value obtained is a restrained swelling

rate. The [redacted] value per 4 GWd/MTU is approximately equal to the [redacted] $\Delta v/v$ per 10^{20} fissions/cm^3 used for the calculation above.

4.2.3.2.9 Potential for Waterlogging Rupture and Chemical Interaction

The potential for waterlogging rupture is considered remote. Basically, the necessary factors, or combination of factors, include the presence of a small opening in the cladding, time to permit filling of the fuel rod with water, and finally, a rapid power transient. The size of the opening necessary to cause a problem falls within a fairly narrow band. Above a certain defect size, the rod can fill rapidly, but during a power increase it also expels water or steam readily without a large pressure buildup. Defects which could result in an opening in cladding are scrupulously checked for during the fuel rod manufacturing process by both ultrasonic and helium leak testing. Clad defects which could develop during reactor operation due to hydriding are also controlled by limiting those factors: e.g., the hydrogen content of fuel pellets, which contributes to hydriding.

The most likely time for a waterlogging rupture incident would be after an abnormally long shutdown period. After this time, however, the startup rate is controlled so that even if a fuel rod were filled with coolant, it would "bake out," thus minimizing the possibility of additional cladding rupture. The combination of control and inspection during the manufacturing process and the limits on the rate of power change restrict the potential for waterlogging rupture to a very small number of fuel rods.

The UO_2 fuel pellets are highly resistant to attack by reactor coolant in the event that cladding defects should occur. Extensive experimental work and operating experience have shown that the design parameters chosen conservatively account for changes in thermal performance during operation and that coolant activity buildup resulting from cladding rupture is limited by the ability of uranium dioxide to retain solid and gaseous fission products.

4.2.3.2.10 Fuel Burnup Experience

The WEC fuel rod design is based on an extensive experimental data base and by an extension of experimental knowledge through design application of WEC fuel rod evaluation codes. The experimental data base includes data from WEC and WEC/Kraftwerk Union (KWU) joint irradiation experiments, from WEC and KWU operating commercial plant performance, and from many basic experiments conducted in various research reactors which are available in the open literature. Some of these sources are discussed below. Evidence currently available indicates that UO_2 fuel performance with ZIRLO cladding and with OPTIN cladding tubes are satisfactory to exposures up to 60,000 MWd/WTU based on the experience of operation of WEC PWR rod.

a. Public Information

General fuel performance information available in the open literature has provided part of the WEC fuel rod design data base. The following particular experiments have been cited in the past as key references:

1. Determination of the effect of fuel-cladding gap on the linear heat rating to melting for UO_2 fuel rods, conducted in the Westinghouse test reactor.

2. Shippingport irradiation experience,

3. Saxton irradiation experience,

4. Combined Vallecitos Boiling Water Reactor (VBWR) Dresden irradiation,

5. Large Seed Blanket Reactor (LSBR) rod experience, and

6. Joint U.S.-Euratom Research and Development Program to evaluate central fuel melting in the Consumers Power Co. Big Rock Point Reactor.

Since the information from these programs is available in the open literature, they will not be described here.

b. Operating Fuel Experience

ZIRLO clad was initially irradiated in the North Anna-1 that is a WEC type plant since 1987 with 2 LTAs and operated for 3 cycles. Since 1991, the ZIRLO clad has been irradiated in the WEC plants and non WEC plants which is currently 32 regions and 65 regions, respectively, after V.C summer plant, some with the average burnups I excess of 60,000 MWD/MTU.

M5 clad was initially irradiated in the Chinon B3 plant as well as plants in France since 1989 with LTAs and operated above 65,000 MWD/MTU. Since 1999, the M5 clad has been irradiated in the 28 plants more than 1150 fuel assemblies, some with the average burnups in excess of 60,000 MWD/MTU.

c. Fuel Irradiation Programs

WEC is involved in diversified fuel irradiation test programs to confirm the adequacy of the WEC fuel rod design bases and models by experiment. Some of these programs involve safety-related research while other programs provide confirmatory data on performance capability or evaluate design and fabrication variables or methods which may improve and extend WEC's current knowledge of fuel rod performance.

The key fuel performance evaluation programs that are summarized below include the following:

1. Fuel densification experiments at the Battelle Research Reactor (BRR).

2. Joint WEC/KWU fuel densification experiments including tests in the MZFR reactor at Karlsruhe, West Germany, and the EEI experiments in the General Electric Test Reactor (GETR),

3. Direct participation in the Halden Project in Norway with access to all Halden base program fuel test data.

4. Irradiation of special instrumented fuel rods to obtain dynamic in-reactor measurements in Halden experimental rigs.

5. Ramp test programs on fuel rods to evaluate fuel load-follow capabilities and the pellet clad interaction/ stress corrosion phenomenon in both the Studsvik and Petten test reactors. Other in-reactor experiments have been conducted in the Obrigheim pressurized water reactor.

6. Irradiation of special test and surveillance assemblies in operating WEC reactors.

d. WEC Fuel Densification Experiments

WEC has conducted several experiments which provided data on the in-reactor densification behavior of various UO_2 fuel types. These include the BRR, EEI, and MZFR densification experiments.

e. BRR Fuel Densification Experiment

The object of this program was to examine the in-pile densification behavior of various fuel types and microstructures fabricated with and

without pore formers. The nonpore former fuel types had initial theoretical densities of 93% to 94% with a grain size of less than 6 m and with a large fraction of pores less than 4 um in diameter. The pore former fuel types had initial densities of 93% to 95% and were characterized by a combination of large grain size and/or large pore size. Fuel pellets of each experimental type were irradiated in six BRR capsules at linear heat ratings between 2.8 and 4.6 kW/ft (91.9-150.9 W/cm) for periods of up to 1500 hours. Post irradiation examination of the BRR results showed significant differences in the densification behavior between pore former and nonpore former fuel. The pore former fuel showed little change in density (high stability) while the nonpore former fuel densified rapidly. A trend towards increased densification with lower initial density was apparent in the nonpore former fuel. It was concluded that the UO_2 micro- structure played a dominant role in the kinetics and extent of in-reactor densification. Consequently, fuel exhibiting the desirable microstructural features to reduce in-reactor densification (i.e., large fraction of the pore volume in the large pore size range) became part of the standard WEC fuel design.

f. WEC/KWU Fuel Densification Experiment (MZFR)

As a follow-up to the WEC experiment in the BRR, a joint WEC/KWU program has been conducted in the German MZFR to evaluate the performance of several nondensifying fuel types at higher power levels for longer times and to higher burnups.

Sixteen full-length fuel rods each containing a different fuel type were irradiated at powers up to 11 kW/ft (360.9 W/cm) for burnups up to 4000 MWd/MTU. Included in these rods are UO_2 and UO_2-$PuUO_2$ fuels, most of which were fabricated using techniques intended to minimize densifi- cation. Six rods employed WEC-fabricated UO_2 fuels, five of

which included pore former additives and one fabricated without a pore former to serve as a control. Eight rods were fabricated using KWU experimental fuel, representing a wide range of sintering times and temperatures, initial densities, and enrichments. The remaining two rods were fabricated using UO_2-PuO_2 fuels of two different densities, with and without a pore former additive. Each of the fuel pellet types and fuel rods was extensively characterized before testing to permit comparison with similar postirradiation measurements.

The results of the postirradiation examination showed that fuel types fabricated with pore formers (similar to current production fuel) experienced significantly less in-pile densification than those fabricated without pore formers. The data also support use of a standardized out-of-pile resintering test developed by WEC to characterize expected in-pile densification at the time of fabrication. This simulation test has been submitted to the NRC and approved for use by WEC in LOCA calculations.

g. EEI Fuel Densification Experiment

The prime objective of the EEI Fuel Irradiation Test Program conducted in the General Electric Test Reactor (GETR) was to isolate and characterize the in-reactor densification behavior of pore former (or stable) fuel types. WEC and KWU were among eleven participants in the program.

This program entitled WEC to obtain densification data on nine base program fuel pellet types with varying microstructures. An additional four fuel types were fabricated by WEC and KWU. These included WEC fuel types, two with and one without a pore former additive, and a KWU standard production fuel. The pellets in the program were well characterized before irradiation. Four of the fuel types were

irradiated in one pressurized (53 atmospheres) capsule. Two of the fuel types were also irradiated in a separate nonpressurized capsule (one atmosphere). Each of the capsules contained thermocouples to continuously monitor capsule power generation during irradiation to assure that the desired operating conditions were maintained. Postirradiation examination of these test capsules confirmed that UO_2 fuel with specific ranges of microstructural characteristics, such as produced by pore former additives, are stable with respect to densification. The largest in-reactor density changes occurred for those types having a combination of the smallest pore size, the largest volume percent of porosity less than 4 m in the smallest initial grain size, and the lowest initial density (Reference 52).

h. Halden Program Participation

The experimental facilities and programs of the OECD Halden Reactor Project in Norway represent one of the most advanced efforts in quantifying the effects and interaction of the various design parameters of Zircaloy-clad fuel rods through measurements made in reactor. WEC has been a member of the project since 1973. WEC reviews the data generated by the project in considerable detail and utilizes the results in various fuel development programs.

The Halden test reactor has unique capability for measuring fuel rod operation during irradiation. This capability has been utilized by WEC with specific experiments to provide information in the following areas:

1. Fuel densification phenomenon including measurements of the rate of fuel column shortening as a function of the initial fuel density, power level, and fuel fabrication process

2. Fuel clad mechanical interaction involving studies of the effects of pellet design (shape and density) and operating parameters on cladding deformation

3. Modeling of fuel rod behavior with emphasis on heat transfer characteristics

The first three test assemblies sponsored jointly by WEC and KWU contained 24 well characterized fuel rods. These assemblies included the following range of design and operating parameters:

1. Helium fill pressures from 22 to 35 atmospheres
2. Initial fuel theoretical densities from 91% to 96%
3. Linear heat ratings to 15 kW/ft (492.1 W/cm)
4. U-235 enrichments from 6% to 12%, nine rods fabricated with mixed-oxide fuel

The objectives of these tests were to determine the dynamic changes in fuel rod internal pressure, fuel centerline temperature and fuel stack length during operation as a function of burnup. Two of these assemblies (six test rods each) were discharged from the reactor after receiving a peak burnup of 24,000 MWd/MTU. The third rig (12 rods) was irradiated to a peak burnup of 40,000 MWd/MTU so that fuel swelling and gas release behavior can be evaluated to high burnups. The objectives of a fourth six rod test assembly were to evaluate the effects of such design variables as pellet-clad gap, fill gas composition, and linear heat rating (to 15 kW/ft) on heat transfer characteristics. This experiment also provided gap conductance data on UO_2 and mixed oxide fuel. This test was discharged from the reactor after reaching a peak burnup of 4,000 MWd/MTU.

Instrumentation used to measure fuel behavior during irradiation includes centerline thermocouples, internal pressure transducers, linear variable-differential transformers (LVDTs) for fuel column length changes, and flux monitors for axial and radial power profiles.

The fuel column length change data that were obtained support the data generated by the EEI, BRR, and MZFR experiments and confirm the in-reactor stability of WEC pore former fuel types. In addition, the internal pressure monitors and centerline thermocouple data have confirmed the adequacy of the WEC thermal performance design models.

In addition to these WEC/KWU test assemblies, WEC has designed and irradiated three rods in the Halden high-temperature, high-pressure loop to simulate PWR coolant temperature and pressure conditions. The purpose of these experiments was to distinguish the effects of pellet configuration on the formation of circumferential ridging and on the elongation of the rods. Each rod contained three pellet types with one type as a standard. This program in combination with the results of other experiments gives WEC a firm basis upon which to optimize fuel rod design with respect to dimensional changes and to improve fuel performance models developed to predict rod dimensional stability.

i. Power Ramp Programs

WEC and KWU participated in the Studsvik and Pathfinder/Petten programs to evaluate fuel rod performance under ramp conditions to power levels not recently attained. These can occur either after refueling or after extended periods of low power operation or during control element maneuvers. The effects of various fuel rod design variables on power ramp limits are also investigated as a means to further optimize design. The Petten/Pathfinder program, which began in 1973,

is being conducted jointly by WEC and KWU in the Obrigheim PWR reactor and Petten test reactor facilities. One special test assembly has been irradiated each year from 1973, to 1980 in the Obrigheim reactor. Included in this assembly, which is designed to facilitate fuel rod removal and replacement, are well-characterized segmented rods or "rodlets" that are axially connected to form a complete fuel rod. These rodlets were "preirradiated" in the Obrigheim reactor for one to four operating cycles and then separated and irradiated in a test reactor to evaluate performance under ramp conditions. Ninety-nine of these rodlets irradiated in Obrigheim have been discharged and ramped in Petten. An additional 40 of these rodlets have been tested at the R-2 reactor at Studsvik. Postirradiation, hot-cell examination programs form an integral part of both the Petten/Pathfinder and Studsvik experiments to characterize fuel rod behavior, particularly with respect to dimensional stability and fission product release. These test programs are designed to distinguish between fuel rod power ramps which occur on startup and those which might occur during reactor power maneuvering operations.

Operating flexibility of a plant requires that the fuel rods maintain integrity during periodic changes in power. Power cycling tests of this type have been jointly conducted by WEC/KWU in Obrigheim and Petten. In the Petten test, a single unpressurized fuel rod was power cycled between 9 kW/ft (295.3 W/cm) and 17 kW/ft (557.7 W/cm) at a power change rate of about 3 kW/ft/min (98.4 W/cm/min). The fuel rod successfully completed 400 cycles and achieved a burnup of 8000 MWd/MTU. Power cycling tests were then conducted in Obrigheim on eight short pressurized and unpressurized fuel rods. The test fuel rods were attached to a control element drive mechanism and driven from the low power to a high power position on a nominal cycle. Power changes from 50% to 100% at rates of 20% per minute for 880 cycles were included. After successfully completing the experiment, the test

rods achieved a peak burnup of 30,000 MWd/MTU without substantial cladding deformation or fuel rod perforation. More recent information has been published in Reference 58.

j. Fuel Surveillance Programs

WEC has conducted a number of fuel surveillance programs on fuel in operating plants. Thus far, a number of poolside fuel inspection programs of varying detail have been performed by WEC (see Table 4.2-4). A large number of assemblies have been visually examined, and dimensional measurements have also been obtained on a large number of these assemblies. Fuel bundle disassembly operations have been conducted either to obtain information of particular aspects of performance of interest or as part of test assembly surveillance programs. A poolside fuel surveilance program for KSNP ZIRLO clad has been being initiated(Refernce 74) and currently for PLUS7 fuels is undertaking(Reference 4.2-7).

4.2.3.2.11 Temperature Transient Effects Analysis

4.2.3.2.11.1 Waterlogged Fuel

The potential for a fuel rod to become waterlogged during normal operation is discussed in Subsection 4.2.3.2.9. If a fuel rod does become waterlogged at low or zero power, it is possible that a subsequent power increase could cause a buildup of hydrostatic pressure. It is unlikely that the pressure would build up to a level that could cause cladding rupture because a fuel rod with the potential for rupture requires the combination of a very small defect together with a long period of operation at low or zero power.

Tests conducted using intentionally waterlogged fuel rods (capsule drive core at SPERT) (References 59 and 60) showed that the resulting failures did eject some fuel material from the rod and greatly deformed the test specimens. However, these test rods were completely sealed, and the transient rates used were several orders of magnitude greater than those allowed in normal operation.

In those instances where waterlogged fuel rods have been observed in commercial reactors, it has not been clear that waterlogging was the cause, and not just the result, of associated cladding failures; and WEC has not observed and is not aware of any case in which material was expelled from waterlogged fuel rods or in which the fuel cladding was significantly deformed in a normal power reactor.

It is therefore concluded that the effect of normal power transients on water-logged fuel rods is not likely to result in cladding rupture, and even if rupture does occur, it will not produce the sort of postulated burst failures that would expel fuel material or damage adjacent fuel rods or fuel assembly structural components.

4.2.3.2.11.2 Intact Fuel

The thermal effects of anticipated operational occurrences on fuel rod integrity are discussed in the following paragraphs:

a. Fuel rod thermal transient effects are basically manifested as the change in internal pressure, the changes in clad thermal gradient and thermal stresses, and the differential thermal expansion between pellets and clad. These effects are discussed in Subsections 4.2.3.2.2 and 4.2.3.2.11.

b. Another possible effect of transients is an axial expansion of the pellet column against a flattened (collapsed) section of the clad.

However, the fuel rod design includes specific provisions to prevent clad flattening, and therefore, such interactions will not occur.

4.2.3.2.12 Energy Release During Fuel Element Burnout

The reactor protective system provides fuel clad protection so that the probability of fuel element burnout during normal operation and anticipated operational occurrences is extremely low. Thus, the potential for fuel element burnout is restricted to faulted conditions. The LOCA is the limiting event since it results in the larger number of fuel rods experiencing burnout; thus, the LOCA analysis, which is very conservative in predicting fuel element burnout, provides an upper limit for evaluating the consequences of burnout. The LOCA analysis explicitly accounts for the additional heat release due to the chemical reaction between fuel cladding and the coolant following fuel element burnout. LOCA analysis results are discussed in Subsection 15.6.5.

4.2.3.2.13 Energy Release on Rupture of Waterlogged Fuel Elements

A discussion of the potential for waterlogging fuel rods and for subsequent energy release is presented in Subsection 4.2.3.2.9.

4.2.3.2.14 Fuel Rod Behavior Effects from Coolant Flow Blockage

An experimental and analytical program was conducted to determine the effects of fuel assembly coolant flow maldistribution during normal reactor operation. In the experimental phase, velocity and static pressure measurements were made in cold, flowing water in an oversize model of a WEC 14 x 14 fuel assembly in order to determine the three-dimensional flow distributions in the vicinity of several types of flow obstruction. The effects of the distributions on thermal behavior were evaluated, where necessary, with the use of the TORC thermal and hydraulic code (Reference 61). Subjects investigated included the following:

a. The assembly inlet flow maldistribution caused by blockage of a core support plate flow hole. Evaluation of the flow recovery data indicated that even the complete blockage of a core support plate flow hole would not produce a W-3 DNBR of less than 1.0 even though the reactor might be operating at a power sufficient to produce a DNBR of 1.3 without the blockage.

b. The flow maldistribution within the assembly caused by complete blockage of one to nine channels. Flow distributions were measured at positions upstream and downstream of a blockage of one to nine channels. The influence of the blockage diminished very rapidly in the upstream direction. Analysis of the data for a single channel blockage indicated that such a blockage would not produce a W-3 DNBR of less than 1.0 downstream of the blockage even though the reactor might be operating at a power sufficient to produce a DNBR of 1.3 without the blockage.

The results presented above were obtained through flow testing an oversize model of a standard 14 x 14 fuel assembly. Because of the great similarity in design between the Standard System 80, 16 x 16 assembly, and the earlier 14 x 14 assembly, these test results also constitute an adequate demonstration of the effects that flow blockage would have on the 16 x 16 assembly. This conclusion is also supported by the fact that the 16 x 16 assembly has been demonstrated to have a greater resistance to axial flow than the 14 x 14 assembly. The effect of the higher flow resistance to produce more rapid flow recovery, i.e., more nearly uniform flow, is analogous to the common use of flow resistance devices (screens or perforated plates) to smooth nonuniform velocity profiles in ducts or process equipment.

4.2.3.2.15 Fuel Temperatures

Steady-state fuel temperatures are determined by the FATES computer program.

The calculational procedure considers the effect of linear heat rate, fuel relocation, fuel swelling, densification, thermal expansion, fission gas release, and clad deformations. The model for predicting fuel thermal performance is discussed in detail in References 15, 63, 64, 70 and 74.

Two sets of burnup and axially dependent linear heat-rate distributions are considered in the calculation. One is the hot rod, time-averaged, distribution expected to persist during long-term operation, and the other is the envelope of the maximum linear heat rate at each axial location. The long-term distributions are integrated over selected time periods to determine burnup, which is in turn used for the various burnup-dependent behavioral models in the FATES computer program. The envelope accounts for possible variations in the peak linear heat rate at any elevation which may occur for short periods of time and is used exclusively for fission gas release calculations.

The power history used assumes continuous 100% reactor power from beginning-of-life. Using this history, the highest fuel temperatures occur at beginning-of-life. It has been shown that fuel temperatures for a given power level at any burnup are insensitive to the previous history used to arrive at the given power level.

Fuel thermal performance parameters are calculated for the hot rod. These parameters for any other rod in the core can be obtained by using the axial location in the hot rod whose local power and burnup corresponds to the local power and burnup in the rod being examined. This procedure will yield conservatively high stored energy in the fuel rod under consideration.

The maximum power density, including local peaking as affected by anticipated operational occurrences, is discussed in Sections 4.3 and 4.4 and in Chapter 15.

4.2.3.3 Burnable Poison Rods

4.2.3.3.1 Burnable Poison Rod Internal Pressure and Cladding Stress Evaluation

The poison rod cladding is analyzed, in a similar manner as the fuel rods cladding, to determine the stress and strain resulting from the various normal, upset, and emergency conditions discussed in Subsection 4.2.1.1. Specific accounting is made for differential pressure, differential thermal expansion, cladding creep, and irradiation-induced swelling of the burnable poison material. Since the peak Gd_2O_3-UO_2 poison rods are operating at power levels lower than the peak power UO_2 fuel rods, all analyses for fuel rods conservatively bound those of the poison rods.

Likewise, the results of the burnable poison rod analyses, as bounded by the fuel rod analysis, confirm that the design criteria of Subsection 4.2.1.3.1 regarding rod internal pressure, stress, strain, and strain fatigue are satisfied, including seismic and LOCA analyses. Seismic and LOCA analyses have been performed using the methodology described in Reference 46. The results of the analyses are within the acceptable limits.

4.2.3.4 Control Element Assemblies

The CEAs are designed for a 10-year lifetime based on the estimates of neutron absorber burnup, allowable plastic strain of the Inconel 625 cladding, and the resultant dimensional clearances of the elements within the fuel assembly guide tubes.

a. Internal Pressure

The value of internal pressure in the control elements is dependent on the following parameters:

1. Initial fill gas pressure
2. Gas temperature
3. Helium generated and released
4. Available volume including B_4C porosity

Of the absorber materials utilized in the CEA design, only the B_4C contributes to the total quantity of gas that must be accommodated within the control element. The helium is produced by the nuclear reaction $_0n^1 + _5B^{10} \longrightarrow _3Li^7 + _2He^4$, and the fraction of the quantity generated which is actually released to the plenum is temperature-dependent and is predicted by the empirical equation discussed in Subsection 4.2.1.4.4, item a.3. Temperatures used for release fraction calculations are the maximum predicted to occur during normal operation.

The results of the CEA analyses confirm that the design of Subsection 4.2.1.4 regarding stress, strain, and fatigue are satisfied. The results of the seismic and LOCA analyses are within the acceptable limits.

b. Thermal Stability of Absorber Materials

None of the materials selected for the control elements are susceptible to thermally induced phase changes at reactor operating conditions. Linear thermal expansion, thermal conductivity, and melting points are given in Subsection 4.2.1.4.

c. Irradiation Stability of Absorber Materials

Irradiated properties of the absorber materials are discussed in Subsection 4.2.1.4. Irradiation-induced chemical transmutations are produced in B_4C. Neutron bombardment of B-10 atoms results in the

production of lithium and helium. The percent of helium released is given by the expression in Subsection 4.2.1.4.

Irradiation-enhanced swelling characteristics of the absorber materials are given in Subsection 4.2.1.4. Accommodations for swelling of the absorbers have been incorporated in the design of the control elements and include the following measures:

1. All B_4C pellets have rounded edges to promote sliding of the pellets in the cladding due to differential thermal expansion and irradiation-enhanced swelling.

2. Dimensionally stable Type 304 stainless steel spacers are located at the bottom of all absorber stacks adjacent to the nose cap to minimize strain at the weld joint.

3. A felt-metal sleeve containing reduced-diameter B_4C pellets is located in the bottom length of the absorber stacks in full-strength control elements. The felt-metal sleeve laterally positions the reduced-diameter B_4C pellets uniformly with respect to the clad, and in addition absorbs the differential thermal expansion and irradiation-induced swelling of the B_4C pellets, thereby limiting the amount of induced strain in the clad.

d. Potential for and Consequences of CEA Function Failure

The probability of a functional failure of the CEA is considered to be very small. This conclusion is based on the conservatism used in the design, on the quality control procedures used during manufacturing, and on testing of similar full size CEA/CEDM combinations under simulated reactor conditions for lengths of travel and numbers of trips greater than those expected to occur during the design life. The con-

sequences of CEA/CEDM functional failure are discussed in Chapter 15.

A postulated CEA failure mode is cladding failure. If an element is assumed to partially fill with water under low or zero power conditions, the possibility exists that upon returning to power, the path of the water to the outside could be blocked. The expansion of the entrapped water could cause the element to swell. In tests, specimens of CEA cladding were filled with a spacer representing the poison material. All but 9% of the remaining volume was filled with water. The sealed assembly was then subjected to a temperature of 650°F (343.3°C) and an external pressure of 2250 lb/in^2 (158.2 kg/cm^2) followed by a rapid removal of the external pressure. The resulting diametral increases of the cladding were on the order of 15 to 25 mils and were not sufficient to impair axial motion of the CEA, which has a 0.084 diametral clearance with the fuel assembly guide tubes. This test result, coupled with the low probability of a cladding failure leading to a waterlogged rod, demonstrates that the probability for a CEA functional failure from this cause is low.

Another possible consequence of failed cladding is the leaching of B_4C due to water ingress and the release of small quantities of CEA filler materials, including helium and lithium (from the neutron-boron reactions). However, the amounts which would be released are too small to have significant effects on coolant chemistry.

e. CEA Axial Growth Analysis

Analysis has shown that adequate axial clearance exists between the bottom of the CEA element and the fuel assembly guide tube. This clearance, representative of the limiting design condition, has been calculated on the basis of worst-case dimensional tolerances and considers the relative thermal growth between the fuel assembly and

the fully inserted CEA.

4.2.4 Testing and Inspection Plan

Fuel assembly and control element assembly quality assurance is attained by adherence to the procedures described in KEPCO Quality Assurance Program.

Vendor product certifications, process surveillance, inspections, tests, and material check analyses are performed to ensure conformity of all fuel assembly and control element assembly components to the design requirements from material procurement through receiving inspection at the plant site. The basic quality assurance measures performed are discussed in the following subsections.

4.2.4.1 Fuel Assembly

A comprehensive quality control plan is established to ensure that dimensional requirements of the drawings are met. In those cases where a larger number of measurements are required and 100% inspection is impractical, these plans provide a high statistical confidence that these dimensions are within tolerance. Sensitivity and accuracy of all measuring devices are within ±10% of the dimensioned tolerance. The basic quality assurance measures performed in addition to dimensional inspections and material verifications are described in the following subsections.

4.2.4.1.1 Weld Quality Assurance Measures

The following paragraphs describe the type and function of each welded joint used in the fuel assembly design and include a brief description of the testing (both destructive and nondestructive) performed to ensure the structural integrity of the joints. The welds are listed from top to bottom in the fuel assembly.

a. GUARDIAN fuel assembly

The CEA guide tube joints (between the tube and threaded upper and lower ends) are butt welds between the two Zircaloy subcomponents. The welds are required to be full penetration welds and must not cause violation of dimensional or corrosion resistance standards.

The joint connecting the upper end fitting center guide post to the lower cast flow plate has a threaded connection that is prevented from unthreading by tack welding the center guide post to the bottom of the lower cast plate using the gas tungsten arc welding (GTAW) process. Each weld is inspected for compliance with a visual standard.

The spacer grid welds at the intersection of perpendicular Zircaloy-4 grid strips are made by the laser welding process. Each intersection is welded top and bottom, and each weld is inspected by comparison with a visual standard.

For the spacer-grid-to-CEA-guide-tube weld (both components Zircaloy-4), each grid is welded to each guide tube with eight small welds, evenly divided between the upper and lower faces of the grid. Each weld is required to be free of cracks and burnthrough, and each weld is inspected by comparison to a visual standard. Also, sufficient testing of sample welds is required to establish acceptable corrosion resistance of the weld region. Each guide tube is inspected after welding to show that welding has not affected clearance for CEA motion.

The lower spacer grid welds at spacer strip intersections and between spacer and perimeter strips (all components Inconel 625) are made using the laser welding process and are all inspected for compliance with the appropriate visual standards.

The lower spacer grid to-lower end fitting (304 stainless steel) weld is made using the GTAW process and each weld is inspected to ensure compliance with a visual standard.

The lower end fitting is fastened to the Zircaloy guide tubes using threaded connections. The connections are prevented from unthreading by stainless steel locking disks welded to the lower end fitting. Each disk is tack welded to the end fitting in four places using the GTAW process, and each weld is inspected for compliance with a visual standard.

The inspection requirements and acceptance standards for each of the welds are established on the basis of providing adequate assurance that the connections will perform their required functions.

b. PLUS7 fuel assembly
Except the below paragraphs, welding type and function of PLUS7 fuel assembly is the same as those of GUARDIAN.

Inconel top and bottom grid welds at the intersection of perpendicular Inconel grid strips are made by the brazing welding process and are inspected for compliance with the appropriate visual standards.

Inconel protective grid welds at the intersection of perpendicular Inconel grid strips are made by the laser beam welding process and are inspected for compliance with the appropriate visual standards.

Protective gird welds at intersection of grid washer with grid strips are made by the laser beam welding process and are inspected for compliance with the appropriate visual standards.

For the spacer grid to CEA guide tube weld, sleeve welded the grid is welded to each guide tube with four small welds. Each weld is required to be free of cracks and burnthrough, and each weld is inspected by comparison to a visual standard. Also, sufficient testing of sample welds is required to establish acceptable corrosion resistance of the weld region. Each guide tube is inspected after welding to show that has not affected clearance for CEA motion.

The lower end fitting is consisting of a plate with flow holes, a support leg at each corner(total of four legs), a skirt plate connected to legs at the side and a cylindrical instrument guide. A leg and skirt is manufactured as one structure by casting process and welded to the flow plate. The instrument guide tube is threaded in the underside of the flow plate and is locked in position by TIG-tack welds and each weld is inspected for compliance with a visual standard.

4.2.4.1.2 Other Quality Assurance Measures

All guide tubes are internally gauged ensuring free passage within the tubes including the reduced diameter buffer region.

Each upper-end-fitting-post-to-guide-tube joint is inspected for compliance with a visual standard.

The spacer-grid-to-fuel-rod relationship is carefully examined at each grid location.

An alpha smear test is performed on the exterior surface of the fuel rods.

Each complete fuel assembly is inspected for cleanliness, wrapped to preserve its cleanliness, and loaded within shipping containers which are later purged and filled with dry air.

Visual inspection of the conveyance vehicle , shipping container , and fuel assembly is performed at the reactor site. Approved procedures are provided for unloading the fuel assemblies. Following unloading, exterior portions of the fuel assembly components are inspected for shipping damage and cleanliness. If damage is detected , the assembly may be repaired onsite or returned to the manufacturing facility for repair. In the event the repair process is other than one normally used by the manufacturing facility , or the repaired assembly does not meet the standard requirements for new fuel, the specific process or assembly is reviewed before the process or assembly is accepted. Each spacer grid is checked to verify compliances with outside dimension, grid cell pitch, and spring tab preset requirements.

4.2.4.2 Fuel Rods

4.2.4.2.1 Fuel Pellets

During the conversion of the UF_6 to ceramic-grade uranium dioxide powder, the UO_2 powder is divided into lots blended to form uniform isotopic , chemical, and physical characteristics. Some of Samples are taken from the total number of containers in each lot and analyzed to verify powder specification limits. 733

Pellets are divided into lots during fabrication with all pellets within the lot being processed under the same conditions. Representative samples are obtained from each lot for product acceptance tests. Total hydrogen content of finished ground pellets is restricted (Subsection 4.2.1.2.4.1).

The pellet main dimensions must meet a 95/95 confidence level. 733

Density requirements of the sintered pellet (Subsection 4.2.1.2.4.3) must meet a 95/95 confidence level. Longitudinal sections of two sample pellets from each pellet lot are prepared for metallo-

graphic examination to ensure conformance to microstructure requirements (Subsection 4.2.1.2.4.2). Pellet surfaces are inspected for chips, cracks, and fissures in accordance with approved standards.

4.2.4.2.2 Cladding

Lots are formed from tubing produced from the same ingot, annealed in the same final vacuum annealing charge, and fabricated using the same procedures. Samples randomly selected from each lot of finished tubing are chemically analyzed to ensure conformance to specified chemical requirements and to verify tensile properties and hydride orientation. Samples from each lot are also used for metallographic tests. Each finished tube is ultrasonically tested over its entire length for internal soundness; visually inspected for cleanliness and the absence of acid stains, surface defects, and deformation; and inspected for inside dimension and wall thickness. The following summarizes the test requirements (refer to Subsection 4.2.1.2.2): 733

a. Chemical analysis

Ingot analysis is required for top, middle, and bottom of each ingot. Finished M5 cladding is tested for hydrogen, nitrogen, and oxygen. 733

b. Tensile test at room temperature (ASTM E8)

c. Corrosion resistance test (ASTM G2)

d. Grain size (ASTM E112)

"Delete" 733

e. Surface roughness

f. Visual examination

g. Ultrasonic test

h. Wall thickness

i. Straightness

j. Inside diameter

733

4.2.4.2.3 Fuel Rod Assembly

Immediately before loading, pellets must be capable of meeting the requirements of approved visual standards or other fabrication process controlled attributes. Each fuel pellet stack is weighed to within 0.1% accuracy. The loading process is such that cleanliness and dryness of all internal fuel rod components are maintained until after the final end cap weld is completed. Loading and handling of pellets is carefully controlled to minimize chipping of pellets.

The procedures described in the following subsections are used during fabrication to ensure that there are axial gaps in fuel rods.

4.2.4.2.3.1 Stack Length Gauge

The operator stacks pellets onto carriers to the proper fuel column height. When pellet stacking is completed, all column heights are verified by Quality Control. The pellets are subsequently loaded into tubes. After loading, the distance from the end of the tube to the end of the pellet column is checked with a gauge.

4.2.4.2.3.2 Rod Scanner

Finished fuel rods, before being loaded into bundles, are scanned to ensure that no significant gaps exist in the fuel column.

Loaded fuel rods are evacuated and backfilled with helium to a prescribed level as determined for the fuel batch. Impurity content of the fill gas shall not exceed 0.5%.

The fuel-rod-end-cap-to-fuel-rod-cladding tube welds are butt welds between the cladding tubes and the Zircaloy-4 end cap machined from bar stock. The weld process is resistance pressure welding (RPW). Quality assurance on the end cap weld includes the following:

a. Burst test and metallographic test on a sufficient number of weld specimens are performed to inspect integrity of the weld zone. As a result of the burst test, burst shall occur outside the weld zone of the end plug and burst pressure shall be higher than the test criteria. Furthermore, there shall be no cracks or pores along the weld line as a result of the examination on the weld zone of the weld specimens using a metallograhpic microscope. 733

b. Visual examination of all end cap welds to establish freedom from cracks, seams, inclusions, and foreign particles after final machining of the weld region.

c. Helium leak checking of all end cap welds to establish that no leak rate greater than 10^{-5} bar mm^3/sec is present.

d. Corrosion testing of a sufficient number of samples to establish that weld zones do not exhibit excessive corrosion compared to a visual standard. Welds must be capable of passing a corrosion test (ASTM G2) with no preferential oxidation at the weld in water at 680 °F (359 ℃), 2700 psi (18.6 Mpa) for minimum 36 hours.

All finished fuel rods are visually inspected to ensure a proper surface finish (scratches greater than 0.001 inch (0.025 mm) in depth, cracks, slivers, and other similar defects are not acceptable).

Each fuel rod is marked to provide a means of identification.

4.2.4.3 Burnable Poison Rods

4.2.4.3.1 Burnable Poison Pellets

The Gd_2O_3-UO_2 pellets that are added to the UO_2 fuel pellets are fabricated with essentially the same as for UO_2 fuel pellets.

"Delete"

The fabrication of Gd_2O_3-UO_2 pellets employs dry blending and mixing of the necessary quantities of UO_2 and Gd_2O_3 powders. As with UO_2 pellets, these powders are then pelletized by blending and sintering processes similar to those employed in the manufacturing of UO_2 pellets. The sintering process promotes formation of a solid solution of UO_2 and Gd_2O_3. As with UO_2 pellets, the Gd_2O_3-UO_2 pellets are tested for, and must meet, stringent specifications on density, grain size, and homogeneity. In particular, the density and densification specifications (% TD), grain size requirements, and blending requirements are essentially the same as for a UO_2 mixture.

"Delete"

4.2.4.3.2 Cladding

The testing and inspection plan for poison rod cladding is identical to that for fuel rod cladding (Subsection 4.2.4.2.2).

4.2.4.3.3 Poison Rod Assembly

The moisture content of poison pellets prior to loading is limited to values below those which would be required to produce primary hydride penetration of the cladding. Total moisture inventory is comparable to that which has been shown to be acceptable in fuel rods (Reference 51). The fabrication process is such that all steps from component drying through final welding are carefully controlled so as to minimize the possibilities for excessive moisture pickup.

164

The following procedure is used during fabrication to ensure that there are no axial gaps in poison rods.

The operator stacks pellets onto V troughs that are gauge-marked to the proper column height. When pellet stacking is completed, all column heights are verified by Quality Control. The pellets are subsequently loaded into tubes. After loading, the distance from the end of the tube to the end of the pellet column is checked with a gauge.

Loaded poison rods are evacuated and backfilled with helium to a prescribed level. Impurity content of the fill gas must not exceed 0.5%.

End cap weld integrity and corrosion resistance is ensured by a Quality Control plan similar to that used in fuel rod fabrication (Subsection 4.2.4.2.3).

Each poison rod is marked to provide a means of identification.

4.2.4.4 Control Element Assemblies

The CEAs are subjected to numerous inspections and tests during manufacturing and after installation in the reactor. A general product specification controls the fabrication, inspection, assembly, cleaning, packaging, and shipping of CEAs. All materials are procured to AMS, ASTM, or WEC specifications. In addition, various CEA hardware tests have been conducted.

During manufacturing, the following inspections and tests are performed:

a. The loading of each control element is carefully controlled to obtain the proper amounts and types of filler materials for each type of CEA application (e.g., full- or part-strength).

b. All end cap welds are liquid penetrant examined, helium leak tested and radiographed. 733

c. Each type of control element has unique external features which distinguish it from other types.

d. Each CEA is serialized to distinguish it from the others. See Figures 4.2-3 through 4.2-5.

e. Fully assembled CEAs are inspected for proper alignment of the neutron absorber elements using a special fixture. The alignment inspection ensures that the frictional force that could result from adverse

tolerances is below the force which could significantly increase scram time.

In addition to the basic measures discussed above, the manufacturing process includes numerous other quality control steps for ensuring that the individual CEA components satisfy design requirements for material quality, detail dimensions, and process control.

After installation in the reactor, but before criticality, each CEA is traversed through its full stroke and tripped. A similar procedure will also be conducted at refueling intervals.

The required 90% insertion scram time for CEAs is 4.0 seconds under worst case conditions. Verification of adequacy has been determined by testing in the WEC TF-2 flow test facility as reported in Appendix 4B1. This test facility contained prototypical (System 80) reactor components consisting of fuel assemblies, CEA shroud, control element drive mechanism, and a simulation of surrounding core internal support components. The test conditions simulated the range of temperatures and flow rates predicted for normal plant operation.

4.2.5 References

1. S. Timoshenko, Strength of Materials, Part II Chapter IX, D. VanNostrand Co., Inc., New York, 1956.

2. "High Temperature Properties of Zircaloy and UO_2 for use in LOCA Evaluation Models," Combustion Engineering, Inc., CENPD-136 (Proprietary)

3. "Zircaloy Growth-In-Reactor Dimensional Changes in Zircaloy-4 Fuel Assemblies," Combustion Engineering, Inc., CENPD-198P (Proprietary), December 1975.

4. "Extended Burnup Operation of Combustion Engineering PWR Fuel," Combustion Engineering, Inc., CENPD-269-P (Proprietary), July 1984.

5. W. J. O'Donnel, "Fracture of Cylindrical Fuel Rod Cladding due to Plastic Instability," WAPD-TM-651, April 1967.

6. J. M. Weber, "Plastic Stability of Zr-2 Fuel Cladding, Effects of Radiation of Structural Metals," ASTM STP 426, Am. Soc. Testing Mats., pp. 653-669, 1967.

7. J. T. Engle and H. B. Meieran, "Performance to Fuel Rods Having 97 Percent Theoretical Density UO_2 Pellets Sheathed in Zircaloy-4 and Irradiated at Low Thermal Ratings," WAPD-TM-631, July 1968.

8. E. Duncombe, J. E. Meyer, and W. A. Coffman, "Comparisons with Experiment of Calculated Dimensional Changes and Failure Analysis of Irradiated Bulk Oxide Fuel Test Rods Using the CYGRO-1 Computer Program," WAPD-TM-583, September 1966.

9. J. E. McCauley et al., "Evaluation of the Irradiation Performance of Zircaloy-4 Clad Test Rod Containing Annular UO_2 Fuel Pellets (Rod 79-19)," WAPD-TM-595, December 1966.

10. M. J. F. Notley, A. S. Bain, and J. A. L. Robertson, "The Longitudinal and Diameteral Expansion of UO_2 Fuel Elements," AECL-2143, November 1964.

11. M. J. F. Notley, "The Thermal Conductivity of Columnar Grains in Irradiated UO_2 Fuel Elements," AECL-1822, July 1962.

12. S. S. Mason, "Fatigue: A Complex Subject - Some Simple Approximations," Experimental Mechanics, Vol. 22, No. 2, pp. 193-226, July 1965.

13. W. J. O'Donnel and B. F. Langer, "Fatigue Design Basis for Zircaloy Components," Nuc. Sci. Eng., Vol. 20, pp. 1-12, 1964.

14. CESSAR Proprietary Appendix, Docket 50-470.

15. "C-E Fuel Evaluation Model Topical Report," Combusting Engineering, Inc., CENPD-139 (Proprietary), CENPD-139 Rev. 01 (Nonproprietary) CENPD-139 Supplement 1, Rev. 01 (Nonproprietary), July 1974.

16. J. B. Conway, "The Thermal Expansion and Heat Capacity of UO_2 to 2200°C," CE-NMPD-TM-63-6-6.

17. J. A. Christensen, "Thermal Expansion of UO_2," HW-75148, 1962.

18. J. M. Jones et al., "Optical Properties of Uranium Oxides," Nature, 205, 663-65, 1965.

19. F. Cabannes and J. P. Store, "Reflection and Emission Factors of UO_2 at High Temperature, " C.R.Acad.Sci., Paris, Ser. B.264 (1) 45-48, 1967.

20. P. C. Held and D. R. Wilder, "High Temperature Hemispherical Spectral Emittance of Uranium Dioxide at 0.65 and 0.70 m," J. Am. Cer. Soc., Vol. 52, No. 4, 1969.

21. M. C. Brassfield, "Recommended Property and Reaction Kinetics Data For Use in Evaluating a Light Water Cooled Reactor Loss-of-Coolant Incident Involving Zircaloy-4 or 324-53 Clad UO_2," GEMP-482, 1968.

22. R. J. Beals, "High Temperature Mechanical Properties of Oxide Fuels," ANL-7577, p. 160, April-May 1969.

23. M. O. Marlowe, "High Temperature Isothermal Elastic Moduli of UO2" Journal of Nuclear Materials, Vol. 33(1969), pages 242-244.

24. M. G. Andrews, G. S. Smith, and A. M. Garde, "Experience and Developments with Combustion Engineering Fuel." ANS Topical Meeting on LWR Fuel Performance, Williamsburg, Virginia, April 17-20, 1988.

25. A. M. Garde and S. R. Pati, "Gas Release Densification, Swelling and Microstructual Evaluation of Four-Cycle Fuel Rods from Calvert-Cliffs-1," CENPSD-211, April 1983.

26. "CEPAN, Method of Analyzing Creep Collapse of Oval Cladding," Combustion Engineering, Inc., CENPD-187 P-A, March 1976.

27. "Westinghouse Evaluation Model for LOCA Analysis of Korea Standard Nuclear Plants", KNF-TR-SGA-01001/N/A, Rev.1, 2004.6. 519

28. "C-E Methodology for Core Designs Containing Gadolinia-Urania Burnable Absorbers," Combustion Engineering, Inc., CENPD-275-P (Proprietary), March 1987.

29. L. W. Newman, T. A. Thorton, and B. J. Wrona, "Thermal and Physical Properties of Urania-Gadolinia Fuel," Babcock and Wilcox Report BAW-1759, May 1984.

30. R. A. Bush, "Properties of the Urania-Gadolinia System," Exxon Report NFIR-RP-03-04D, October 1985.

31. S. Fukushima, T. Ohmichi, A. Maeda, and H. Watanaba, "The Effect of Gadolinia Content on the Thermal Conductivity of Near-Stoichiometric $(UGd)O_2$ Solid Solutions," Journal of Nuclear Materials, Vol. 105, p. 201-210, 1982.

32. G. Gradel, "Heat Conductivity, Temperature Conductivity and Specific Heat of UO_2 Fuel With Up to 10 wt.% Gd_2O_3," KWU Technical Report, B 22/84/13, January 19, 1984.

33. H. J. Lee and C. W. Kim, "Thermophysical Properties of UO_2 Fuel Materials," J. Korean Nuclear Society, Vol. 8, No. 2, p. 81, June 1976.

34. W. D. Kingrey, "Introduction to Ceramics," John Wiley & Sons, pp. 486-504.

35. T. Wada, K. Noro, and K. Tsukui, "Behavior of UO_2-Gd_2O_3 Fuel," Paper 63 Presented at BNES Conference, London, October 1973.

36. A. L. Pitner, "The WDC-1-1 Instrumental Irradiation of Boron Carbine in a Spectrum-Hardened ETR Flux," HEDL-TME-73-38, April 1973.

37. R. G. Gray and L. R. Lynam, "Irradiation Behavior of Bulk B_4C and B_4C-SiC Burnable Poison Plates," WAPD-261, October 1963.

38. "HEDL Quarterly Technical Report for October, November and December 1974," Vol. 1, HEDL-TME-74-4, pp A-51 to A-53, January 1975.

39. D. E. Mahagan, "Boron Carbide Thermal Conductivity," HEDL-TME-73-78, September 1973.

40. F. J. Homan, "Performance Modeling of Neutron Absorbers," Nuclear Technology, Vol. 16, pp 216-225, October 1972.

41. A. L. Pitner and G. E. Russcher, "Irradiation of Boron Carbide Pellets and Powders in Hanford Thermal Reactors," WHAN-FR-24, December 1970.

42. A. L. Pitner and G. E. Russcher, "A Function to Predict LMFBR Helium Release Based on Boron Carbide Irradiation Data from Thermal Reactors," HEDL-TME-71-127, September 30, 1971.

43. "Materials Technology Program Report for October, November, and December 1973," HEDL-73-6, pp A-69 to A-72.

44. "National Alloy Development Program Information Meeting," PP 39-63 TC-291, May 22, 1975.

45. "Quarterly Progress Report - Irradiation Effects on Reactor Structural Materials," HEDL-TME-71-161, pp GE-5 to GE-10, Aug. ~ Oct. 1971.

46. "Structural Analysis of Fuel Assemblies for Seismic and Loss of Coolant Accident Loading," Combustion Engineering, Inc., CENPD-178, Rev. 1, August 1981.

47. "Fuel and Poison Rod Bowing," Combustion Engineering, Inc., CENPD-225-P-A (Proprietary), June 1983.

48. "Joint C-E/EPRI Fuel Performance Evaluation Program, Task C, Evaluation of Fuel Rod Performance on Maine-Yankee Core I," Combustion Engineering, Inc., CENPD-221, December 1975.

49. "Application of Zircaloy Irradiation Growth Correlations for the Calculation of Fuel Assembly and Fuel Rod Allowances," Supplement 1 to CENPD-198P, (Proprietary), December 1977.

50. D. O. Pickman, "Properties of Zircaloy Cladding," Nuclear Engineering and Design, Vol. 21, No. 2, 1972.

51. K. Joon, "Primary Hydride Failure of Zircaloy Clad Fuel Rods," - ANS Transactions, Vol. 15. No. 1.

52. D. W. Brite et al., "EEI/EPRI Fuel Densification Program Final Report," Battelle Pacific Northwest Laboratories, March 1975.

53. R. M. Berman, H. B. Meieran, and P. Patterson, "Irradiation Behavior of Zircaloy-Clad Fuel Rods Containing Dished End UO_2 Pellets," (LWBR-LSBR Development Program), WAPD-TM-629, July 1967.

54. S. J. Baroch et al., "Comparative Performance of Zircaloy and Stainless Steel Clad Fuel Rods Operated to 10,000 MWd/MTU in the VBWR," GEAP-4849, April 1966.

55. F. H. Megerth, "Zircaloy-Clad UO_2 Fuel Rod Evaluation Program," Quarterly Progress Report No. 8, August 1969-October 1969, GEAP-10121, November 1969.

56. F. H. Megerth, "Zircaloy-Clad UO_2 Fuel Rod Evaluation Program," Quarterly Progress Report No. 1, November 1967-January 1968, CEAP-5598, March 1968.

57. J.C. Lavake and M. Gartner, "High Burnup Ramp Test Program, Final Report" DOE/ET/34030-10, December 1984.

58. Inchikawa, Uchida, Yanagisawa, Nakajima, Nakamura, and Kawasaki, JAERI: Hauevik, Knudsen, and Kolstad, Halden, "Studies of LWR Fuel Performance Under Power Ramping and Power Cycling Utilizing In-Pile Measurement and Fuel Modeling", Proceedings of the ANS Topical Meeting, Williamsburg, Virginia, April 1988.

59. L. A. Stephan, "The Response of Waterlogged UO_2 Fuel Rods to Power Bursts," IDO-ITR-106, April 1969.

60. L. A. Stephan, "The Effects of Cladding Material and Heat Treatment on the Response of Waterlogged UO_2 Fuel Rods to Power Burst," IM-ITR-111, January 1970.

61. "TORC Code: A Computer Code for Determining the Thermal Margin of a Reactor Core," Combustion Engineering, Inc., CENPD-161-P-A (Proprietary), 1986.

62. T. E. Caye, "Saxton Plutonium Project Quarterly Progress Report for the Period Ending March 31, 1972," WCAP-3385-31, November 1972.

63. "Improvements to Fuel Evaluation Model," CEN-161(B)-P, July 1981.

64. "Improvements to Fuel Evaluation Model," CEN-161(B)-P Supplement 1-P, April 1986.

65. "CEPAN Method of Analyzing Creep Collapse of Oval Cladding," Vol. 5, EPRI NP-3966-CCM, April 1985.

66. Anand M. Grade, "Effects of Irradiation and Hydriding on the Mechanical Properties of zircaloy-4 at High Fluence", ASTM STP 1023, 1989.

67. "Improvements to Fuel Evaluation Model", CEN-161(B)-P Supplement 1-P-A, Jannuary 1992.

68. "Verification of the Acceptability of a 1-Pin Burnup Limit of 60 MWd/kgU for Combustion Engineering 16 × 16 PWR Fuel", CEN-386-P-A, August 1992.

69. "Evaluation of the Acceptability of ZIRLO Cladding for Korean Standard Nuclear Plant Fuel", KNF-TR-NFR-99001/N/A Rev.0, February 2001.

70. "Extention of the Rod Burnup Limit in KSNP Fuel with ZIRLO Cladding", KNF-TR-NFR-02003, Rev.0, July 2002.

71. " Verification Report for Oxide Thickness Prediction Model of OPTIN cladding", KNF-TR-NFR-01002 Rev.0, September 2001.

72. "PLUS7 Fuel Design and Safety Evaluation Report for Korean Standard Nuclear Power Plants", KNF-TR-DMR-04001/N/A, Rev. 0, 2006. 03.

73. "Evaluation of the Acceptability of M5 Cladding for Korean Standard Nuclear Plant Fuel", KNF-TR-NFR-01001/N/A Rev.0, Dec. 2002.

74. "In-Reactor Performance Evaluation Report for the 1st Cycle Irradiated PLUS7 LTAs", KNF-TR-AFD-04001, April 2004.

TABLE 4.2-1 (Sh. 1 of 3)

SIGNIFICANT THERMAL AND PHYSICAL PROPERTIES USED IN THE MECHANICAL ANALYSIS OF THE ABSORBER MATERIALS

Parameter		Value		
a. Boron Carbide (B_4C)				
Configuration		Right cylinder		
Outside diameter, in (cm)	(a)	0.737	(1.87)	164
	(b)	0.664	(1.69)	
Pellet length, in (nominal) (cm)	(a)	1(2.54) or 2(5.08)		733
	(b)	0.961(2.44) or 1.786(4.54)		
End chamfer, in		0.007 to 0.040 radius		
Density, (gm/cm^3)		1.84		
weight % boron		78		733
Open porosity in pellet, %		27		
Ultimate tensile strength, lb/in^2		NA		
Yield strength, lb/in^2		NA		
Elongation, %		NA		
Young's modules, psi		NA		
Melting point, °F (℃)		4,440 (2448.9)		
Thermal linear expansion, %		0.23% @ 1000°F		
Thermal conductivitv. Btu/hr-ft-°F (cal/sec-cm-℃)		Irradiated	Unirradiated	
		3×10^{22} nvt (E > 1 Mev)		

TABLE 4.2-1 (Sh. 2 of 3)

Parameter	Value	
at 800°F (426.7 ℃)	2.0(8.3×10^{-3}) 6.8(28×10^{-3})	
at 1000°F (537.8 ℃)	1.9(7.9×10^{-3}) 5.8(24×10^{-3})	
b. Type 347 Stainless Steel Felt Metal		
Configuration	Cylindrical sleeves formed from sheets	
Thickness, in (cm)	0.032 (0.08)	164
Length of sheet, in (nominal) (cm)	12.34 (31.3)	
Density, lb/in^3 (gm/cm^3)	0.059 (1.633)	
Ultimate tensile strength, lb/in^2 (kg/cm^2)	NA	
Elongation, %	NA	
Young's Modulus, lb/in^2 (kg/cm^2)	NA	
Thermal conductivitv. Btu/hr-ft-°F (cal/sec-cm-℃)		
at 500°F (260℃)	0.305(1.26×10^{-3})	
at 1000°F (537.8℃)	0.341(1.41×10^{-3})	
c. Inconel Alloy 625 (Ni-Cr-Fe)		
Configuration (as absorber)	Cylindrical bar	
Diameter, in (cm)	0.737 (1.87)	733
Density, lb/in^3 (gm/cm^3)	0.305 (8.442)	
Ultimate tensile strength, ksi (kg/cm^2)	120 - 150 (8.44×10^3 - 10.5×10^3)	733

TABLE 4.2-1 (Sh. 3 of 3)

Parameter	Value
Specified minimum yield strength @ 650°F, ksi (kg/cm^2)	65 (4,570)
Elongation in 2 inches, %	30
Linear thermal expansion, (70° to 600°F), in/in-°F	7.4×10^{-6}
Young's modulus, lb/in^2 (kg/cm^2)	
at 70°F (21°C)	29.7×10^6 (2.1×10^6)
at 650°F (343°C)	27.0×10^6 (1.9×10^6)
Thermal conductivity, Btu/hr-ft-°F (cal/sec-cm-°C)	
at 70°F (21°C)	5.7 (2.35×10^{-2})
at 600°F (316°C)	8.2 (3.39×10^{-2})

TABLE 4.2-2 (Sh. 1 of 5)

MECHANICAL DESIGN PARAMETERS

CORE ARRANGEMENT

Parameter	Value(GUARDIAN)	Value(PLUS7)
Number of fuel assemblies in core, total	177	177
Number of CEAs	73	73
Number of fuel rod locations	41,772	41,772
Spacing between fuel assemblies, fuel rod surface to surface, inches(cm)	0.208 (0.528)	0.216 (0.549)
Spacing, outer fuel rod surface to core shroud, inches (cm)	0.214 (0.544)	0.218 (0.554)
Hydraulic diameter, Nominal channel, feet (cm)	0.0393 (1.198)	0.04147(1.264)
Total flow area (excluding guide tube), ft^2 (m^2)	44.831 (4.165)	46.209 (4.293)
Total Core area, ft^2 (m^2)	82.6 (7.67)	82.6 (7.67)
Core equivalent diameter, in (m)	123 (3.124)	123 (3.124)
Core circumscribed diameter, in (m)	130 (3.302)	130 (3.302)
Total fuel loading, assuming all rod locations are fuel rod, lb U (kg U)	167.4×10^3 (75.93×10^3)	168.1×10^3 (76.25×10^3)
Total fuel weight, assuming all rod locations are fuel rod, lb UO_2 (kg UO_2)	189.9×10^3 (86.15×10^3)	190.7×10^3 (86.50×10^3)
Total weight of Zircaloy, lb (kg)	54,327.5 (24,642.5)	44,023.7 (19,968.81)
Fuel Volume, including dishes, ft^3 (m^3)	300.8 (8.518)	292.6 (8.286)

TABLE 4.2-2 (Sh. 2 of 5)

FUEL ASSEMBLIES

ASSEMBLY TYPE	NUMBER OF ASSEMBLIES	FUEL ENRICHMENT wt.% U235	NO. OF FUEL RODS PER ASSEMBLY	NO. OF Gd RODS PER ASSEMBLY	Gd_2O_3 wt.% IN NAT'L UO_2
A	45	1.28	236	-	-
B	20	2.34	236	-	-
B1	8	2.34/1.28	176/52	8	4
B2	16	2.34	232	4	4
C	12	2.84/2.34	184/52	-	-
C1	32	2.84/2.34	176/52	8	4
D	12	3.34/2.84	184/52	-	-
D1	8	3.34/2.84	176/52	8	4
D2	24	3.34/2.84	128/100	8	4
	177(Total)				

NOTE : Fuel rod array = 16 x 16 square
Fuel rod pitch = 0.506 inches

TABLE 4.2-2 (Sh.3 of 5)

FUEL ASSEMBLIES (Cont'd)

PARAMETER	VALUE (GUARDIAN)	VALUE (PLUS7)
Spacer Grid		
Type	Leaf spring	
Material	Zicaloy-4	ZIRLO
Number of assembly	10	9
Weight each, lb (kg)	2.0 (0.907)	1.9 (0.852)
(Top,PLUS7)Bottom Spacer grid		
Type	Leaf spring	
Material	Inconel-625	Inconel-718
Number per assembly	1	2 (top,bottom)
Weight each, lb (kg)	2.1 (0.953)	1.4(0.651)
Protective grid		
Material		Inconel-718
Number per assembly		1
Weight each, lb (kg)		0.9(0.415)
Weight of fuel assembly, lb (kg)	1,437.0 (651.8)	1,409.6 (639.4)
Outside dimensions	7.972 x 7.972	7.964 x 7.964
Fuel rod to fuel rod, in(cm)	(20.25 × 20.25)	(20.23 x 20.23)
Fuel rod		
Pellet material	UO_2	
Pellet diameter, inches (cm)	0.325 (0.826)	0.3225 (0.819)
Pellet length, inches (cm)	0.390 (0.991) (enriched)	0.387 (0.983) (enriched) 0.40 (1.016) (axial blanket)
Pellet Density, (g/cm^3)	10.44	
Pellet theoretical density,(g/cm^3)	10.96	
Pellet Density, (% theoretical)	95.25	
Stack height density, (g/cm^3)	10.114 (enriched)	10.313 (enriched)
Clad material	ZIRLO	ZIRLO or M5
Clad ID, inches(cm)	0.332 (0.843)	0.329 (0.836)
Clad OD, nominal, inches (cm)	0.382 (0.97)	0.374 (0.950)
Clad thickness, nominal, in (cm)	0.025 (0.0635)	0.0225 (0.05715)
Diametral gap,Cold,nominal,in(cm)	0.007 (0.01778)	0.0065 (0.01651)
Active length, inches(cm)	150.0 (381.0)	150.0 (381.0)
Plenum length, inches(cm)	8.248 (20.95)	10.0 (25.4)

TABLE 4.2-2 (Sh. 4 of 5)

FUEL ASSEMBLIES (Cont'd)

MECHANICAL DESIGN PARAMETERS

CONTROL ELEMENT ASSEMBLIES(CEA)	FULL-STRENGTH	PART-STRENGTH
Number	65	8
Absorber elements, No. Per assy. Type	12 및 4 Cylindrical rods	4 Cylindrical rods
Clad mateial	Inconel 625	Inconel 625
Clad thickness, inches (mm)	0.035 (0.889)	0.035 (0.889)
Clad OD, inches (mm)	0.816 (20.73)	0.816 (20.73)
Diametral gap, inches (mm)	0.009 (0.2286)	0.009 (0.2286)
Elements Poison material	B_4C/Felt metal and reduced dia, B_4C pellet	Inconel 625 slug
Poison length, inches (B_4C pellet Inconel 625 slug)	135.5/12.5	149
Diameter, inch	0.737/0.664	N/A
Density, (% of theoretical density of 2.52 g/cm^3)	73	N/A
Weight % boron	78	N/A
Inconel slug		
Diameter, inches (mm)	N/A	0.737
Density, lb/in^3 (g/cm^3)	N/A	0.305 (8.442)

733

POISON ROD

PARAMETER	VALUE (GUARDIAN)	VALUE (PLUS7)
Absorber material	Gd_2O_3-UO_2	
Pellet diameter, inch (cm)	0.325 (0.826)	0.3225 (0.819)
Pellet length, inch (cm)	0.390 (0.991)	0.387 (0.983)

TABLE 4.2-2 (Sh. 5 of 5)

FUEL ASSEMBLIES (Cont'd)

POISON ROD (Cont'd)

PARAMETER	VALUE (GUARDIAN)	VALUE (PLUS7)
Pellet density, % theoretical density	95.25	
Theoretical density, UO_2, g/cm^3	10.96	
Theoretical density, Gd_2O_3, g/cm^3	7.41	
Clad material	ZIRLO	ZIRLO or M5
Clad ID, inches(cm)	0.332 (0.843)	0.329 (0.836)
Clad OD, inches(cm)	0.382 (0.970)	0.374 (0.950)
Clad thickness, nominal, inches(cm)	0.025 (0.064)	0.0225 (0.05715)
Diameteral gap, cold,nominal, inch(cm)	0.007 (0.01778)	0.0065 (0.01651)
Active length, inches (cm)	150.0 (381.0)[1)]	150.0 (381.0)[1)]
Plenum length, inches (cm)	8.248 (20.95)	10.0 (25.4)

1) Include top and bottom Axial Cutback region

TABLE 4.2-3

TENSILE TEST RESULTS ON IRRADIATED CLADDING

ROD ID	LOCATION FROM BOTTOM (in)	TESTING TEMP (°F)	0.2% YIELD STRESS ($lb/in^2 \times 10^3$)	ULTIMATE TENSILE STRENGTH ($lb/in^2 \times 10^3$)	UNIFORM STRAIN IN 2-IN GAUGE LENGTH (%)	TOTAL STRAIN IN 2-IN GAUGE LENGTH
B0	11-17	650	61.4	65.6	2.2	6.8
B0	26-32	650	58.1	68.9	2.4	11.3
RD	3-9	650	62.2	70.0	2.0	4.2
RD	12-18	650	60.5	65.4	1.7	5.8
MQ	12-18	675	70.4	77.4	1.9	6.1
MQ	28-34	675	66.0	75.1	1.6	6.2
FS	28-34	675	57.2	71.4	3.9	12.9
GL	12-18	675	60.5	71.5	2.4	9.3
KJD008(**)	90-95	392	96	118	0.70	5.2
KJD015	95-100	572	98	111	0.80	9.1
KJD051	94-99	752	75	92	0.75	6.2

TENSILE TEST RESULTS of ZIRLO CLAD

733

REACTOR	TEMP. (°F)	FLUX 10^{21} n/cm^2	YIELD STRESS (ksi)	UNIFORM STRAIN (%)	TOTAL STRAIN (%)
BR-3	650	6.4	88.5	1.9	3.6
BR-3	650	6.4	85.9	1.1	1.6
BR-3	650	7.1	89.1	2.0	4.2
BR-3	650	7.1	68.2	2.5	3.2

Note : (*) Saxon Core III (Reference 62)(Assumed Flux [>1 MeV] 4.7×10^{21} nvt)
(**) Fort Calhoun (Reference 66)(Assumed Flux [>1 MeV] 11.0×10^{21} nvt)

TABLE 4.2-4

POOLSIDE FUEL INSPECTION PROGRAM SUMMARY

REACTOR	SHUTDOWN DATE/CYCLE	CYCLE AVERAGE BURNUP (MWD/MTU)	INSPECTION PROGRAM SCOPE
Palisades	1973.8/IA	6,800	Visual exam, Gama Scanning, Crud sampling
BR-3	-	62.6 (Rod Average)	Irradiation growth
BR-3	-	67.9 (Rod Average)	Clad corrosion
North Anna-1	-	> 40.3 (Rod Average)[1]	Irradiation growth
North Anna-1	-	62.0 (Rod Average)[2]	clad corrosion
YGN 4	EOC-8[2]	47.6 (Assembly average)	Visual exam, clad outer diameter, grid-to-rod fretting wear
UCN 3	EOC-7[3]		Visual exam, irradiation growth, clad outer diameter, clad corrosion

1) estimated from fast neutron fluence of 10×10^{21} n/cm^2
2) Planned at November 2005
3) Planned at March 2007

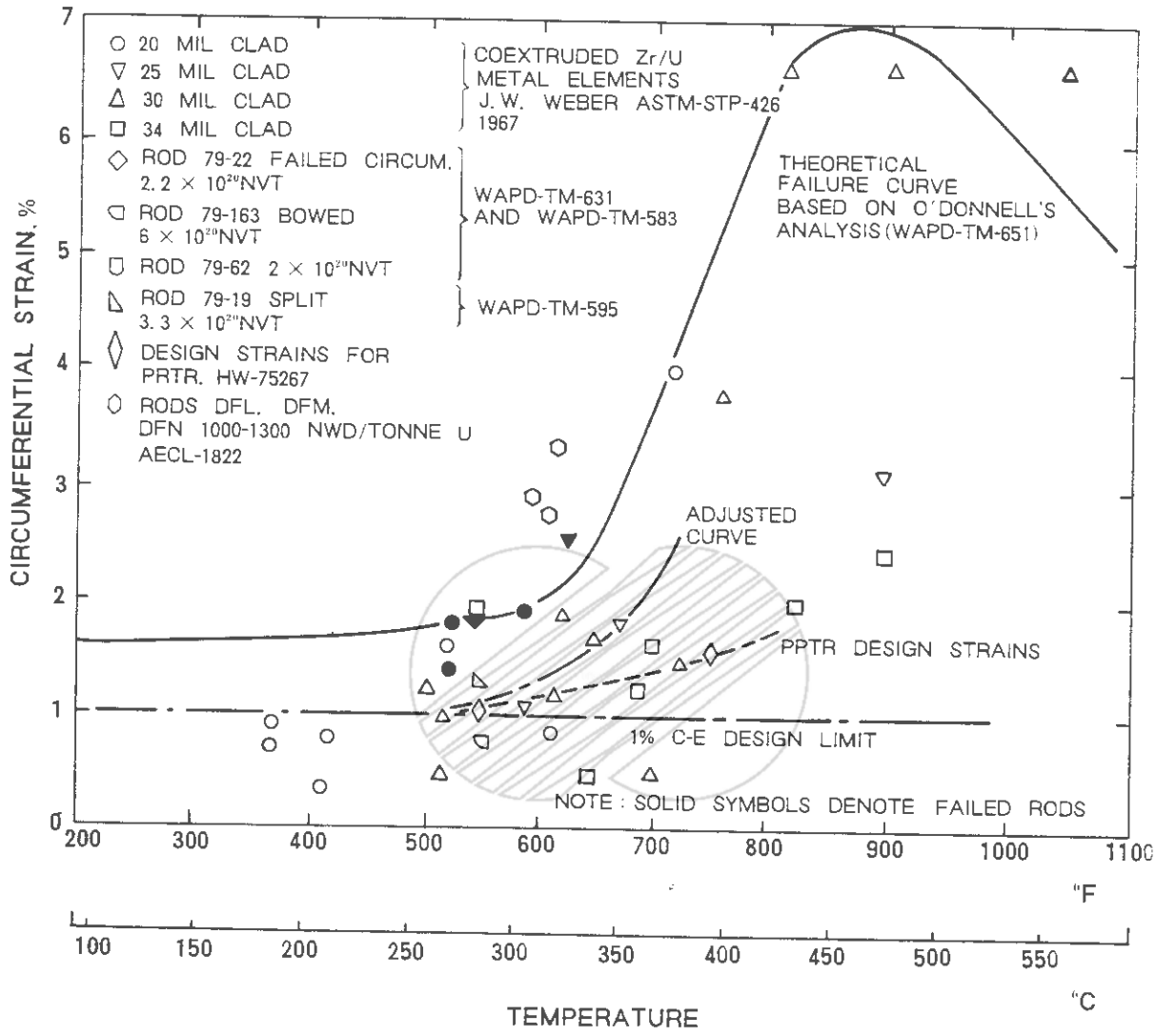

KOREA ELECTRIC POWER CORPORATION
YONGGWANG 3 & 4
FSAR

CIRCUMFERENTIAL STRAIN VS.
TEMPERATURE

Figure 4.2-1

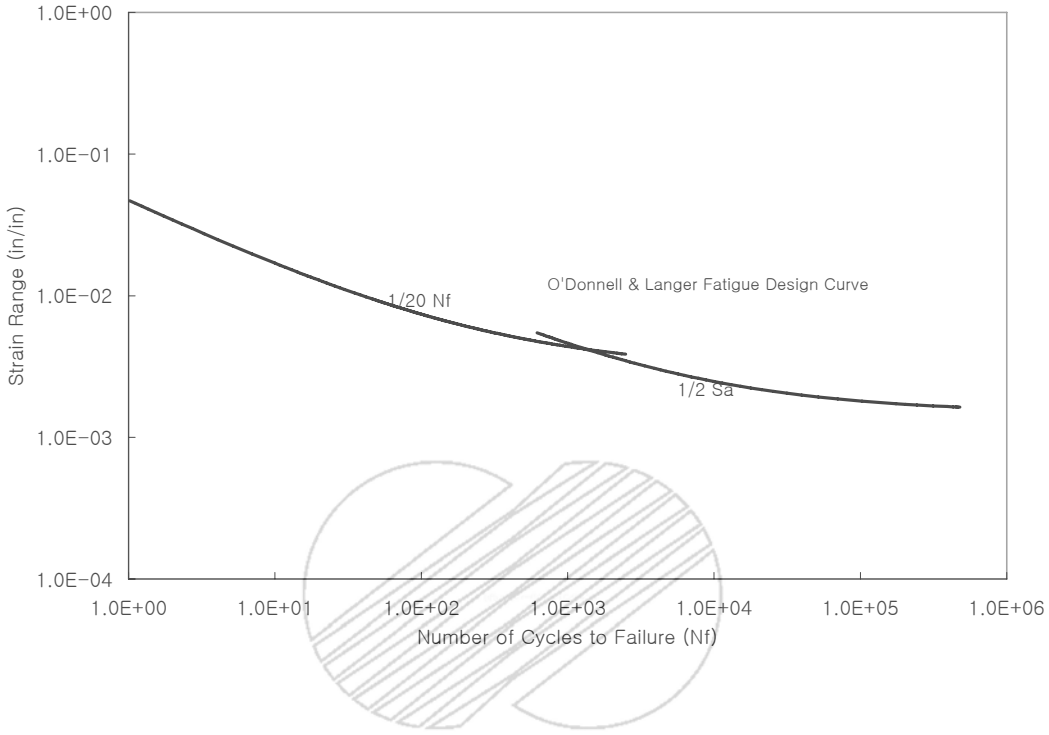

KOREA HYDRO & NUCLEAR POWER COMPANY
YONGGWANG 3 & 4
FSAR

FATIGUE DESIGN CURVE FOR CYCLIC STAIN USAGE of ZIRLO and M5

Figure 4.2-2

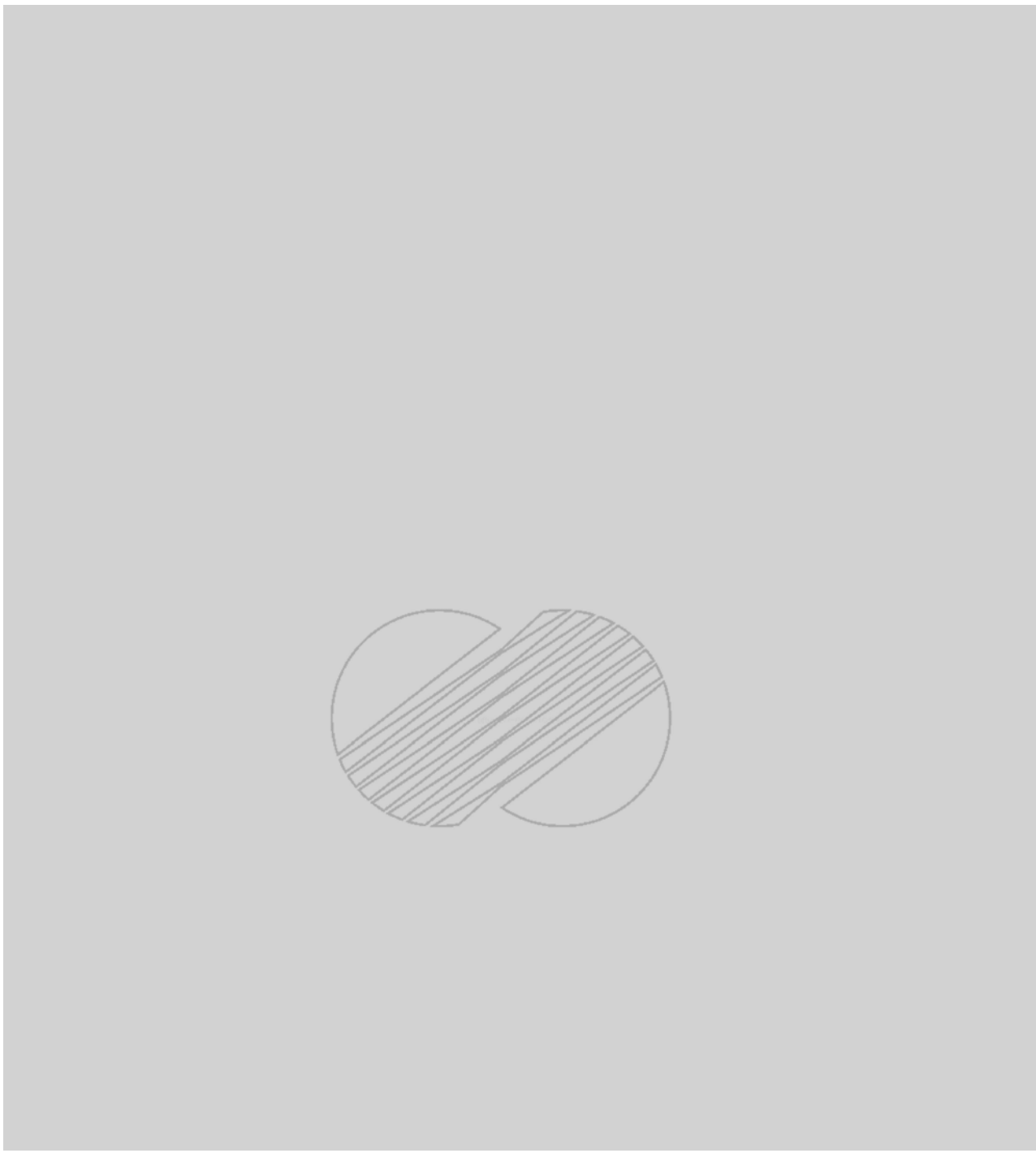

KOREA ELECTRIC POWER CORPORATION
YONGGWANG 3 & 4
FSAR

FULL-STRENGTH CONTROL ELEMENT
ASSEMBLY (4-ELEMENT)

Figure 4.2-3

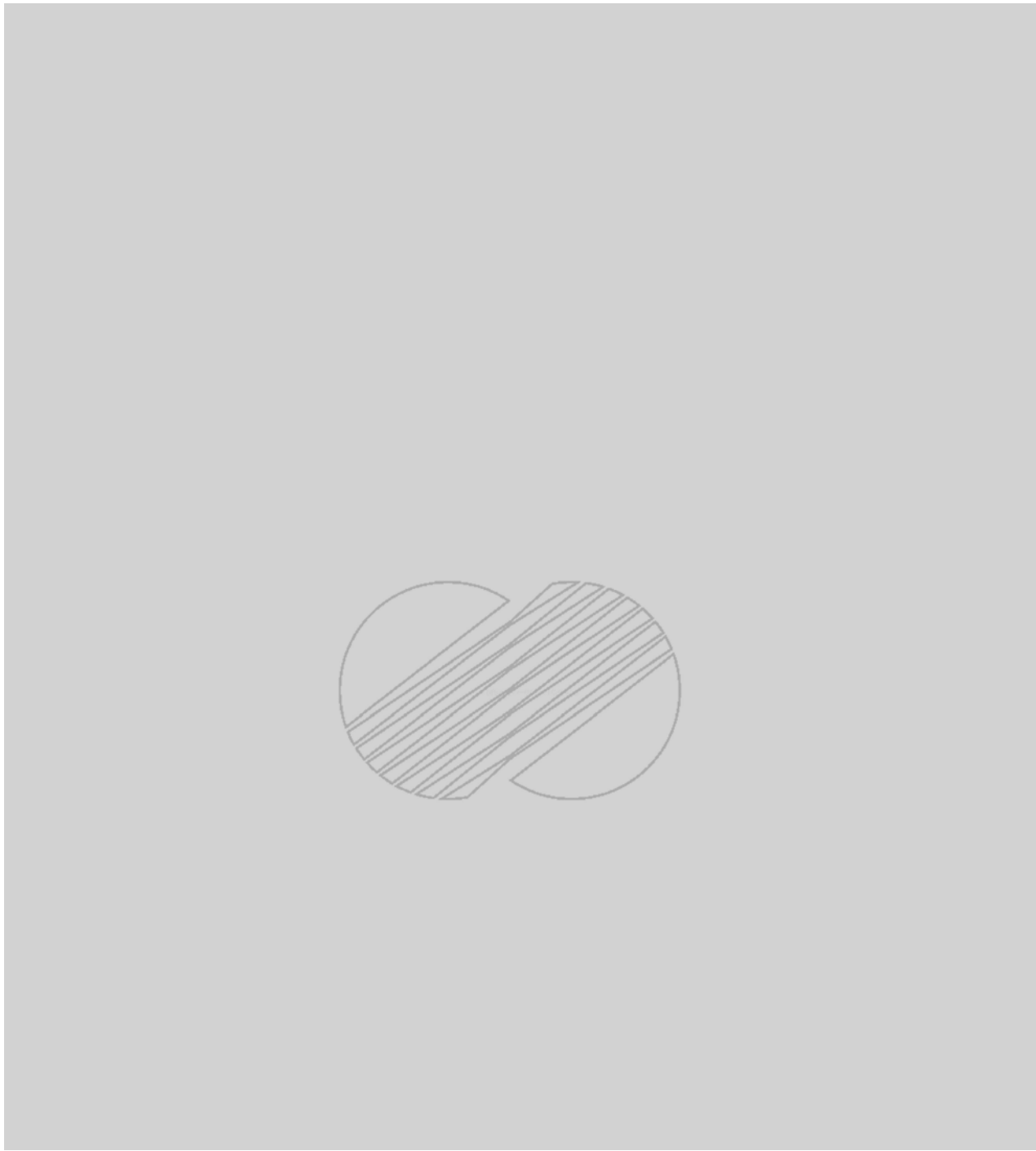

KOREA ELECTRIC POWER CORPORATION
YONGGWANG 3 & 4
FSAR

FULL-STRENGTH CONTROL ELEMENT
ASSEMBLY (12-ELEMENT)

Figure 4.2-4

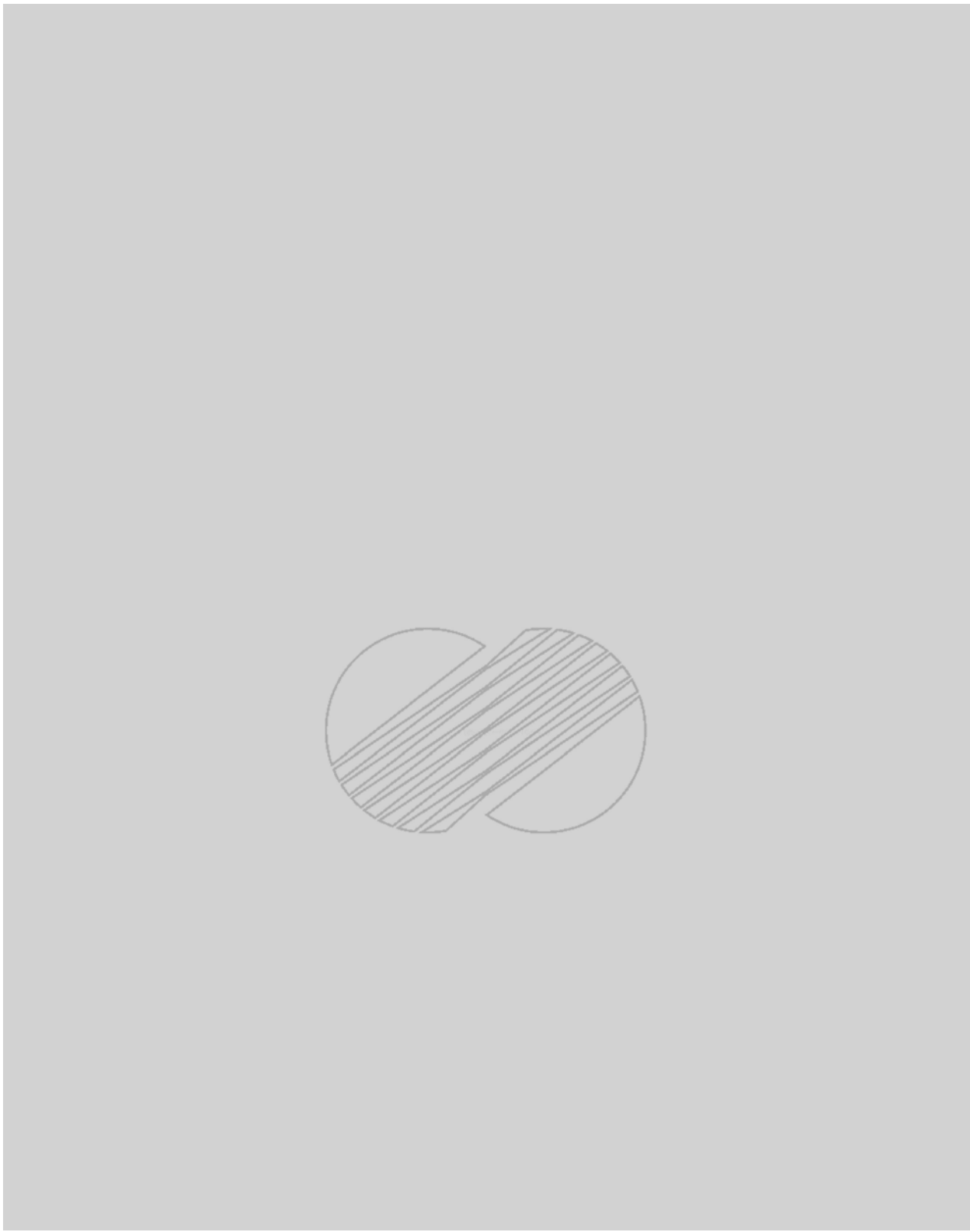

KOREA ELECTRIC POWER CORPORATION
YONGGWANG 3 & 4
FSAR

PART-STRENGTH CONTROL
ELEMENT ASSEMBLY

Figure 4.2-5

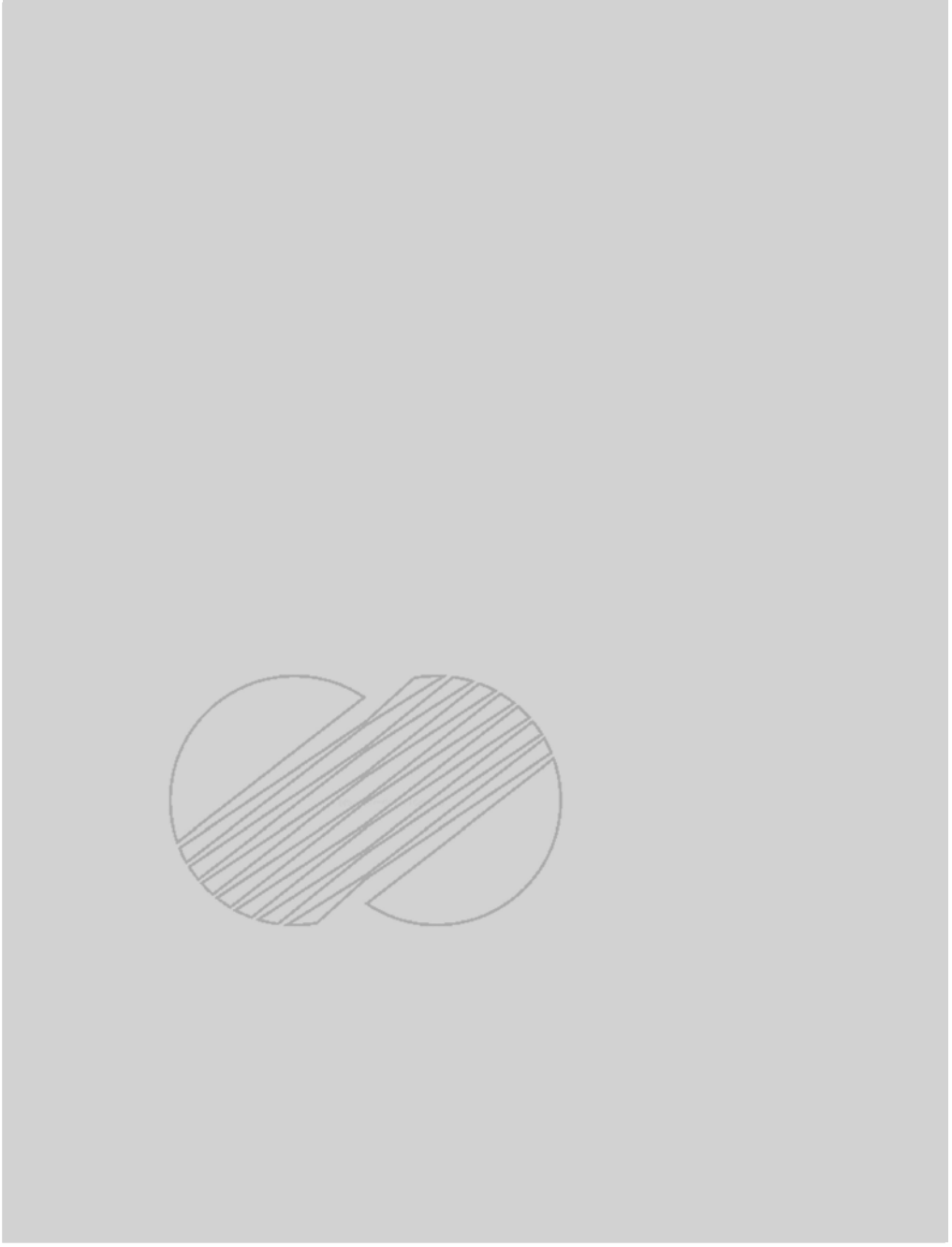

KOREA HYDRO & NUCLEAR POWER COMPANY
YOUNGGWANG 3 & 4
FSAR

FUEL ASSEMBLY

Figure 4.2-6

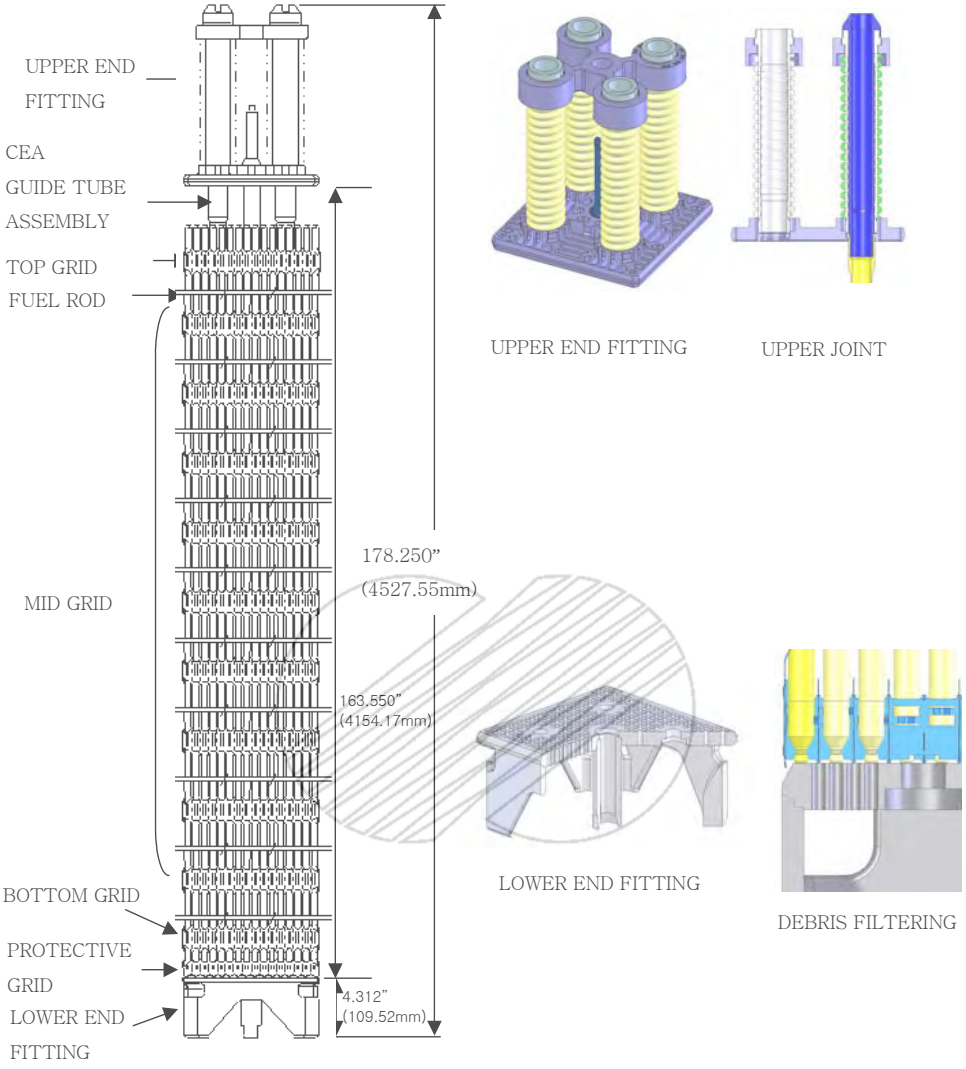

KOREA HYDRO & NUCLEAR POWER COMPANY
YONGGWANG 3 & 4
FSAR

FUEL ASSEMBLY

Figure 4.2-6 a

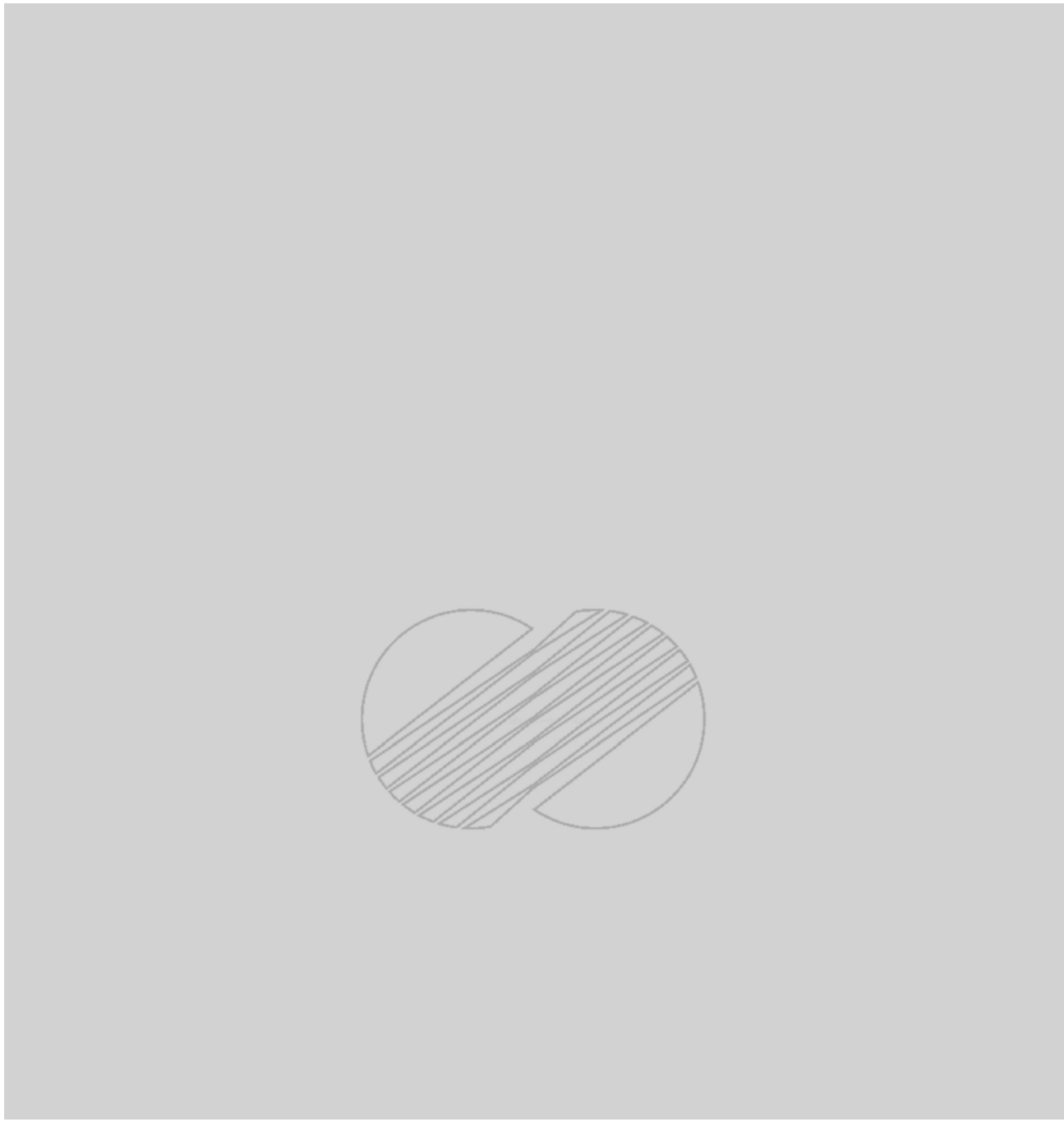

KOREA ELECTRIC POWER CORPORATION
YONGGWANG 3 & 4
FSAR

FUEL SPACER GRID

Figure 4.2-7

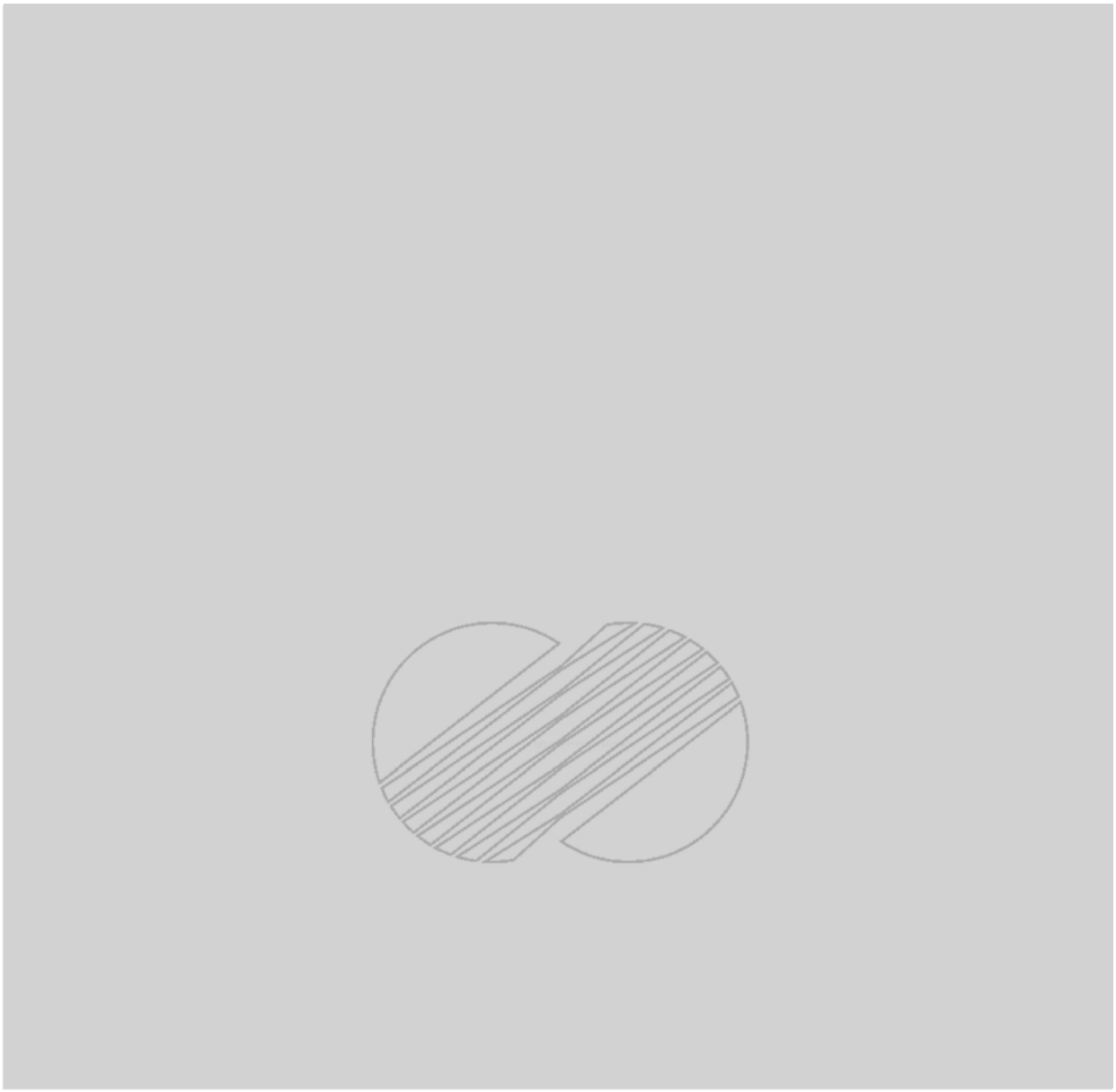

KOREA HYDRO & NUCLEAR POWER COMPANY
YONGGWANG 3 & 4
FSAR

Spacer Grid

Figure 4.2-7 a

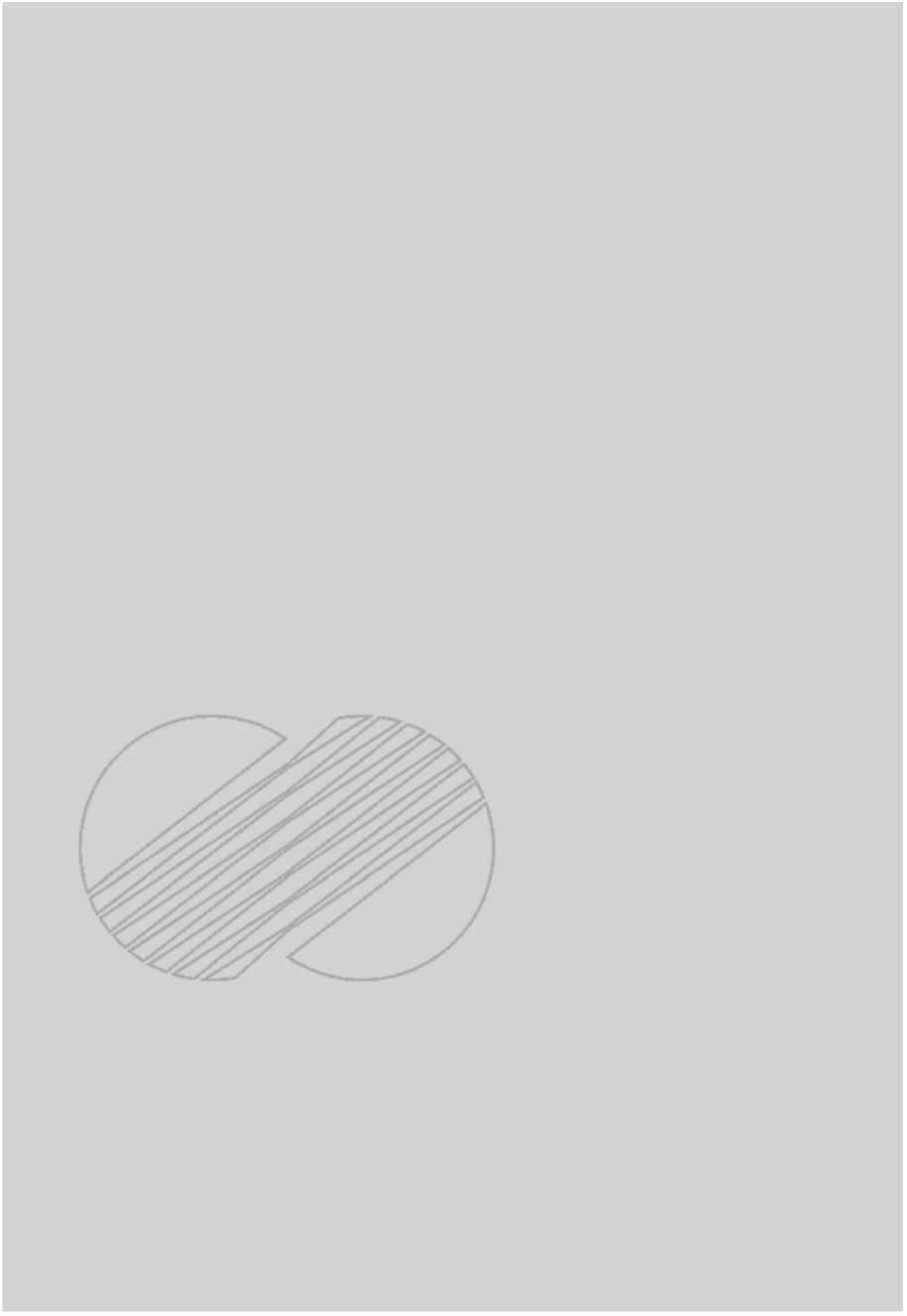

KOREA HYDRO & NUCLEAR POWER COMPANY
YONGGWANG 3 & 4
FSAR

FUEL ROD

Figure 4.2-8

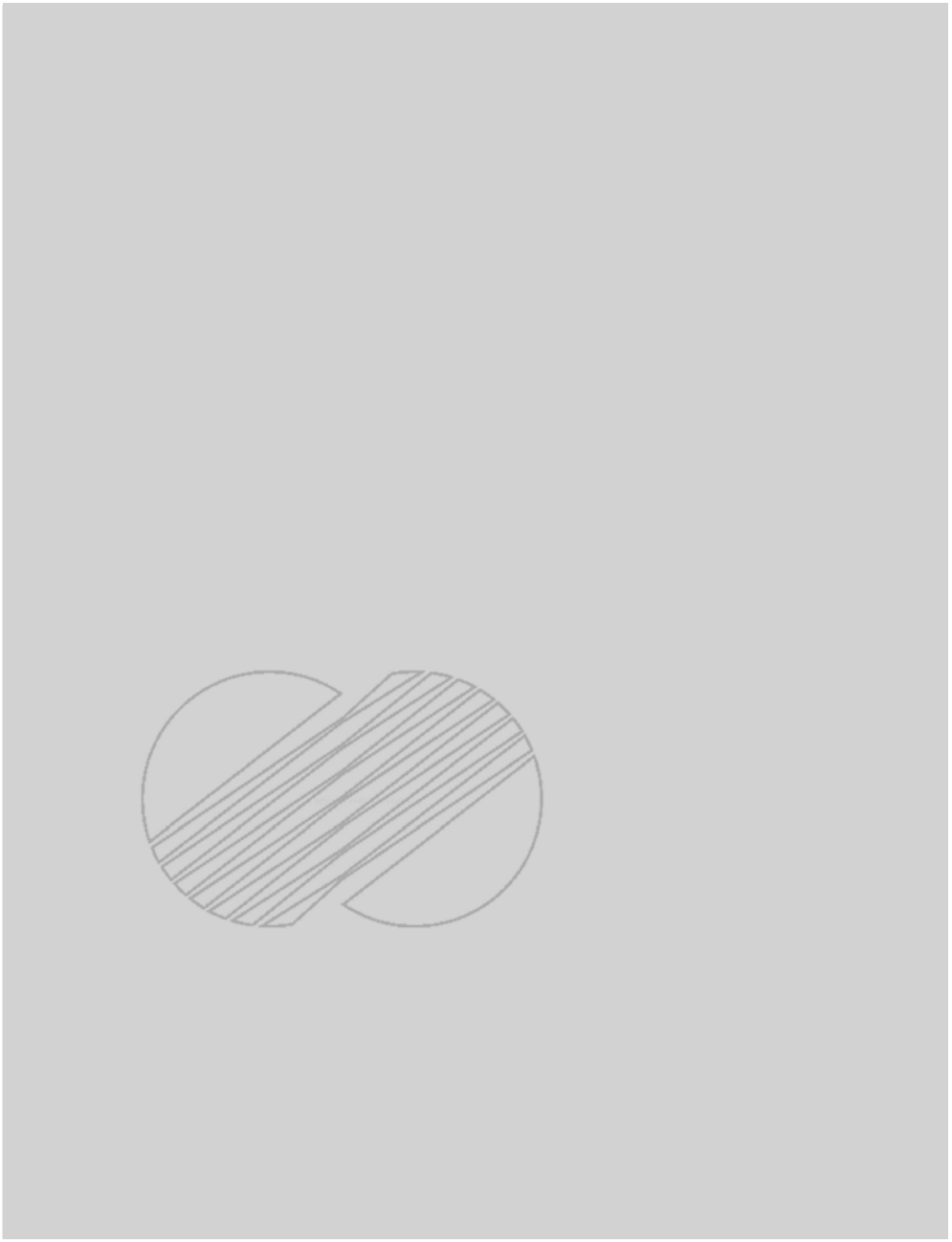

KOREA HYDRO & NUCLEAR POWER COMPANY
YONGGWANG 3 & 4
FSAR

FUEL ROD

Figure 4.2-8 a

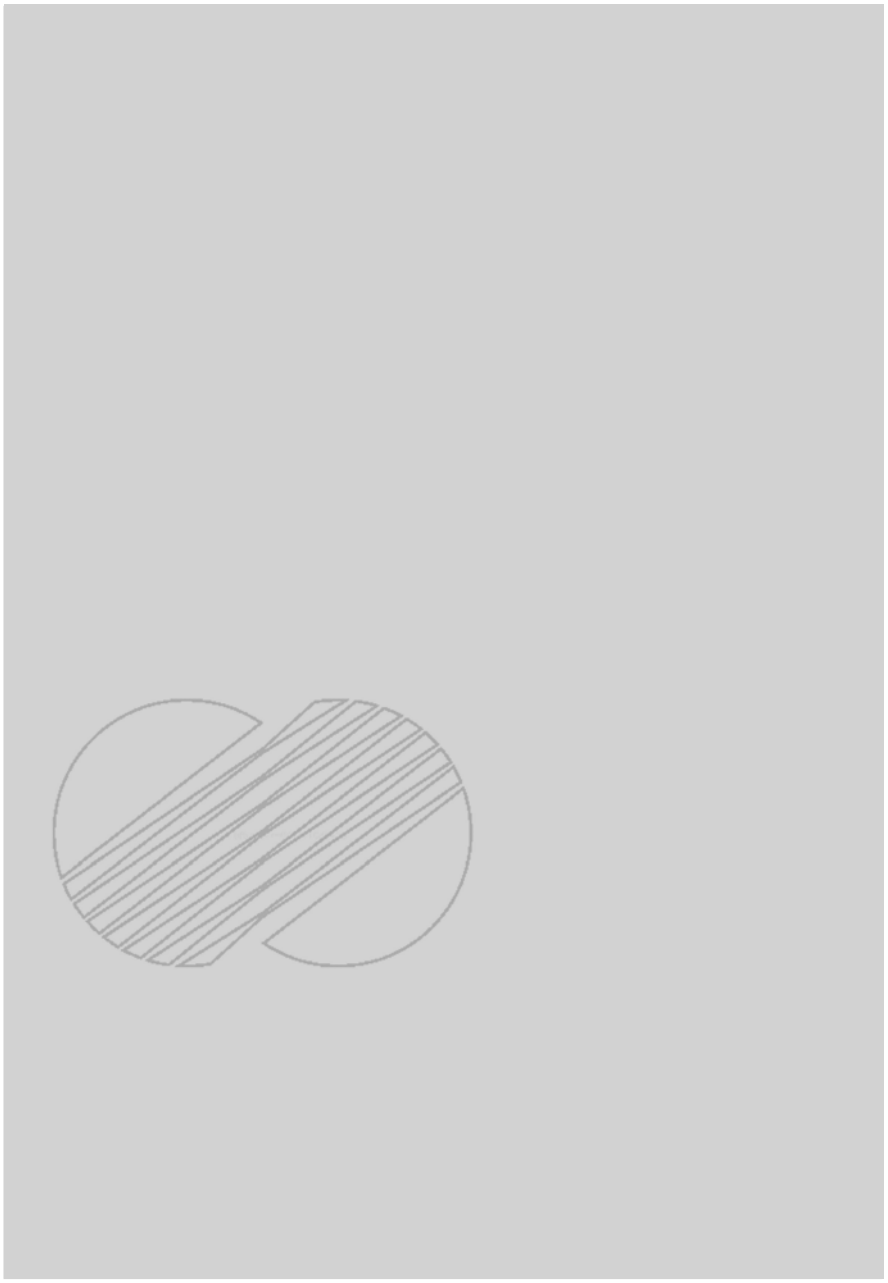

KOREA HYDRO & NUCLEAR POWER COMPANY
YONGGWANG 3 & 4
FSAR

POISON ROD

Figure 4.2-9

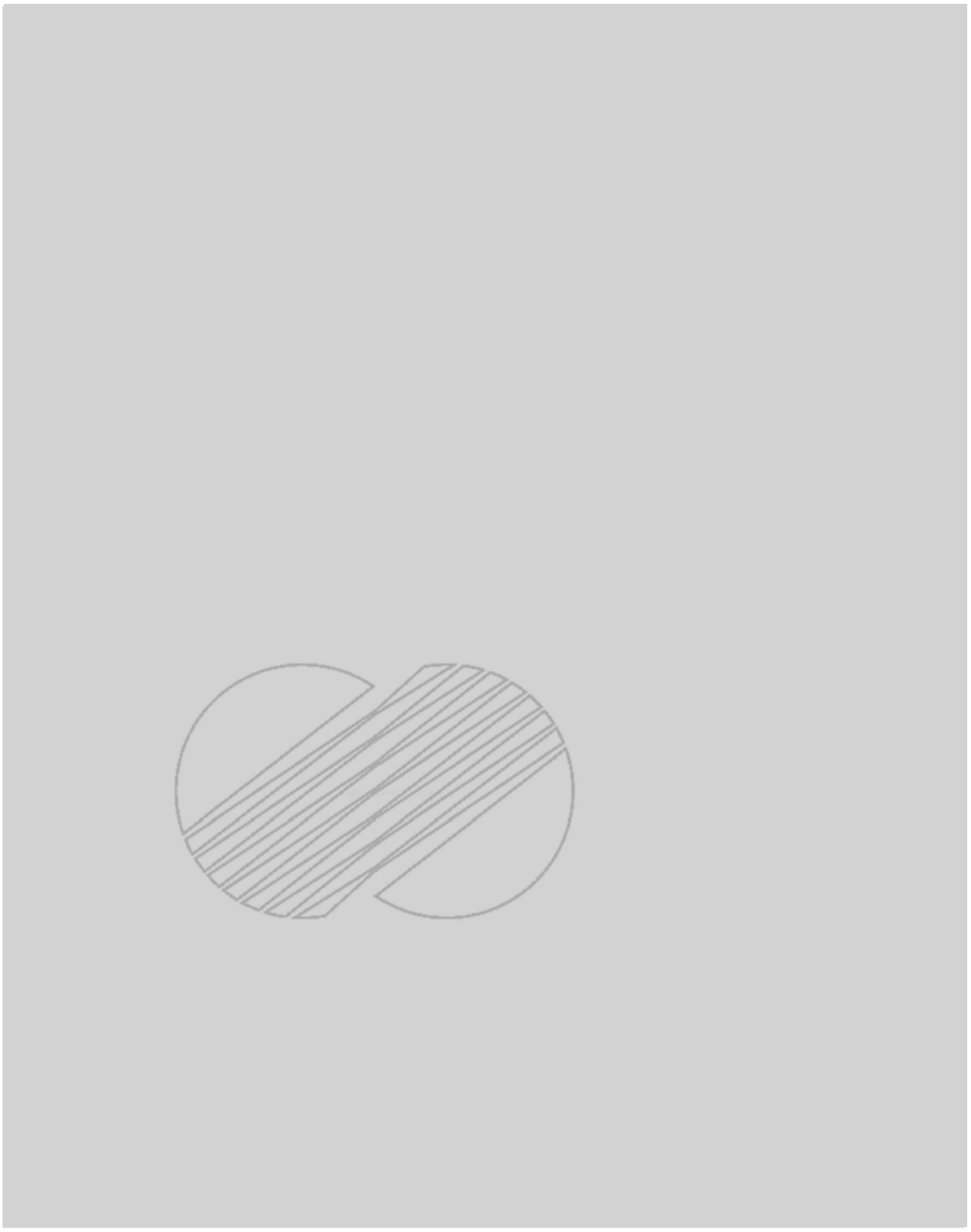

KOREA HYDRO & NUCLEAR POWER COMPANY
YONGGWANG 3 & 4
FSAR

POISON ROD

Figure 4.2-9 a

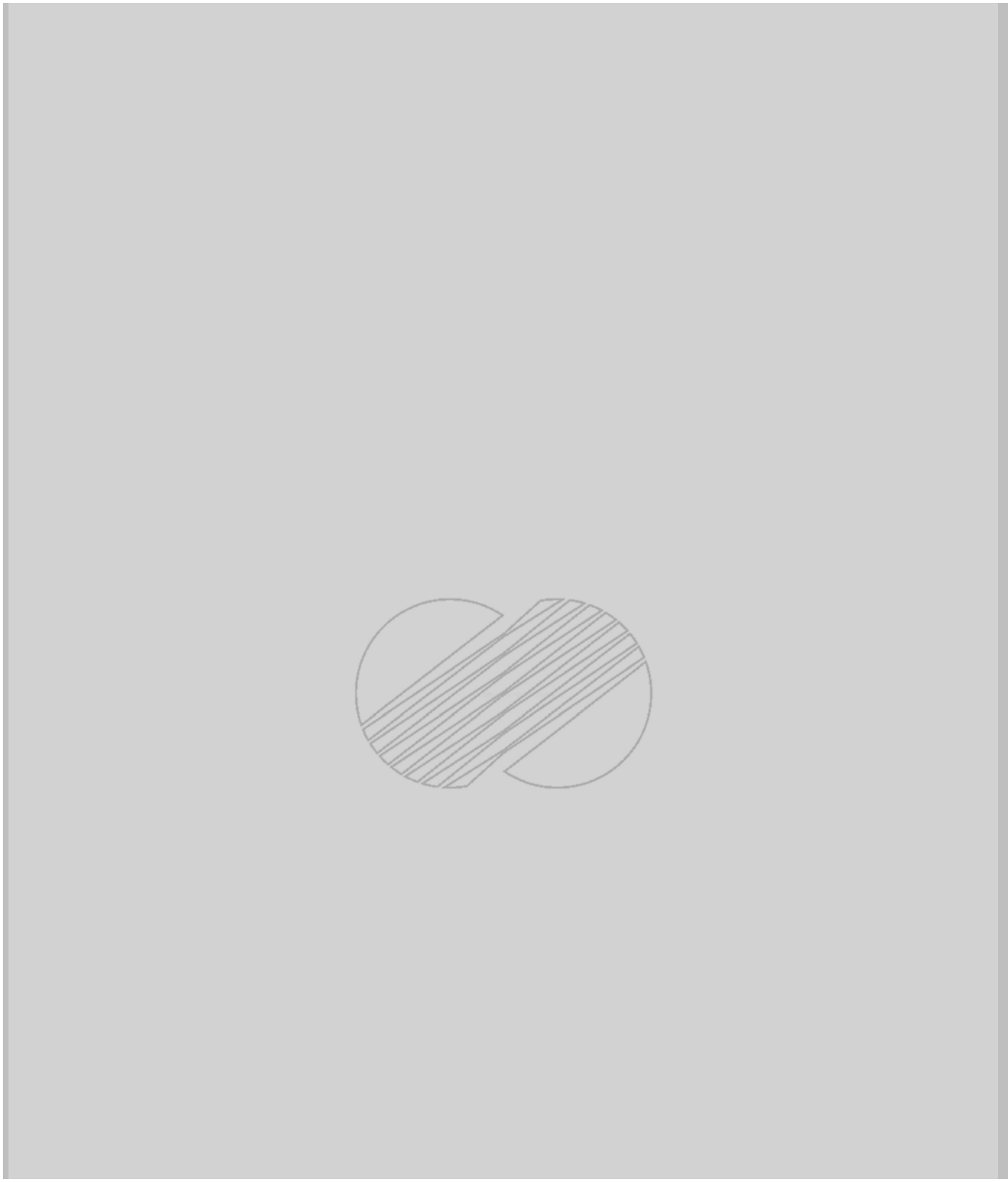

KOREA ELECTRIC POWER CORPORATION
YONGGWANG 3 & 4
FSAR

CEA & NSA LOCATIONS

Figure 4.2-10

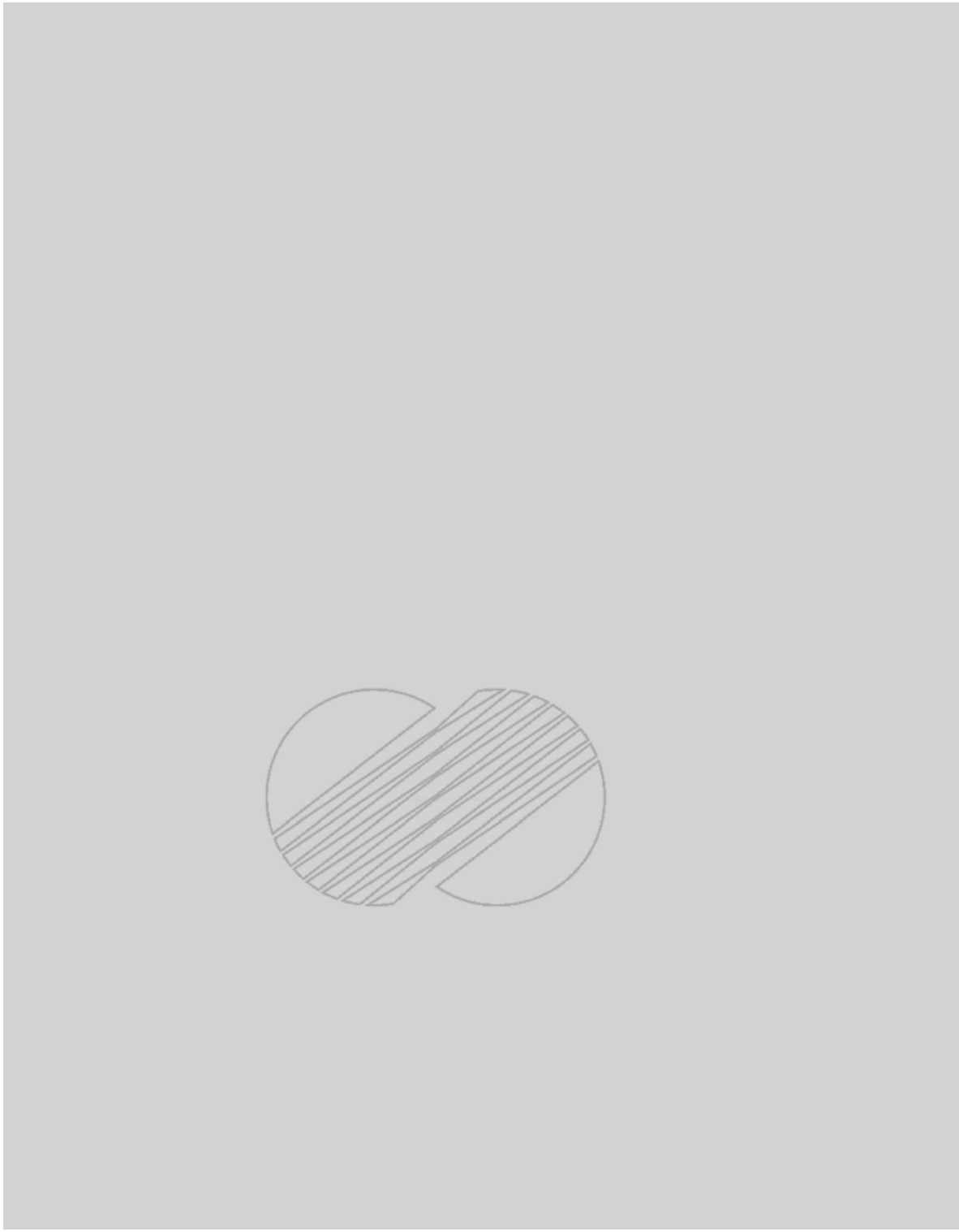

KOREA ELECTRIC POWER CORPORATION
YONGGWANG 3 & 4
FSAR

NEUTRON SOURCE ASSEMBLY

Figure 4.2-11

4.3 NUCLEAR DESIGN

4.3.1 Design Bases

The bases for the nuclear design of the fuel and reactivity control systems are discussed in the following subsections.

4.3.1.1 Excess Reactivity and Fuel Burnup

The excess reactivity provided for each cycle is based on the depletion characteristics of the fuel and burnable poison and on the desired burnup for each cycle. The desired burnup is based on an economic analysis of the fuel cost and the projected operating load cycle for YGN 3&4. The average burnup is chosen to ensure that the peak burnup is within the limits discussed in Subsection 4.2.3.2.12. This design basis, along with the design basis in Subsection 4.3.1.8, satisfies General Design Criterion 10.

4.3.1.2 Core Design Lifetime and Fuel Replacement Program

The core design lifetime and fuel replacement program are based on approximately annual refueling with approximately one-fourth of the fuel assemblies replaced at each refueling in later cycles. The first cycle design lifetime is longer than later cycles to permit a more orderly transition to equilibrium cycle conditions.

4.3.1.3 Negative Reactivity Feedback

In the power operating range, the net effect of the prompt inherent nuclear feedback characteristics (fuel temperature coefficient, moderator temperature coefficient, and moderator pressure coefficient) tends to compensate for a rapid increase in reactivity. The negative reactivity feedback provided by the design satisfies General Design Criterion 11.

4.3.1.4 Reactivity Coefficients

The values of each coefficient of reactivity are consistent with the design basis for net reactivity feedback (Subsection 4.3.1.3), and analyses that predict acceptable consequences of postulated accidents and anticipated operational occurrences, where such analyses include the response of the reactor protection system (RPS).

4.3.1.5 Burnable Poison Requirements

The burnable poison reactivity worth provided in the design is sufficient to ensure that the moderator coefficients of reactivity are consistent with the design bases in Subsection 4.3.1.4.

4.3.1.6 Stability Criteria

The reactor and the instrumentation and control systems are designed to detect and suppress xenon-induced power distribution oscillations that could, if not suppressed, result in conditions that exceed the specified acceptable fuel design limits. The design of the reactor and associated systems precludes the possibility of power level oscillations. This basis satisfies General Design Criterion 12.

4.3.1.7 Maximum Controlled Reactivity Insertion Rate

The core, control element assemblies (CEAs), reactor regulating system, and boron charging portion of the chemical and volume control system are designed so that the potential amount and rate of reactivity insertion due to normal operation and postulated reactivity accidents do not result in the following:

a. Violation of the specified acceptable fuel design limits

b. Damage to the reactor coolant pressure boundary

c. Disruption of the core or other reactor internals sufficient to impair the effectiveness of emergency core cooling system

This design basis, along with Subsection 4.3.1.11, satisfies General Design Criteria 25 and 28.

4.3.1.8 Power Distribution Control

The core power distribution is controlled such that, in conjunction with other core operating parameters, the power distribution does not result in violation of the limiting conditions for operation. Limiting conditions for operation and limiting safety system settings are based on the accident analyses described in Chapters 6 and 15 such that specified acceptable fuel design limits and other criteria are not exceeded for accidents. This basis, along with Subsection 4.3.1.1, satisfies General Design Criterion 10.

4.3.1.9 Excess CEA Worth with Stuck Rod Criteria

The amount of reactivity available from insertion of withdrawn CEAs under all power operating conditions, even when the highest worth CEA fails to insert, will provide for at least 1.4% excess CEA worth after cooldown to hot zero power, plus any additional shutdown reactivity requirements assumed in the safety analyses. This basis, along with Subsection 4.3.1.10, satisfies General Design Criteria 26 and 27.

4.3.1.10 Chemical Shim Control

The chemical and volume control system (CVCS) (Subsection 9.3.4) is used to adjust the dissolved boron concentration in the moderator. After a reactor shutdown, this system is able to compensate for the reactivity changes

associated with xenon decay and reactor coolant temperature decreases to ambient temperature, and it provides adequate shutdown margin during the refueling. This system also has the capability of controlling, independently of the CEAs, long-term reactivity changes due to fuel burnup and reactivity changes during xenon transients resulting from changes in reactor load. This design basis, along with Subsection 4.3.1.9, satisfies General Design Criteria 26 and 27.

4.3.1.11 Maximum CEA Speeds

Maximum CEA speeds are consistent with the maximum controlled reactivity insertion rate design basis discussed in Subsection 4.3.1.7. Maximum CEA speeds are also discussed in Subsection 15.4.2.

4.3.2 Description

4.3.2.1 Nuclear Design Description

This subsection summarizes the nuclear characteristics of the core and discusses the important design parameters that affect the performance of the core in steady-state and normal transient operation. Summaries of nuclear design parameters are presented in Tables 4.3-1 and 4.3-2 and Figures 4.3-1 and 4.3-2. These data are intended to be descriptive of the first cycle design. Design limit values for these and other parameters are discussed in the appropriate sections.

The first cycle design features a four-batch loading scheme in which the type B, C, and D fuel assemblies contain rods of two different enrichments. This system of enrichment zoning shown in Figure 4.3-2 offers improved long-term control over the local assembly power distribution.

The fuel loading pattern, fuel enrichment, and burnable poison distributions are shown in Figures 4.3-1 and 4.3-2. The other three quadrants of the core are symmetric to the displayed quadrant. Physical features of the lattice, fuel assemblies, and CEAs are described in Section 4.2.

Core average enrichment, core burnup, critical soluble boron concentrations and worths, plutonium buildup, and delayed neutron fractions and neutron lifetime are shown in Table 4.3-1. The soluble boron insertion rates available, as discussed in Subsection 9.3.4, are sufficient to compensate for the maximum reactivity addition due to xenon burnout and normal plant cooldown. This maximum reactivity addition rate for which the CVCS will be required to compensate is given in Table 4.3-1. The maximum reactivity addition rate requirement occurs for an end-of-cycle cooldown, where the moderator temperature coefficient is most negative.

The k_{eff}, reactivity, and reactivity defect data associated with the cold zero power, hot standby, hot full power without xenon or samarium, and hot full power with equilibrium xenon and samarium conditions are shown in Table 4.3-2.

4.3.2.2 Power Distribution

4.3.2.2.1 General

Power distribution and coolant conditions are controlled so that the peak linear heat rate and the minimum departure from nucleate boiling ratio (DNBR) are maintained within operating limits supported by the safety analyses (Chapters 6 and 15) with due regard for the correlations between measured quantities, the power distribution, and uncertainties in the determination of power distribution.

Methods of controlling the power distribution include the use of full- or part-strength CEAs to alter the axial power distribution; decreasing CEA

insertion by boration, thereby improving the radial power distribution; and correcting off-optimum conditions that cause margin degradations (e.g., CEA misoperation).

The core operating limit supervisory system (COLSS) indicates continuously to the operator how far the core is from the operating limits and provides an audible alarm should an operating limit be exceeded. Such a condition signifies a reduction in the capability of the plant to withstand an anticipated transient, but does not necessarily imply a violation of fuel design limits. If the fuel design margin limits continue to decrease, the RPS assures that the specified acceptable fuel design conditions are not exceeded by initiating a trip.

The COLSS, described in Section 7.7 and Reference 22, continually generates an assessment of the margin to linear heat rate and DNBR operating limits. The data required for these assessments include measured incore neutron flux data, CEA positions, and coolant inlet temperature, pressure, and flow rate. In the event of an alarm indicating that an operating limit has been exceeded, power must be reduced unless the alarm can be cleared by improving either the power distribution or another process parameter. The accuracy of the COLSS calculations are verified periodically as discussed in Chapter 16.

In addition to the monitoring by COLSS, the RPS core protection calculator (CPC, see Section 7.2) continually infers the core power distribution and DNBR by processing reactor coolant data; signals from excore neutron flux detectors, each containing three axially stacked elements; and input from redundant reed switch assemblies to indicate CEA position. In the event the power distributions or other parameters are perturbed as the result of an anticipated operational occurrence that would violate fuel design limits, the high local power density or low DNBR trips in the RPS will initiate a reactor trip.

4.3.2.2.2 Nuclear Design Limits on the Power Distribution

The design limits on the power distribution stated here were employed during the design process both as design input and as initial conditions for the accident analyses described in Chapters 6 and 15. However, for the monitoring system, it is the final operating limit determination that is used to assure that the consequences of an anticipated operational occurrence or postulated accident will not be any more severe than the consequences shown in Chapters 6 and 15. The initial conditions used in this operating limit determination are actually stated in terms of peak linear heat generation rate and required power margin for minimum DNBR.

The design limits on power distribution are as follows:

a. The limiting three-dimensional heat flux peaking factor, F_q^n, was established for full power conditions at 2.58. This is based directly upon the LOCA limit of 13.9 kW/ft (456.0 W/cm) and the full power core average linear heat rate of 5.39 kW/ft (176.8 W/cm). Of course, a higher F_q^n is allowed for reduced core power levels.

   Implementation in the Technical Specification is via a power operating limit based on peak linear heat generation rate.

b. The thermal margin to a minimum DNBR of 1.30 (using the CE-1 CHF correlation as discussed in Subsections 4.4.2.2 and 4.4.4.1), which is available to accommodate anticipated operational occurrences, is a function of several parameters, including

   1. the coolant conditions,

   2. the axial power distribution, and

3. the axially integrated radial peaking factor, F_r^n; where F_r^n is the rod radial nuclear factor or the rod radial peaking factor and is defined in Subsection 4.4.2.2.2.1., Paragraph a. (referred to as F_r in that section).

The coolant conditions assumed in the safety analyses, the F_r^n design target chosen to be 1.55 as shown in Figure 4.3-44, and the set of axial shapes displayed in Figure 4.4-3 constitute a set of limiting combinations of parameters for full-power operation. Other combinations giving acceptable accident analysis consequences are equally acceptable. Implementation of these limits in the Technical Specification is via a power operating limit based on DNBR, which maintains an appropriate amount of thermal margin to the DNBR limit. It is shown in the following subsections that operation within these design limits is achievable.

4.3.2.2.3 Expected Power Distributions

Figures 4.3-3 through 4.3-17 and 4.3-18 through 4.3-23 show typical first-cycle planar average radial and unrodded core average axial power distributions, respectively. They illustrate conditions expected at full power for various times in the fuel cycle as specified on the figures. It is expected that the normal operation of the reactor will be with limited CEA insertion so that these power distributions represent the expected power distribution during most of the cycle. The maximum expected value of F_q^n is 2.07 during the first cycle and, as can be seen from the above-named figures, occurs near the beginning-of-cycle for steady-state, baseloaded operation with no CEA insertion. The uncertainty associated with these calculated power distributions is discussed in Subsection 4.3.3.1.2.2.3.

Figures 4.3-24 through 4.3-35 show the planar average radial power distribution of later cycles which are used in fuel rod integrity analyses.

Since the F_r and F_q design limits should be met in the design of later cycles, the power distributions of later cycles will be similar to those of the first cycle.

The capability of the core to follow load transients without exceeding power distribution limitations depends on the margin to operating limits compared to the margin required for baseloaded, unrodded operation. In order to illustrate the maneuvering capability available in YGN 3&4, the results of calculations of the power distributions and power peaking factors during several load following transients are discussed below. The axial power distributions are calculated by VISIONS (Reference 24), a three-dimensional neutron diffusion code that considers the effects of the time and spatial variations of xenon and iodine concentration, CEA position, fuel temperature and moderator density feedback mechanisms, and the burnup distribution. The nuclear peaking factors F_q^n and F_r^n are synthesized in VISIONS using the calculated three-dimensional coarse mesh power distribution and the input pin-to-box factors (from MC), which can be dependent on the presence of CEAs at each axial height. Figures 4.3-36 through 4.3-43 show the calculated axial power distributions and associated nuclear peaking factors at the beginning-of-cycle (BOC), middle-of-cycle (MOC), and near end-of-cycle (EOC) during a typical 100-50-100%, 2-6-2-14 daily load-cycle maneuvering transient. Also shown on these figures are the CEA locations during each transient. Throughout the calculation of the power distribution during each transient, it is assumed that the part-strength CEAs are available for control of the axial power distribution. The part-strength CEAs are moved to the position that minimizes the difference between the current shape index and the reference value of shape index that existed before the initiation of the maneuver. The maneuvers simulated here are considered typical and were chosen to illustrate the power shape control capabilities of the part-strength CEAs, with reactivity balance maintained by soluble boron. Near EOC, regulating CEAs can be used in addition to the part-strength CEAs to maintain power shape control during the maneuver.

The detailed radial power distribution within any assembly is a function of the location of that assembly within the core as well as the time in life, CEA insertion, etc. The normalized assembly power distribution used for the sample DNB calculation discussed in Subsection 4.4.2.2 is shown on Figure 4.3-44. In Subsection 4.3.3.1.1 the accuracy of calculations of the power distribution within a fuel assembly is discussed.

4.3.2.2.4 Allowances and Uncertainties on Power Distributions

In comparing the expected power distributions and implied peak linear heat generation rate (PLHGR) produced by analysis with the design limits stated in Subsection 4.3.2.2.2, consideration must be given to the uncertainties and allowances associated with online monitoring by COLSS (Reference 22), and to calculational uncertainties. The design limit F_q^n mentioned in Subsection 4.3.2.2.2 for hot full power (HFP), that is, 2.58, will be determined by COLSS to have been reached if a COLSS-measured F_q^n of 2.20 occurs. This is because COLSS applies a factor to account for the power level measurement uncertainty (typically 1.02) and a factor to account for the COLSS LHR measurement uncertainty, expected to be no greater than 1.15. Thus, in order to avoid a COLSS alarm on PLHGR, the COLSS-measured F_q^n at HFP must be no greater than 2.20. This value (2.20) is chosen as a design target maximum F_q^n for HFP.

4.3.2.2.5 Comparisons Between Limiting and Expected Power Distributions

As was discussed in Subsection 4.3.2.2.3, the maximum expected unrodded F_q^n that occurs during the first cycle at full power is 2.07. Augmenting this value by the required calculational uncertainty provides 95/95 confidence upper limit on F_q^n of 2.19, which is below the design target of 2.20. Additionally, the calculations described in Subsection 4.3.2.2.3 show that, with proper use of the part-strength CEAs, no appreciable increase in the peak linear heat rate occurs during these maneuvering transients. In the event that the part-strength CEAs are not moved properly, the power distribution

could become unacceptable. In this case, the monitoring system indicates whether insufficient margin to operating limits has been reached, and indicates that action has to be taken to improve the core power distribution, to improve the coolant conditions, or to reduce core power.

Similarly, even allowing for calculational uncertainty, the maximum expected unrodded F_r^n that occurs at full power is not higher than the design target stated in Subsection 4.3.2.2.2 of 1.55. Again, as demonstrated by the calculations of the power distributions expected to occur during maneuvering transients, no appreciable loss in thermal margin is expected to occur during these transients.

4.3.2.3 Reactivity Coefficients

Reactivity coefficients relate changes in core reactivity to variations in fuel or moderator conditions. The data presented in this subsection and associated tables and figures illustrate the range of reactivity coefficient values calculated for a variety of operating and accident conditions. Subsection 4.3.3 presents comparisons of calculated and measured moderator temperature coefficients and power coefficients for operating reactors. The good agreement shown in that subsection provides confidence that the data presented in this section adequately characterize the YGN 3&4 reactors. Table 4.3-3 presents a comparison of the reactivity coefficients calculated for YGN 3&4 reactors with those used in the safety analyses described in Chapters 6 and 15. For each accident analysis, suitably conservative reactivity coefficient values are used. Since uncertainties in the coefficient values, as discussed in Subsection 4.3.3.1.2, and other conservatisms are taken into account in the safety analyses, values used in the safety analyses may fall outside the ranges in a conservative direction of the data presented in this subsection. A more extensive list of reactivity coefficients is given in Table 4.3-4.

The calculational methods used to compute reactivity coefficients are discussed in Subsection 4.3.3.1.1. All data discussed in subsequent subsections were calculated with two-dimensional and three-dimensional quarter-core nuclear models. Spatial distributions of materials and flux weighting are explicitly performed for the particular conditions at which the reactivity coefficients are calculated. The adequacy of this method is discussed in Subsection 4.3.3.1.2.

4.3.2.3.1 Fuel Temperature Coefficient

The fuel temperature coefficient is the change in reactivity per unit change in fuel temperature. A change in fuel temperature affects the reaction rates in both the thermal and epithermal neutron energy regimes. Epithermally, the principal contributor to the change in reaction rate with fuel temperature is the Doppler effect arising from the increase in absorption widths of the resonances with an increase in fuel temperature. The ensuing increase in absorption rate with fuel temperature causes a negative fuel temperature coefficient. In the thermal energy regime, a change in reaction rate with fuel temperature arises from the effect of temperature dependent scattering properties of the fuel matrix on the thermal neutron spectrum. In typical PWR fuels containing strong resonance absorbers such as U-238 and Pu-240, the magnitude of the component of the fuel temperature coefficient arising from the Doppler effect is more than a factor of 10, larger than the magnitude of the thermal energy component.

Figure 4.3-45 shows the dependence of the calculated fuel temperature coefficient on the fuel temperature, both at the beginning and the end of the first cycle.

4.3.2.3.2 Moderator Temperature Coefficient

The moderator temperature coefficient relates changes in reactivity to uniform changes in moderator temperature, including the effects of moderator density change with changes in moderator temperature. Typically, an increase in the moderator temperature causes a decrease in the core moderator density and, therefore, less thermalization, which reduces the core reactivity. However, when soluble boron is present in the moderator, a reduction in moderator density causes a reduction in the content of soluble boron in the core, thus producing a positive contribution to the moderator temperature coefficient. In order to limit the dissolved boron concentration, rods with burnable poison are provided in the form of Gd_2O_3-doped UO_2 fuel rods. The number of poison rods is given in Table 4.3-1 and their distribution in one quadrant of the core is shown in Figure 4.3-1. The distribution is identical for the other three quadrants. The reactivity control provided by the poison rods is given in Table 4.3-1. This control makes possible a reduction in the dissolved boron concentration to the values given in Table 4.3-1.

The calculated moderator temperature coefficients for various core conditions at beginnings and end of first cycle are given in Table 4.3-4. The moderator temperature coefficients are more negative at end-of-cycle because the soluble boron in the coolant is reduced. The buildup of equilibrium xenon produces a net negative change of -0.38×10^{-4} $\Delta\rho/°F$ in the moderator temperature coefficient; this change is due mainly to the accompanying reduction in critical soluble boron. The changing fuel isotopic concentrations and the changing neutron spectrum during the fuel cycle depletion also contribute a small negative component to the moderator temperature coefficient.

The dependence of the moderator temperature coefficient on moderator temperature at BOC and EOC (at constant soluble boron) is shown in Figures 4.3-46 and 4.3-47, respectively. These figures also show the expected moderator temperature coefficient at reduced power levels (corresponding to

reduced moderator temperature) based on power reductions accomplished with soluble boron only and with CEAs only. These two modes of power reduction result in the most positive and most negative moderator temperature coefficients expected to occur at reduced power levels. These figures show the expected moderator temperature coefficient for the full range of expected operating conditions and accident conditions addressed in Chapter 15.

4.3.2.3.3 Moderator Density Coefficient

The moderator density coefficient is the change in reactivity per unit change in the core average moderator density at constant moderator temperature. A positive moderator density coefficient translates into a negative contribution to the total moderator temperature coefficient, which is defined in Subsection 4.3.2.3.2. The density coefficient is always positive in the operating range, although the magnitude decreases as the soluble boron level in the core is increased. The calculated density coefficient is shown in Table 4.3-4, and curves of density coefficient as a function of density for several soluble boron concentrations are presented in Figure 4.3-48. These curves are based upon 3-D ROCS calculations and have been generated over a wide range of core conditions. The density coefficients explicitly used in the accident analyses are based upon core conditions with the most limiting temperature coefficients allowed by the Technical Specification. Table 4.3-3 shows a comparison of the expected values of the moderator temperature coefficients with those actually used in the accident analyses.

4.3.2.3.4 Moderator Nuclear Temperature Coefficient

The moderator nuclear temperature coefficient is the change in reactivity per unit change in core average moderator temperature, at constant moderator density. The source of this reactivity dependence is the spectral effects associated with the change in thermal scattering properties of water molecules as the internal energy, which is represented by the bulk water temperature, is

changed. The magnitude of the moderator nuclear temperature coefficient is equal to the difference between the moderator temperature coefficient, defined in Subsection 4.3.2.3.2, and the moderator density coefficient, defined in Subsection 4.3.2.3.3.

4.3.2.3.5 Moderator Pressure Coefficient

The moderator pressure coefficient is the change in reactivity per unit change in reactor coolant system pressure. Since an increase in pressure, at constant moderator temperature, increases the water density, the pressure coefficient is merely the density coefficient expressed in a different form. The calculated pressure coefficient at full power is shown in Table 4.3-4.

4.3.2.3.6 Moderator Void Coefficient

The anticipated occurrence of small amounts of local subcooled boiling in the reactor during full-power operation results in a predicted core average steam (void) volume fraction of substantially less than 1%. Changes in the moderator void fraction produce reactivity changes that are quantified by the void coefficient of reactivity. An increase in voids decreases core reactivity, but the presence of soluble boron tends to add a positive contribution to the coefficient.

The calculated values of moderator void coefficient are shown in Table 4.3-4. Curves showing void coefficient vs. void content can be inferred directly from the density coefficient curves provided in Figure 4.3-48.

4.3.2.3.7 Power Coefficient

The power coefficient is the change in reactivity per unit change in core power level. All previously described coefficients contribute to the power coefficient, but only the moderator temperature coefficient and the fuel

temperature coefficient contributions are significant. The contributions of the pressure and void coefficients are negligible, because the magnitudes of these coefficients and the changes in pressure and void fraction per unit change in power level are small. The contribution of moderator density change is included in the moderator temperature coefficient contribution.

In order to determine the change in reactivity with power, it is necessary to know the changes in the average moderator and effective fuel temperature with power. The average moderator (coolant) temperature is controlled to be a linear function of power.

The core average linear heat rate is also linear with power. The average effective fuel temperature dependence on the core average linear heat rate is calculated from the following semiempirical relation:

$$T_f = T_{MOD}(p) + \left(\sum_{i=0}^{2} B_i * M^i\right) * p + \left(\sum_{j=0}^{3} C_j * M^j\right) * p^2 \qquad (4.3\text{-}1)$$

T_{MOD} is the average moderator temperature (°F), M is the exposure in MWd/MTU, p is the linear heat generation rate in the fuel in kW/ft, and T_f is the average effective fuel temperature (°F). The coefficients B_i and C_j are determined from least squares fitting of the fuel temperature generated by FATES (Reference 9). For a YGN 3&4 fuel rod, the following values apply:

$Bo = 146.526$ $\qquad$ $Co = -2.0355$

$B_1 = 0.8841 \times 10^{-3}$ $\qquad$ $C1 = -0.5121 \times 10^{-3}$

$B_2 = -0.2052 \times 10^{-6}$ $\qquad$ $C_2 = 0.5043 \times 10^{-7}$

$C_3 = -0.1071 \times 10^{-11}$

The basis for this relation is discussed in Reference 8.

The total power coefficient at a given core power can be determined by evaluation, for the conditions associated with the given power level, the following expression:

$$\frac{d\rho}{dp} = \frac{\partial \rho}{\partial T_f} \cdot \frac{\partial T_f}{\partial p} + \frac{\partial \rho}{\partial T_m} \cdot \frac{\partial T_m}{\partial p} \qquad (4.3\text{-}2)$$

The first term of Equation 4.3-2 provides the fuel temperature contribution to the power coefficient, which is shown as a function of power in Figure 4.3-49.

The first factor of the first term is the fuel temperature coefficient of reactivity discussed in Subsection 4.3.2.3.1 and shown in Figure 4.3-45. The second factor of the first term is obtained by calculating the derivative of Equation 4.3-1.

$$\frac{\partial T_f}{\partial p} = \frac{\partial T_{MOD}(p)}{\partial p} + \left(\sum_{i=0}^{2} B_i * M^i\right) + 2\left(\sum_{j=0}^{3} C_j * M^j\right) * p \qquad (4.3\text{-}3)$$

The second term in Equation 4.3-2 provides the moderator contribution to the power coefficient. The first factor, the moderator temperature coefficient, is discussed in Subsection 4.3.2.3.2 and shown in Figures 4.3-46 and 4.3-47. The second factor is a constant since the moderator temperature is controlled to be a linear function of power.

Since the factors $\partial\rho/\partial T_f$ and $\partial\rho/\partial T_m$ are functions of one or more independent variables (e.g., burnup, temperature, soluble boron content, xenon worth and CEA insertion), the total power coefficient, $d\rho/dp$, also depends on these variables.

The power coefficient tends to become more negative with burnup because the fuel and moderator temperature coefficients become more negative (see Figures 4.3-45 through 4.3-47). The insertion of the CEAs, while maintaining constant

power, results in a more negative power coefficient, because the soluble boron level is reduced and because of the spectral effects of the CEAs.

The full power values of the overall power coefficient for the unrodded core at BOC and EOC are shown in Table 4.3-4.

4.3.2.4 Control Requirements

There are three basic types of control requirements that influence the design of this reactor:

a. Reactivity control so that the reactor can be operated in the unrodded critical, full-power mode for the design cycle length.

b. Power level and power distribution control so that the reactor power may be safely varied from full rated power to cold shutdown, and so that the power distribution at any given power level is controlled within acceptable limits.

c. Shutdown reactivity control sufficient to mitigate the effects of postulated accidents.

Reactivity control is provided by several different means. The amount and enrichment of the fuel and burnable poison rods are design variables that determine the initial and end-of-cycle reactivity for an unrodded, unborated condition. Soluble boron and CEA poisons are flexible means of controlling long-term and short-term reactivity changes, respectively.

The following paragraphs discuss the reactivity balances associated with each type of control requirement.

4.3.2.4.1 Reactivity Control at BOC and EOC

The reactivities of the unrodded core with no soluble boron are shown in Table 4.3-2. This table includes the reactivity worth of equilibrium xenon and samarium, and shows the reactivity available to compensate for burnup and fission product poisoning. Soluble boron concentrations required for criticality at various core conditions are shown in Table 4.3-1. Soluble boron is used to compensate for slow reactivity changes such as those due to burnup and changes in xenon content. The reactivity controlled by burnable poison rods is also given in Table 4.3-1. At EOC, the reactivity worth of the residual poison is less than 1%, and the soluble boron concentration is near zero. The reactor is to be operated in essentially an unrodded condition at power. The CEA insertion at power is limited by the power-dependent insertion limit (PDIL) for short-term reactivity changes.

4.3.2.4.2 Power Level and Power Distribution Control

The regulating CEA groups may be used to compensate for changes in reactivity associated with routine power level changes. In addition, regulating CEAs may be used to compensate for minor variations in moderator temperature and boron concentrations during operation at power, and to dampen axial xenon oscillations. The reactivity worth of regulating CEA control groups is shown in Table 4.3-5. Soluble boron is used to maintain shutdown reactivity at cold zero power conditions. Soluble boron can also be used to compensate for changes in reactivity due to power level changes and minor changes in reactivity that might occur during normal reactor operation. Eight part-strength CEAs are provided in the design to help control the core power distribution. Their function includes the suppression of xenon-induced axial power oscillations.

4.3.2.4.3 Shutdown Reactivity Control

The reactivity worth requirements of the full complement of CEAs is primarily determined by the power defect, the excess CEA worth with the stuck rod criteria discussed in Subsection 4.3.1.9. Table 4.3-6 shows the reactivity component allowances that define the total reactivity allowance. These data are based on the end-of-cycle conditions when the fuel and moderator temperature coefficients are the most negative and thus when the shutdown reactivity requirement is a maximum. Each allowance component is further discussed below. No CEA allowance is provided for xenon reactivity effects, e.g., undershoot, since these effects are controlled with soluble boron rather than with CEAs.

The worth of all CEAs except the most reactive, which is assumed stuck in the fully withdrawn position, provides more shutdown capability than required by the total reactivity allowance shown in Table 4.3-6. This margin is shown in Table 4.3-7 for end of cycle one. The margin is more than sufficient to compensate for calculated uncertainties in the nominal design allowances and in the CEA reactivity worth. Thus, the shutdown reactivity control provided in this design is sufficient at all times in the cycle.

4.3.2.4.3.1 Fuel Temperature Variation

The increase in reactivity that occurs when the fuel temperature decreases from the full power value to the zero power value is due primarily to the Doppler effect in U-238. The CEA reactivity allowance for fuel temperature variation shown in Table 4.3-6 is a conservative allowance for the end-of-cycle conditions.

4.3.2.4.3.2 Moderator Temperature Variation

The moderator temperature variation allowance is large enough to compensate

for any reactivity increase that may occur when the moderator temperature decreases from the full power value to the zero power (hot standby) value. This reactivity increase, which is primarily due to the negative moderator temperature coefficient, is largest at the end-of-cycle when the soluble boron concentration is near zero and the moderator coefficient is strongly negative. At beginning-of-cycle, when the moderator temperature coefficient is less negative, the reactivity change is smaller.

The CEA reactivity allowance for moderator temperature variation given in Table 4.3-6 is actually the sum of three allowances. The first, and most important, is the allowance for the moderator temperature coefficient effect. The second is an allowance for the reduction in CEA worth resulting from the shorter neutron diffusion length at the zero power moderator density relative to the full power moderator density. This allowance is necessary because the CEA worths shown in Table 4.3-5 were calculated at full power. The third allowance is intended to cover the reactivity effects associated with the greatest expected axial flux redistribution resulting from the difference in moderator temperature profile between full and zero power, and the asymmetric axial isotopic distribution at EOC.

4.3.2.4.3.3 Moderator Voids

Reducing the power level from full power to zero power causes an increase in reactivity resulting from the collapsing of steam bubbles caused by local boiling at full power. The amount of void in the core is small and is estimated to be substantially less than 1% at full power. As with the moderator temperature effect, the maximum increase in reactivity from full to zero power occurs at end-of-cycle, when the least amount of dissolved boron is present. The reactivity effect is small, and allowance for this effect is shown in Table 4.3-6.

4.3.2.4.3.4 Control Element Assembly Bite

The CEA bite is the amount of reactivity worth in CEAs that can be inserted in the core at full power to initiate ramp changes in reactivity associated with load changes and to compensate for minor variations in moderator temperature, boron concentration, xenon concentration, part-strength CEA (PSCEA) movement, and power level. The reactivity allowance for this effect is shown in Table 4.3-6.

4.3.2.4.3.5 Accident Analysis Allowance

The allowance shown in Table 4.3-6 for accident analysis is consistent with that assumed under various postulated accident conditions addressed in Chapter 15, which result in predicted acceptable consequences.

4.3.2.4.3.6 Available Reactivity Worth

Table 4.3-7 shows the reactivity worths of the full complement of CEAs, and the highest reactivity worth of a single CEA in the fully withdrawn position, at the end of cycle one. This table also compares the available net shutdown worth (including the effects of the stuck CEA) to the reactivity worth requirements from Table 4.3-6. All required biases and uncertainties have been included in the CEA worths of Table 4.3-7. Subsection 4.3.3 presents detailed information on biases and uncertainties.

4.3.2.5 Control Element Assembly Patterns and Reactivity Worths

The locations of all CEAs are shown in Figure 4.3-50. The CEAs designated as regulating control rods are divided into five groups; the shutdown CEAs are divided into two groups; and the PSCEAs comprise one group. These groups are identified, for first cycle operation, in Figure 4.3-51. Figures 4.3-51a, 4.3-51b, 4.3-51c show CEA Group Arrangement and Number of Fingers, CEA Number, and Excore Detector Locations. All CEAs in a group are withdrawn or inserted quasi-simultaneously. Shutdown groups are inserted

85

after the regulating groups are inserted and are withdrawn before the regulating groups are withdrawn. The reactivity worths of sequentially inserted CEA groups are shown in Table 4.3-5 at the beginning and end of the first cycle where the integrated rod radial peaking factors (F_r^n)for these configurations occur. The values of F_r^n for these times are shown in Table 4.3-8.

The core will be essentially unrodded during full-power steady-state operation, except for limited insertion of the first regulating group in order to compensate for minor variations in moderator temperature and boron concentration. For operation with substantial CEA insertion, the relationship between power level and the maximum permitted CEA insertion is typified in Figure 4.3-52. This figure also illustrates the regulating group insertion order (5-4-3-2-1) and the 40% fixed overlap between successive regulating groups. Compliance with the power dependent insertion limits throughout the cycle ensures that adequate shutdown margin is maintained and that the core conditions are no more severe than the initial conditions assumed in the accident analyses described in Chapter 15.

Reactivity insertion rates for the safety analysis of the core are presented in Chapter 15. The full power CEA ejection accident considers the ejection of one CEA from the maximum insertion of the lead bank allowed by PDIL. The ejected CEA worth is calculated by taking the difference between the pre-ejection and post-ejection reactivity of the core computed by static methods. Similar CEA ejection event analyses are performed for zero power and several intermediate powers. The initial rod configuration assumed for each power is the maximum transient insertion limit allowed by the Power Dependent Insertion Limit of the regulating banks (Chapter 16, Technical Specification) at that power.

The CEA withdrawal incident from low power is analyzed with the maximum calculated differential reactivity insertion rate resulting from a sequential

CEA bank withdrawal with 40% overlap. The CEA withdrawal incident from full power is analyzed from the insertion of the lead bank which corresponds to the PDIL insertion limit at full power. Reactivity insertion rates are calculated by a static axial model of the YGN 3&4 core. The calculated reactivity insertion resulting from a sequential CEA withdrawal is presented in Figures 4.3-53 and 4.3-54.

The CEA drop incident is analyzed by selecting the dropped CEA that maximizes the increase in the radial peaking factor. The radial peaking factors used include an allowance for 15 minutes of xenon redistribution. A conservatively small negative reactivity insertion is used in the accident analysis.

The typical reactivity insertion during a reactor scram is presented in Chapter 15. This reactivity insertion is computed using axial models at various scram CEA positions, and it is used for all accidents which are terminated by a scram, unless otherwise indicated. The reactivity insertion is conservative since only the minimum shutdown worth of 10.0% is assumed to be available at hot full power. The scram reactivity insertion for the loss of flow is implicit in the kinetic axial analysis.

4.3.2.6 Criticality of Reactor During Refueling

The soluble boron concentrations during refueling are shown in Table 4.3-1. These concentrations ensure that the k_{eff} of the core during refueling does not exceed 0.95.

4.3.2.7 Stability

4.3.2.7.1 General

Pressurized water reactors (PWRs) with negative overall power coefficients are inherently stable with respect to power oscillations. Therefore, this

discussion will be limited to xenon-induced power distribution oscillations. Xenon-induced oscillations occur as a result of rapid perturbations to the power distribution that cause the xenon and iodine distributions to be out of phase with the perturbed power distribution. This results in a shift in the iodine and xenon distribution that causes the power distribution to change in an opposite direction from the initial perturbation, and thus an oscillatory condition is established. The magnitude of the power distribution oscillation can either increase or decrease with time. Thus, the core can be considered to be either unstable or stable with respect to these oscillations. Discussed below are the methods of analyzing the stability of the core with respect to xenon oscillations. The tendency of certain types of oscillations to increase or to decrease is calculated, and the method of controlling unstable oscillations is presented.

4.3.2.7.2 Method of Analysis

Xenon oscillations may be analyzed by two methods. The first method consists of an explicit analysis of the spatial flux distribution accounting for the space-time solution of the xenon concentrations. Such a method is useful for testing various control strategies and evaluating transitional effects (such as power maneuvers). The second method consists of modal perturbation theory analysis, which is useful for the evaluation of the sensitivity of the stability to changes in the reactor design characteristics, and for the determination of the degree of stability for a particular oscillatory mode.

The stability of a reactor can be characterized by a stability index or a damping factor which is defined as the natural exponent that describes the growing or decaying amplitude of the oscillation. A xenon oscillation may be described by the following equation.

$$\phi(\bar{r},t) = \phi_o(\bar{r}) + \Delta\phi_o(\bar{r})\, e^{bt} \sin(\omega t + \delta) \qquad (4.3\text{-}4)$$

where:

$\phi(\bar{r},t)$ = the space-time solution of the neutron flux

$\phi_o(\bar{r})$ = the initial fundamental flux

$\Delta\phi_o(\bar{r})$ = the perturbed flux mode

b = the stability index

ω = the frequency of the oscillation

δ = a phase shift

Modal analysis consists of an explicit solution of the stability index b using known fundamental and perturbed flux distributions. A positive stability index b indicates an unstable core, and a negative value indicates stability for the oscillatory mode being investigated. The stability index is generally expressed in units of inverse hours, so that a value of -0.01/hr would mean that the amplitude of each subsequent oscillation cycle decreases by about 25% (for a period of about 30 hours for each cycle).

Xenon oscillation modes in PWRs can be classified into three general types: radial, azimuthal, and axial. To analyze the stability for each oscillation mode, only the first overtone needs to be considered since higher harmonic modes decay more rapidly than the first overtone.

4.3.2.7.3 Expected Stability Indices

4.3.2.7.3.1 Radial Stability

A radial xenon oscillation consists of a power shift inward and outward from

the center of the core to the periphery. This oscillatory mode is generally more stable than an azimuthal mode. This effect is illustrated in Figure 4.3-55, which shows that for a bare cylinder the radial mode is more stable than the azimuthal mode. Discussion of the stability for radial oscillatory mode is therefore deferred to the azimuthal mode.

4.3.2.7.3.2 Azimuthal Stability

An azimuthal oscillation consists of a X-Y power shift from one side of the reactor to the other. Simulation of this type of oscillation is performed for a range of expected reactor operating conditions.

The expected variation of the stability index during the first cycle is shown in Figure 4.3-56. These results are obtained from analyses that consider the spatial flux shape changes during the cycle, the changes in the moderator and Doppler coefficient during the cycle, and the change in xenon and iodine fission yield due to plutonium buildup during the cycle. As is shown on the figure, the expected stability index is no greater than -0.03/hr at any time during the cycle for the expected mode of reactor operation. 1

4.3.2.7.3.3 Axial Stability

An axial xenon oscillation consists of a power shift toward the top and bottom of the reactor core. This type of oscillation may be unstable during the first cycle. Table 4.3-9 shows the calculated variation of the axial stability index during the first cycle. It is anticipated that control action with part-strength rods and/or full-strength rods may be required to limit the magnitude of the oscillation. As discussed in Subsection 4.3.2.2, the axial power distribution is monitored by COLSS and the RPS. Based on the COLSS measurement of the axial power distribution, the operator may move either the full-strength or the part-strength CEAs to control any axial oscillations.

4.3.2.7.4 Control of Axial Instabilities

The control of axial oscillations during a power maneuver is illustrated in Figures 4.3-36 through 4.3-43. PSCEAs are used throughout these maneuvers to limit the change in the power distribution. The difference between an uncontrolled and a controlled xenon oscillation is illustrated in Figure 4.3-57. It was assumed in the calculation of the controlled oscillation that the PSCEAs were moved in such a way as to preserve the initial shape in the core prior to the initiating perturbation. The calculations are performed at the end of the first cycle which corresponds to the expected least stable condition for axial xenon oscillations.

4.3.2.7.5 Summary of Special Features Required by Xenon Instability

The RPS described in Subsection 7.2.2 is designed to prevent exceeding acceptable fuel design limits and to limit the consequences of postulated accidents. In addition, a means is provided to ensure that under all allowed operating modes, the state of the reactor is confined to conditions not more severe than the initial conditions assumed in the design and analysis of the protection system.

Since the reactor is predicted to be stable with respect to radial and azimuthal xenon oscillations, no special protection system features are needed to accommodate radial or azimuthal mode oscillations. Nevertheless, a maximum quadrant tilt is prescribed in the Technical Specifications along with prescribed operating restrictions in the event that the tilt is exceeded. The azimuthal power tilt is determined by COLSS and included in the COLSS determination of core margin. The azimuthal power tilt limit is accounted for in the reactor protection system (RPS).

4.3.2.7.5.1 Features Provided for Azimuthal Xenon Effects

a. Administrative limits on azimuthal power tilt.

b. Monitoring and indicating the azimuthal power tilt in COLSS as well as accounting for this tilt in the COLSS determination of core margin.

c. Accounting for azimuthal power tilt limit in the RPS.

4.3.2.7.5.2 Features Provided for Axial Xenon Effects and Power Distribution Effect and Control

a. PSCEAs or regulating CEAs for control of the axial power distribution, if required.

b. Monitoring and accounting for changes in the axial power distribution in COLSS.

c. Monitoring and accounting for the axial power distribution in the RPS.

4.3.2.8 Vessel Irradiation

The design of the reactor internals and of the water annulus between the active core and vessel wall is such that for reactor operation at the full power rating and an 80% capacity factor, the vessel fluence greater than 1 MeV at the vessel wall will not exceed 5.8×10^{19} n/cm^2 over the 40-year design life of the vessel. The calculated exposure includes a 30% uncertainty factor.

The maximum fast neutron fluxes greater than 1 MeV incident on the vessel ID are based on a time-averaged equilibrium cycle radial power distribution and an axial power distribution with a peak to average of 1.15. The models used in these calculations are discussed in Subsection 4.3.3.3.

4.3.3 Analytical Methods

4.3.3.1 Reactivity and Power Distribution

4.3.3.1.1 Method of Analysis

The nuclear design analysis of low enrichment PWR cores is based on the two-dimensional transport code DIT (References 1 and 2), which provides cross sections appropriately averaged over a few broad energy groups for the whole assembly or individual cells, and few group one-, two-, and three-dimensional diffusion theory calculations of integral and differential reactivity effects and power distributions. Errors between calculated and measured data for various nuclear parameters of interest in the nuclear design and safety analysis are presented in Subsection 4.3.3.1.2. As improvements in analytical procedures are developed and improved data become available, they are incorporated into the design procedures after validation by comparison with related experimental data.

4.3.3.1.1.1 Cross Section Generation

Few group cross sections for coarse mesh and fine mesh diffusion theory codes are prepared by the DIT lattice code. These cross sections are used in ROCS (coarse mesh) and in MC (fine mesh). The ROCS/DIT code system is documented in an NRC-approved Topical Report (Reference 2).

The essential components of the DIT lattice code are as follows:

a. Spectrum calculations using integral transport theory in up to 85 energy groups for typical portions of the assembly geometry (e.g., fuel cell, fuel cell and burnable absorber, and fuel cell and water hole).

b. Few group spatial calculations in exact assembly geometry followed by a leakage calculation to maintain a critical spectrum.

c. Isotopic depletion calculations for every cell in the assembly.

Thus, the use of the two dimensional integral transport theory code DIT ensures that the effects of lattice heterogeneities are explicitly treated. Few group cross sections for coarse mesh spatial calculations are obtained without laborious intermediate fine mesh calculations to perform accurate weighting of the various types of fuel, absorber, and water hole cells.

The assembly calculation, which is performed in several broad energy groups (ranging from 2 to 12), is preceded by a sequence of spectrum calculations performed in the basic cross section library energy group structure of up to 85 groups.

The geometries used in the spectrum calculations are replicas of portions of the true assembly geometry. Boundary conditions recycled from the assembly calculation are used for each spectrum geometry.

Group condensation based on the spectra calculated for all the different types of cells and subregions within them is performed to obtain few group macroscopic cross sections that are passed on directly to the assembly calculations. Since the accuracy of the spectrum calculations is high, the group condensation can normally be performed with a standard four-group structure.

In cases where conventional group condensation methods break down, more groups can be (and are) used in the assembly calculation (e.g., seven-group condensation is used for gadolinium bearing assembly).

The assembly calculation, as well as the spectrum calculations, is performed by integral transport theory with multigroup interface current used to couple adjacent cells.

This entire sequence of calculations is normally performed assuming that there is no net leakage from the assembly geometry. Following the assembly calculation, fine mesh spectra are constructed for all subregions in the assembly based on the spatial distribution of the few group assembly flux and on the energy and space distribution of the fine mesh flux from the spectrum calculations. A correction for the influence of global leakage is then made on the basis of a B1 calculation with the fine energy group structure for the homogenized assembly to maintain criticality of the assembly.

Few group microscopic cross sections for use in the depletion stage of DIT are formed using the basic cross section library and the spectra calculated as described.

Spatial averages of microscopic and macroscopic cross sections are performed for editing and are passed onto the ROCS and MC.

The above calculations are performed in one single job step without manual intervention. Few group coarse mesh cross sections are prepared in the HARMONY format (Reference 7) for ROCS by the editing code CESAW, and fine mesh cross sections are input to MC via the editing code MCXSEC.

The DIT code utilizes a data library containing multigroup cross sections, fission spectra, fission product yields and other supplemental data. The principal source of data for the library is ENDF/B-IV. Three adjustments to

the library data have been made to reflect changes to ENDF/B-IV recommended by the Cross Sections Evaluation Working Group for incorporation into ENDF/B-V:

a. A reduction of about 3% in the shielded resonance integral of U-238.

b. The adoption of the harder Watt fission spectra for U-235 and Pu-239, later incorporated in ENDF/B-V.

c. A moderate upward adjustment of U-235 and Pu-239 thermal $\bar{\nu}$ values of about 0.1%, improving the $\bar{\nu}$, η discrepancy but not going as far as ENDF/B-V.

In the epithermal region, the ENDF/B-IV files are processed with ETOG (Reference 3) to provide cross section resonance parameters and scattering matrices for the isotopes contained in the library. ETOG prepares these data in 99 energy groups spanning the range from 14.9 MeV to 0.414 eV. The GAM portion of GGC3 (Reference 4) is used to condense the 99 group data into 50 energy groups spanning the energy range from 14.8 MeV to 1.855 eV weighted with a spectrum representative of that in a PWR assembly.

In the resolved energy (9.1 keV to 1.855 eV), the capture and fission cross sections of resonant absorbers are replaced with resonance tables.

In the thermal region, the ENDF/B-IV files are processed with FLANGE II (Reference 5) to provide cross sections and full scattering matrices in the thermal region (1.855 eV to 0.00025 eV). The cross sections of isotopes containing resonances in the thermal region are Doppler broadened. For hydrogen, scattering matrices are prepared with FLANGE II using ENDF/B-IV thermal scattering low parameters for H_2O.

The cross sections and scattering matrices are tabulated on the library for a sufficient number of temperatures to span the range expected during power reactor operation and to permit linear interpolation. 1

reactor operation and to permit linear interpolation.

Cross sections for the resolved resonance region (9.1 keV to 1.855 eV) are prepared with CE RABBLE, an extension of the RABBLE (Reference 6) code using resolved resonance parameters from ENDF/B-IV. The cosine current approximation in RABBLE was replaced with an integral transport routine. Group-averaged resonance cross sections are generated with the modified RABBLE code, which performs a space-dependent calculation of the slowing down sources. The cross sections from the CE RABBLE calculations are corrected to include the proper group-dependent smooth calculations, which are derived from the ETOG/GGC3 calculations. RABBLE is also used to validate inteference effects among resonance absorbers as calculated by the DIT algorithm.

Following the assembly spectrum calculation, a depletion time step takes place for each individual rod in the assembly and when required for subdivisions of a rod. At the end of the depletion step, new isotopic compositions are defined for use in the spectrum calculation of the next time step. This process is extended over the expected life of the fuel assembly.

Several improvements have been made to the DIT calculational methodology originally described in Reference 2. These improvements, described in Reference 31 and approved in Reference 32, include the use of anisotropic scattering and higher-order currents.

4.3.3.1.1.2 Coarse-Mesh Methods

Static- and depletion dependent reactivities, nuclide concentrations, fluxes, and power distributions in two- and three-dimensional representations of the core are determined by a diffusion depletion program, ROCS-MC, which is described in Reference 2. ROCS was approved for use as a PWR core-design analysis code by the USNRC in Reference 2. The ROCS code is designed to perform two- or three-dimensional coarse-mesh reactor core calculations based

on the two-group nodal expansion method (NEM) with full-, half-, or quarter-core symmetric geometries. The mesh consists of rectangular parallel piped "nodes" arranged contiguously in the xy-plane, with one or more axial meshes (or planes) in the z-direction. In most applications, only the active core region is represented, with albedo-like boundary conditions assigned to exterior nodes. A typical ROCS core geometry uses four nodes per assembly in the xy-plane and 20 to 30 axial planes depending upon core height and incore instrument locations.

The nodal macroscopic group constants used in the neutronics calculation are constructed from detailed isotopic concentrations and microscopic cross sections processed by the code. The isotopes specified include fixed depletable isotopes and a lumped residual representing nondepletable isotopes. The depletable isotopes include fission chain isotopes, fission products, and burnable absorbers. Control rods are represented by macroscopic cross sections specific to different rod banks.

The ROCS system performs coarse mesh depletion calculations for each node in a two- or three-dimensional core configuration. The allowed depletion chains are internally modeled with fixed depletion equations so that beyond the input cross section data, the user need supply only such data as initial concentrations, decay constants, and fission yields for each depletion nuclide. These include the principal uranium and plutonium isotopes, a fuel exposure chain, xenon and samarium fission product chains, and boron and gadolinium burnable absorber chains.

The fixed depletion equations used in the ROCS code are derived through the standard procedure of analytically integrating the coupled linear rate equations that represent each chain.

The depletion equations are solved using the flux and microscopic cross section values based on the neutronics and thermal-hydraulic feedback

calculations preceding the depletion time step. The initial flux and cross sections are assumed constant over the depletion time step.

Cross section information used in the ROCS system is derived from macroscopic cross sections supplied by DIT for each nuclide in two energy groups. This information is utilized in two basic forms. First, two-group macroscopic cross sections are used in the basic flux and eigenvalue calculation. The microscopic contributions due to thermal-hydraulic feedbacks, xenon, soluble boron, and control rods are added before the flux calculation. Second, two-group microscopic cross sections are used explicitly in the depletion and xenon short-term time stepping calculations.

The two-group microscopic cross sections for each nuclide are supplied in table form. The following are represented for each nuclide and energy group:

σ_{tr} = transport cross section (b)

σ_a = absorption cross section (b)

σ_r = removal cross section (b)

σ_f = fission cross section (b)

ν = average number of neutrons released per fission

κ = average energy release per fission (watt-sec)

The tables represent the above values as nonlinear functions of important independent variables (e.g., exposure, initial enrichment, and soluble boron concentration) evaluated for nominal thermal-hydraulic conditions. In addition, multipliers (called G-factors) may be included in the table for any of the cross sections. The G-factors may also be represented as functions of

pertinent independent variables. Thus, a typical cross-section table interpolation can be represented symbolically by the following equation:

$$\sigma(\rho_o, T_{Mo}, T_{Fo}) = \sigma(N_1, N_2, N_3)G(N_4, N_5, N_6) \Big|_{\rho_o, T_{Mo}, T_{Fo}} \qquad (4.3\text{-}5)$$

where:

ρ_o = nominal moderator density

T_{Mo} = nominal moderator temperature

T_{Fo} = nominal fuel temperature

$N_1, \ldots, N_6$ = independent variables for table interpolation.

The cross sections are assumed to vary with moderator temperature, moderator density, and the square root of the fuel temperature for small changes about the nominal. The dependence of the cross sections on the thermal-hydraulic parameters is usually approximated by the inclusion of the first derivative of the cross section, for example;

$$\sigma(\rho, T_M, T_F) = \sigma(\rho_o, T_{Mo}, T_{Fo}) + \frac{\partial \sigma}{\partial \rho}\Delta\rho + \frac{\partial \sigma}{\partial T_M}\Delta T_M + \frac{\partial \sigma}{\partial (T_F)^{1/2}}\Delta (T_F)^{1/2} \qquad (4.3\text{-}6)$$

where:

$\Delta\rho = \rho - \rho_o$ = change in density from nominal value

$\Delta T_M = T_M - T_{Mo}$ = change in moderator temperature from nominal

$\Delta(T_F)^{1/2} = (T_F)^{1/2} - (T_{Fo})^{1/2}$ = change in square root of fuel temperature from nominal

The ROCS neutronics calculation is linked to optional independent feedback calculations for thermal-hydraulic parameters (moderator density, moderator temperature, fuel temperature (References 7 and 8)) and for equilibrium ^{135}I and ^{135}Xe distributions. The thermal-hydraulic calculation is performed iteratively with the flux calculation when any combination of thermal-hydraulic feedbacks is specified. For each feedback variable specified, the macroscopic cross sections used in the flux calculation are updated through the appropriate feedback term. In the case of xenon, the macroscopic cross sections are updated each iteration cycle using calculated ^{135}I and ^{135}Xe equilibrium concentrations based on the two-group flux distribution from the previous iteration. The number of feedback iterations is governed by independent convergence criteria for each feedback parameter, so that the final flux solution is obtained after all specified feedbacks have converged.

In addition to the above feedback models, the ROCS code contains optional eigenvalue search models for the following control variables: control rod bank insertion, soluble boron concentration, reactor power level, and inlet moderator temperature. The search calculations employ numerical iteration techniques that update the specified control variable to obtain convergence on the search eigenvalue, and are generally used along with feedback calculations. The power level and inlet temperature searches require use of thermal-hydraulic feedbacks. These latter search calculations are performed after alternate feedback iterations while the boron and rod search calculations are performed after each feedback iteration.

4.3.3.1.1.3 Fine-Mesh Methods

The MC code, described and approved in Reference 2, performs pin peaking calculations for each node in two- or three-dimensional core geometries. MC uses an embedded fine-mesh diffusion theory method for obtaining pin power distributions from coarse-mesh calculations.

Two improvements made to the ROCS methodology originally described in Reference 2 are the use of a predictor/corrector method for gadolinium-bearing fuel, which was described and approved in Reference 30, and the use of assembly discontinuity factors, which was described in Reference 31 and approved in Reference 32.

A method has been developed for determining diffusion coefficients which, when combined with the finite difference formulation of MC, permits the inclusion of transport effects in a rigorous fashion. The diffusion coefficients have the property of conserving cell averaged fluxes, reaction rates, and net leakage across cell boundaries. Thus, MC has the capability to effectively reproduce DIT local power distributions.

Having determined diffusion coefficients that exactly reproduce average fluxes, reaction rates, and net currents from transport theory for a particular geometry, it is then asserted that they are universally applicable independent of the size of the flux gradients seen in the core.

The nodal diffusion equations are solved as a boundary source problem for the embedded calculation. The partial in-currents on each nodal face and the global eigenvalue are supplied by the ROCS coarse mesh calculation.

After completion of the fine-mesh embedded calculation, the fine-mesh power distribution is renormalized to the coarse mesh power level to ensure that coarse mesh and fine mesh node average powers and burnups will remain the same during depletion.

The MC-embedded calculation uses a macroscopic cross section model based upon interpolation of multidimensional macroscopic tables. These tables are created by the MCXSEC code which process DIT results for all assembly types, and are typically burnup, enrichment, moderator, and fuel temperature dependent for each fine-mesh pin type. Lagrange linear interpolations are

performed to obtain the macroscopic cross sections. The interpolated absorption cross section is then corrected for soluble boron and xenon changes by using boron and xenon microscopic cross sections along with number densities obtained from the core soluble boron and local xenon equilibrium concentrations. In addition, axial leakage is represented by adding a DB^2 term to the absorption cross section.

4.3.3.1.1.4 Other Analysis Methods

As the size of large power reactors increases, space-time effects during reactor transients become more important. In order not to penalize reactor performance unduly with overconservative design methods, it is desirable to have the capability of performing detailed space-time neutronics calculations for both design and off-design transients.

The HERMITE (Reference 10) computer code has been developed to meet this objective. It solves the few-group, space-time-dependent neutron diffusion equation including feedback effects of fuel temperature, coolant temperature, coolant density, and control rod motion. The neutronics equations in one, two, and three dimensions are solved by the nodal expansion method. The fuel temperature model explicitly represents the pellet, gap, and clad regions of the fuel rod, and the governing heat conduction equations are solved by a finite difference method. Continuity and energy conservation equations are solved in order to determine the coolant temperature and density. In the one-dimensional mode, HERMITE also has the option of finding the axial-dependent poison distribution required to produce a particular user specified axial power shape. This option is often used to produce conservative axial power shapes corresponding to the LCO limits on axial power shape from which simulations of core transients are subsequently initiated.

For a one-dimensional analysis of the axial behavior of the core, the QUIX (Reference 25) code is used. Three-dimensional ROCS depletion calculations

are used to supply the necessary input to the QUIX code, which generates some of the data required by the monitoring and control systems. In addition to the eigenvalue problem, QUIX performs three types of search calculations to attain a specific eigenvalue; viz., a poison search, a CEA region boundary search, and a moderator-density-dependent poison search. The effects of moderator and fuel temperature feedback on the power distribution can be treated. The program can also perform power shaping searches to simulate the use of PSCEAs.

The QUIX code has the capability of simulating two-level excore detector responses expected during operation. The calculated normalized core average power distribution is first corrected by the application of CEA shadowing factors to simulate the peripheral fuel assembly power distribution. Shape annealing factors (defined below) are then applied to the peripheral axial power distribution to simulate the integrated response of the subchannels of the excore detectors. For reactors with three-element excore detectors, either auxiliary calculational procedures or another code must be used. Calculational evaluation of the responses of the three-element excore detectors to power shape variation can be made directly using the code VISIONS, which is a reactor core focused PWR power plant simulator. This code is a fast-running neutronics model for the three-dimensional representation of a core with 1 x 1 x 20 nodes per fuel assembly. This code accepts as input the shape-annealing functions for two- or three-element excore detector systems, and factors representing the relative contribution of each of the peripheral assemblies to the excore detector signals. The code combines the peripheral assemblies power distributions and weighting factors and the shape-annealing functions to calculate the excore detector responses for the calculated three-dimensional power shape.

CEA shadowing is the change in excore detector response resulting from changing the core configuration from an unrodded condition to a condition with CEAs inserted, while maintaining constant power operation. Although CEA

shadowing is a function of the relative azimuthal locations of the high power peripheral assemblies and the excore detectors, its effect is minimized by placing the excore detectors at azimuthal locations where minimum CEA shadowing occurs. CEA shadowing factors can be determined using detailed power distributions (ROCS-MC) representing the cumulative presence of the various CEA banks and the SHADRAC (Reference 11) code. SHADRAC calculates fast neutron and gamma ray spectra, heating, and dose rates in a three-dimensional system utilizing a moments method solution of the transport equation. The core, vessel internals, vessel, and excore detector location are treated explicitly in the calculation.

Normalized CEA shadowing factors are relatively constant with burnup and power level changes made without moving CEAs. CEA shadowing factors at the beginning and end of the first cycle life are as shown in Table 4.3-10.

Figure 4.3-58 shows the typical behavior of the CEA shadowing factor during a CEA insertion and withdrawal sequence. QUIX simulated factors and experimentally measured CEA shadowing factors during this transient situation are shown to have quite good agreement over a significant range of CEA insertions.

Shadowing factors account for the radial power distribution effects and shape annealing accounts for the axial power distribution effects on the excore detector responses. Due to neutron scattering in the various regions separating the core and the excore detectors, each detector subchannel responds to neutrons from the entire length of the core and not just from the section immediately opposite the subchannel. This effect is independent of the axial power shape and the azimuthal CEA shadowing factors. Typical axial annealing functions, given as fractional response per percent of core height for a three subchannel system, are shown in Figure 4.3-59.

Axial shape annealing is determined by utilizing a fixed source DOT calculation. DOT is a two-dimensional discrete ordinates transport code. The R-Z

geometry option is used for the annealing calculation with representation of the core, vessel, vessel internals, air gap, and biological shield. The fixed source is distributed over 15 uniform axial segments of the active core height. Figure 4.3-60 illustrates the radial regions represented in the DOT calculation as well as one of the axial fixed source segments.

By integrating the total pointwise response along the length of the subchannel, one can determine the subchannel response for each axial fixed source element. Utilizing this same technique for all 15 axial segments of the core and normalizing to the total excore detector response, annealing curves similar to those shown in Figure 4.3-59 are determined.

As the annealing is determined using a flat axial shape, the resulting annealing factors (S(z)) must be multiplied by the appropriate peripheral axial power shape, P(z), to obtain the total detector response.

$$D_{Lower} = \int_0^H P(z)\ S(z)_{lower}\ dz = \text{lower detector response} \qquad (4.3\text{-}7)$$

$$D_{Middle} = \int_0^H P(z)\ S(z)_{middle}\ dz = \text{middle detector response} \qquad (4.3\text{-}8)$$

$$D_{Upper} = \int_0^H P(z)\ S(z)_{upper}\ dz = \text{upper detector response} \qquad (4.3\text{-}9)$$

The shape-annealing factors are essentially geometric correction factors applied to the peripheral axial power distribution. As such, the effects of time in fuel cycle, transient xenon redistribution, and CEA insertion, although affecting the peripheral bundle power shape, do not affect the geometric shape annealing correction factors. Figure 4.3-61 compares the peripheral axial shape index with the external shape index, inferred from detector signals at the core boundary during a CEA and PSCEA motion test for the Palisades reactor. Shown are the results of QUIX simulations of the test

as well as experimental data taken during the test.

From this curve, it can be concluded that even though the axial power distribution in the core and on the core periphery was changing during this transient, the relationship between the excore response and the peripheral response was not. These results justify not only the separability of CEA shadowing and shape annealing as summed in QUIX, but also demonstrate that shape annealing is essentially a geometric effect, independent of the peripheral axial power distribution.

The excore detector temperature decalibration effect is the relative change in detector response as a function of reactor water inlet temperature at constant power. The temperature decalibration effect is calculated utilizing ANISN with explicit representation of core, vessel internals, vessel, and detector location for various reactor inlet temperatures, and their associated power distributions. The typical detector temperature of decalibration effect, as a function of inlet temperature normalized to an inlet temperature of 565°F (296.1°C), is as shown in Figure 4.3-62.

Final normalization of the CEA shadowing, shape annealing, and temperature decalibration constants will be accomplished during startup testing.

4.3.3.1.2 Comparisons with Experiments

The nuclear analytical design methods in use for YGN 3&4 have been checked against a variety of critical experiments and operating power reactors. In the first type of analysis, reactivity and power distribution calculations are performed, which lead to information concerning the validity of the basic fuel cell calculation. The second type of analysis consists of a core-follow program in which power distributions, reactivity coefficients, reactivity depletion rate, and CEA worths are routinely analyzed to provide an ongoing global verification of the nuclear design package.

The comparison of calculations to measurements not only serves to verify the calculational methodology, but also provides a set of calculational biases and uncertainties which are applied to the calculational results to yield best-estimate and 95/95 confidence limit predictions for use in the safety analysis. Verification of the basic methodology was demonstrated and approved in Reference 2. Biases and uncertainties were also documented and approved in Reference 2. Implementation of the improvements described in References 30 and 31 necessitated an update of the biases and uncertainties in order to assure that 95/95 confidence limits are maintained in all results used for licensing-related analyses. These updated biases appear in summary form in Reference 33. Reference 31, which was approved by the USNRC in Reference 32, reported that the revised bias and uncertainty values were equivalent to those contained in Reference 2 and therefore did not require explicit NRC review.

4.3.3.1.2.1 Critical Experiments

Selected critical experiments have been analyzed with the DIT code. Selections of criticals are based on the following criteria:

a. Applicability to CE PWR fuel and assembly designs
b. Self consistency of measured parameters
c. Availability of adequate data to model the experiments

Two groups of critical experiments using rod arrays representative of the 14 x 14 assembly have been employed in this evaluation. The first is a series of clean experiments with UO_2 fuel carried out in 1967 (Reference 12), and the second is a set of experiments carried out in 1969 (Reference 13). Tables 4.3-11 and 4.3-12 give the principal parameters for each of the experimental configurations. The moderator-to-fuel volume ratios were varied by changing the cell pitch of the fuel rod arrangement. The moderator and reflector material for the entire core was H_2O.

Measurements included the criticality parameters and the fission rate distributions in selected fuel rods. This section addresses the comparisons between measured and calculated criticality, as well as between measured and calculated fissions rate distributions done to establish calculative biases and uncertainties in predicting intra-assembly power peaking for both 14 x 14 and 16 x 16 assemblies.

Description of the Experiments

A. Combustion Engineering-Sponsored UO_2 Critical Experiments.

A series of critical experiments were performed for CE by Westinghouse Corporation at the Westinghouse Reactor Evaluation Center (WREC) employing the CRX reactor. The experimental program consisted of approximately 70 critical configurations of fuel rods. The basic core configuration was a 30 x 30 square, fuel rod array of Zr-4 clad UO_2 fuel having an enrichment of 2.72 wt.% U-235. Fuel rods were removed to create internal water holes or channels to accommodate control rods or to simulate control rod channels and water gaps representative of the CE 14 x 14 fuel assembly design.

The majority of the experiments employed a lattice pitch of 0.600 inch (1.524 cm) with several experiments repeated with a lattice pitch of 0.575 inch (1.46 cm). These values of 0.600 inch (1.524 cm) and 0.575 inch (1.46 cm), together with the fuel pellet dimensions and enrichment and the rod diameter, resulted in hydrogen-to-fuel ratios representative of the 14 x 14 design at room temperature and at operating temperature, respectively.

B. KRITZ Experiments

A program of critical experiments, sponsored jointly by CE and KWU, was performed at the KRITZ CRITICAL FACILITY of AB Atomenergi, Studsvik, Sweden. The program consisted of analyzing a number of core configurations of interest to CE and KWU. The CE configurations were representative of the 14 x 14 fuel assembly, including the five large control rod channels. A basic cell pitch of 0.5650 inch (1.435 cm) was used for all lattices. The cores were relatively large, both in cross sectional area and height. Each core contained about 1450 rods, 265 cm in length. The core was reflected with water on the four sides and the bottom. Soluble boron was employed for gross reactivity control.

Results of Analyses

The results of the analyses of the six critical experiments are summarized in Table 4.3-13. The average k_{eff} is 1.0016.

As part of the CE Criticals and the KRITZ CRITICALS experimental programs, pin-by-pin power distributions were also measured to provide a data base with which to define biases and uncertainties in predicted water hole peaking factors. This analysis is described in detail in Reference 14. The bias and K(95/95) x σ in assembly peaking factor are +0.42% and +1.42%, (Reference 33) respectively. 1

4.3.3.1.2.2 Power Reactors

The accuracy of the calculational system in its entirety is assessed through the analysis of experimental data collected on operating power reactors. The data under investigation consist of critical conditions, reactivity coefficients, and rod worths measured during the startup period, and of

critical conditions, power distributions, and reactivity coefficients measured throughout the various cycles.

4.3.3.1.2.2.1 Startup Data

Measured data obtained during reactor startup are the most reliable, because they consist of well-controlled conditions.

Analysis of errors in the calculated reactivity as a function of power (fraction of full power) showed that the gradient of reactivity bias against the power is -0.145 (Reference 33). This value has been incorporated into the total reactivity bias for DIT/ROCS, described in the depletion data of the next section 1

Isothermal Temperature Coefficient

The isothermal temperature coefficient (ITC) is the change in core reactivity resulting from a 1°F change in moderator and fuel temperatures.

The error in the calculated ITC has been determined by comparing the isothermal temperature coefficients measured for a number of reactors and cycles, both at power and at zero power and for a wide range of soluble boron concentrations, against three-dimensional ROCS calculations performed at the same conditions.

The error in the calcuated ITCs was found to consist of a ppm dependent bias curve and the associated ppm-dependent tolerance band at the 95/95 confidence level about that curve (Figure 4.3-63).

The best estimated ITC and 95/95-tolerance limit are computed as follows:

$$ITC_{be} = ITC_{calc} - B_{itc}$$
$$= ITC_{calc} - 0.0718 - 0.738 \times 10^{-4} \times PPM \times 10^{-4} \ \Delta\rho/°F \quad (4.3\text{-}10)$$ 1

where:

ITC_{be} = the best estimated ITC
ITC_{calc} = the calculated ITC
B_{itc} = the ITC bias

$$ITC\ (\pm\ 95/95) = ITC_{calc} + (B_{itc} \pm K(95/95) \times \sigma \times z) \times 10^{-4} \Delta\rho/°F \quad (4.3\text{-}11)$$ 1

where:

$K(95/95) = 2.023$
$\sigma = 0.0736 \times 10^{-4}$
$z = (1.0255 + \beta^2)^{1/2}$
$\beta = (PPM - 1215)/2293$

Control Element Assembly Bank Worths

The errors in calculated CEA bank worths were found to be +4.32 ± 6.28% for total and net worth and +4.92 ± 15.5% for individual bank worths (Reference 33). The difference in uncertainties between group and total worths is because most of the individual bank worths were very small and hence the effects of measurement uncertainty result in greater relative errors. 1

Dropped, Ejected, and Net CEA Worths

The dropped worth bias and uncertainty are chosen as those of the bank worth. Dropped and bank worths are comparable because they have similar and small biases and uncertainties in absolute units. The large relative uncertainties are misleading because they apply to very small worths. 1

The ejected worth bias and uncertainty are expressed in relative units for

very small worths and absolute units for larger worths:

	Bias	Kσ
Worth < 0.24 %Δρ	4.0 % rel	31 % rel
Worth ≥ 0.24 %Δρ	0.006 %Δρ	0.077 %Δρ

The net worth bias and uncertainty are chosen as those of the total worth, since the total worth is representative of the rod density at the N-1 condition. The assumption is conservative because the N-1 configuration is strongly affected by the reactivity of the unrodded zone. Thus, the N-1 configuration is less sensitive to the precision of the calculated control rod cross section than the fully rodded configuration of the total worth. 1

Power Coefficient

The error in ROCS/DIT power coefficients is characterized by a bias of -0.040×10^{-4} $\Delta\rho/\%$ power and an uncertainty of $\pm 0.171 \times 10^{-4}$ $\Delta\rho/\%$ power with a 95/95 probability/confidence level. 1

4.3.3.1.2.2.2 Depletion Data

The two quantities monitored on a continuing basis during nominal full-power operation are the reactivity depletion rate and the power distributions. The constant monitoring of these quantities establishes the validity of the nuclear design.

The reactivity depletion rate is monitored by comparing measured critical steady-state conditions with corresponding calculated conditions. These conditions are characterized by exposure, power level, boron concentration, inlet temperature, and control rod insertion.

The reactivity bias and uncertainty at BOC and EOC estimated from the comparisons of measurement and calculations (Reference 33) are as follows: 1

B(F,BOC)	=	$+0.515 - 0.145 \times P - X$	± 0.24 (%$\Delta\rho$)	(4.3-12)
B(L,BOC)	=	$+0.657 - 0.145 \times P - 0.258 \times \varepsilon - X$	± 0.23 (%$\Delta\rho$)	(4.3-13)
B(EOC)	=	$-0.083 - 0.086 \times \varepsilon - X$	± 0.37 (%$\Delta\rho$)	(4.3-14)

where:

P = the fraction of full power

ε = is the reactor enrichment (% U-235 as if all fuels are fresh)

X = is the differential grid worth which depends on the reactor (Since System 80 and YGN 3&4 have the same grid structures and number of grids in the effective core, it is appropriate to use 0.04%$\Delta\rho$ (Reference 33) for both types of plants.)

The power dependence of the reactivity bias is measured by the power ascension test performed during startup test described in Subsection 4.3.3.1.2.2.1. The adjustment for grid worth is required, since the DIT/ROCS system does not accout for the grid effect on the calculated reactivity.

4.3.3.1.2.2.3 Assembly Power Distributions

The uncertainty to be attributed to calculated fuel assembly power distributions is obtained by comparing detailed three-dimensional calculations of the assembly powers with those inferred from incore measurements with the CECOR (Reference 16) system using fixed incore rhodium detectors. The resulting differences are a reflection of both measurement and calculative errors. In order to determine the uncertainty to be attributed to the calculation, the measurement uncertainty has been subtracted out from these difference distributions as described below. The measurement uncertainty is taken from an evaluation of the uncertainty associated with the CECOR system (Reference 15). 1

Table 4.3-14 summarizes the calculational uncertainties.

4.3.3.2 Spatial Stability

4.3.3.2.1 Methods of Analysis

An analysis of xenon-induced spatial oscillations may be done by two classes of methods: time-dependent spatial calculations and linear modal analysis. The first method is based on computer simulation of the space, energy, and the time dependence of neutron flux and power density distributions. The second method calculates the damping factor based on steady-state calculations of flux, importance (adjoint flux), xenon and iodine concentrations, and other relevant variables.

The time-dependent calculations are indispensable for studies of the effects of CEA, core margin, out-of-core and incore detector responses, and are performed in one, two, and three dimensions with few-group diffusion theory, using tested computer codes and realistic modeling of the reactor core.

The linear modal analysis methods are used to calculate the effect on the damping factors of changes in fuel zoning, enrichment, CEA patterns, operating temperature, and power levels. These methods, using information at a single point in time, are particularly suited to survey-type calculations. Methods are based on the work of Randall and St. John (Reference 17) as extended by Stacy (Reference 18). These methods are verified by comparison with time-dependent calculations.

4.3.3.2.2 Radial Xenon Oscillations

To confirm that the radial oscillation mode is extremely stable, a space-time calculation was run for a reflected, zoned core representative of YGN 3&4 without including the damping effects of the negative power coefficient. The initial perturbation was a poison worth of 0.4% in reactivity placed in the central 20% of the core for 1 hour. Following removal of the perturbation, the resulting oscillation was followed in 4-hour steps for a period of 80 hours. The resulting oscillation died out very rapidly with a damping factor of about -0.06 per hour. When this damping factor is corrected for a finite time step size by the formula in Reference 19, a more negative damping factor is obtained indicating an even more strongly convergent oscillation. On this basis, it is concluded that a radial oscillation instability will not occur.

4.3.3.2.3 Azimuthal Xenon Oscillations

The azimuthal xenon stability was analyzed by using the ROCS code to perform explicit simulation of the core behavior following as azimuthal perturbation.

temperature distribution and included the effects of power and moderator feedback term. The effect of finite time step length used in the ROCS simulation has been corrected as described in Reference 19.

4.3.3.2.4 Axial Xenon Oscillations

To check and confirm the predictions of the linear modal analysis approach, numerical space-time calculations were performed for both beginning and end-of-cycle. The fuel and poison burnup distributions were obtained by depletion with soluble boron control, so that the power distribution was strongly flattened. Spatial Doppler feedback was included in these calculations. In Figure 4.3-64, the time variation of the power distribution along the core axis is shown near end-of-cycle with reduced Doppler feedback.

The initial perturbation used to excite the oscillations was a 50% insertion into the top of the core of a 1.5% reactivity CEA bank of 1 hour. The damping factor for this case was calculated to be about + 0.02 per hour; however, when corrected for finite time step intervals by the methods of Reference 19, the damping factor is increased to approximately +0.04 per hour. When this damping factor is plotted on Figure 4.3-65 at the appropriate eigenvalue separation for this mode at end-of-cycle, it is apparent that good agreement is obtained with the modified Randall-St. John distribution of the moderator coefficient about the core midplane, and its consequent flux and adjoint weighted integrals of approximately zero.

Axial xenon oscillation experiments performed at Omaha at a core exposure of 7,000 MWd/MTU and at Stade at beginning-of-cycle and at 12,000 MWd/MTU (Reference 20) were analyzed with a space-time one-dimensional axial mode. The results are given in Table 4.3-15 and show no systematic error between the experimental and analytical results.

4.3.3.3 Reactor Vessel Fluence Calculation Model

The reactor vessel fluence calculated in Subsection 4.3.2.8 is obtained from two-dimensional transport theory calculations using the DOT-4.3 discrete ordinates code (Reference 26). The DOT-4.3 model uses an R-Θ coordinate system and octant symmetry to represent the geometry of the reactor core, surrounding water, reactor internals, and reactor vessel. A two-dimensional pin power distribution is used for the source term.

The DLC-23F/CASK library (Reference 27) is used for the cross section data. The material macroscopic cross sections are generated using the GIP4.3 code (Reference 28).

The calculated reactor vessel fluence includes a +30% uncertainty factor.

4.3.4 PLUS7 Equilibrium Core Description

4.3.4.1 Design Changes for PLUS7 Loaded Core

This subsection describes the design limits on the power distribution and the average effective fuel temperature dependence on the core average linear heat rate for equilibrium cycles loaded with PLUS7 fuel assembly.

4.3.4.1.1 Nuclear Design Limits on the Power Distribution

The design limits on power distribution for YGN 3&4 with PLUS7 are as follows:

a. The limiting three-dimensional heat flux peaking factor, F_q^n, was established for full power conditions at 2.65. This is based directly upon the LOCA limit of 469.2 W/cm (14.3 kW/ft) and the full power core average linear heat rate of 176.8 W/cm (5.39 kW/ft). Of course, a higher F_q^n is allowed for reduced core power levels. 645

Implementation in the Technical Specification is via a power operating limit based on peak linear heat generation rate.

b. The thermal margin to a minimum DNBR of 1.21 (using the KCE-1 CHF correlation as discussed in Subsections 4.4.2.2 and 4.4.4.1) is available to accommodate anticipated operational occurrences.

4.3.4.1.2 Fuel Temperature Dependence on the Core Average Linear Heat Rate

The average effective fuel temperature dependence on the core average linear heat rate described in Subsection 4.3.2.3.7 is expressed as the following semiempirical formula for PLUS7 fuel:

$$T_f(p) = T_{MOD}(p) + \left(\sum_{i=0}^{3} B_i \times M^i\right) \times p + \left(\sum_{j=0}^{3} C_j \times M^j\right) \times p^2 + \left(\sum_{k=0}^{3} D_k \times M^k\right) \times p^3 \qquad (4.3\text{-}15)$$

T_{MOD} is the average moderator temperature (°F), M is the exposure in MWd/MTU, p is the linear heat generation rate in the fuel in kW/ft, and T_f is the average effective fuel temperature (°F). The coefficients B_i, C_j, and D_k are determined from least squares fitting of the fuel temperature generated by FATES (Reference 35). For a PLUS7 fuel rod, the following values apply:

$B_0 = 128.0$	$C_0 = -0.5793$	$D_0 = -0.8422 \times 10^{-1}$
$B_1 = 0.1767 \times 10^{-2}$	$C_1 = -0.9705 \times 10^{-3}$	$D_1 = 0.1597 \times 10^{-4}$
$B_2 = -0.2376 \times 10^{-6}$	$C_2 = 0.5008 \times 10^{-7}$	$D_2 = 0.2712 \times 10^{-8}$
$B_3 = 0.2348 \times 10^{-11}$	$C_3 = -0.6352 \times 10^{-12}$	$D_3 = -0.1278 \times 10^{-12}$

The second factor of the first term in Equation 4.3-2 represented in Subsection 4.3.2.3.7 is obtained as follows for PLUS7 fuel assembly:

$$\frac{\partial T_f(p)}{\partial p} = \frac{\partial T_{MOD}(p)}{\partial p} + \left(\sum_{i=0}^{3} B_i \times M^i\right) + 2\left(\sum_{j=0}^{3} C_j \times M^j\right) \times p + 3\left(\sum_{k=0}^{3} D_k \times M^k\right) \times p^2 \qquad (4.3\text{-}16)$$

4.3.4.2 Nuclear Design Description

This subsection summarizes the nuclear characteristics of the equilibrium cycle loaded with PLUS7 fuel. Nuclear design parameters of PLUS7 equilibrium cycle are compared with those of Guardian equilibrium cycle in Table 4.3-16. Table 4.3-16 shows the moderator temperature coefficient, Doppler coefficient, kinetic parameters, inverse boron worth, and shutdown margin calculated for typical PLUS7 and Guardian equilibrium cycle with those used in the safety analysis described in Chapter 6 and 15. For each parameter, suitably conservative values are used in safety analysis, considering the calculated parameters for both PLUS7 and Guardian equilibrium cycle. Table 4.3-16 also shows the moderator temperature coefficient and shutdown margins are maintained within the limits specified in Chapter 16.

4.3.5 PARAGON/ANC Code System

With the application of the PARAGON/ANC code system instead of the DIT/ROCS code system, the analytical methods for the DIT/ROCS code system in subsection 4.3.3 are substituted to those of the PARAGON/ANC code system in this section. The information described on this section is effective for the cycles to which the PARAGON/ANC code system is applied.

519

4.3.5.1 Analytical Methods for Reactivity and Power Distribution

The nuclear design analysis of low enrichment PWR cores is based on the transport code, which provides cross sections appropriately averaged over a few broad energy groups for the whole assembly or individual cells, and diffusion theory calculations of integral and differential reactivity effects and power distributions.

4.3.5.1.1 Cross Section Generation

Few group cross sections for coarse mesh and fine mesh diffusion theory codes are prepared by the PARAGON code. These cross sections are used in ANC which is a diffusion code. The description of PARAGON is documented in an MEST-approved Topical Report (Reference 36).

PARAGON is developed by Westinghouse to replace the PHOENIX-P (Reference 37) code which has been used for the nuclear design of Westinghouse type plants. The methodology and verification of PARAGON have already been licensed by NRC. The details for the PARAGON code is described in Reference 38. Therefore, this subsection only provides the main features of the PARAGON code.

PARAGON is a two-dimensional multi-group neutron (and gamma) transport code, and it uses the Collision Probability Theory within the interface current method to solve the integral transport equation. Throughout the whole calculation, PARAGON uses the exact heterogeneous geometry of the assembly and the same energy groups as in the cross-section library to compute the multi-group fluxes for each micro-region location of the assembly. PARAGON cross section library uses ENDF/B-VI as the basic evaluated nuclear data files. Currently the library has 70 neutron energy groups and 48 gamma energy groups. This library has been generated using the NJOY processing code. PARAGON provides the same functions as PHOENIX-P. These include macroscopic cross sections, microscopic cross sections for feedback adjustments to the macroscopic cross sections, pin factors for pin power reconstruction calculations, and discontinuity factors for a nodal method solution. The energy group of PARAGON cross section is the same as the energy group of PHOENIX-P. 519

Using the resonance self shielding tables which are tabulated as function of both temperature and background scattering cross section, PARAGON computes the isotopic self shielded cross section. And then, PARAGON goes through three steps of calculations: flux solution for heterogeneous cell lattices,

homogenization of assembly and burnup calculation. The followings describe PARAGON's basic modules performing these 4 step calculations.

a. Cross-section Resonance Self Shielding Module

PARAGON uses the same resonance self-shielding theory as in PHOENIX-P. The non-regularity of the lattice is taken into account using space dependent Dancoff factor corrections. PARAGON uses the Collision Probability Theory to solve the slowing-down equation in pin cells with the real heterogeneous geometry.

b. Flux Calculation Module

The neutron (or gamma) flux, obtained from the solution of the transport equation is a function of three variables: energy, space and angle. For the energy variable, PARAGON uses the multi-group method where the flux is integrated over the energy groups. For the spatial variable, the assembly is subdivided into a number of sub-domains or cells and the integral transport equation is solved in the cells using the collision probability method. At each cell interface, the solid angle of neutron (or gamma) is discretized into a set of cones where the surface fluxes are assumed to be constant over each angular cone. 519

c. Homogenization Module

The next step in PARAGON calculation after the flux solution is the leakage correction. The purpose of this module is to compute the multi-group diffusion coefficients and the multi-group critical flux spectrum for the entire homogenized assembly. The flux solution to the transport equation is assumed to be separable in a space part and an energy and angle part. This assumption leads to the B1 system of equations to be solved.

d. Depletion Module

PARAGON uses the predictor-corrector technique to better account for the flux level variation during the burnup depletion.

Fuel average temperature and Doppler coefficient required to the calculation of neutron cross section and core calculations are generated by the FIGHT-H code (Reference 39). After temperature distribution is calculated with dividing fuel pellet into ten equal volume rings radially and by applying radial weighting factors the FIGHT-H code calculates the average and effective temperature for U^{238} and Pu^{240}. The temperature distribution for ten rings is calculated by Fourier conduction equation.

Based on the temperature distribution for ten equal volume rings, pellet average temperature is calculated and fuel effective temperatures are determined so as to preserve resonance capture rates for U^{238} and Pu^{240} in the Doppler Broadening range. These fuel temperatures are approximated to a polynomial equation as a function of power at each burnup step and then used to the various 3D ANC calculations.

4.3.5.1.2 Coarse-Mesh and Fine-Mesh Methods 519

Static- and depletion dependent reactivities, nuclide concentrations, fluxes, and power distributions are determined by a three-dimensional core simulator, ANC. ANC was approved for use as a PWR core-design analysis code by the USNRC in Reference 40. The details for the ANC code is described in Reference 40. This subsection only provides the main features of the ANC code.

ANC uses the Nodal Expansion Method (NEM) to solve the coupled 2D diffusion equations and three types of boundary conditions are allowed in ANC. Cyclic and rotational boundary conditions may be applied to quarter core problems, and reflective boundary conditions may be applied to quarter core and eighth core problems. The albedo boundary condition is applied at the outer surface of the problem. If no reflector nodes are explicitly specified, the albedos are applied to the outer surfaces of the fuel. Otherwise, the albedos are applied at the outer surfaces of the reflector nodes.

A typical ANC core geometry uses four nodes per assembly in the XY-plane and

20 to 26 axial planes depending upon core height and incore instrument locations. ANC code performs modeling up to 52 axial planes. Also, ANC code can calculate in a different axial mesh structure for 1/8 reflective symmetric core, 1/4 rotational symmetric core, 1/4 reflective symmetric core, and each core structure can be unfold to 1/4 or full core.

In nodal methods, group constants are traditionally obtained by simple volume and flux weighting. However, because node average flux using these volume-flux weighted group constants can not consider the effects of heterogeneity, the calculations for node average reaction rate, eigenvalue, etc., differ from the cases of heterogeneity. This problem is solved by adopting discontinuity factors. Discontinuity factors are used to modify the homogeneous cross-sections to preserve the node surface fluxes and currents that would be obtained from an equivalent heterogeneous model.

519

The cross section table in ANC contains macroscopic cross sections evaluated at a reference water density and a reference effective fuel temperature. These cross sections must be corrected for differences between the actual water density and fuel temperature in the model and the reference values, and microscopic cross sections are used at this time. Similarly, the microscopic cross sections in the core design calculation are used for boron, xenon, samarium, and actinides. Control rods are represented by macroscopic cross sections specific to different rod banks.

ANC contains options for fuel, burnable absorber, xenon, samarium, and other fission product depletion. The allowed depletion chains are internally modeled with fixed depletion equations so that beyond the input cross section data, the user needs to supply only such data as initial concentrations, decay constants, and fission yields for each depletion nuclide. ANC solves the two group diffusion equation and the resultant two group average nodal fluxes are available for power and depletion calculation. ANC also has the option to track the effects of B^{10} depletion throughout a cycle depletion.

After obtaining nodal solutions for a core by the Nodal Expansion Method, the rodwise pin power distribution within a node is calculated using pin factor data from PARAGON and average node power and flux distribution in a homogenized node from ANC. In a homogenized node, the flux distribution is approximated by a plane wave expansion and fitted to the four surface flux average values and the four corner flux values.

ANC code calculates not only rodwise neutron flux and fluence but also enthalpy rise and moderator density in an axial flow cell. In this calculation, it is considered that the core pressure is constant and there is no cross flow between assemblies. Also, ANC code has functions that modeling void for subcooled boiling in transient states.

4.3.5.1.3 Other Analysis Methods

For a one-dimensional analysis of the axial behavior of the core and axial power distribution calculation, the APOLLO code (Reference 41) is used. APOLLO is a two-group, one dimensional neutron diffusion code. The code can handle a maximum of 250-mesh intervals. Space-dependent feedback effects due to xenon, samarium, boron, fuel temperature, water density and rod position are accounted for. The buckling search methodology was developed to force agreement of the 1D model with the 3D ANC from which it was derived. The buckling term accounts for radial leakage effects, as well as fitting errors and other approximations in the 1D collapsed cross sections generated by ANC. 519

4.3.5.2 Comparisons with Experiments

The nuclear analytical design methods in use for the PARAGON/ANC code system have been checked against a variety of critical experiments and operating power reactors. For critical experiments, the reactivity and power distribution calculations have been performed by PARAGON code, which lead to information concerning the validity of the basic fuel cell calculation. Also the PARAGON/ANC code system have been verified by analyzing reactivity

coefficient, control rod worth, critical boron concentration and power distribution in operating power reactors.

4.3.5.2.1 Critical Experiments

Accuracy verification of nuclear fuel cell calculation in the PARAGON code was performed by comparing and analyzing various measures which were used in Strawbridge-Barry 101 criticals, KRITZ high temperature criticals and B&W physics verification program. These methods of verification are same with the existing method of verification and authorization in PHOENIX-P code (Reference 37) and detailed calculation results are described in References 36 and 38. As described in the references, compared to the analysis results of criticality experiments, the accuracy of PARAGON has been shown to be applicable to the nuclear design for PWR core.

4.3.5.2.2 Operating Reactor Measurement Data

519

In order to perform an overall verification of the PARAGON/ANC code system, Low Power Physics Test results of domestic plants for critical boron concentration, isothermal temperature coefficient, boron worth and control rod worth were compared and analyzed. Expected and measured critical boron concentration and radial/axial power distributions during power operation were also compared and analyzed as a core depletes. Also the main parameter for nuclear design relating to the experiment of control rod drop and ejection that were performed at which core was transient were verified and finally analysis for bias and uncertainty of the PARAGON/ANC code system was performed by comparing and analyzing expected value of the PARAGON/ANC code system with measured value. Verification results of the PARAGON/ANC method are described in References 36 and 38, and bias and uncertainty of the PARAGON/ANC code system are described in Reference 42. As stated in Reference 42, uncertainties of the PARAGON/ANC code system are within those of from the DIT/ROCS code system. Although uncertainty of the PARAGON/ANC code system is evaluated to be smaller than those of the DIT/ROCS code system, the same uncertainties for the

main parameters are applied to nuclear design for the consistency with the previous design methodology and procedure. In case of minor changes in the calculation method or being necessary to maintain the accuracy of codes considering a variety of measurement data, biases or uncertainties can be revised. However, if the revised values are comparable, then licensing process is unnecessary. 519

4.3.6 References

519

1. A. Jonsson, R. R. Rec, and U. N. Singh, "Verification of a Fuel Assembly Spectrum Code Based on Integral Transport Theory," Trans. Am. Nucl. Soc., 28, 778, 1978.

2. "The ROCS and DIT Computer Codes for Nuclear Design," CENPD-266-P-A, CE Proprietary Topical Report, April 1983.

3. D. E. Kusner et al., "ETOG-1, A FORTRAN IV Program to Process Data from the ENDF/B File to the MUFT, GAM and ANISN Formats," WCAP-3845-1, (ENDF-114), 1969.

4. J. Adin and K. D. Lathrop, "Theory of Methods Used in the GGC-3 Multigroup Cross Section Code," GA-715G, July 19, 1967.

5. H. C. Honeck and D. R. Finch, "FLANGE-II, A Code to Process Thermal Neutron Data from an ENDF/B Tape," DP-1278, ENDF-152, 1971.

6. P. Kier and A. Robba, "RABBLE, A Program for Computation of Resonance Absorption in Multiregion Reactor Cells," ANO-7326, 1967.

7. B. J. Breen et al., "HARMONY-System for Nuclear Reactor Depletion Computation," WAPD-TM-478, January 1965.

8. P. H. Gavin and P. C. Rohr, "Development and Verification of a Fuel Temperature Correlation for Power Feedback and Reactivity Coefficient Application," Trans. Am. Nucl. Soc., 30, 765, 1978

9. "C-E Fuel Evaluation Model Topical Report," Combustion Engineering, Inc., CENPD-139 (Proprietary), CENPD Rev.01 (Nonproprietary), CENPD-139 Supplement 1 (Proprietary), CENPD-139 Supplement 1 Rev.01 (Nonproprietary), July 1974.

10. P. E. Rohan, S. G. Wagner, and S. E. Ritterbusch, "HERMITE, A Multi-Dimensional Space-Time Kinetics Code for PWR Transients," Combustion Engineering Topical Report CENPD-188-A, March 1976.

11. SHADRAC, "Shield Heating and Dose Rate Attenuation Calculation," G30-1365, March 25, 1966.

12. E. G. Taylor et al., "Combustion Engineering, Inc., Critical Experiments," WCAP-7102, October 16, 1967.

13. "Plutonium Experiments for KWU," A. B. Atomenergie, Studsvik, Sweden, October 1969.

14. P. H. Gavin and H. G. Joo, "Evaluation of Assembly Peaking Factors by DIT with P1 Scattering and DP2 Cell Coupling, PHA-88-109, November 2, 1988.

15. "INCA/CECOR Power Peaking Uncertainty," CENPD-153-P, Rev. 1-P-A, May 1980. 1

16. "A Method of Analyzing In-Core Detector Data in Power Reactor," CENPD-145, C-E Topical Report, April 1975.

17. D. Randall and St. D. S. John, "Xenon Spatial Oscillations," Nucleonics, 16, 3, pp. 82-86, 1958.

18. W. M. Stacey, Jr., "Linear Analysis of Xenon Spatial Oscillations," Nuclear Science Engineering 30, pp. 453-455, 1967.

19. C. G. Poncelet, "The Effect of a Finite Time Step Length on Calculated Spatial Xenon Stability Characteristics in Large PWR's," Trans. ANS. 10, 2, p 571, 1967.

20. A. Gruen, "Messung Physikalischer Kerngroessen an Leistungsreakoren," Atom Kernenergie, 25, 2, 1975.

21. W. W. Engle, Jr., "A User's Manual for ANISN, A One-Dimensional Discrete Ordinates Transport Code with Anisotropic Scattering," K-1693, March 30, 1967.

22. "COLSS, Assessment of the Accuracy of PWR Operating Limits as Determined by the Core Operating Limit Supervisory System," CENPD-169, C-E Propietary Topical Report, July 1975, and "Overview Description of the Core Operating Limit Supervisory Systems (COLSS)," November 1986, CEN-312-P, Rev. 01-P.

23. Deleted.

24. D. Bollacasa and J. C. Stork, "VISIONS - Versatile, Interactive Simulator of Nuclear Systems," presented at American Nuclear Society Winter Meeting, November 29 - December 3, 1981.

25. QUIX User's Manual, CE-CES-79, Rev. 0-P, May 1987.

26. W. A. Rhoades and R. L. Childs, "An Updated Version of the DOT-4 One- and Two-Dimensional Neutron/Photon Transport Code," ORNL-5851, April 1982.

27. R. W. Roussin, "Cask-81 22 Neutron, 18 Gamma-Ray Group, P_3, Cross Sections for Shipping Cask Analysis," DLC-23, Oak Ridge National Laboratory, June 1981.

28. W. A. Rhoades, "The GIP Program for Preparation of Group-Organized Cross Section Libraries," Oak Ridge National Laboratory, April 1978.

29. Deleted.

30. "CE Methodology for Core Design Containing Gadolinia-Urania Burnable Absorbers," CENPD-275-P Rev. 1-P-A, May 1988.

31. "Palo Verde Nuclear Generating Station (PVNGS) Unit 1 - Proposed Reload Technical Specification Changes - Unit 1 Cycle 4," File : 91-056-026; 91-005-419-5.

32. USNRC, "Safety Evaluation by the Office of Nuclear Reactor Regulation Related to Amendment No. 61 to Facility Operating License No. NPF-41, Arizona Public Service, et al., Palo Verde Nuclear Generating Station, Unit No. 1, Docket No. STN 50-528".

33. CE-CES-129 Revision 1-P, "Methodology Manual - Physics Biases and Uncertainties," August 2, 1991.

34. "Yonggwang Unit 3&4 - The Question and Response for Operation Permission Inspection(the second), Question H-7.7-1," December, 1994.

35. J. S. Chung, "Evaluation of Fuel Temperature Correlation of PLUS7 for Korean Standard Nuclear Power Plants," KNF-TR-ND1-05001 Rev. 00, KNFC Topical Report, March, 2005.

36. "Qualification of PARAGON/ANC Code System for PWR Applications," TR-KHNP-0008 Rev.1, May 2007.

519

37. "Qualification of the PHOENIX-P/ANC Nuclear Design System for Pressurized Water Reactor Cores," WCAP-11596-P-A, June 1988.

38. "Qualification of the Two Dimensional Transport Code PARAGON," WCAP-16045-P-A, August 2004.

39. "FIGHTH User Manual," October 2006.

40. "ANC: A Westinghouse Advanced Nodal Computer Code," WCAP-10965-P-A, September 1986. 519

41. "APOLLO: An One Dimensional Neutron Diffusion Theory Program," WCAP-13524, Rev. 1, August 1994.

42. P. H. Gavin, "Methodology Manual for Physics Biases and Uncertainties," CE-CES-129, Rev. 11-P, February 2005.

TABLE 4.3-1 (Sh. 1 of 2)

NUCLEAR DESIGN CHARACTERISTICS

ITEM	VALUE
General Characteristics	
Fuel management	4 batch, mixed central zone
Core average burnup (MWd/MTU), 10 ppm soluble boron	13650
Core average U-235 enrichment (wt.%)	2.33
Core average H_2O/UO_2 volume ratio, hot (core cell)	2.04
Number of control element assemblies	
Full strength	65
Part strength	8
Burnable poison rods	
Number	640
Material	Gd_2O_3 in natural UO_2
Worth % $\Delta\rho$, at BOC	
Hot, 594°F (312°C)	5.0
Cold, 68°F (20°C)	4.5
Dissolved boron	
Dissolved boron content for criticality, ppm, (CEAs withdrawn, BOC)	
Cold, 68°F (20°C)	1109
Hot, zero power, clean 565°F (296°C)	1141
Hot, full power, clean, 595°F (313°C)	1016
Hot, full power, equilibrium Xe	778
Dissolved boron content (ppm) for:	
Refueling	2150
5% subcritical, cold, first cycle (all CEAs out) 0 MWd/MTU	1461
5% subcritical, hot, first cycle (all CEAs out) 0 MWd/MTU	1582

TABLE 4.3-1 (Sh. 2 of 2)

ITEM	VALUE
Inverse Boron worth, ppm/% $\Delta\rho$ (BOC/EOC)	
Hot, 594°F (312°C)	85/83
Cold, 68°F (20°C)	68/58
Neutron parameters	
Neutron lifetime (cycle average) microseconds	29.2
Delayed neutron fraction (cycle average)	0.0059
Plutonium buildup (first cycle)	
$\frac{\text{grams fissile Pu (final)}}{\text{kg U (original)}}$	4.34
$\frac{\text{grams total Pu (final)}}{\text{kg U (original)}}$	5.54

TABLE 4.3-2

EFFECTIVE MULTIPLICATION FACTORS AND REACTIVITY DATA

CONDITION	keff	Δρ
Cold, 68°F (20°C) (0 ppm) BOC	1.202	0.168
Cold, (68°F, 20°C) at minimum refueling boron concentration (2,100 ppm) BOC	0.879	-0.138
Hot, 564°F (296°C), zero power, clean, (0 ppm) BOC	1.163	0.140
Hot, full power, no Xe or Sm, 594°F (312°C) (0 ppm) BOC	1.138	0.121
Hot, full power, equilibrium Xe (0 ppm)	1.104	0.094
Hot, full power, equilibrium Xe and Sm (0 ppm)	1.097	0.089
Reactivity decrease, hot		
Zero to full power, BOC (749 ppm)		0.013
Fuel temperature		0.012
Moderator temperature		0.001
Reactivity decrease, hot		
Zero to full power, EOC (0 ppm)		0.020
Fuel temperature		0.009
Moderator temperature		0.011

NOTE: No control element assemblies or dissolved boron except as noted, initial core

TABLE 4.3-3 (Sh. 1 of 2)

COMPARISON OF CORE REACTIVITY COEFFICIENTS WITH THOSE USED IN VARIOUS SAFETY ANALYSES

	MODERATOR TEMPERATURE COEFFICIENT ($\Delta\rho$/°F x 10^4)	DOPPLER* COEFFICIENT	DENSITY COEFFICIENT ($\Delta\rho$/gm/cm^3)
COEFFICIENTS FROM TABLE 4.3-4			
Full power			
BOC	-0.52	Figure 4.3-45	0.027
EOC	-2.30	Figure 4.3-45	NA**
Zero power, CEAs banks 5,4 and 3 inserted			
BOC	-0.40	Figure 4.3-45	NA
EOC	-1.78	Figure 4.3-45	NA
COEFFICIENTS USED IN ACCIDENT ANALYSES			
CEA withdrawal			
Full/zero power	0/+.5****	0.794/0.794	NA
CEA misoperation			
Dropped CEA	-3.5****	1.206	NA
Loss of flow	0****	NA	NA
CEA ejection			
BOC, full/zero power	0/+.5****	0.794	NA
Loss-of-coolant accident			
Small break	0	Figure 4.3-45	***
Large break	+.5	Figure 4.3-45	***

TABLE 4.3-3 (Sh. 2 of 2)

---

* Nominal values of the Doppler coefficient ($\Delta\rho$/°F) as a function of the fuel temperature are shown in Figure 4.3-45. The numbers entered in the Doppler column of this table are the multipliers applied to the nominal value for analysis of designated accidents.

** Not applicable.

*** A curve of reactivity vs. moderator density is used for the LOCA evaluation. The value of density coefficient used corresponds to a 0 MTC for the small break events and $+.5 \times 10^{-4} \Delta\rho$/°F for the large breaks, resulting in rapid depressurization.

**** These values are the ones used at the nominal Tave = 594°F. For other temperatures, the set of curves shown on Figues 4.3-46 and 4.3-47 corresponding to the extreme (i.e., most positive at BOC, most negative at EOC) will be used.

TABLE 4.3-4

REACTIVITY COEFFICIENTS

PARAMETER	VALUE
Moderator Temperature Coefficient, $\Delta\rho$ /°F	
Beginning-of-cycle (0-50 MWd/MTU)	
Cold, 68°F, clean, 1,109 ppm	$+0.17 \times 10^{-4}$
Hot, zero power, 564°F, no CEAs, clean, 1141 ppm	$+0.16 \times 10^{-4}$
Hot, full power, 594°F, no CEAs, clean, 1016 ppm	-0.14×10^{-4}
Hot, full power, 594°F, no CEAs, equilibrium Xe, 778 ppm	-0.52×10^{-4}
Hot, zero power, 564°F regulating CEAs banks 5, 4 and 3 inserted, 0 MWd/MTU, 778 ppm, hot full power equilibrium Xe	-0.40×10^{-4}
End-of-cycle (10 ppm soluble boron, 13,650 MWd/MTU)	
Cold, 68°F approximate	$+0.10 \times 10^{-4}$
Hot zero power, 564°F, no CEAs, hot full power equilibrium Xe	-1.70×10^{-4}
Hot full power, equilibrium Xe, no CEAs, 594°F	-2.30×10^{-4}
Hot zero power, 564°F rodded, regulating CEAs banks 5, 4 and 3 inserted, hot full power equilibrium Xe	-1.78×10^{-4}
Moderator Density Coefficient, $\Delta\rho$/gm/cm^3	
Hot, operating, 594°F Beginning-of-cycle, 749 ppm soluble boron, 0 MWd/MTU	+0.027
Fuel temperature contribution to power coefficient, $\Delta\rho$ /(kW/ft), 749 ppm, 0 MWd/MTU	
Hot zero power	-2.81×10^{-3}
Full power	-1.85×10^{-3} 1
Moderator void coefficient, $\Delta\rho$/% void	
Hot operation, 594°F Beginning-of-cycle, 749 ppm soluble boron, 0 MWd/MTU	-0.19×10^{-3}
Moderator pressure coefficient, $\Delta\rho$ /psi	
Hot operating, 594°F Beginning-of-cycle, 749 ppm soluble boron, 0 MWd/MTU	0.44×10^{-6}
Overall power coefficient, $\Delta\rho$ /(kW/ft) Hot operating, 594°F	
Beginning-of-cycle, 700 ppm soluble boron, 0 MWd/MTU	-2.27×10^{-3}
End-of-cycle, 1 ppm soluble boron, 13,650 MWd/MTU	-3.69×10^{-3}

TABLE 4.3-5

WORTHS OF CEA GROUPS (%$\Delta\rho$)

	BOC (749 ppm)	EOC (1 ppm)
Shutdown CEAs	13.24	15.00
Regulating CEAs		
Group 1	1.74	1.73
Group 2	0.66	0.56
Group 3	0.73	0.62
Group 4	0.57	0.65
Group 5 (Lead Bank)	0.44	0.46
Total	17.38	19.02
PSCEA	0.22	0.31

TABLE 4.3-6

CEA REACTIVITY ALLOWANCES

REACTIVITY COMPONENT	ALLOWABLE (% $\Delta\rho$)
Fuel temperature variation	0.94
Moderator temperature variation	2.25
Moderator voids	0.10
CEA bite	0.27
Accident analysis allowance	5.86
Total reactivity allowance	9.42

TABLE 4.3-7

COMPARISON OF AVAILABLE CEA WORTHS AND ALLOWANCES

CONDITION	REACTIVITY (% $\Delta\rho$)
All full-strength inserted, hot, 594°F	19.02
Total reactivity allowance full power (from Table 4.3-6)	9.42
Stuck rod worth	7.45
Uncertainty in net rod worth	0.68
Excess reactivity	1.47

TABLE 4.3-8

COMPARISON OF RODDED AND UNRODDED PEAKING FACTORS FOR VARIOUS RODDED CONFIGURATIONS

CONFIGURATIONS	INTEGRATED ROD RADIAL PEAKING FACTOR F_r^n BOC	EOC
Unrodded	1.51	1.35
Bank 5	1.63	1.45
PSCEA	1.52	1.39
Bank 5 and PSCEA	1.63	1.45
Bank 5+4	1.71	1.42
Bank 5+4+3	1.75	1.71
Bank 5+4+3+2	2.43	2.13
Bank 5+4+3+2+1	2.07	1.93

TABLE 4.3-9

CALCULATED VARIATION OF THE AXIAL STABILITY INDEX DURING THE FIRST CYCLE

POWER LEVEL (% of full power)	BOC (hr^{-1})	EOC (hr^{-1})
100	-0.007	+0.042

1

NOTE: Equilibrium xenon conditions

TABLE 4.3-10

CONTROL ELEMENT ASSEMBLY SHADOWING FACTORS

	BOC	EOC
Bank 5	1.067	1.056
PSCEAs	0.992	0.994
Bank 5 + PSCEAs	1.082	1.073

TABLE 4.3-11

CE CRITICALS

CORE CONFIGURATION

LATTICE	FUEL ROD ARRAY	FUEL CELL PITCH (in)	NO. OF FUEL RODS	TEMPERATURES OF CORE (°F)	SOLUBLE BORON CONC. (ppm)	NO. OF CONTROL ROD CHANNELS
12	30x30	0.600	880	68	0	5
32	30x30	0.600	832	68	0	17
43	30x30	0.600	880	68	323	5
53	30x30	0.575	832	68	0	17
56	30x30	0.575	832	68	302	17

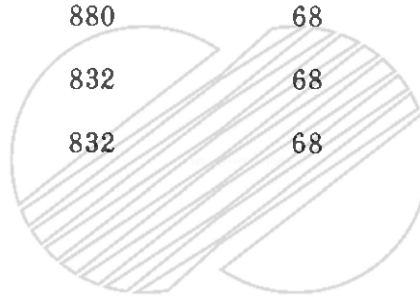

FUEL ROD DESIGN

PARAMETER	VALUE
Clad OD	0.4683 in (11.895 mm)
Clad Thickness	0.03145 in (0.7988 mm)
Clad Material	Zr-4
Fuel Pellet OD	0.400 in (10.16 mm)
Fuel Density	10.40 g/cm^3
Fuel Enrichment	2.72 wt.%

TABLE 4.3-12

FUEL SPECIFICATION (KRITZ EXPERIMENTS)

PARAMETER	VALUE
Fuel material (pellets)	UO_2
Fuel density (dishing including), g/cm^3	10.15
U-235 in U, wt.%	3.10
Fuel length, mm	2650
Pellet length, mm	11
Oxide diameter ,mm	9.08
Clading material	Zircaloy-4
Density, g/cm^3	6.55
Outer diameter, mm	10.74
Inner diameter, mm	9.30

TABLE 4.3-13

COMPARISON OF REACTIVITY LEVELS FOR NONUNIFORM CORE

LATICE	VOL MOD/ VOL FUEL	NO. OF LARGE WATER HOLES	MEASURED AXIAL BUCKLING M-2	SOLUBLE BORON CONCENTRATION (ppm)	k_{eff}
CE criticals 2.7wt.% U-235(68°F)					
#12	1.49	5	3.53	0	1.0017
#32	1.49	17	3.70	0	1.0006
#43	1.49	5	1.64	323	1.0032
#53	1.26	17	2.82	0	1.0021
#56	1.26	17	1.07	302	1.0006
KRITZ CO_2 (445°F)	1.79	21	2.20	959	1.0014

TABLE 4.3-14

SUMMARY OF ROCS, DIT, AND CALCULATIVE UNCERTAINTIES

ROCS CALCULATIONAL UNCERTAINTY		F_{XY}	F_Q	F_R	
Bias	D(%)	0	0	0	
Degrees of freedom	f_c	10	153	16	
Confidence multiplier	$k_{95/95}$	2.62	1.82	2.33	
Percent deviation	S_C(%)	1.88	2.89	1.47	
95/95 upper tolerance limit	$D+KS_C$(%)	+4.94	+5.25	+3.44	1

ROCS/MC CALCULATIONAL UNCERTAINTY		F_{XY}	F_Q	F_R	
Bias	D(%)	+0.42	+0.42	+0.42	1
Degrees of freedom	f_c	13	166	23	
Confidence multiplier	$k_{95/95}$	2.44	1.81	2.18	
Percent deviation	S_C(%)	2.02	2.98	1.64	
95/95 upper tolerance limit	$D+KS_C$(%)	+5.35	+5.82	+4.00	1

TABLE 4.3-15

AXIAL XENON OSCILLATIONS

		Period (hr)		Damping (hr^{-1})	
Reactor	Exposure (MWd/MTU)	Measured	Calculated	Measured	Calculated
Omaha	7,075	29	32	-0.027	-0.030
Stade	BOC	36	36	-0.096	-0.090
Stade	12,200	27	30	-0.021	-0.019

TABLE 4.3-16

REACTIVITY COEFFICIENTS, KINETIC PARAMETERS, AND SHUTDOWN MARGIN FOR PLUS7 EQUILIBRIUM CYCLE

PARAMETER	COEFFICIENTS USED IN ACIDENT ANALYSIS	CALCULATED VALUE FOR PLUS7 CORE	CALCULATED VALUE FOR GUARDIAN CORE
Moderator Temperature Coefficient, $x10^{-4}\Delta\rho/°F$			
Hot, full power, BOC	0.0	-0.61	-0.02
Hot, 75% power, BOC	0.0	-0.39	-0.01
Hot, full power, EOC	-3.8	-3.59	-3.49
Hot, zero power, BOC	0.5	0.09	0.26
Hot, zero power, EOC	-3.3	-2.00	-2.25
Doppler Temperature Coefficient, $pcm/\sqrt{K}$			
Least negative	-132	-145	-140
Most negative	-240	-212	-219
Delayed neutron fraction β_{eff} (cycle average) %			
Maximum	0.79	0.62	0.63
Minimum	0.41	0.52	0.52
Neutron lifetime (cycle average) microseconds			
Maximum	35.0	26.2	26.4
Minimun	15.0	16.5	16.0
Inverse Boron worth, ppm/%Δρ (BOC/EOC)			
Hot, 594°F (312℃)	N/A	137/108	145/108
Shudown margin, %Δρ			
BOC	5.5	7.69	6.56
EOC	5.5	8.04	6.79

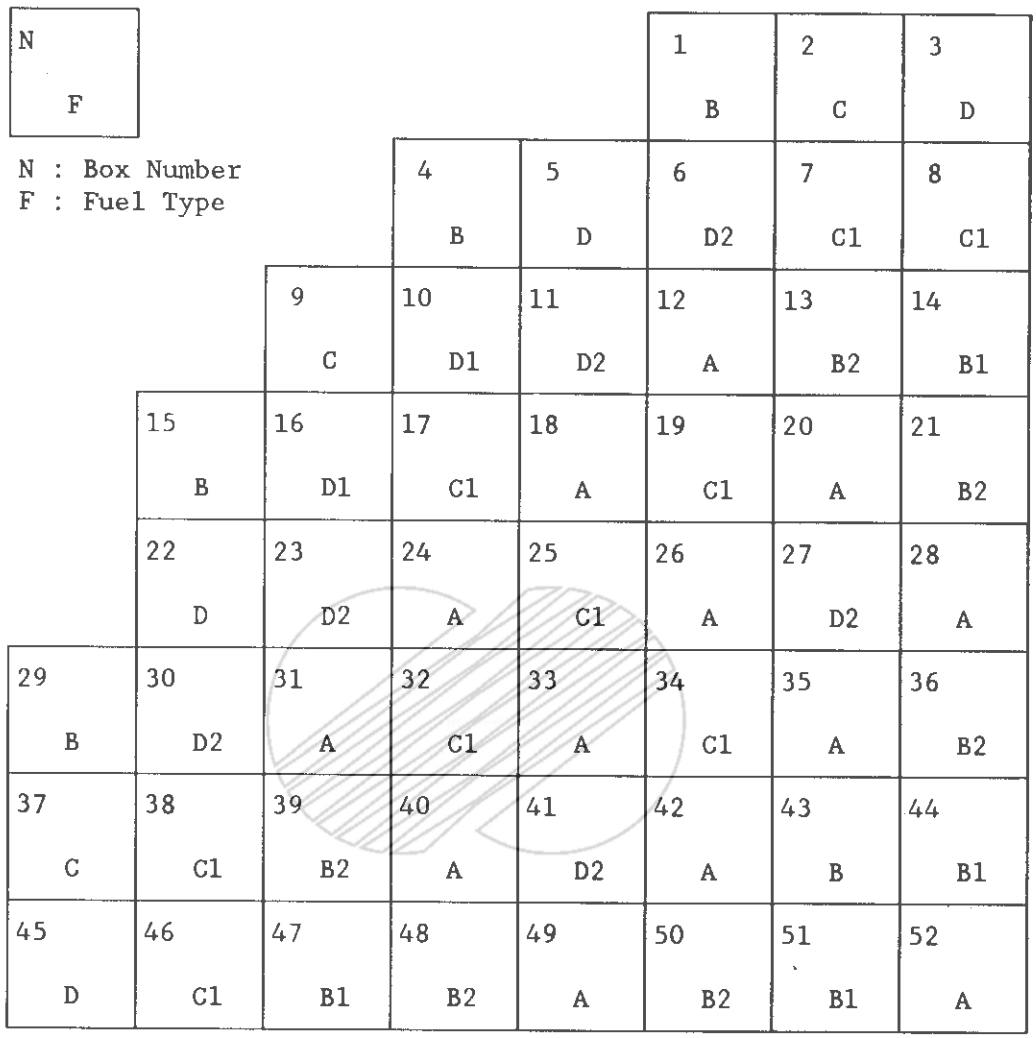

KOREA ELECTRIC POWER CORPORATION
YONGGWANG 3 & 4
FSAR

FIRST CYCLE FUEL
LOADING PATTERN

Figure 4.3-1

Assembly Type	Number of Fuel Assemblies	Fuel Enrichment (w/o)	No. of Rods per Assembly	No. of Gd_2O_3 Rods per Assembly	w/o in Nat'l UO_2
A	45	1.28	236	-	-
B	20	2.34	236	-	-
B1	8	2.34/1.28	176/52	8	4
B2	16	2.34	232	4	4
C	12	2.84/2.34	184/52	-	-
C1	32	2.84/2.34	176/52	8	4
D	12	3.34/2.84	184/52	-	-
D1	8	3.34/2.84	176/52	8	4
D2	24	3.34/2.84	128/100	8	4

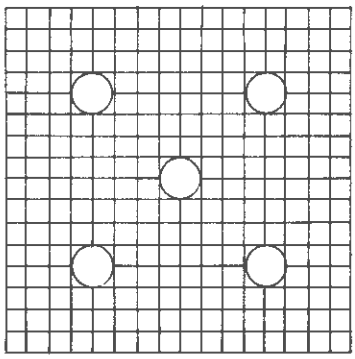

A, B

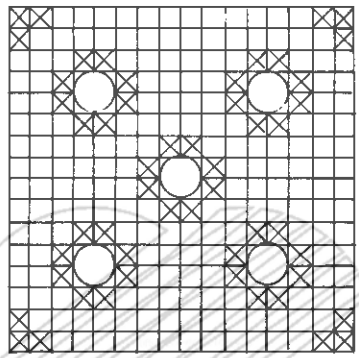

C, D

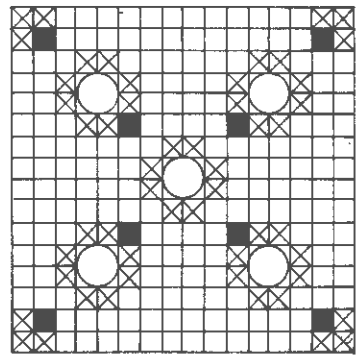

B1, C1, D1

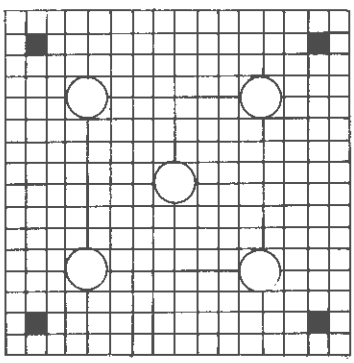

B2

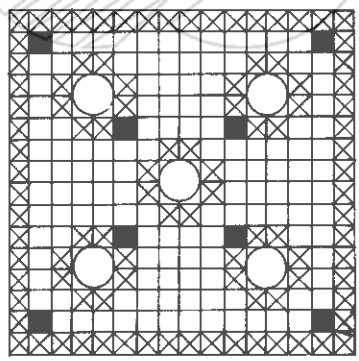

D2

WATER HOLE

NORMAL ENRICHED FUEL PIN

LOWER ENRICHED FUEL PIN

GADOLINIA FUEL PIN

KOREA ELECTRIC POWER CORPORATION
YONGGWANG 3 & 4
FSAR

FIRST CYCLE ASSEMBLY FUEL LOADING
WATERHOLE AND SHIM PLACEMENT

Figure 4.3-2

FORMAT IS BOX TYPE NO.	MAX. VALUE IN BOX		BATCH	BOXES	PWR. FR	AVG. PWR
BOX RPD	1.33	11	A	45	0.20	0.78
MAX 1-PIN	1.55	11	B	44	0.23	0.92
WITH CORE AVG. POWER	1.00		C	44	0.27	1.10
			D	44	0.30	1.20

			B 1 0.62 1.06	C 2 0.95 1.34	D 3 1.12 1.51
	B 4 0.63 1.08	D 5 1.12 1.45	D2 6 1.22 1.53	C1 7 1.27 1.47	C1 8 1.31 1.46
C 9 0.75 1.18	D1 10 1.20 1.45	D2 11 1.33 1.55	A 12 0.87 0.97	B2 13 1.24 1.41	B1 14 1.07 1.31
	C1 17 1.21 1.44	A 18 0.82 0.93	C1 19 1.13 1.37	A 20 0.80 0.89	B2 21 1.14 1.26
		C1 25 1.08 1.30	A 26 0.73 0.81	D2 27 1.15 1.32	A 28 0.76 0.83
			C1 34 1.04 1.21	A 35 0.74 0.81	B2 36 1.04 1.16
				B 43 1.06 1.15	B1 44 0.88 1.05
					A 52 0.68 0.73

KOREA ELECTRIC POWER CORPORATION
YONGGWANG 3 & 4
FSAR

PLANAR AVERAGE POWER
DISTRIBUTION, UNRODDED,
FULL POWER, NO XENON, 0 MWd/MTU
Figure 4.3-3

FORMAT IS BOX TYPE NO.	MAX. VALUE IN BOX		BATCH	BOXES	PWR. FR	AVG. PWR
BOX RPD	1.28	11	A	45	0.21	0.82
MAX 1-PIN	1.50	11	B	44	0.23	0.94
WITH CORE AVG. POWER	1.00		C	44	0.27	1.08
			D	44	0.29	1.16

			B 1 0.59 0.99	C 2 0.89 1.25	D 3 1.04 1.40
	B 4 0.60 1.02	D 5 1.05 1.38	D2 6 1.16 1.48	C1 7 1.20 1.39	C1 8 1.24 1.40
C 9 0.71 1.12	D1 10 1.13 1.38	D2 11 1.28 1.50	A 12 0.86 0.96	B2 13 1.22 1.38	B1 14 1.06 1.29
	C1 17 1.18 1.41	A 18 0.83 0.93	C1 19 1.16 1.37	A 20 0.83 0.93	B2 21 1.18 1.30
		C1 25 1.12 1.32	A 26 0.79 0.87	D2 27 1.23 1.40	A 28 0.82 0.91
			C1 34 1.12 1.33	A 35 0.82 0.91	B2 36 1.15 1.27
				B 43 1.18 1.29	B1 44 0.98 1.17
					A 52 0.78 0.84

KOREA ELECTRIC POWER CORPORATION
YONGGWANG 3 & 4
FSAR

PLANAR AVERAGE POWER
DISTRIBUTION, UNRODDED,
FULL POWER, EQUILIBRIUM XENON,
50 MWd/MTU
Figure 4.3-4

FORMAT IS BOX TYPE NO.	MAX. VALUE IN BOX		BATCH	BOXES	PWR. FR	AVG. PWR
BOX RPD	1.27	27	A	45	0.22	0.86
MAX 1-PIN	1.44	11	B	44	0.23	0.94
WITH CORE AVG. POWER	1.00		C	44	0.27	1.07
			D	44	0.28	1.13

			B 1 0.55 0.95	C 2 0.83 1.19	D 3 0.98 1.33
	B 4 0.57 0.98	D 5 0.99 1.31	D2 6 1.12 1.43	C1 7 1.17 1.37	C1 8 1.22 1.38
C 9 0.68 1.08	D1 10 1.10 1.35	D2 11 1.25 1.44	A 12 0.87 0.97	B2 13 1.21 1.35	B1 14 1.08 1.28
	C1 17 1.16 1.37	A 18 0.85 0.95	C1 19 1.18 1.36	A 20 0.87 0.96	B2 21 1.20 1.31
		C1 25 1.15 1.32	A 26 0.84 0.92	D2 27 1.27 1.43	A 28 0.87 0.96
			C1 34 1.17 1.36	A 35 0.87 0.96	B2 36 1.19 1.30
				B 43 1.21 1.32	B1 44 1.03 1.22
					A 52 0.84 0.91

KOREA ELECTRIC POWER CORPORATION
YONGGWANG 3 & 4
FSAR

PLANAR AVERAGE POWER
DISTRIBUTION, UNRODDED,
FULL POWER, EQUILIBRIUM XENON,
1000 MWd/MTU
Figure 4.3-5

FORMAT IS BOX TYPE NO.	MAX. VALUE IN BOX		BATCH	BOXES	PWR. FR	AVG. PWR
BOX RPD	1.27	11	A	45	0.23	0.90
MAX 1-PIN	1.43	11	B	44	0.23	0.91
WITH CORE AVG. POWER	1.00		C	44	0.27	1.08
			D	44	0.28	1.12

			B 1 0.53 0.93	C 2 0.77 1.12	D 3 0.88 1.23
	B 4 0.55 0.97	D 5 0.93 1.25	D2 6 1.12 1.36	C1 7 1.18 1.34	C1 8 1.23 1.38
C 9 0.68 1.10	D1 10 1.14 1.39	D2 11 1.27 1.43	A 12 0.91 0.98	B2 13 1.18 1.30	B1 14 1.14 1.29
	C1 17 1.24 1.36	A 18 0.92 1.02	C1 19 1.21 1.33	A 20 0.90 0.97	B2 21 1.14 1.25
		C1 25 1.21 1.34	A 26 0.89 0.97	D2 27 1.25 1.38	A 28 0.88 0.95
			C1 34 1.18 1.29	A 35 0.87 0.95	B2 36 1.10 1.19
				B 43 1.10 1.17	B1 44 1.03 1.15
					A 52 0.85 0.91

KOREA ELECTRIC POWER CORPORATION
YONGGWANG 3 & 4
FSAR

PLANAR AVERAGE POWER
DISTRIBUTION, UNRODDED,
FULL POWER, EQUILIBRIUM XENON,
6000 MWd/MTU
Figure 4.3-6

FORMAT IS BOX TYPE NO.	MAX. VALUE IN BOX		BATCH	BOXES	PWR. FR	AVG. PWR
BOX RPD	1.26	27	A	45	0.23	0.92
MAX 1-PIN	1.39	11	B	44	0.23	0.91
WITH CORE AVG. POWER	1.00		C	44	0.26	1.06
			D	44	0.27	1.11

			B 1 0.53 0.91	C 2 0.75 1.08	D 3 0.85 1.17
	B 4 0.56 0.96	D 5 0.92 1.22	D2 6 1.10 1.32	C1 7 1.15 1.29	C1 8 1.18 1.32
C 9 0.69 1.08	D1 10 1.13 1.36	D2 11 1.24 1.39	A 12 0.92 0.99	B2 13 1.15 1.25	B1 14 1.12 1.23
	C1 17 1.22 1.33	A 18 0.94 1.02	C1 19 1.20 1.30	A 20 0.92 0.99	B2 21 1.13 1.21
		C1 25 1.21 1.31	A 26 0.93 1.00	D2 27 1.26 1.36	A 28 0.91 0.98
			C1 34 1.19 1.29	A 35 0.91 0.98	B2 36 1.12 1.19
				B 43 1.12 1.19	B1 44 1.06 1.17
					A 52 0.90 0.95

KOREA ELECTRIC POWER CORPORATION
YONGGWANG 3 & 4
FSAR

PLANAR AVERAGE POWER
DISTRIBUTION, UNRODDED,
FULL POWER, EQUILIBRIUM XENON,
9000 MWd/MTU
Figure 4.3-7

FORMAT IS BOX TYPE NO.	MAX. VALUE IN BOX		BATCH	BOXES	PWR. FR	AVG. PWR
BOX RPD	1.26	27	A	45	0.24	0.95
MAX 1-PIN	1.34	27	B	44	0.23	0.92
WITH CORE AVG. POWER	1.00		C	44	0.26	1.05
			D	44	0.27	1.08

			B 1 0.55 0.90	C 2 0.76 1.05	D 3 0.84 1.13
	B 4 0.57 0.94	D 5 0.91 1.19	D2 6 1.08 1.27	C1 7 1.11 1.24	C1 8 1.14 1.26
C 9 0.69 1.05	D1 10 1.10 1.30	D2 11 1.20 1.32	A 12 0.93 1.01	B2 13 1.12 1.21	B1 14 1.10 1.18
	C1 17 1.18 1.27	A 18 0.96 1.03	C1 19 1.19 1.28	A 20 0.95 1.02	B2 21 1.13 1.19
		C1 25 1.20 1.28	A 26 0.96 1.04	D2 27 1.26 1.34	A 28 0.96 1.02
			C1 34 1.20 1.28	A 35 0.96 1.03	B2 36 1.14 1.21
				B 43 1.14 1.21	B1 44 1.09 1.18
					A 52 0.95 1.01

KOREA ELECTRIC POWER CORPORATION
YONGGWANG 3 & 4
FSAR

PLANAR AVERAGE POWER
DISTRIBUTION, UNRODDED,
FULL POWER, EQUILIBRIUM XENON,
13,650 MWd/MTU
Figure 4.3-8

FORMAT IS BOX TYPE NO.	MAX. VALUE IN BOX		BATCH	BOXES	PWR. FR	AVG. PWR
BOX RPD	1.39	11	A	45	0.20	0.80
MAX 1-PIN	1.63	11	B	44	0.22	0.89
WITH CORE AVG. POWER	1.00		C	44	0.28	1.11
			D	44	0.30	1.21

			B 1 0.62 1.03	C 2 0.92 1.29	D 3 1.07 1.45
	B 4 0.66 1.12	D 5 1.15 1.51	D2 6 1.22 1.56	C1 7 1.22 1.40	C1 8 1.24 1.40
C 9 0.80 1.24	D1 10 1.26 1.54	D2 11 1.39 1.63	A 12 0.89 1.00	B2 13 1.16 1.36	B1 14 0.93 1.21
	C1 17 1.29 1.54	A 18 0.88 1.00	C1 19 1.15 1.42	A 20 0.72 0.84	B2 21 0.74 0.85
		C1 25 1.16 1.41	A 26 0.77 0.86	D2 27 1.11 1.31	A 28 0.69 0.80
			C1 34 1.10 1.29	A 35 0.79 0.88	B2 36 1.09 1.22
				B 43 1.27 1.21	B1 44 1.15 1.18
					A 52 0.77 0.83

KOREA ELECTRIC POWER CORPORATION
YONGGWANG 3 & 4
FSAR

PLANAR AVERAGE POWER
DISTRIBUTION, BANK 5 FULL IN,
FULL POWER, ARO EQUILIBRIUM XENON,
0 MWd/MTU
Figure 4.3-9

FORMAT IS BOX TYPE NO.	MAX. VALUE IN BOX		BATCH	BOXES	PWR. FR	AVG. PWR
BOX RPD	1.36	11	A	45	0.22	0.86
MAX 1-PIN	1.53	11	B	44	0.22	0.88
WITH CORE AVG. POWER	1.00		C	44	0.28	1.11
			D	44	0.28	1.15

			B 1 0.55 0.96	C 2 0.78 1.13	D 3 0.89 1.23
	B 4 0.61 1.07	D 5 1.01 1.34	D2 6 1.16 1.40	C1 7 1.18 1.33	C1 8 1.20 1.34
C 9 0.77 1.22	D1 10 1.26 1.53	D2 11 1.36 1.53	A 12 0.93 1.01	B2 13 1.10 1.21	B1 14 0.99 1.11
	C1 17 1.35 1.48	A 18 0.99 1.09	C1 19 1.21 1.32	A 20 0.79 0.85	B2 21 0.74 0.80
		C1 25 1.25 1.38	A 26 0.90 0.97	D2 27 1.16 1.27	A 28 0.76 0.82
			C1 34 1.17 1.28	A 35 0.86 0.93	B2 36 1.06 1.15
				B 43 1.10 1.17	B1 44 1.04 1.15
					A 52 0.87 0.93

KOREA ELECTRIC POWER CORPORATION
YONGGWANG 3 & 4
FSAR

PLANAR AVERAGE POWER
DISTRIBUTION, BANK 5 FULL IN,
FULL POWER, ARO EQUILIBRIUM XENON,
7000 MWd/MTU
Figure 4.3-10

FORMAT IS BOX TYPE NO.	MAX. VALUE IN BOX		BATCH	BOXES	PWR. FR	AVG. PWR
BOX RPD	1.30	11	A	45	0.24	0.93
MAX 1-PIN	1.44	11	B	44	0.22	0.87
WITH CORE AVG. POWER	1.00		C	44	0.27	1.07
			D	44	0.28	1.13

			B 1 0.57 0.92	C 2 0.78 1.05	D 3 0.86 1.13
	B 4 0.63 1.02	D 5 0.98 1.27	D2 6 1.12 1.29	C1 7 1.12 1.21	C1 8 1.12 1.19
C 9 0.77 1.16	D1 10 1.21 1.44	D2 11 1.30 1.44	A 12 0.96 1.05	B2 13 1.06 1.16	B1 14 0.95 1.09
	C1 17 1.29 1.39	A 18 1.02 1.12	C1 19 1.19 1.32	A 20 0.83 0.96	B2 21 0.72 0.83
		C1 25 1.25 1.36	A 26 0.96 1.06	D2 27 1.17 1.32	A 28 0.82 0.96
			C1 34 1.20 1.31	A 35 0.94 1.03	B2 36 1.11 1.21
				B 43 1.15 1.24	B1 44 1.11 1.22
					A 52 0.97 1.05

KOREA ELECTRIC POWER CORPORATION
YONGGWANG 3 & 4
FSAR

PLANAR AVERAGE POWER
DISTRIBUTION, BANK 5 FULL IN,
FULL POWER, ARO EQUILIBRIUM XENON,
13,650 MWd/MTU
Figure 4.3-11

FORMAT IS BOX TYPE NO.	MAX. VALUE IN BOX		BATCH	BOXES	PWR. FR	AVG. PWR
BOX RPD	1.28	8	A	45	0.21	0.81
MAX 1-PIN	1.51	11	B	44	0.24	0.96
WITH CORE AVG. POWER	1.00		C	44	0.27	1.07
			D	44	0.29	1.17

			B 1 0.60 1.01	C 2 0.92 1.30	D 3 1.08 1.47
	B 4 0.61 1.02	D 5 1.06 1.40	D2 6 1.18 1.51	C1 7 1.23 1.45	C1 8 1.28 1.44
C 9 0.72 1.12	D1 10 1.14 1.40	D2 11 1.27 1.51	A 12 0.85 0.96	B2 13 1.23 1.42	B1 14 1.08 1.31
	C1 17 1.17 1.40	A 18 0.80 0.91	C1 19 1.04 1.25	A 20 0.82 0.92	B2 21 1.18 1.31
		C1 25 1.08 1.29	A 26 0.76 0.85	D2 27 1.22 1.41	A 28 0.83 0.91
			C1 34 1.12 1.34	A 35 0.83 0.92	B2 36 1.17 1.31
				B 43 1.20 1.32	B1 44 1.01 1.20
					A 52 0.80 0.87

KOREA ELECTRIC POWER CORPORATION
YONGGWANG 3 & 4
FSAR

PLANAR AVERAGE POWER
DISTRIBUTION, PART-STRENGTH ROD FULL IN,
FULL POWER, ARO EQUILIBRIUM XENON,
0 MWd/MTU
Figure 4.3-12

FORMAT IS BOX TYPE NO.	MAX. VALUE IN BOX		BATCH	BOXES	PWR. FR	AVG. PWR
BOX RPD	1.26	8	A	45	0.23	0.89
MAX 1-PIN	1.41	11	B	44	0.23	0.93
WITH CORE AVG. POWER	1.00		C	44	0.26	1.06
			D	44	0.28	1.12

			B 1 0.54 0.95	C 2 0.79 1.14	D 3 0.91 1.26
	B 4 0.56 0.98	D 5 0.94 1.26	D2 6 1.13 1.37	C1 7 1.21 1.36	C1 8 1.26 1.40
C 9 0.70 1.11	D1 10 1.15 1.39	D2 11 1.25 1.41	A 12 0.89 0.97	B2 13 1.17 1.29	B1 14 1.15 1.28
	C1 17 1.23 1.35	A 18 0.90 0.99	C1 19 1.07 1.18	A 20 0.89 0.95	B2 21 1.14 1.24
		C1 25 1.17 1.28	A 26 0.87 0.94	D2 27 1.25 1.36	A 28 0.90 0.97
			C1 34 1.18 1.29	A 35 0.90 0.97	B2 36 1.13 1.22
				B 43 1.14 1.21	B1 44 1.08 1.20
					A 52 0.90 0.96

KOREA ELECTRIC POWER CORPORATION
YONGGWANG 3 & 4
FSAR

PLANAR AVERAGE POWER
DISTRIBUTION, PART-STRENGTH ROD FULL IN,
FULL POWER, ARO EQUILIBRIUM XENON,
7000 MWd/MTU
Figure 4.3-13

FORMAT IS BOX TYPE NO.	MAX. VALUE IN BOX		BATCH	BOXES	PWR. FR	AVG. PWR
BOX RPD	1.26	27	A	45	0.24	0.94
MAX 1-PIN	1.38	27	B	44	0.23	0.94
WITH CORE AVG. POWER	1.00		C	44	0.26	1.03
			D	44	0.27	1.09

			B 1 0.56 0.92	C 2 0.79 1.08	D 3 0.88 1.17
	B 4 0.58 0.93	D 5 1.10 1.19	D2 6 1.10 1.28	C1 7 1.15 1.27	C1 8 1.18 1.29
C 9 0.69 1.05	D1 10 1.10 1.30	D2 11 1.19 1.30	A 12 0.91 0.99	B2 13 1.13 1.22	B1 14 1.12 1.20
	C1 17 1.17 1.26	A 18 0.92 1.01	C1 19 1.05 1.15	A 20 0.93 1.02	B2 21 1.14 1.20
		C1 25 1.15 1.26	A 26 0.93 1.04	D2 27 1.26 1.38	A 28 0.97 1.06
			C1 34 1.21 1.33	A 35 0.99 1.08	B2 36 1.18 1.27
				B 43 1.20 1.29	B1 44 1.15 1.27
					A 52 1.01 1.09

KOREA ELECTRIC POWER CORPORATION
YONGGWANG 3 & 4
FSAR

PLANAR AVERAGE POWER
DISTRIBUTION, PART-STRENGTH ROD FULL IN,
FULL POWER, ARO EQUILIBRIUM XENON,
13,650 MWd/MTU
Figure 4.3-14

FORMAT IS BOX TYPE NO.	MAX. VALUE IN BOX		BATCH	BOXES	PWR. FR	AVG. PWR
BOX RPD	1.39	11	A	45	0.20	0.78
MAX 1-PIN	1.62	11	B	44	0.22	0.90
WITH CORE AVG. POWER	1.00		C	44	0.27	1.10
			D	44	0.29	1.22

			B 1 0.64 1.06	C 2 0.96 1.34	D 3 1.12 1.51
	B 4 0.68 1.14	D 5 1.16 1.52	D2 6 1.25 1.57	C1 7 1.26 1.44	C1 8 1.28 1.45
C 9 0.81 1.26	D1 10 1.28 1.55	D2 11 1.39 1.62	A 12 0.87 1.00	B2 13 1.16 1.37	B1 14 0.95 1.24
	C1 17 1.29 1.53	A 18 0.86 0.99	C1 19 1.03 1.29	A 20 0.70 0.81	B2 21 0.74 0.85
		C1 25 1.12 1.37	A 26 0.74 0.82	D2 27 1.10 1.30	A 28 0.69 0.89
			C1 34 1.09 1.30	A 35 0.79 0.89	B2 36 1.10 1.25
				B 43 1.17 1.29	B1 44 0.98 1.18
					A 52 0.79 0.85

KOREA ELECTRIC POWER CORPORATION
YONGGWANG 3 & 4
FSAR

PLANAR AVERAGE POWER
DISTRIBUTION, BANK 5 PART-STRENGTH ROD
FULL IN, FULL POWER, ARO EQUILIBRIUM
XENON, 0 MWd/MTU
Figure 4.3-15

FORMAT IS BOX TYPE NO.	MAX. VALUE IN BOX		BATCH	BOXES	PWR. FR	AVG. PWR
BOX RPD	1.35	11	A	45	0.22	0.87
MAX 1-PIN	1.55	10	B	44	0.22	0.88
WITH CORE AVG. POWER	1.00		C	44	0.27	1.09
			D	44	0.29	1.17

			B 1 0.57 0.99	C 2 0.81 1.18	D 3 0.92 1.28
	B 4 0.63 1.09	D 5 1.02 1.36	D2 6 1.18 1.43	C1 7 1.21 1.37	C1 8 1.24 1.38
C 9 0.78 1.24	D1 10 1.28 1.55	D2 11 1.35 1.52	A 12 0.92 0.99	B2 13 1.10 1.21	B1 14 1.01 1.13
	C1 17 1.35 1.48	A 18 0.96 1.05	C1 19 1.07 1.18	A 20 0.77 0.83	B2 21 0.74 0.80
		C1 25 1.21 1.33	A 26 0.87 0.94	D2 27 1.15 1.25	A 28 0.77 0.83
			C1 34 1.17 1.28	A 35 0.87 0.95	B2 36 1.09 1.17
				B 43 1.13 1.20	B1 44 1.08 1.20
					A 52 0.91 0.97

KOREA ELECTRIC POWER CORPORATION
YONGGWANG 3 & 4
FSAR

PLANAR AVERAGE POWER
DISTRIBUTION, BANK 5 PART-STRENGTH ROD
FULL IN, FULL POWER, ARO EQUILIBRIUM
XENON, 7000 MWd/MTU
Figure 4.3-16

FORMAT IS BOX TYPE NO.	MAX. VALUE IN BOX		BATCH	BOXES	PWR. FR	AVG. PWR
BOX RPD	1.29	11	A	45	0.23	0.92
MAX 1-PIN	1.44	10	B	44	0.22	0.89
WITH CORE AVG. POWER	1.00		C	44	0.26	1.06
			D	44	0.28	1.14

			B 1 0.59 0.95	C 2 0.81 1.10	D 3 0.90 1.18
	B 4 0.64 1.03	D 5 1.00 1.28	D2 6 1.15 1.31	C1 7 1.15 1.23	C1 8 1.16 1.23
C 9 0.78 1.17	D1 10 1.22 1.44	D2 11 1.29 1.43	A 12 0.93 1.03	B2 13 1.06 1.17	B1 14 0.97 1.11
	C1 17 1.28 1.38	A 18 0.98 1.10	C1 19 1.05 1.18	A 20 0.80 0.91	B2 21 0.72 0.83
		C1 25 1.20 1.32	A 26 0.93 1.03	D2 27 1.16 1.32	A 28 0.83 0.97
			C1 34 1.20 1.32	A 35 0.97 1.07	B2 36 1.14 1.26
				B 43 1.20 1.31	B1 44 1.16 1.29
					A 52 1.02 1.11

KOREA ELECTRIC POWER CORPORATION
YONGGWANG 3 & 4
FSAR

PLANAR AVERAGE POWER
DISTRIBUTION, BANK 5 PART-STRENGTH ROD
FULL IN, FULL POWER, ARO EQUILIBRIUM
XENON, 13,650 MWd/MTU
Figure 4.3-17

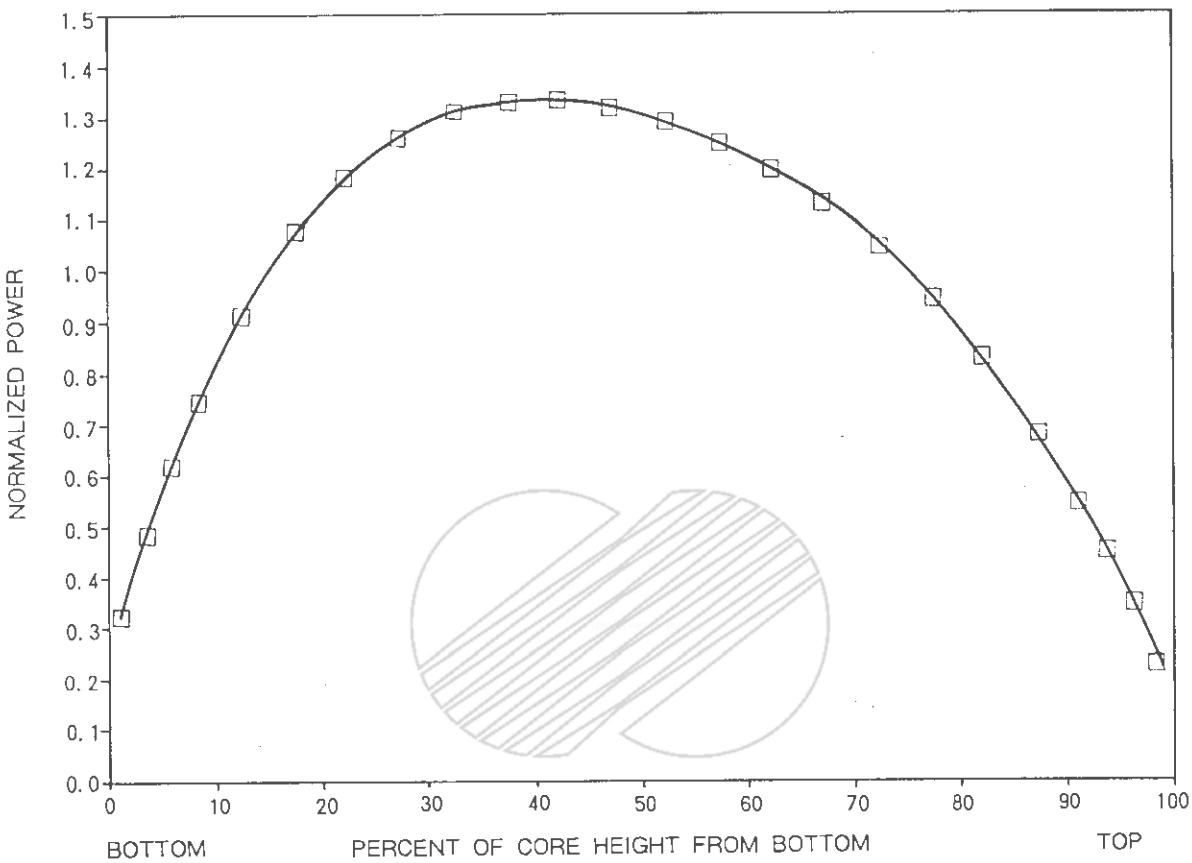

KOREA ELECTRIC POWER CORPORATION
YONGGWANG 3 & 4
FSAR

AXIAL POWER DISTRIBUTION,
BOC, UNRODDED

Figure 4.3-18

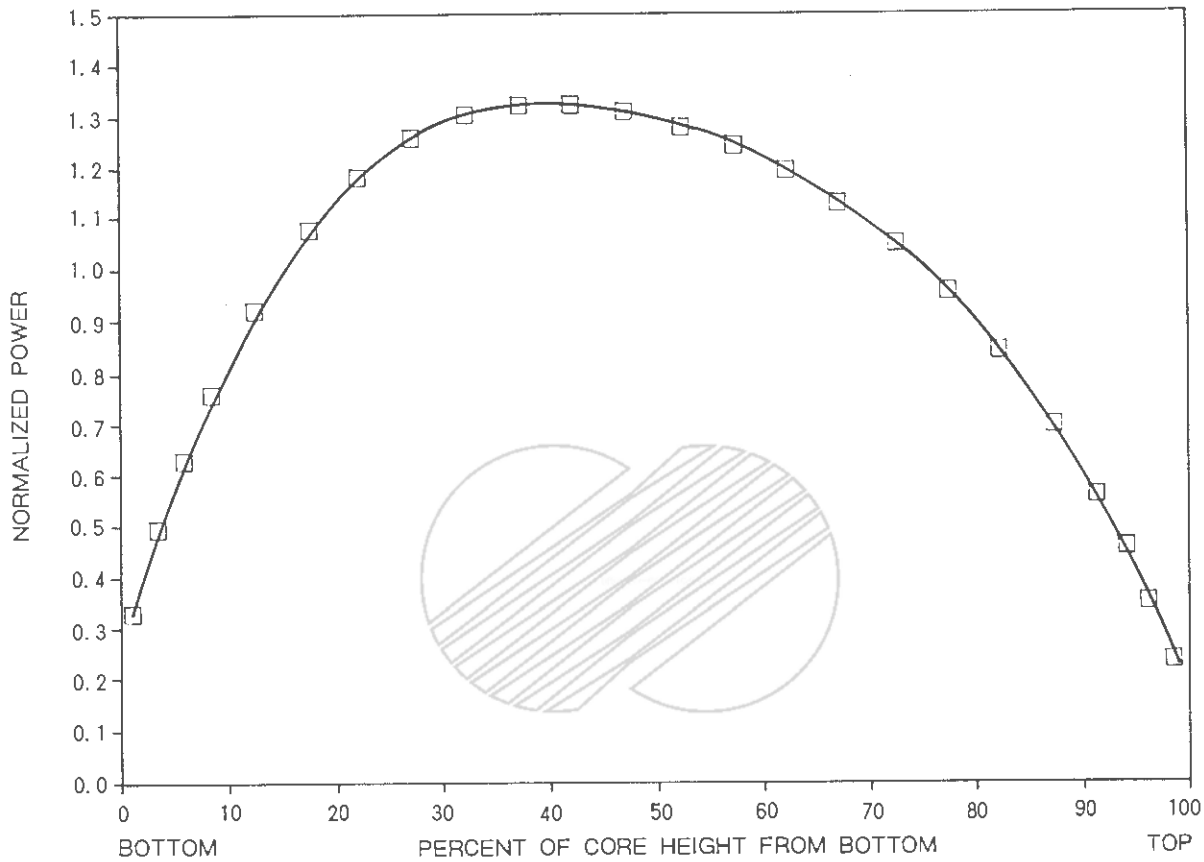

KOREA ELECTRIC POWER CORPORATION
YONGGWANG 3 & 4
FSAR

AXIAL POWER DISTRIBUTION
AT 50 MWd/MTU, UNRODDED

Figure 4.3-19

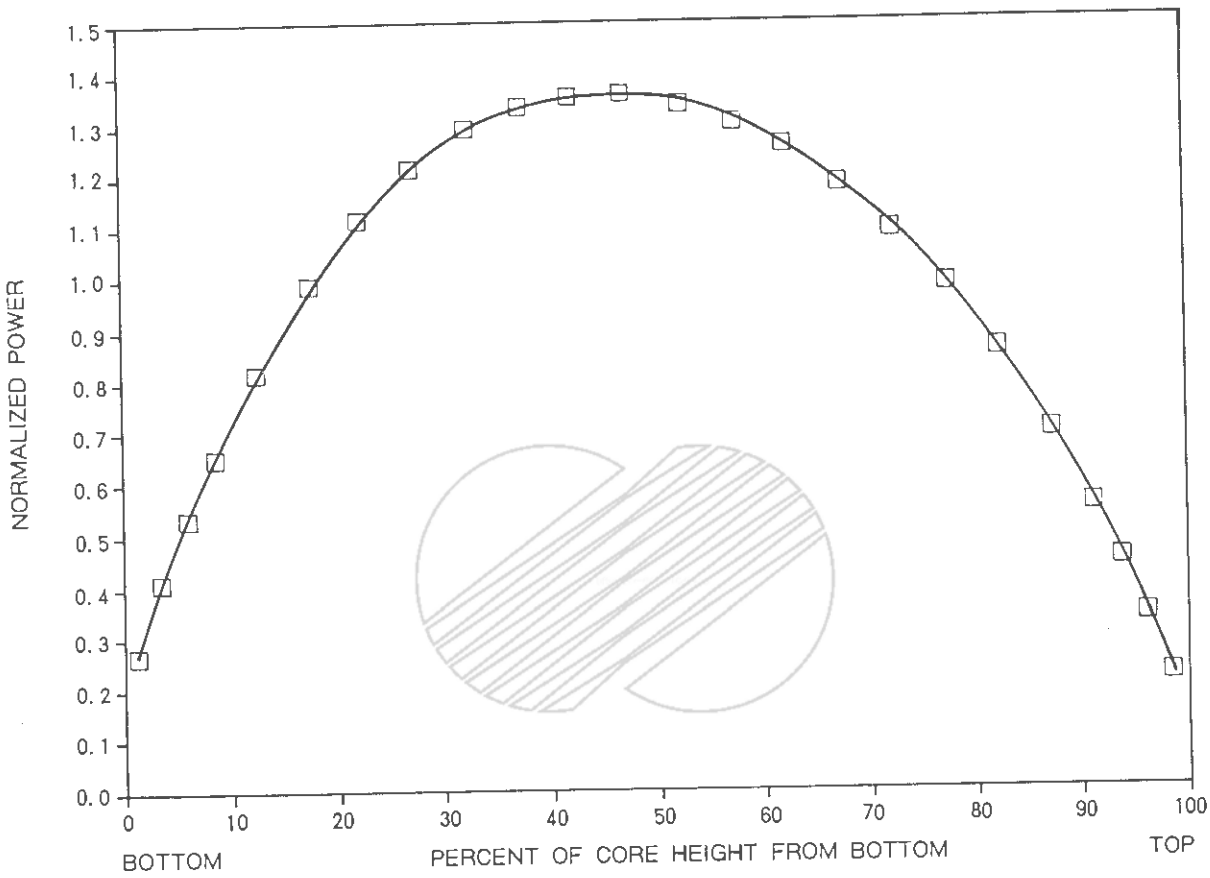

KOREA ELECTRIC POWER CORPORATION
YONGGWANG 3 & 4
FSAR

AXIAL POWER DISTRIBUTION
AT 3000 MWd/MTU, UNRODDED

Figure 4.3-20

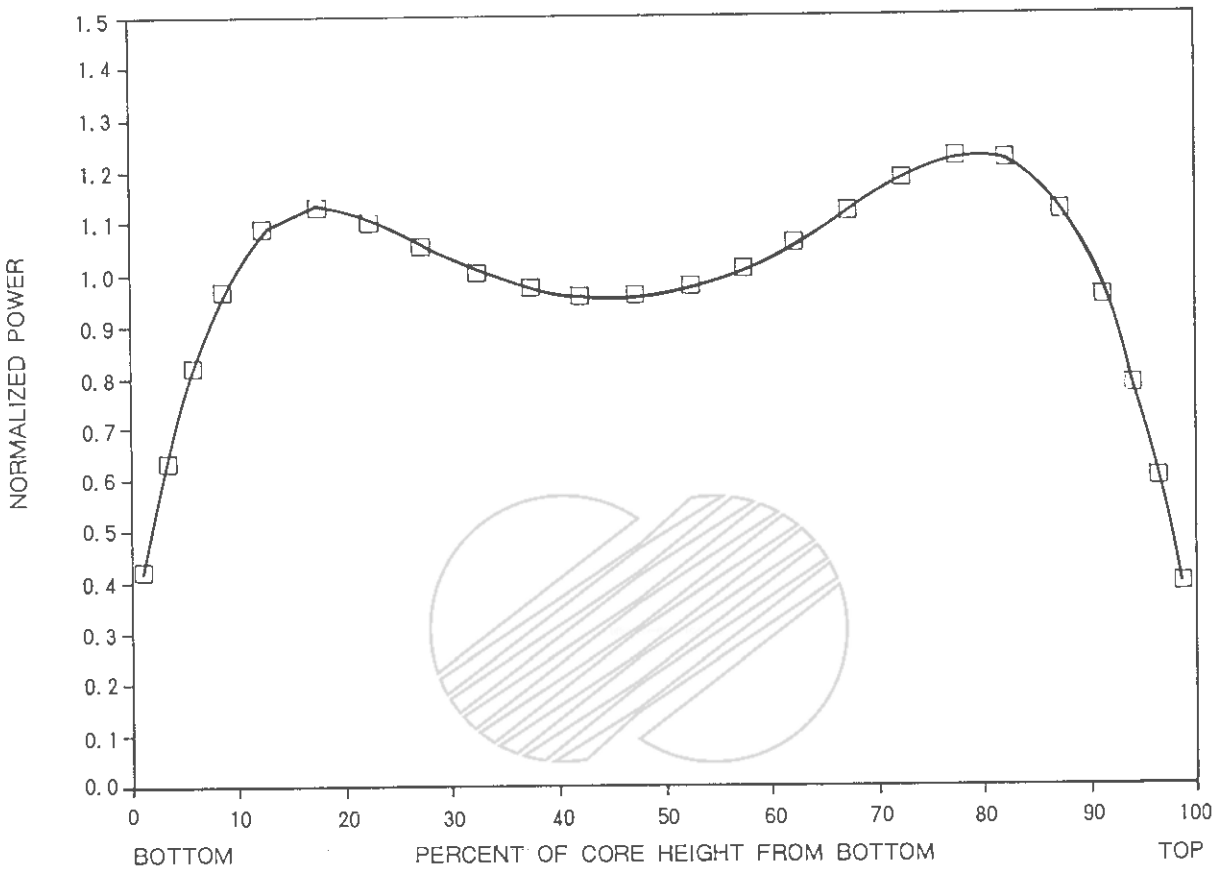

KOREA ELECTRIC POWER CORPORATION
YONGGWANG 3 & 4
FSAR

AXIAL POWER DISTRIBUTION
AT 7,000 MWd/MTU, UNRODDED

Figure 4.3-21

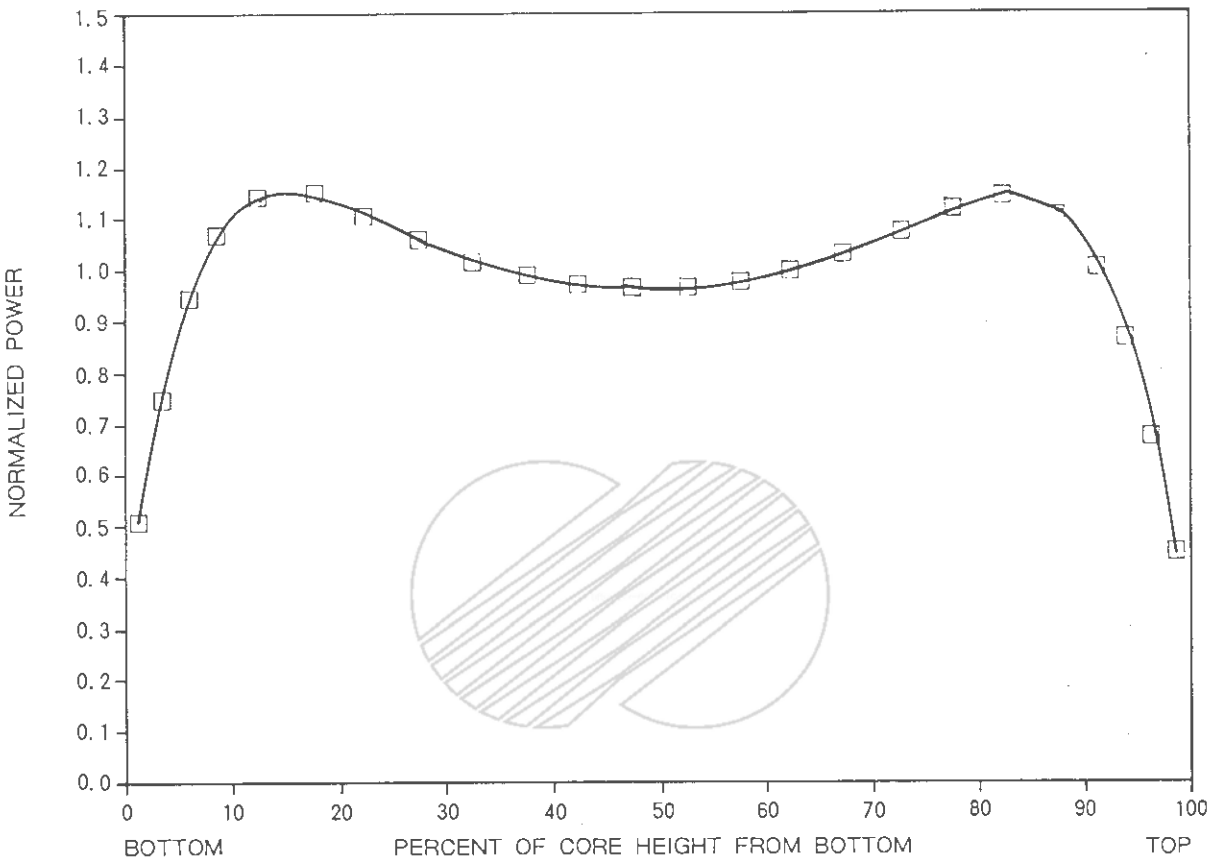

KOREA ELECTRIC POWER CORPORATION
YONGGWANG 3 & 4
FSAR

AXIAL POWER DISTRIBUTION
AT 10,000 MWd/MTU, UNRODDED

Figure 4.3-22

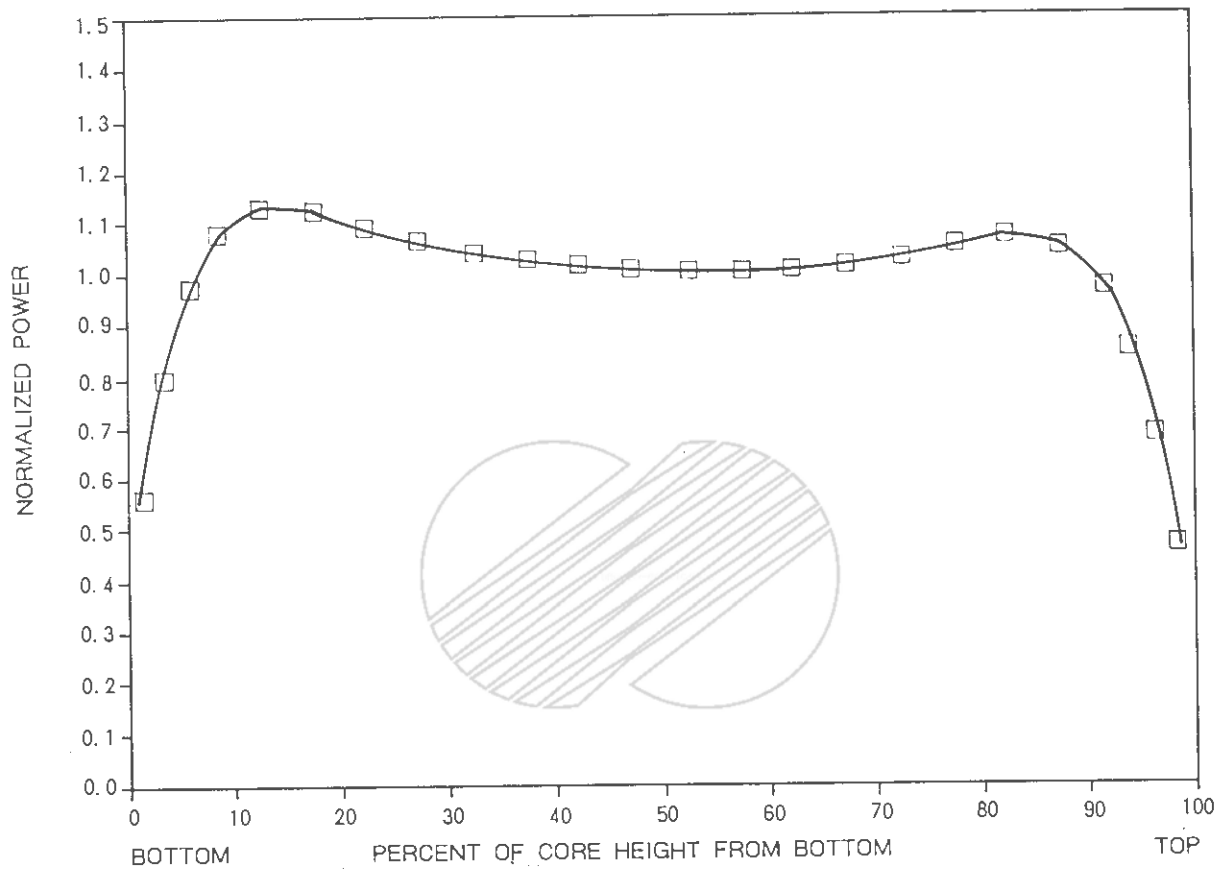

KOREA ELECTRIC POWER CORPORATION
YONGGWANG 3 & 4
FSAR

AXIAL POWER DISTRIBUTION
AT 13,650 MWd/MTU, UNRODDED

Figure 4.3-23

			D1 0.48	E 0.98	B2 0.61
	D2 0.44	E 1.07	D2 0.95	B 1.03	E2 1.34
B 0.42	E1 1.11	B2 0.91	E3 1.34	D2 1.07	B1 0.89
	C1 0.95	D 1.16	C 1.15	B 1.09	B2 0.94
		B1 0.90	C1 1.00	C1 1.04	E3 1.34
			E3 1.33	C1 1.04	C1 1.06
				C 1.23	D 1.30
					A 0.90

KOREA ELECTRIC POWER CORPORATION
YONGGWANG 3 & 4
FSAR

TYPICAL UNRODDED PLANER POWER DISTRIBUTION (BOX RELATIVE POWER DENSITY), CYCLE 2 AT 0 MWd/MTU
Figure 4.3-24

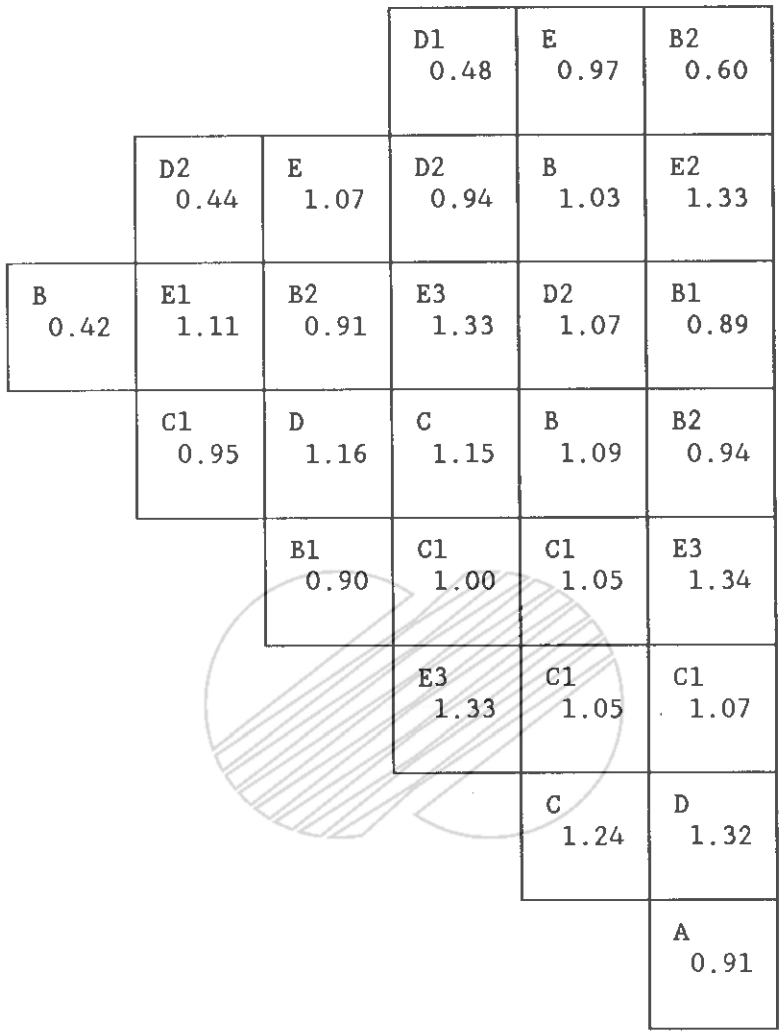

KOREA ELECTRIC POWER CORPORATION
YONGGWANG 3 & 4
FSAR

TYPICAL UNRODDED PLANER POWER DISTRIBUTION (BOX RELATIVE POWER DENSITY), CYCLE 2 AT 50 MWd/MTU
Figure 4.3-25

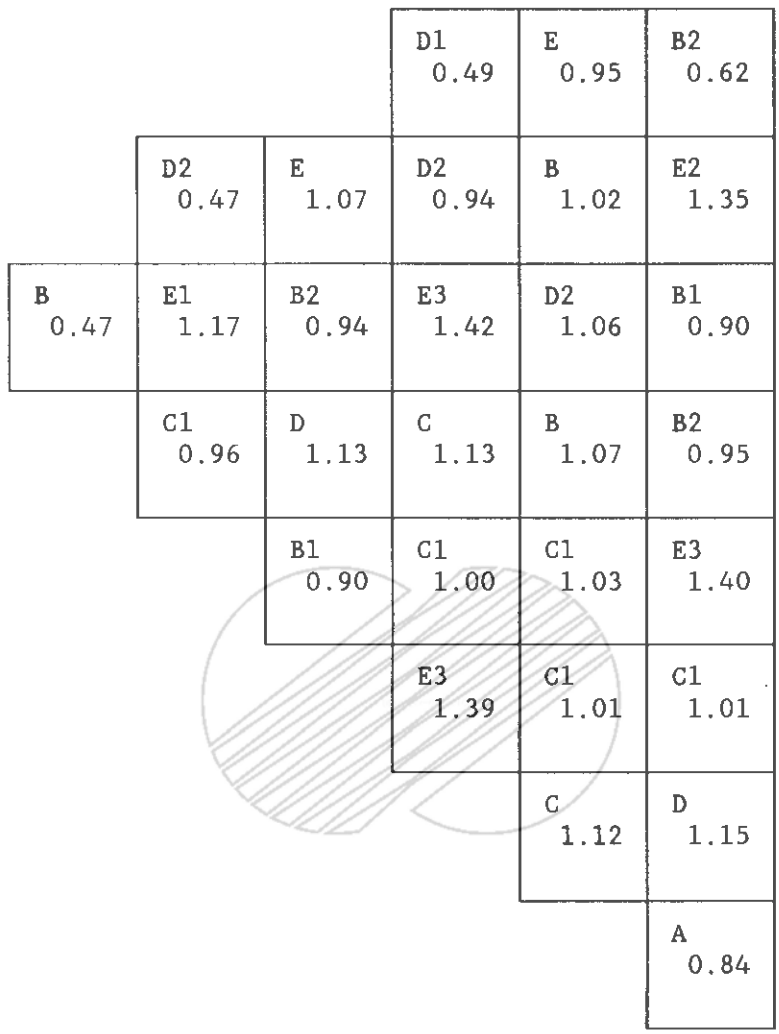

KOREA ELECTRIC POWER CORPORATION
YONGGWANG 3 & 4
FSAR

TYPICAL UNRODDED PLANER POWER DISTRIBUTION (BOX RELATIVE POWER DENSITY), CYCLE 2 AT 6,000 MWd/MTU
Figure 4.3-26

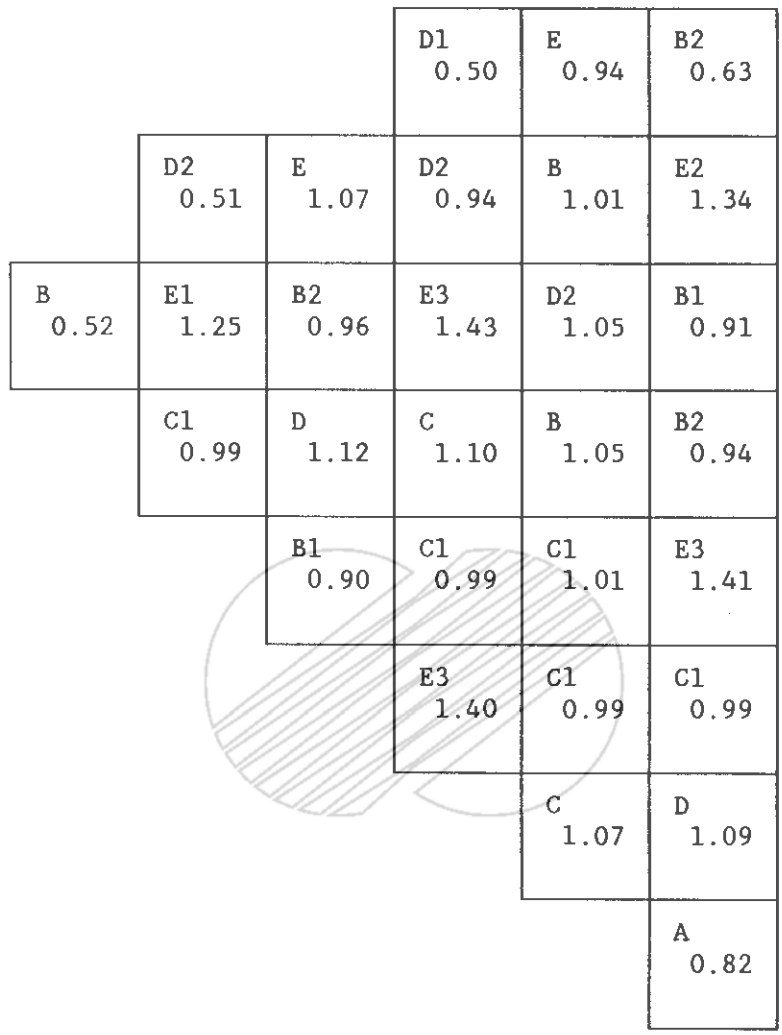

KOREA ELECTRIC POWER CORPORATION
YONGGWANG 3 & 4
FSAR

TYPICAL UNRODDED PLANER POWER DISTRIBUTION (BOX RELATIVE POWER DENSITY), CYCLE 2 AT EOC
Figure 4.3-27

			D2 0.38	F 0.79	D 0.54
		D1 0.40	F 1.00	F1 1.14	D2 0.85	F1 1.23
C 0.38		F1 1.01	D 0.93	B 0.93	E 1.41	C1 0.89
		B 0.85	E 1.41	E1 1.41	C 0.99	E3 1.23
			C1 0.91	B 0.94	F2 1.34	C1 0.89
				E3 1.20	D2 0.95	E3 1.29
					E3 1.36	E2 1.43
						C1 1.04

KOREA ELECTRIC POWER CORPORATION
YONGGWANG 3 & 4
FSAR

TYPICAL UNRODDED PLANER POWER DISTRIBUTION (BOX RELATIVE POWER DENSITY), CYCLE 3 AT 0 MWd/MTU
Figure 4.3-28

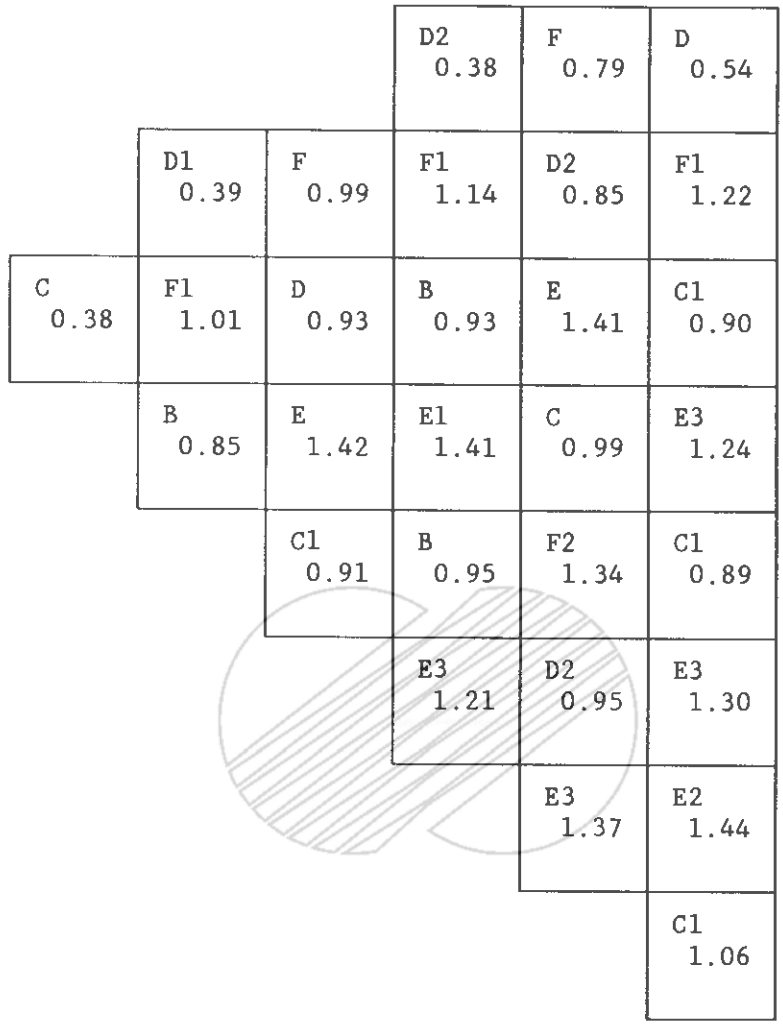

KOREA ELECTRIC POWER CORPORATION
YONGGWANG 3 & 4
FSAR

TYPICAL UNRODDED PLANER POWER DISTRIBUTION (BOX RELATIVE POWER DENSITY), CYCLE 3 AT 50 MWd/MTU
Figure 4.3-29

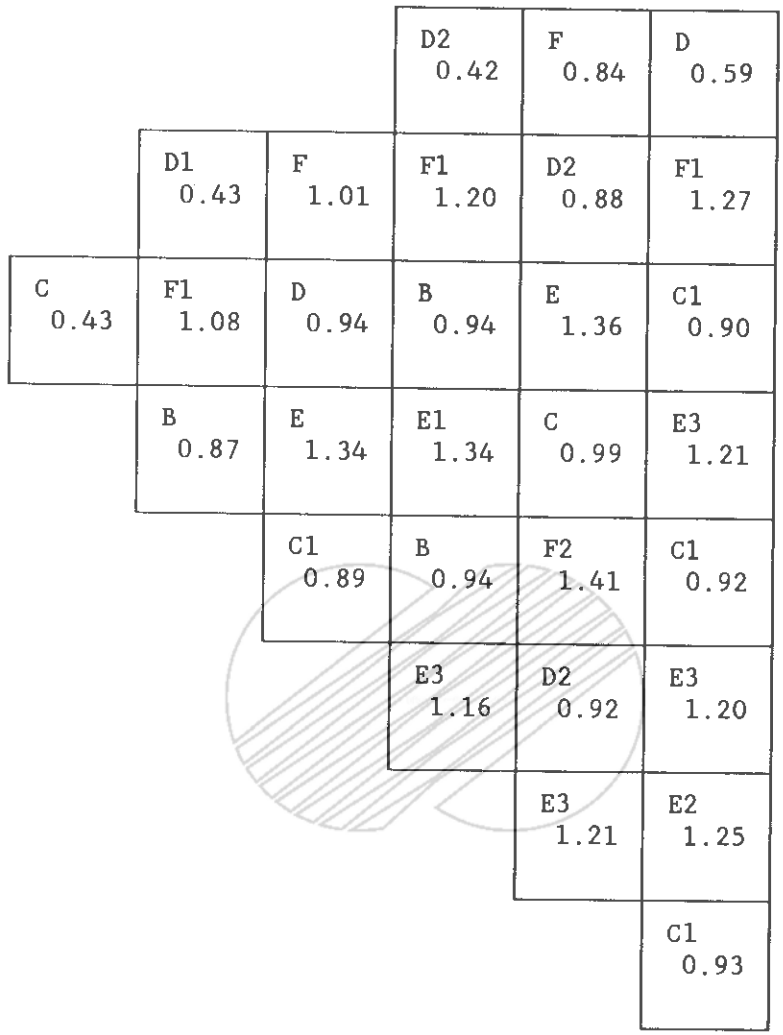

KOREA ELECTRIC POWER CORPORATION
YONGGWANG 3 & 4
FSAR

TYPICAL UNRODDED PLANER POWER DISTRIBUTION (BOX RELATIVE POWER DENSITY), CYCLE 3 AT 6,000 MWd/MTU
Figure 4.3-30

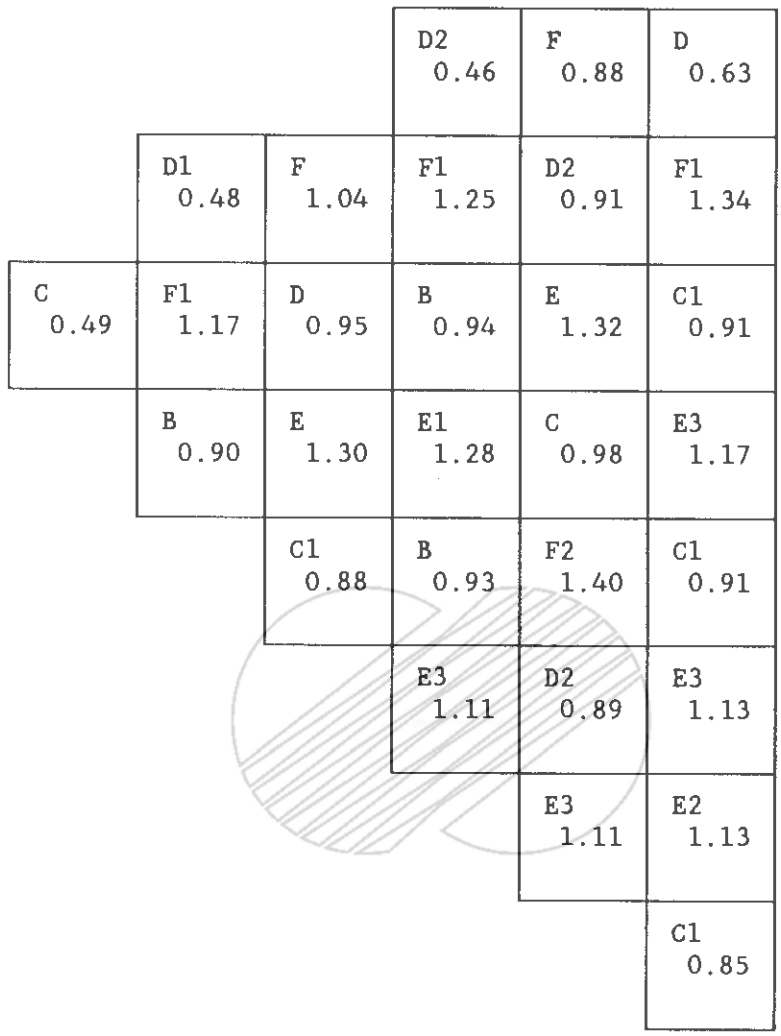

KOREA ELECTRIC POWER CORPORATION
YONGGWANG 3 & 4
FSAR

TYPICAL UNRODDED PLANER POWER DISTRIBUTION (BOX RELATIVE POWER DENSITY), CYCLE 3 AT EOC
Figure 4.3-31

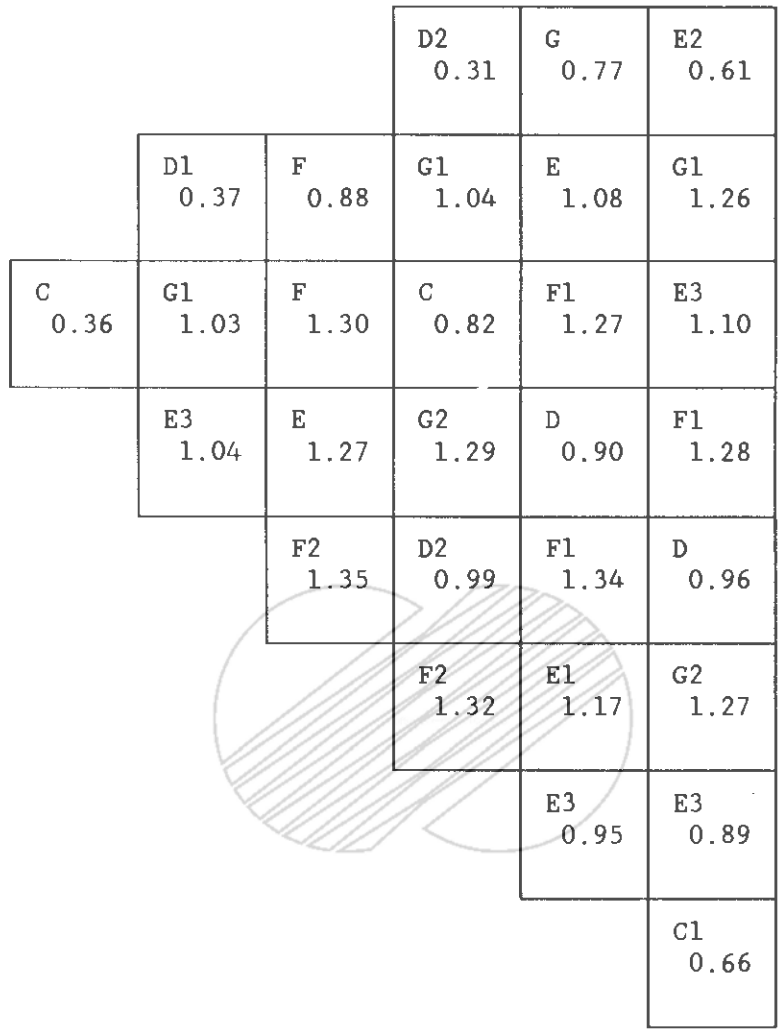

KOREA ELECTRIC POWER CORPORATION
YONGGWANG 3 & 4
FSAR

TYPICAL UNRODDED PLANER POWER DISTRIBUTION (BOX RELATIVE POWER DENSITY), CYCLE 4 AT 0 MWd/MTU
Figure 4.3-32

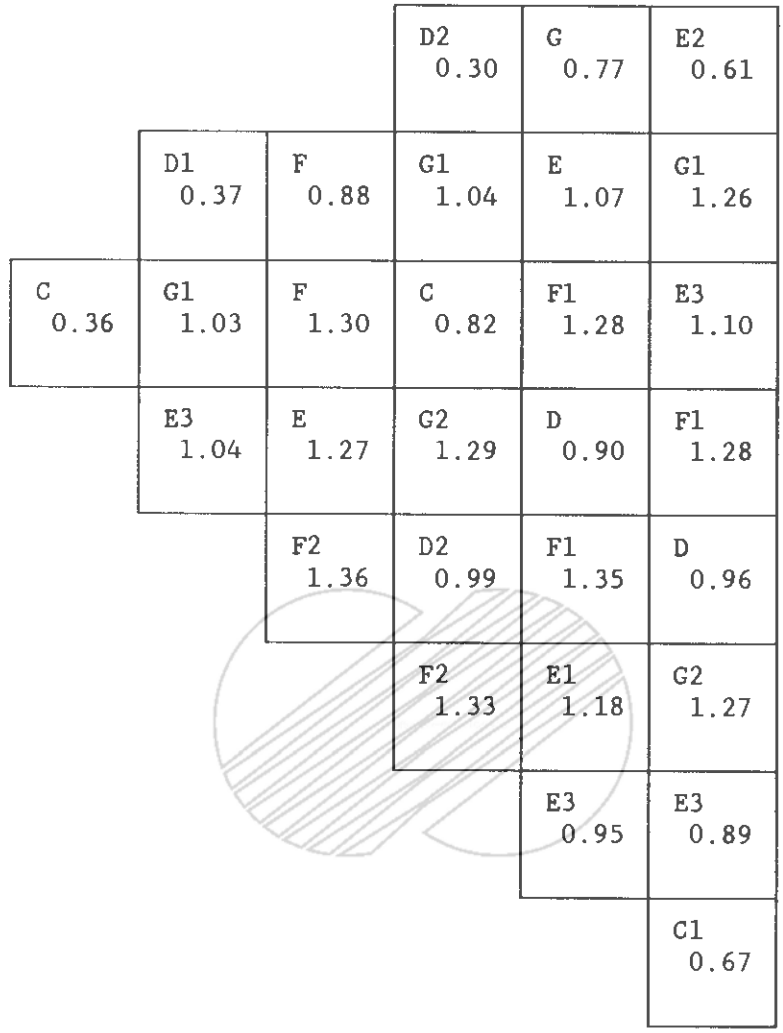

KOREA ELECTRIC POWER CORPORATION
YONGGWANG 3 & 4
FSAR

TYPICAL UNRODDED PLANER POWER DISTRIBUTION (BOX RELATIVE POWER DENSITY), CYCLE 4 AT 50 MWd/MTU
Figure 4.3-33

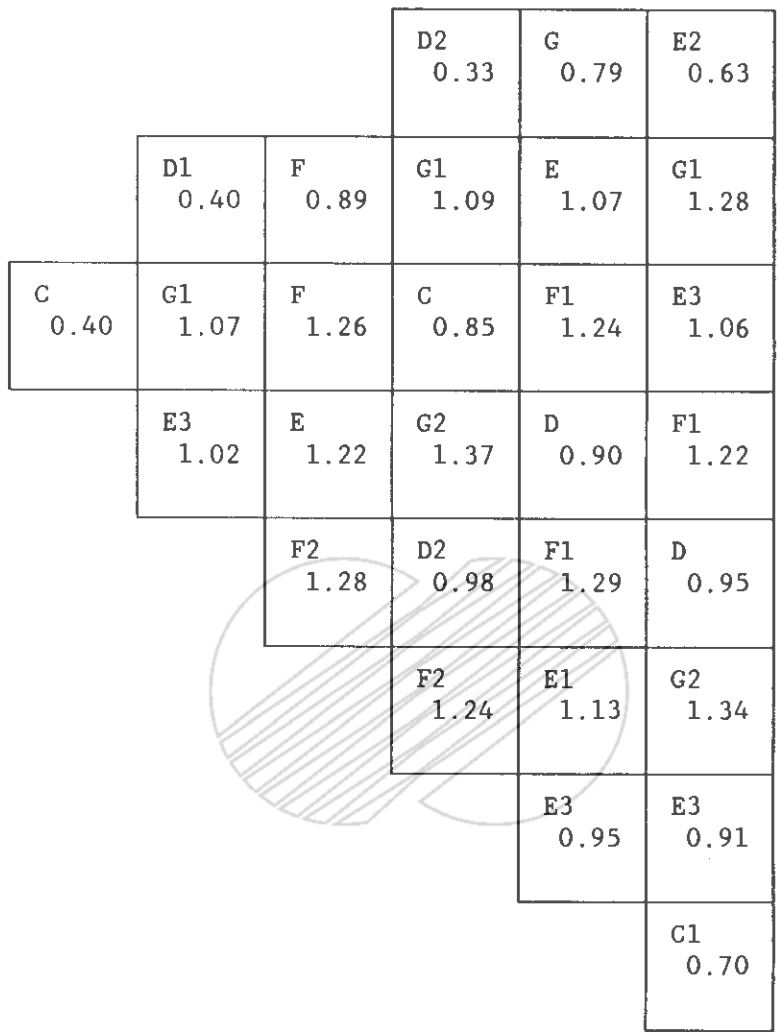

KOREA ELECTRIC POWER CORPORATION
YONGGWANG 3 & 4
FSAR

TYPICAL UNRODDED PLANER POWER DISTRIBUTION (BOX RELATIVE POWER DENSITY), CYCLE 4 AT 6,000 MWd/MTU
Figure 4.3-34

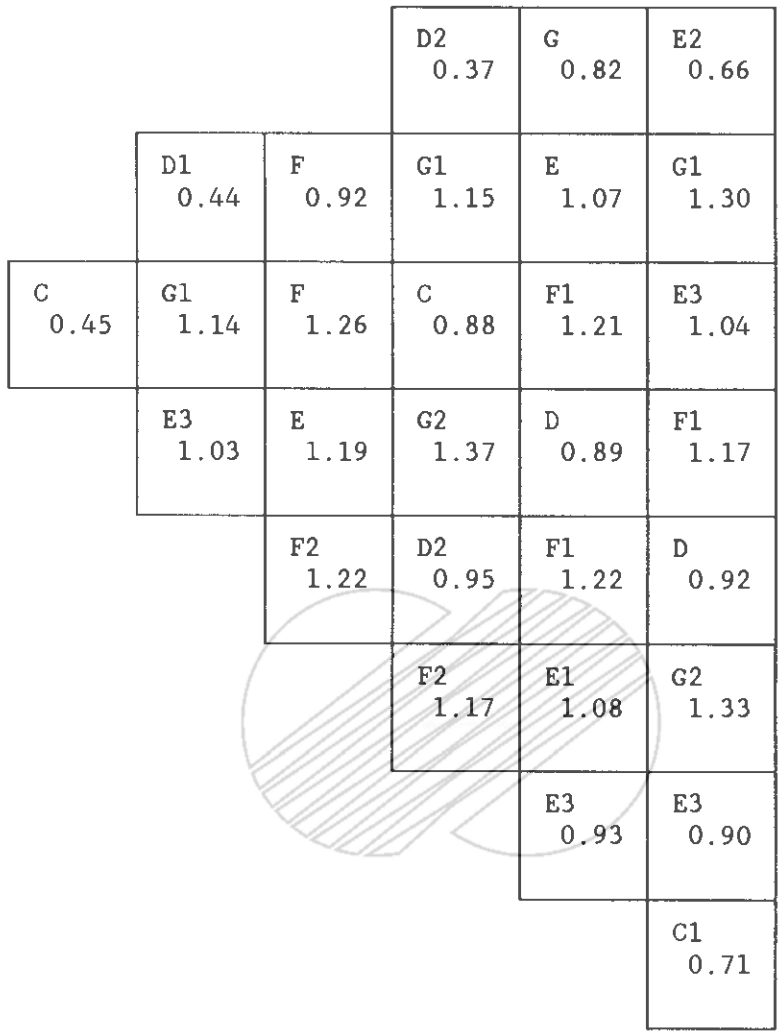

KOREA ELECTRIC POWER CORPORATION
YONGGWANG 3 & 4
FSAR

TYPICAL UNRODDED PLANER POWER DISTRIBUTION (BOX RELATIVE POWER DENSITY), CYCLE 4 AT EOC
Figure 4.3-35

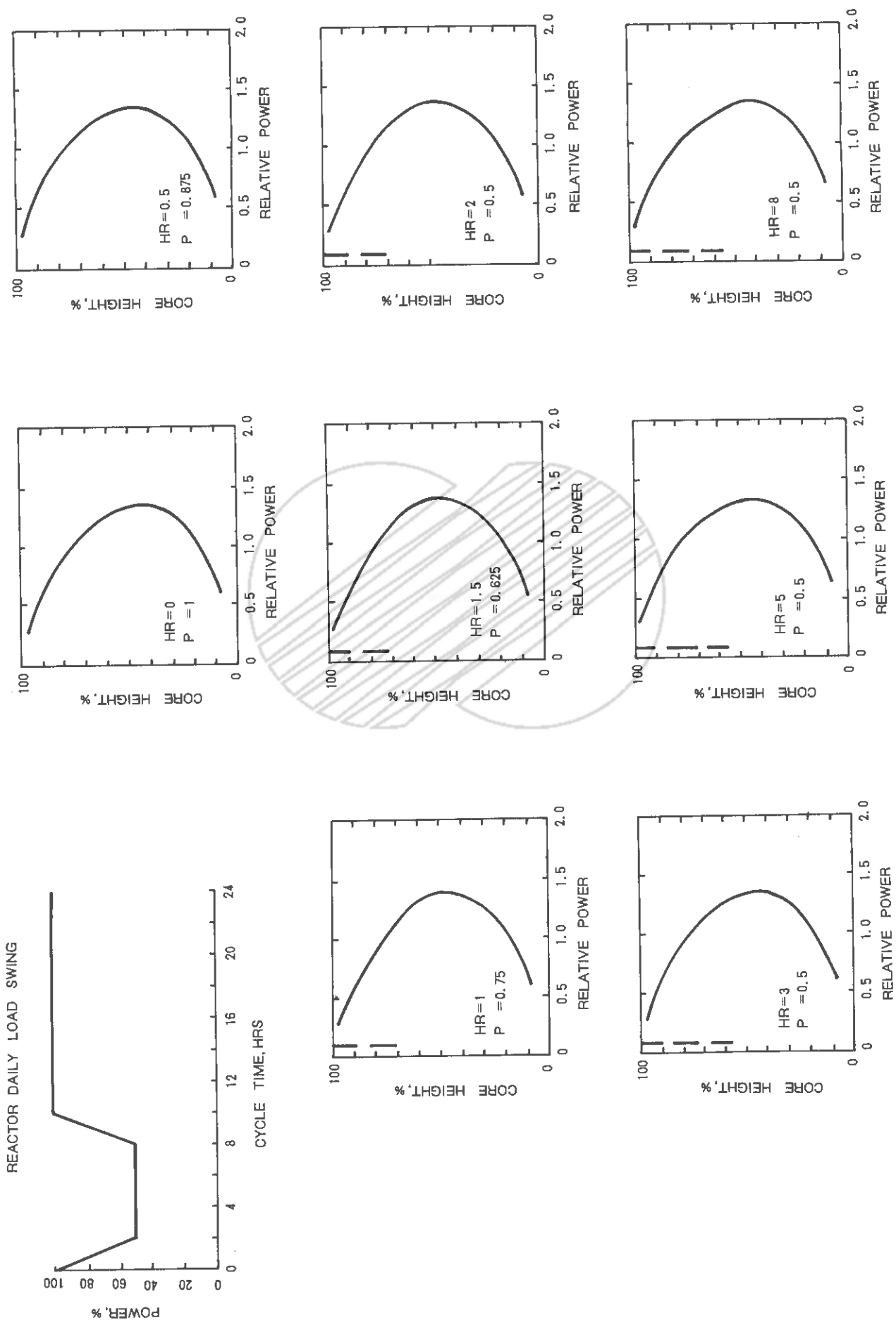

KOREA ELECTRIC POWER CORPORATION
YONGGWANG 3 & 4
FSAR

DAILY LOAD-CYCLE MANEUVERING TRANSIENT
AT BOC (100% TO 50% TO 100% POWER,
0-8 HOURS)

Figure 4.3-36

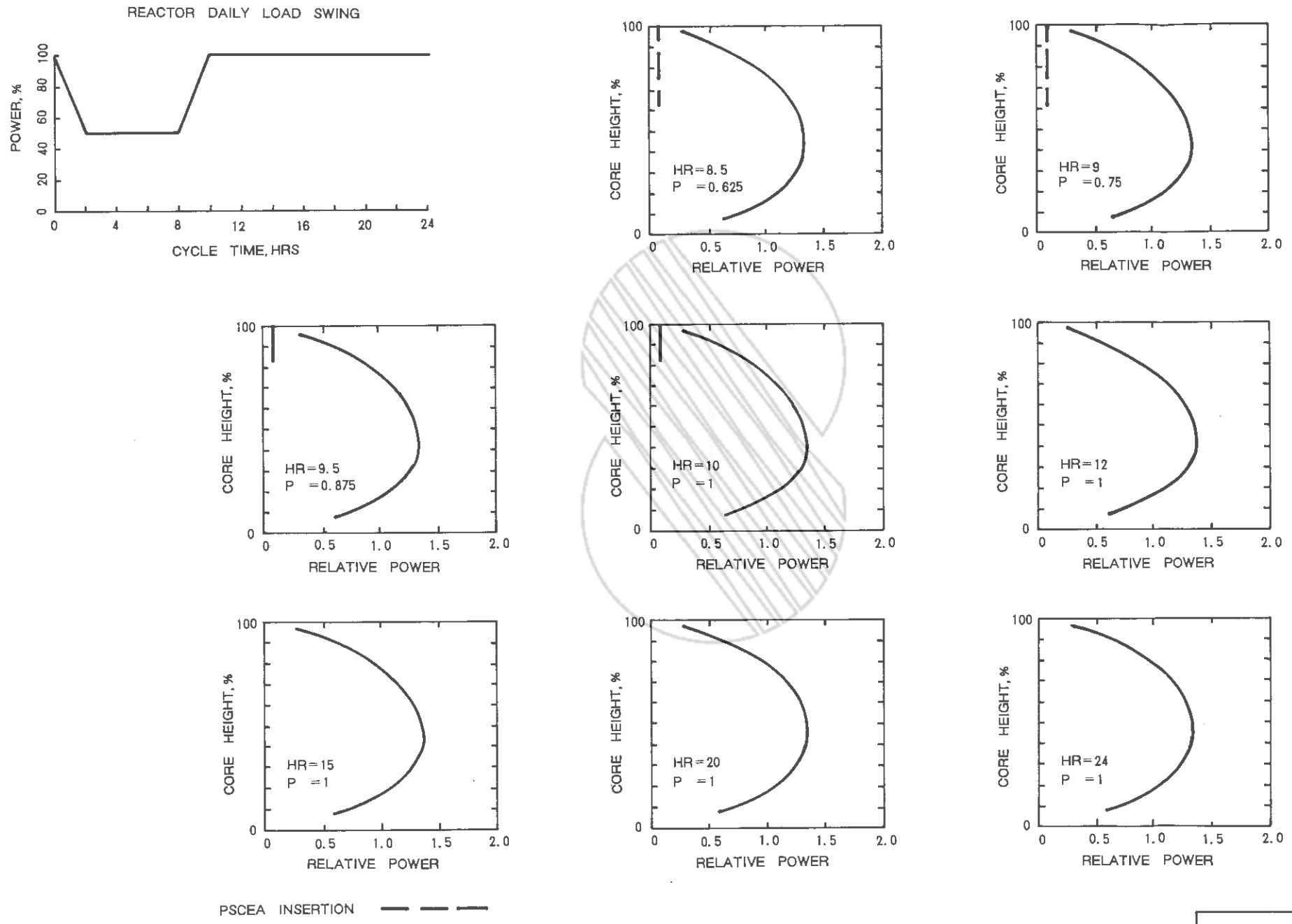

KOREA ELECTRIC POWER CORPORATION
YONGGWANG 3 & 4
FSAR

DAILY LOAD-CYCLE MANEUVERING TRANSIENT AT BOC (100% TO 50% TO 100% POWER, 8-24 HOURS)

Figure 4.3-37

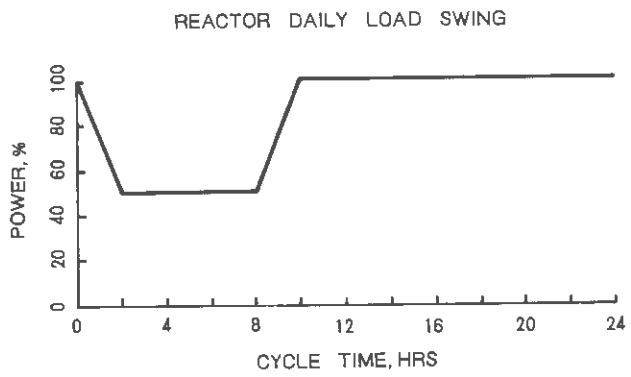

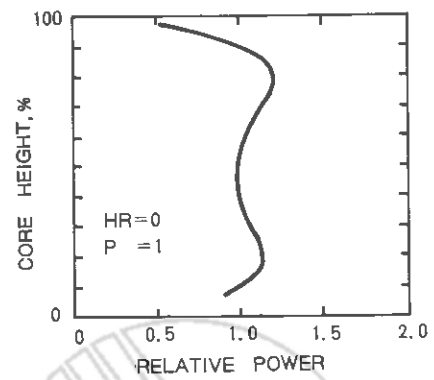

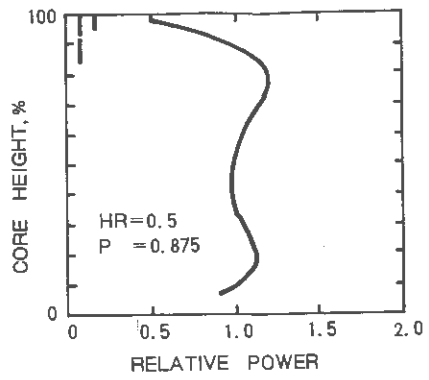

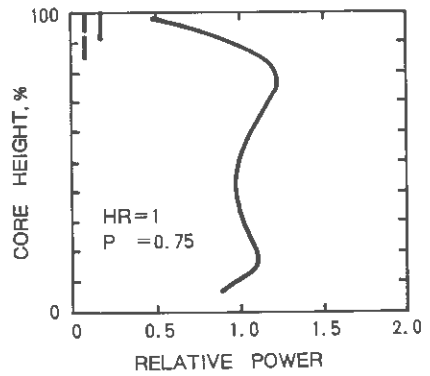

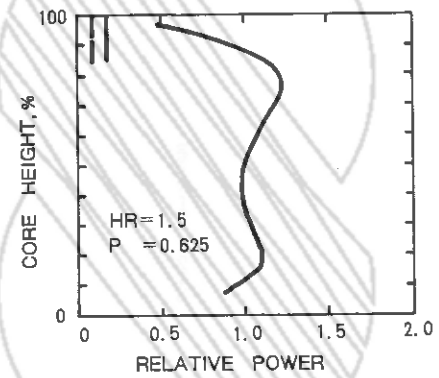

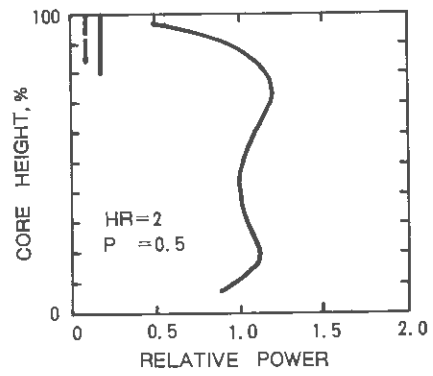

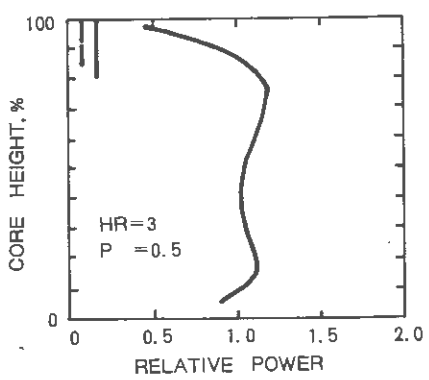

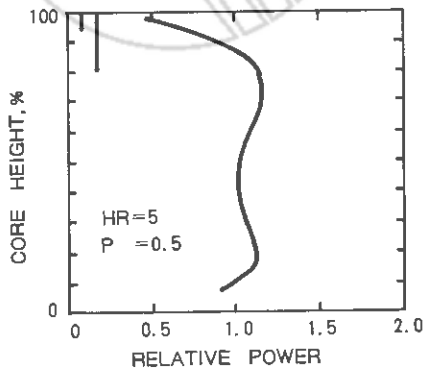

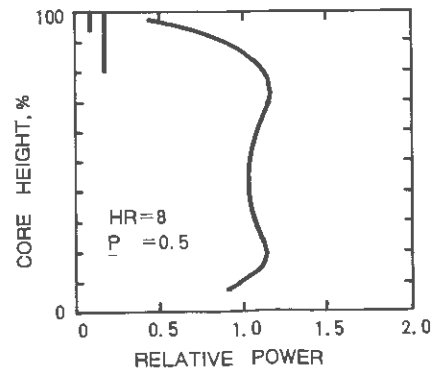

PSCEA INSERTION — — —

BANK 5 INSERTION ———

KOREA ELECTRIC POWER CORPORATION
YONGGWANG 3 & 4
FSAR

DAILY LOAD-CYCLE MANEUVERING TRANSIENT AT MOC (100% TO 50% TO 100% POWER, 0-8 HOURS)

Figure 4.3-38

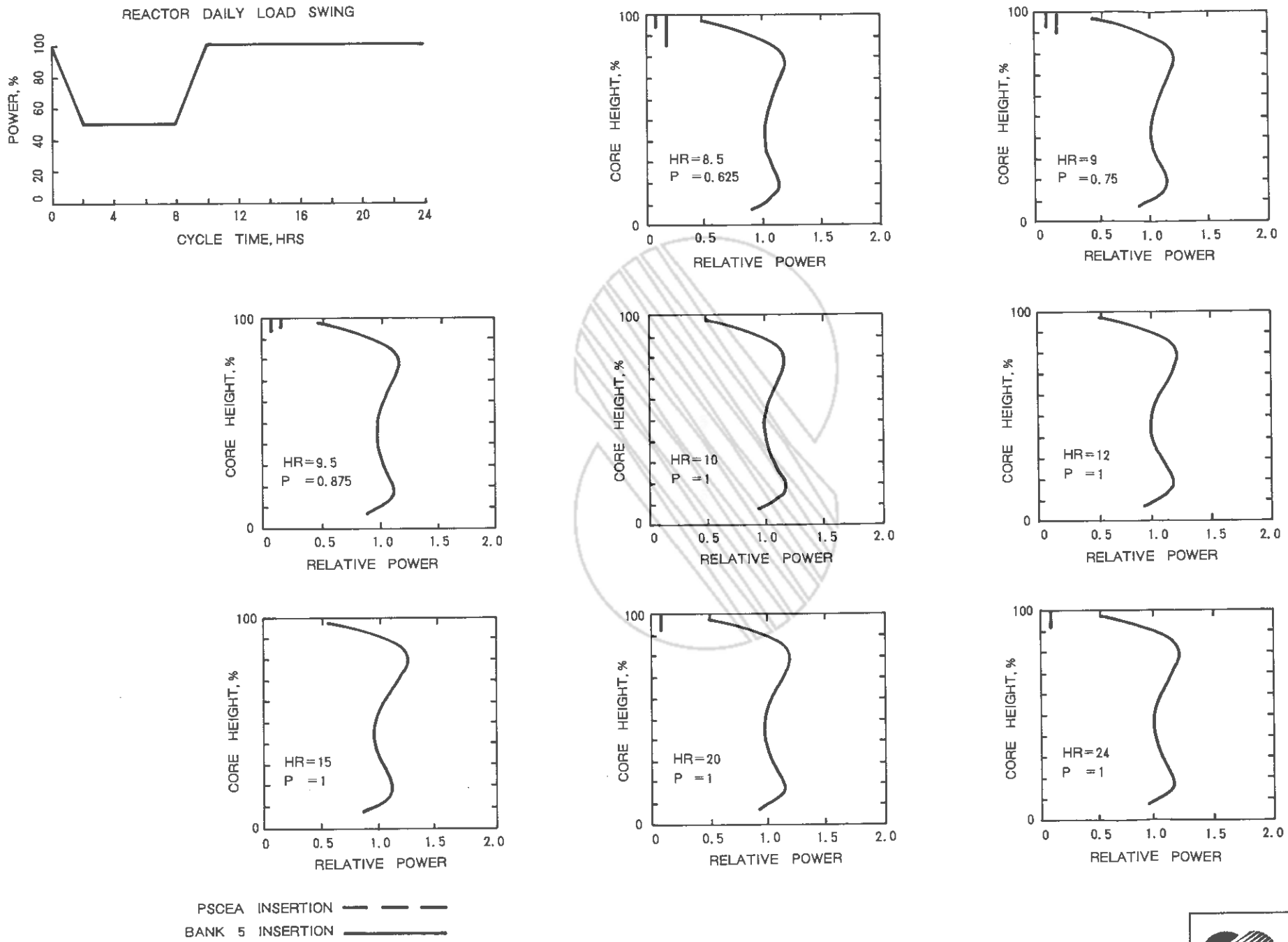

KOREA ELECTRIC POWER CORPORATION
YONGGWANG 3 & 4
FSAR

DAILY LOAD-CYCLE MANEUVERING TRANSIENT AT MOC (100% TO 50% TO 100% POWER, 8-24 HOURS)

Figure 4.3-39

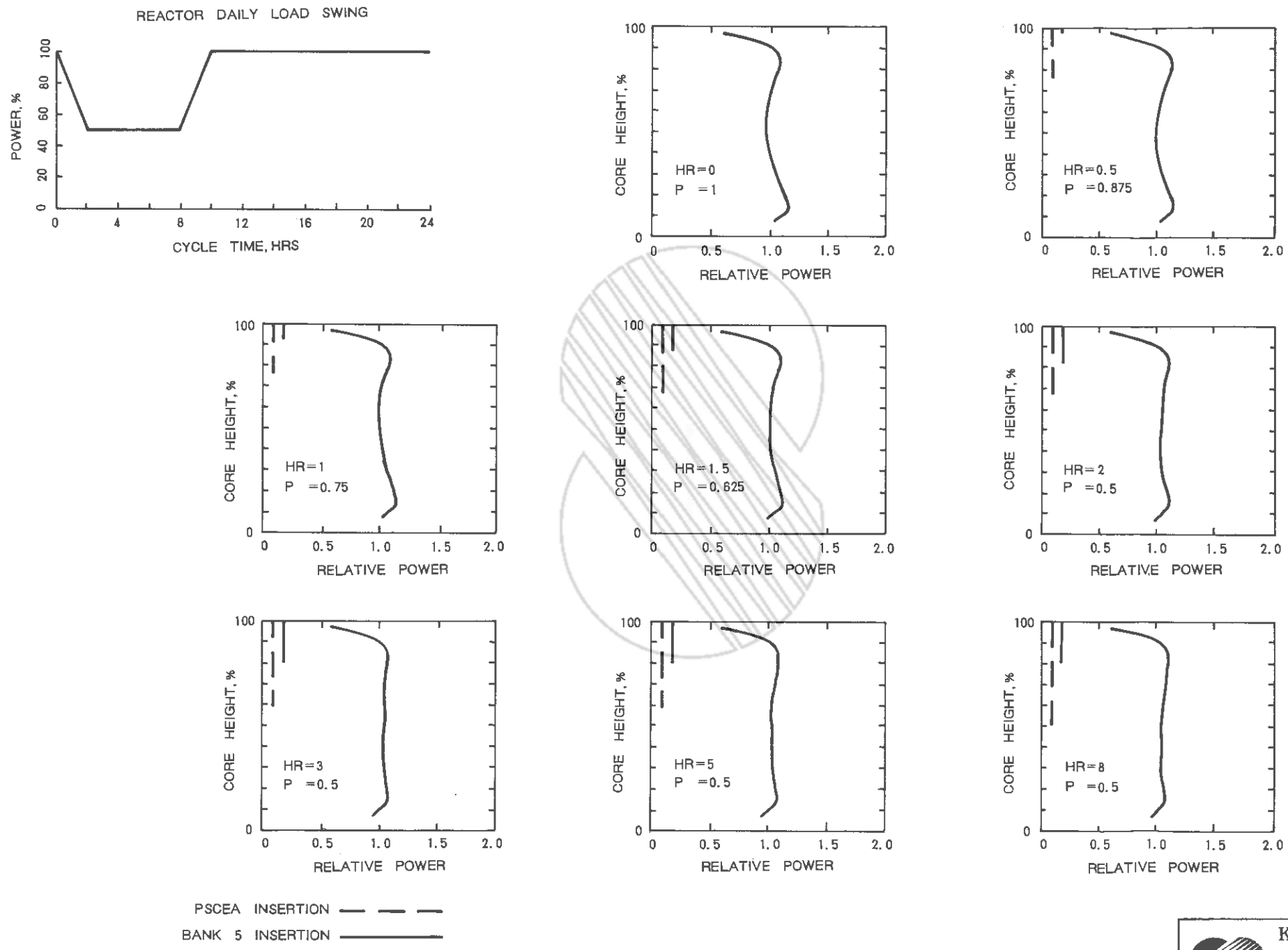

KOREA ELECTRIC POWER CORPORATION
YONGGWANG 3 & 4
FSAR

DAILY LOAD-CYCLE MANEUVERING TRANSIENT NEAR EOC (100% TO 50% TO 100% POWER, 0-8 HOURS)

Figure 4.3-40

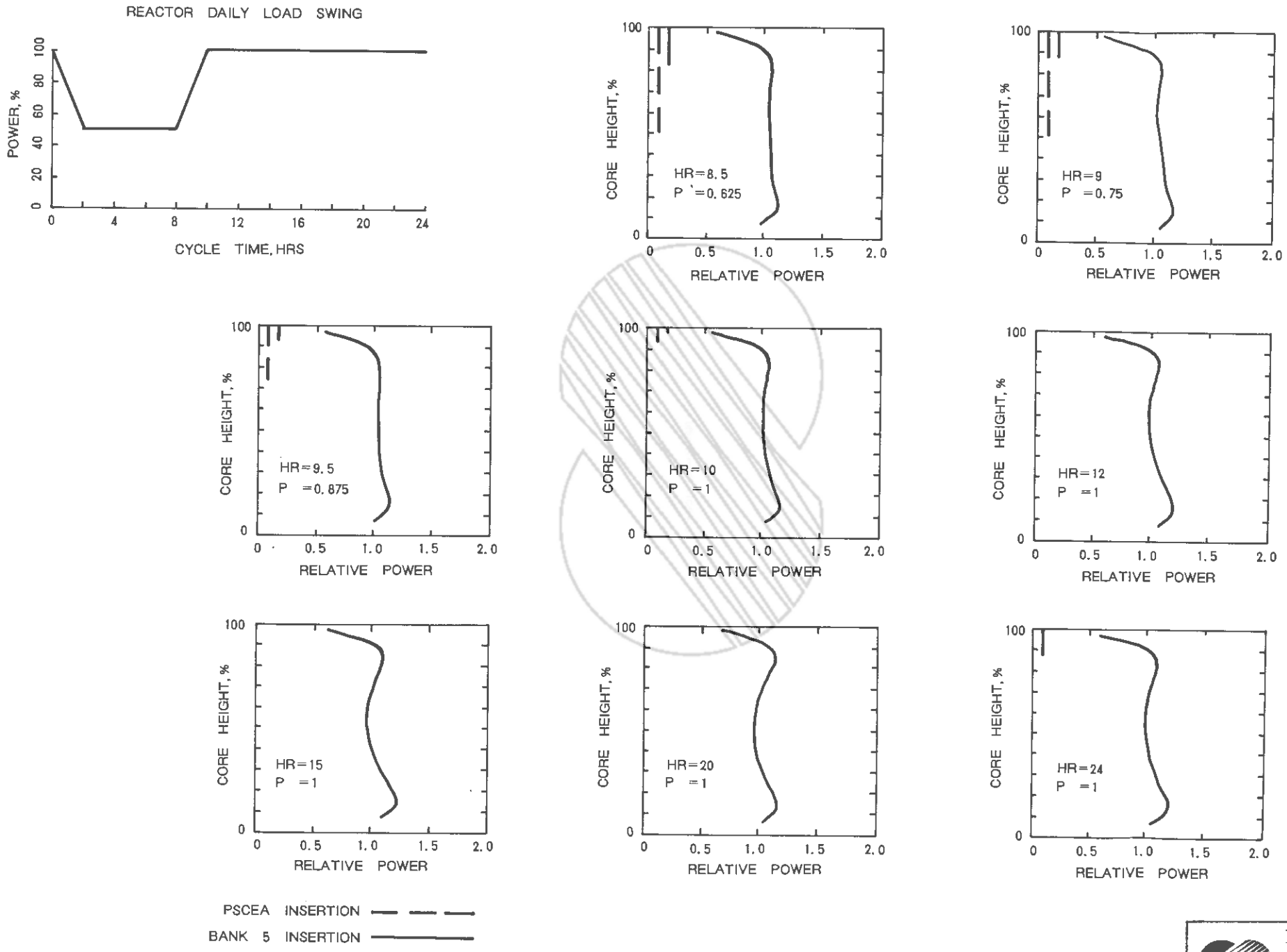

KOREA ELECTRIC POWER CORPORATION
YONGGWANG 3 & 4
FSAR

DAILY LOAD-CYCLE MANEUVERING TRANSIENT NEAR EOC (100% TO 50% TO 100% POWER, 8-24 HOURS)

Figure 4.3-41

Amendment 1
October 1994

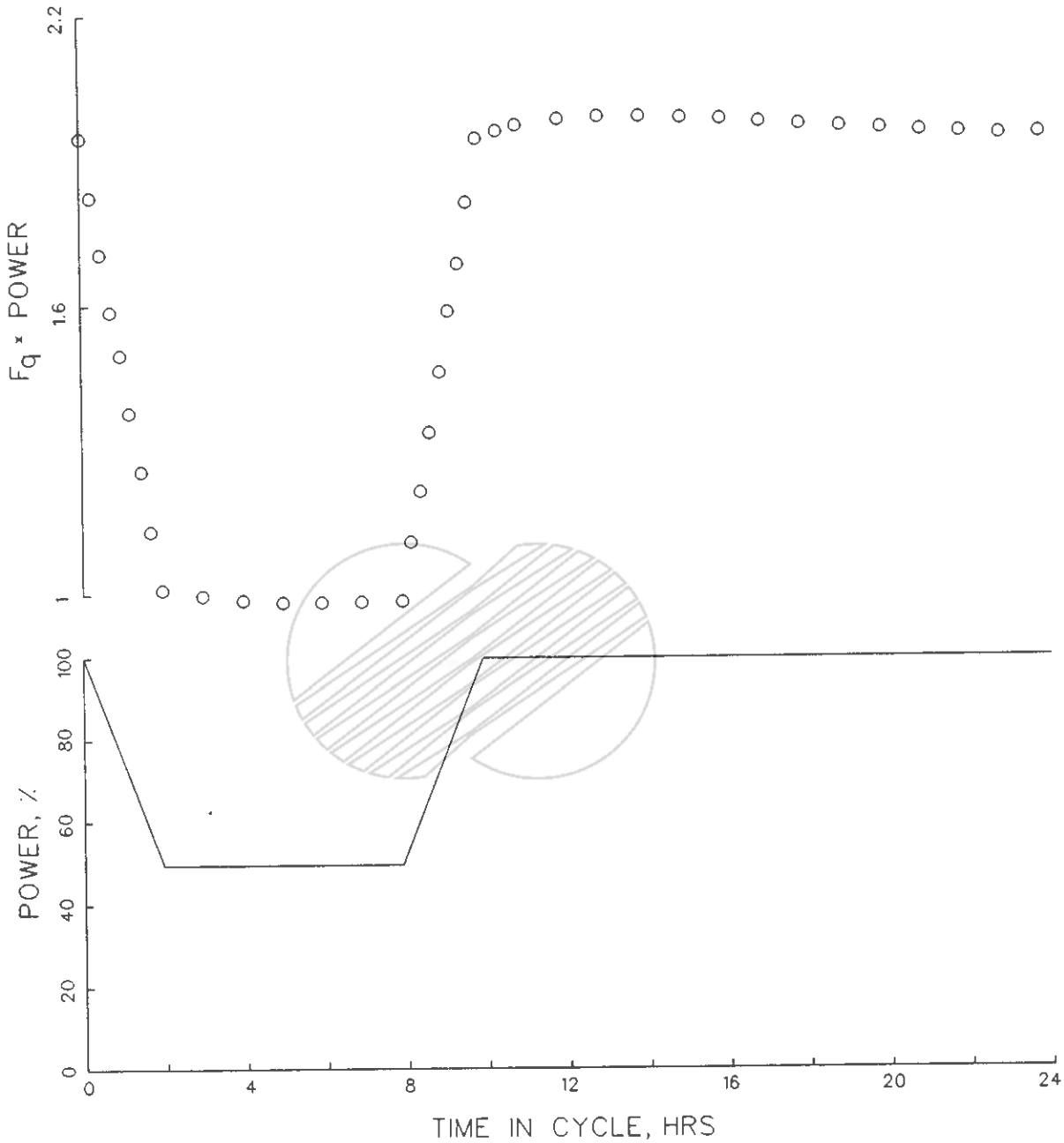

KOREA ELECTRIC POWER CORPORATION
YONGGWANG 3 & 4
FSAR

F_q VS. TIME DURING DAILY LOAD CYCLE
AT BOC
(Sheet 1 of 3)

Figure 4.3-42

Amendment 1
October 1994

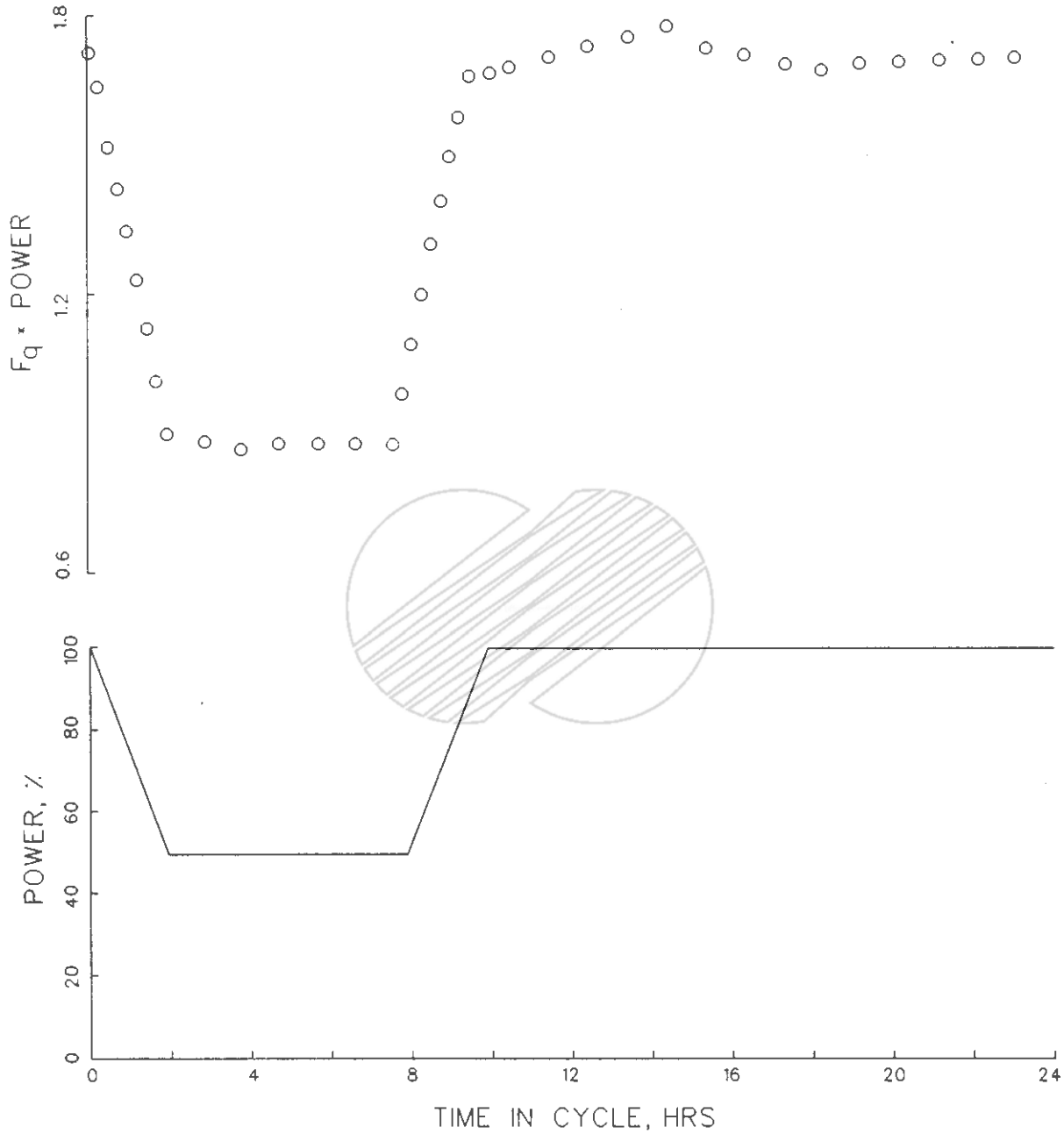

KOREA ELECTRIC POWER CORPORATION
YONGGWANG 3 & 4
FSAR

F_q VS. TIME DURING DAILY LOAD CYCLE
AT MOC
(Sheet 2 of 3)

Figure 4.3-42

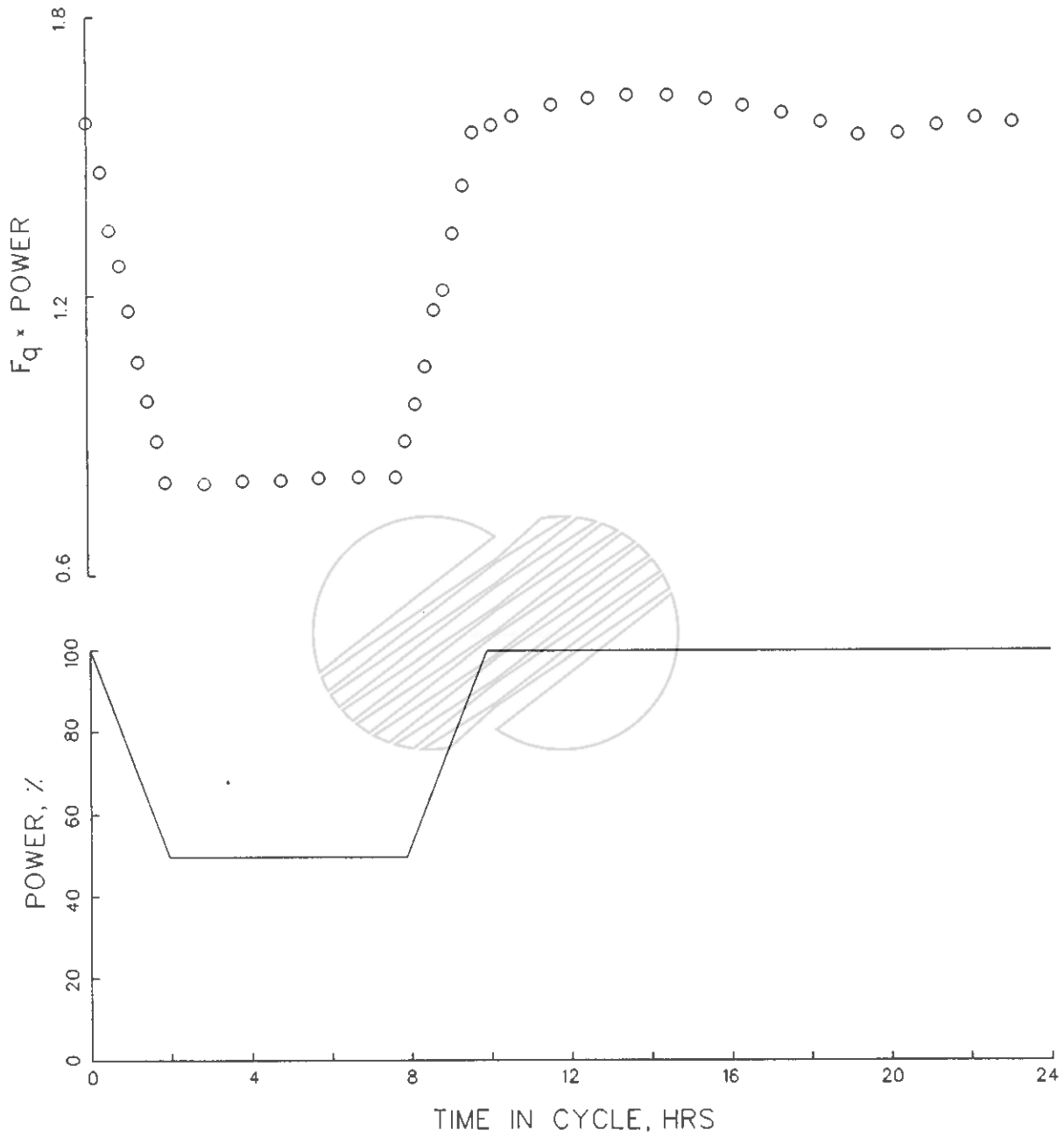

KOREA ELECTRIC POWER CORPORATION
YONGGWANG 3 & 4
FSAR

F_q VS. TIME DURING DAILY LOAD CYCLE
NEAR EOC
(Sheet 3 of 3)

Figure 4.3-42

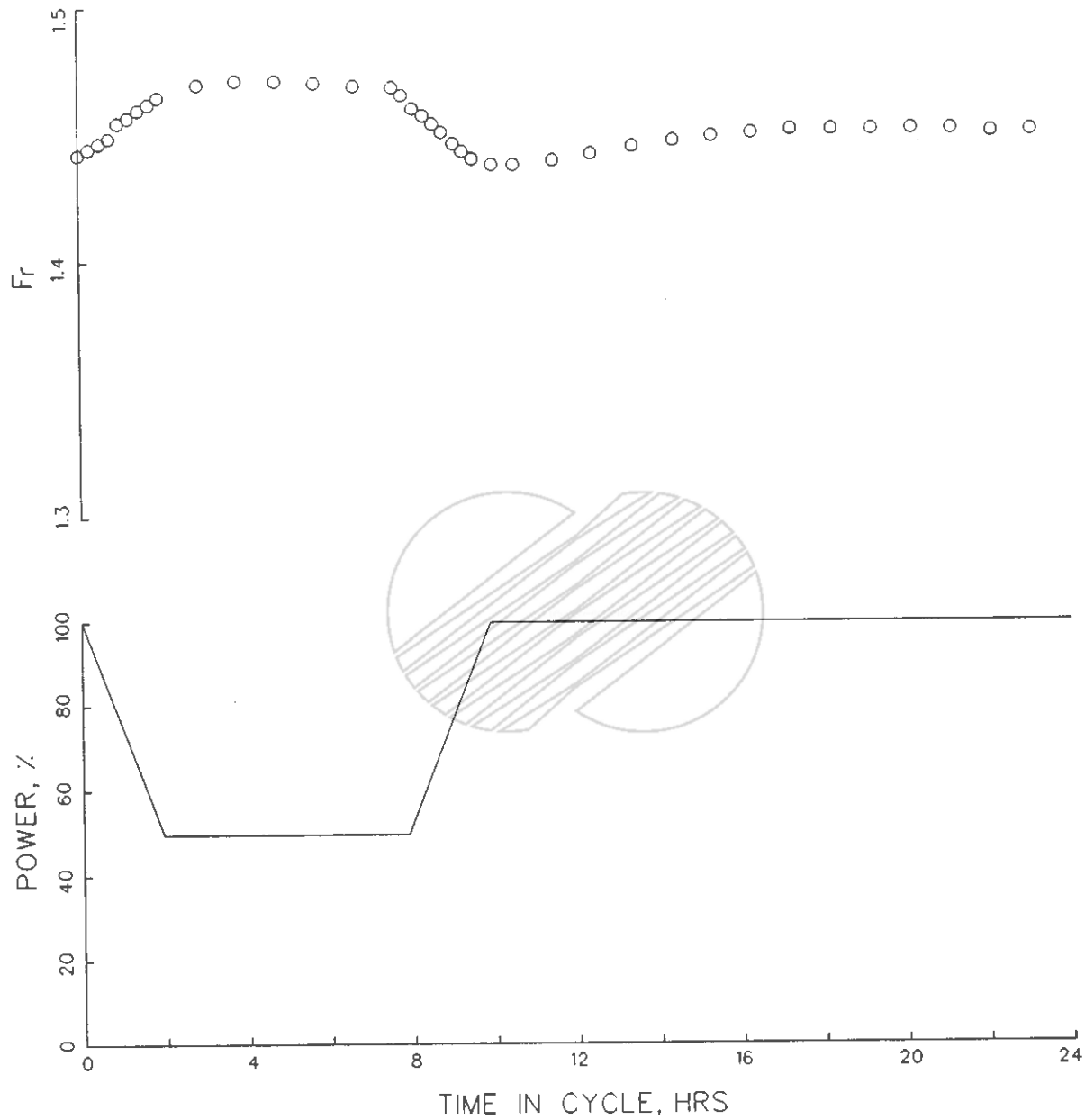

KOREA ELECTRIC POWER CORPORATION
YONGGWANG 3 & 4
FSAR

F_r VS. TIME DURING DAILY LOAD CYCLE
AT BOC
(Sheet 1 of 3)

Figure 4.3-43

Amendment 1
October 1994

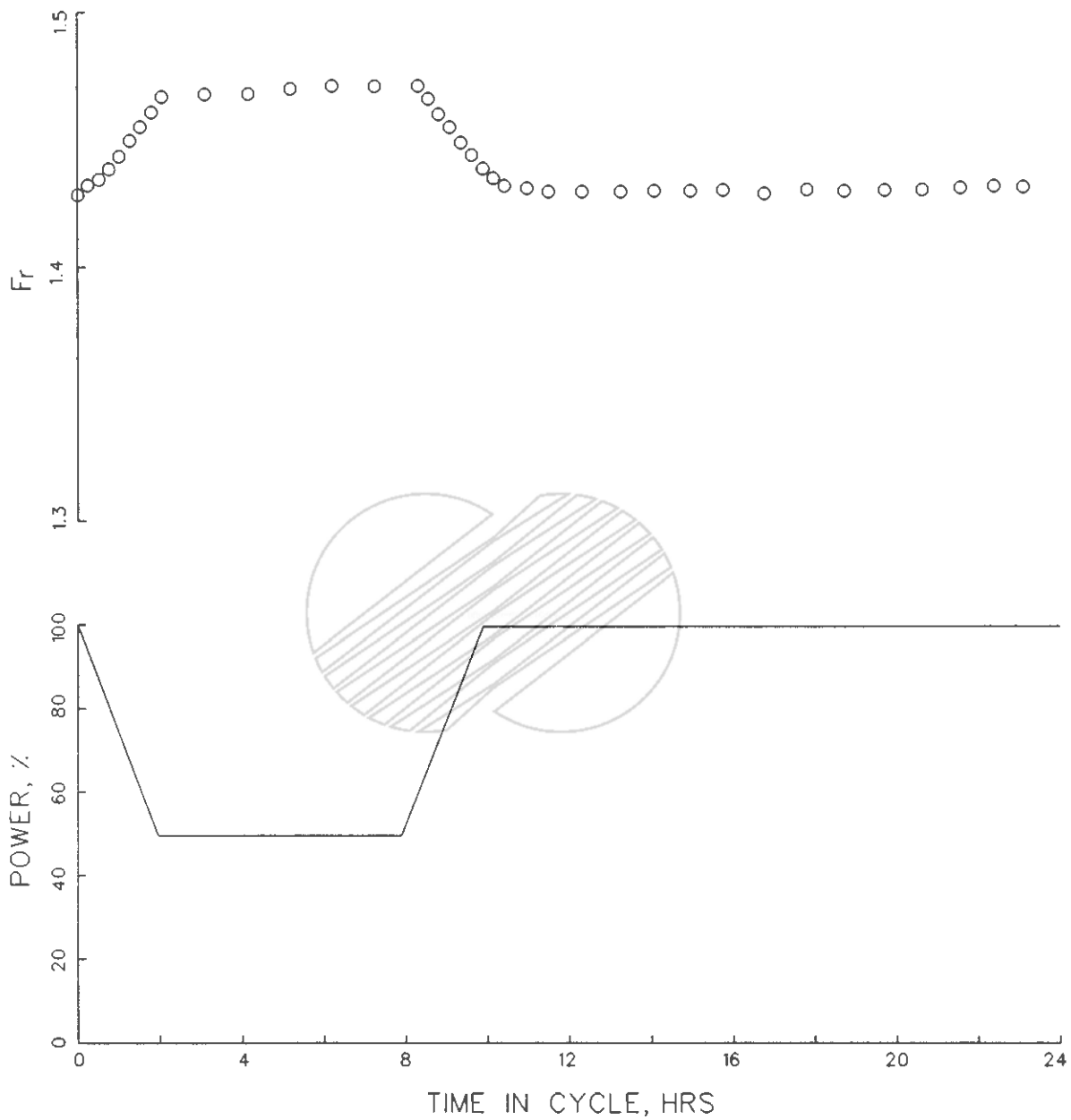

KOREA ELECTRIC POWER CORPORATION
YONGGWANG 3 & 4
FSAR

F_r VS. TIME DURING DAILY LOAD CYCLE
AT MOC
(Sheet 2 of 3)

Figure 4.3-43

Amendment 1
October 1994

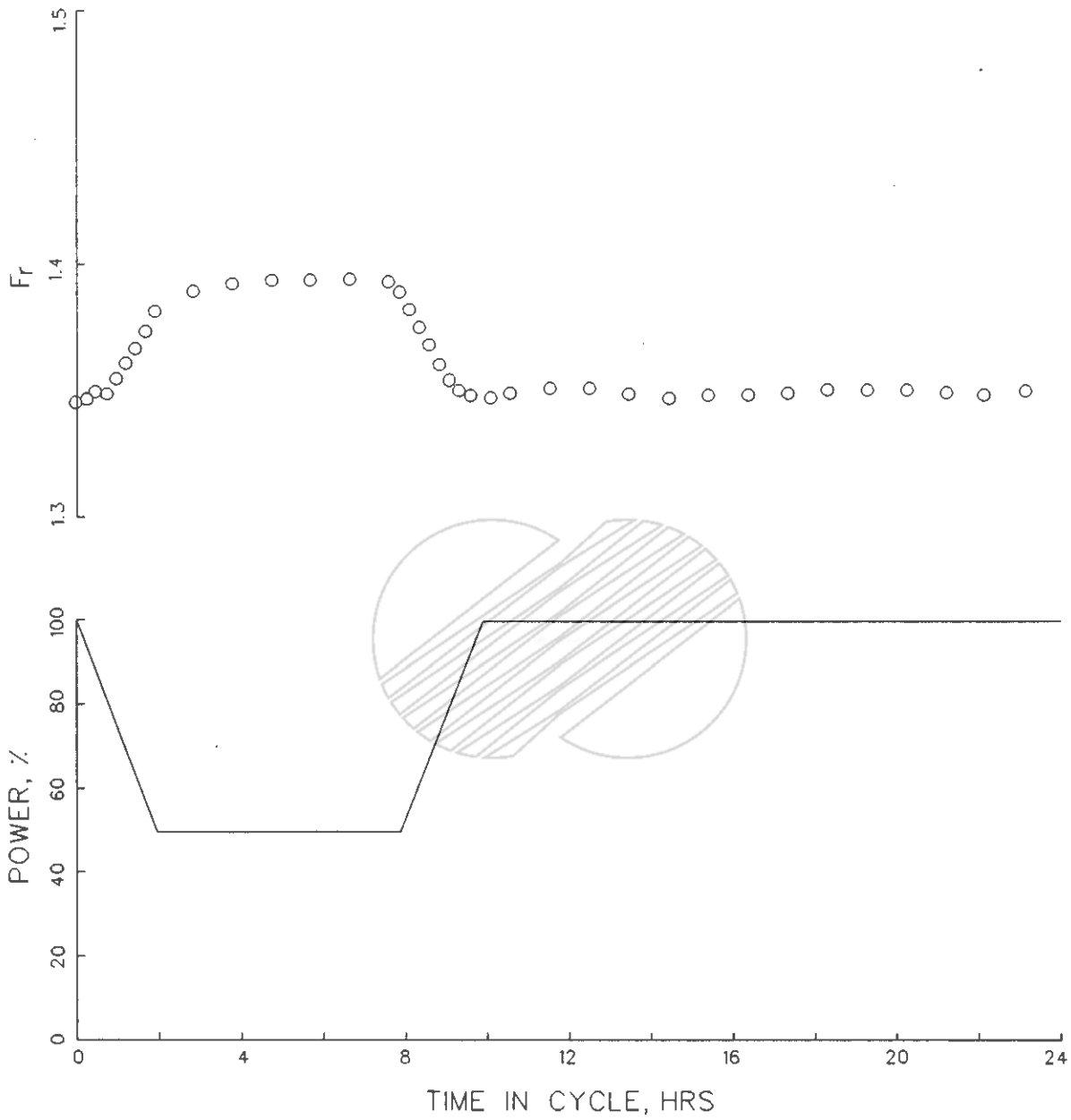

KOREA ELECTRIC POWER CORPORATION
YONGGWANG 3 & 4
FSAR

F_r VS. TIME DURING DAILY LOAD CYCLE
NEAR EOC
(Sheet 3 of 3)

Figure 4.3-43

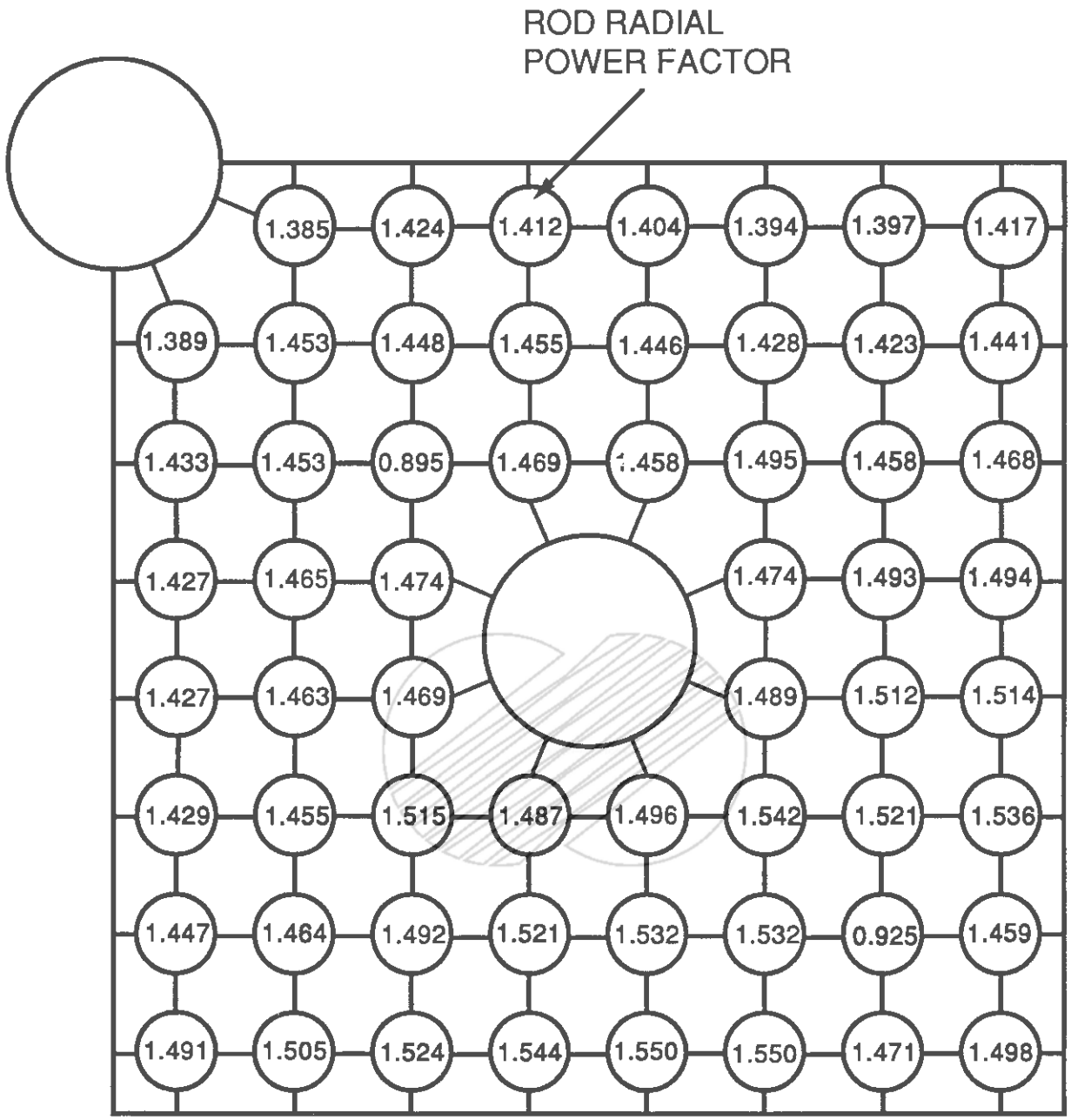

KOREA ELECTRIC POWER CORPORATION
YONGGWANG 3 & 4
FSAR

ROD RADIAL POWER FACTORS IN HOT ASSEMBLY FOR SAMPLE DNB ANALYSIS

Figure 4.3-44

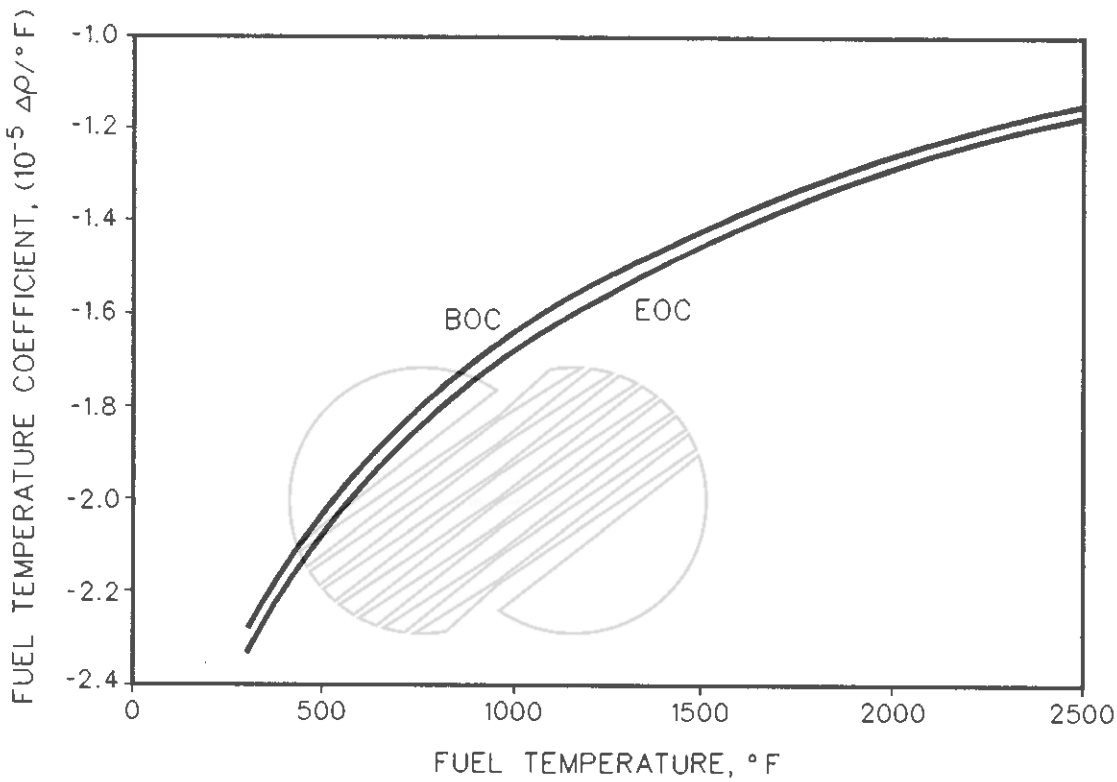

KOREA ELECTRIC POWER CORPORATION
YONGGWANG 3 & 4
FSAR

FUEL TEMPERATURE COEFFICIENT
VS. EFFECTIVE FUEL TEMPERATURE

Figure 4.3-45

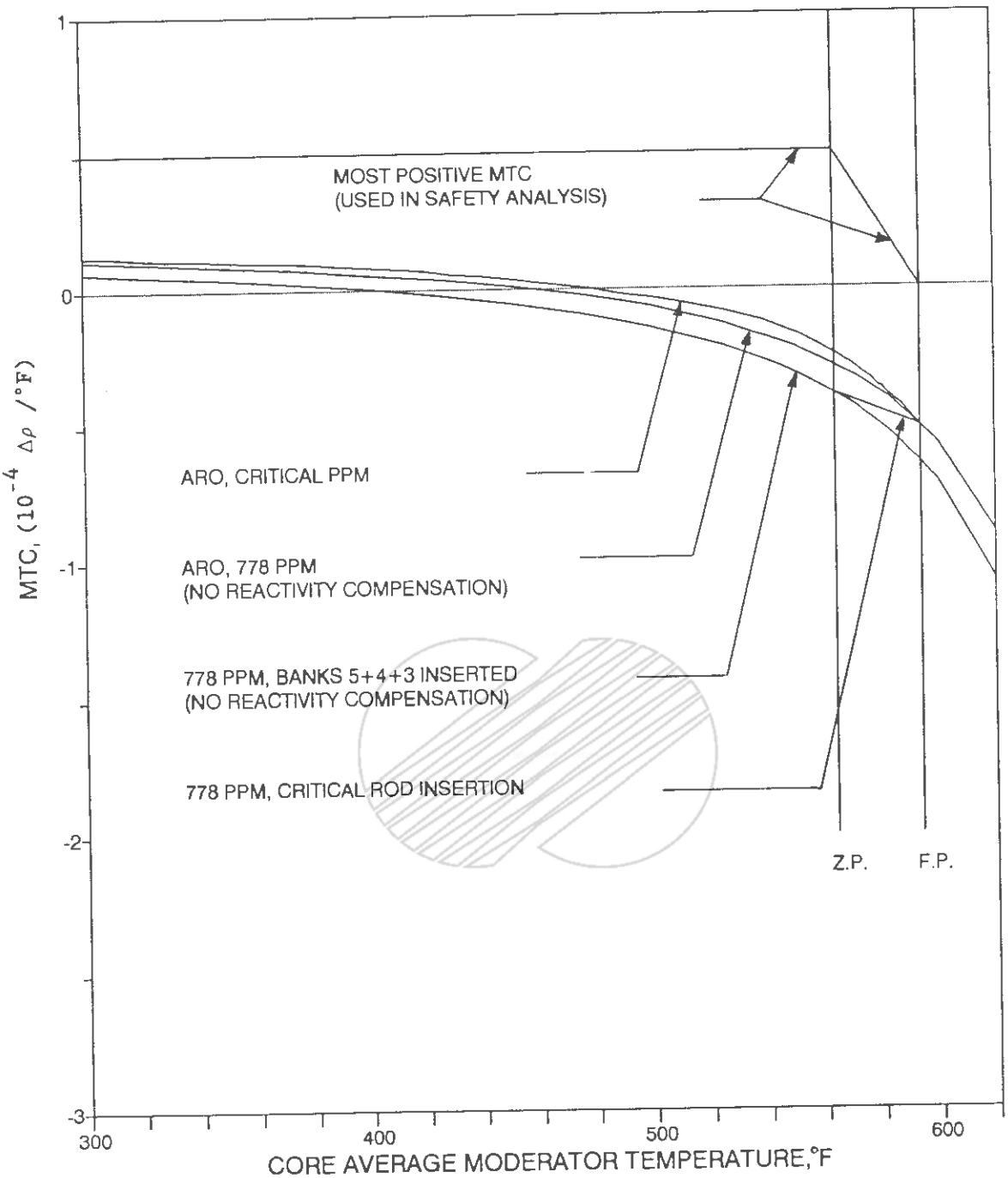

KOREA ELECTRIC POWER CORPORATION
YONGGWANG 3 & 4
FSAR

MODERATOR TEMPERATURE COEFFICIENT
VS. MODERATOR TEMPERATURE AT BOC 1,
HFP EQUILIBRIUM XENON AND
FUEL TEMPERATURE
Figure 4.3-46

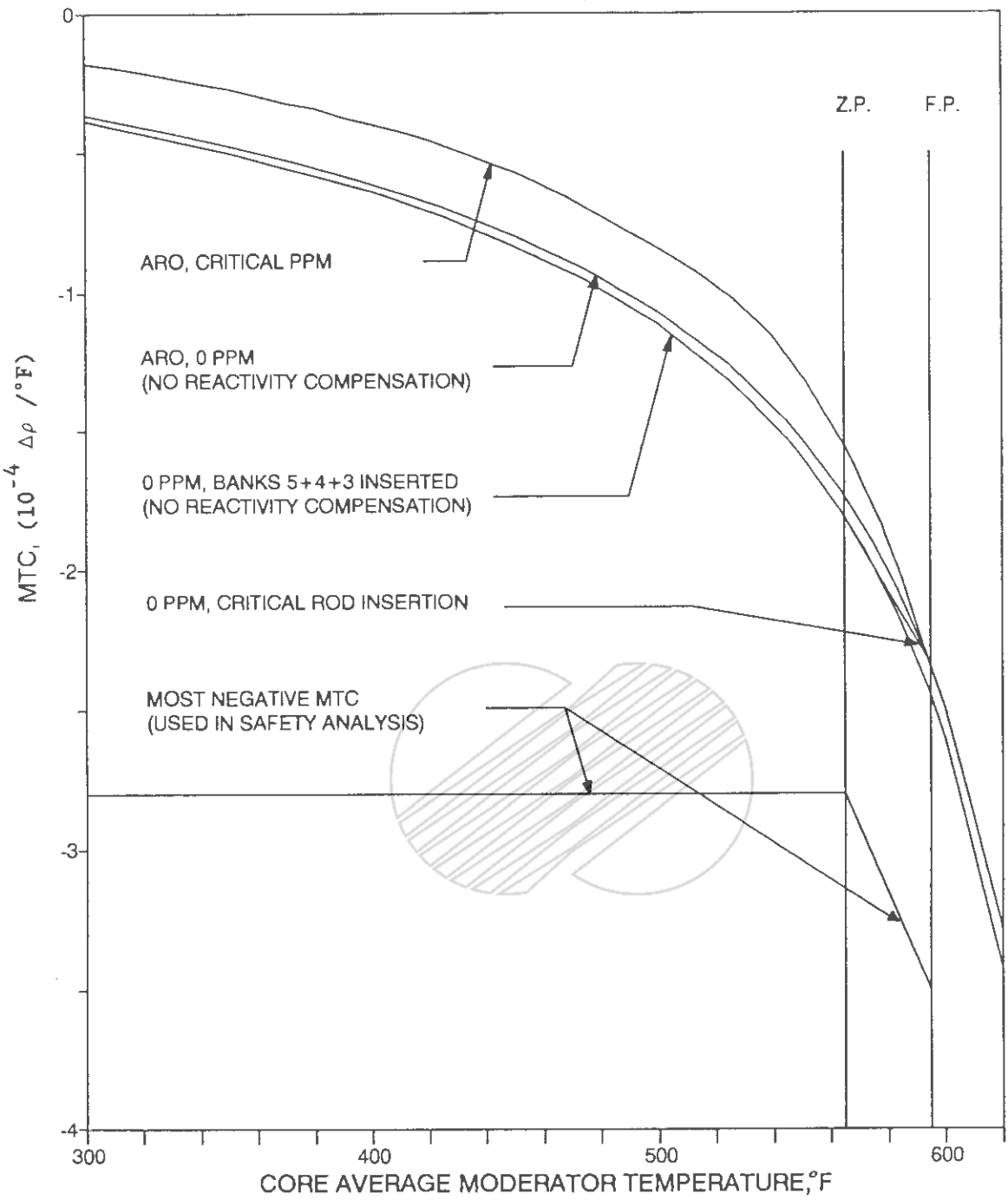

KOREA ELECTRIC POWER CORPORATION
YONGGWANG 3 & 4
FSAR

MODERATOR TEMPERATURE COEFFICIENT
VS. MODERATOR TEMPERATURE AT EOC 1,
HFP EQUILIBRIUM XENON AND
FUEL TEMPERATURE
Figure 4.3-47

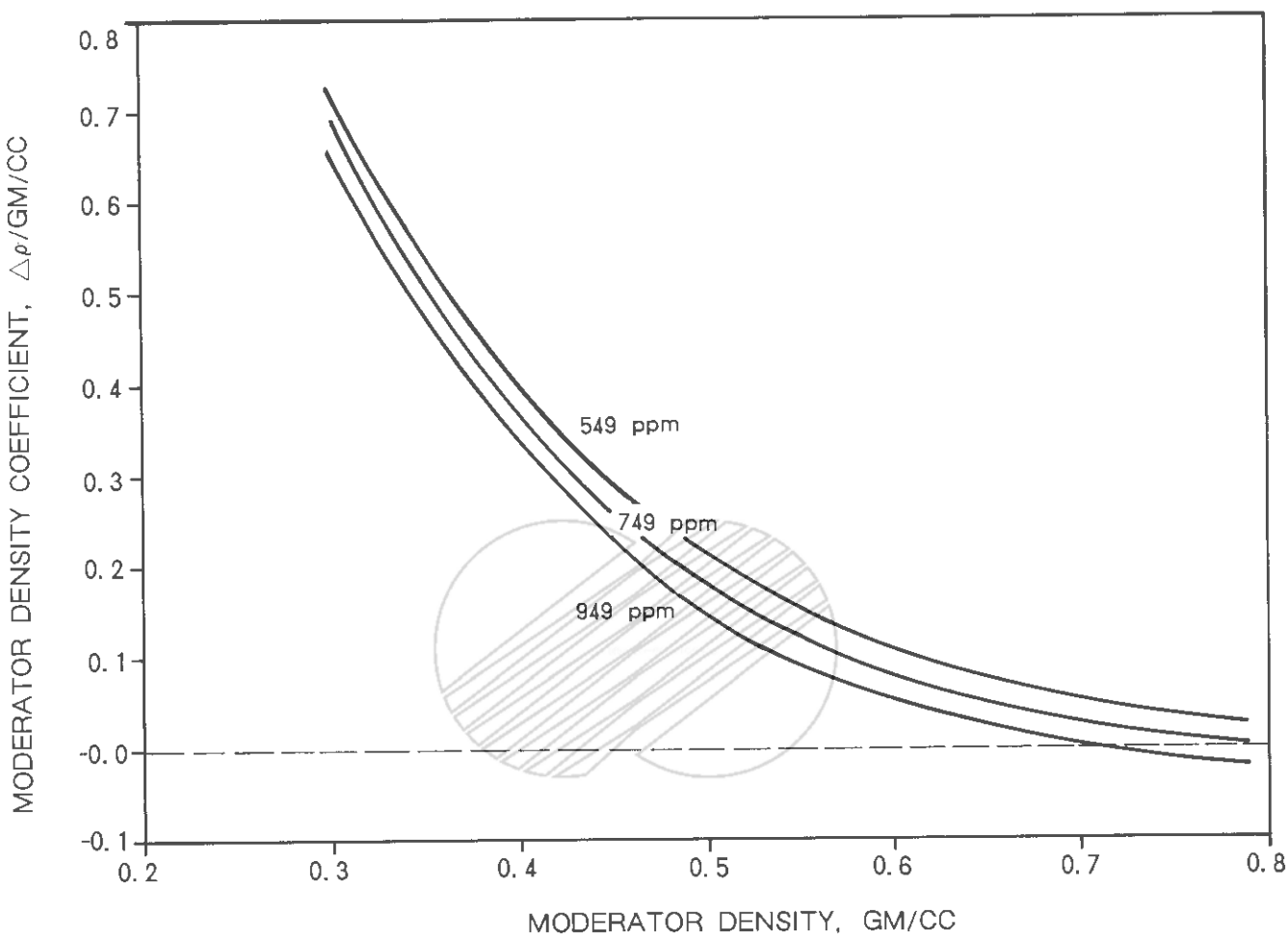

KOREA ELECTRIC POWER CORPORATION
YONGGWANG 3 & 4
FSAR

MODERATOR DENSITY COEFFICIENT
VS. MODERATOR DENSITY

Figure 4.3-48

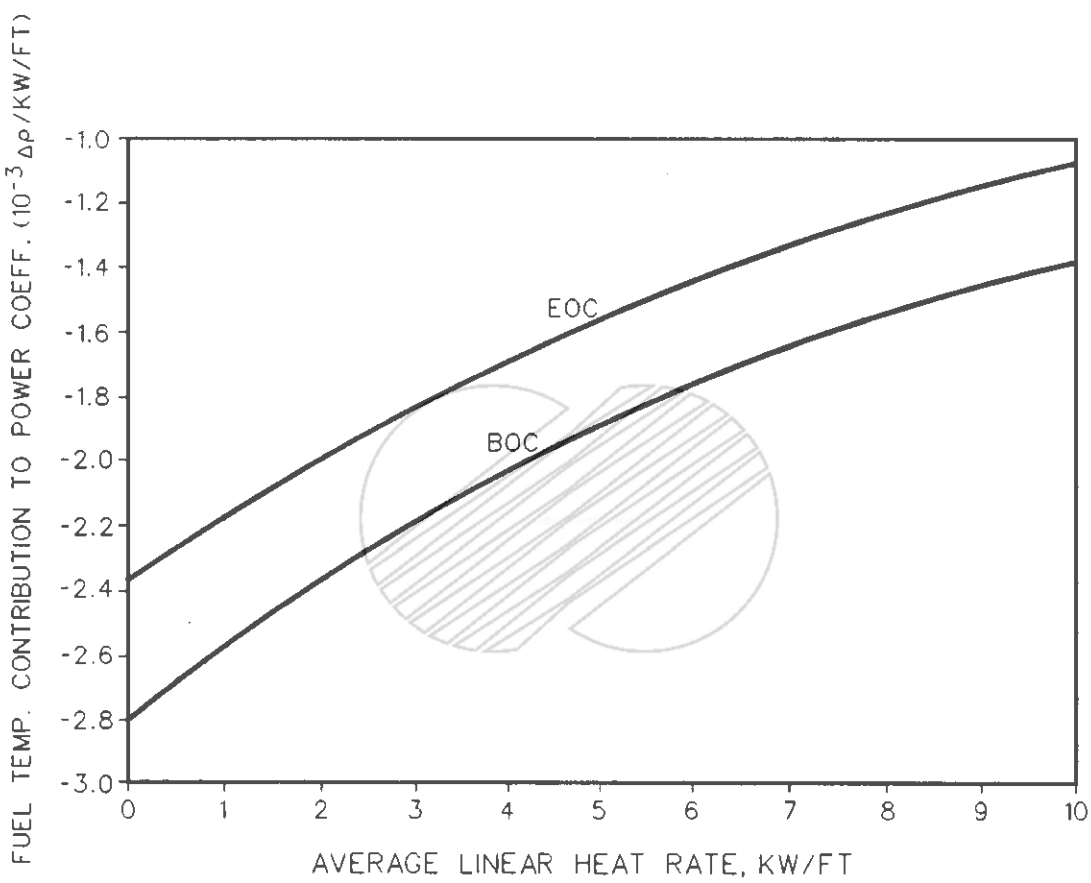

KOREA ELECTRIC POWER CORPORATION
YONGGWANG 3 & 4
FSAR

FUEL TEMPERATURE CONTRIBUTION
TO POWER COEFFICIENT AT BOC & EOC

Figure 4.3-49

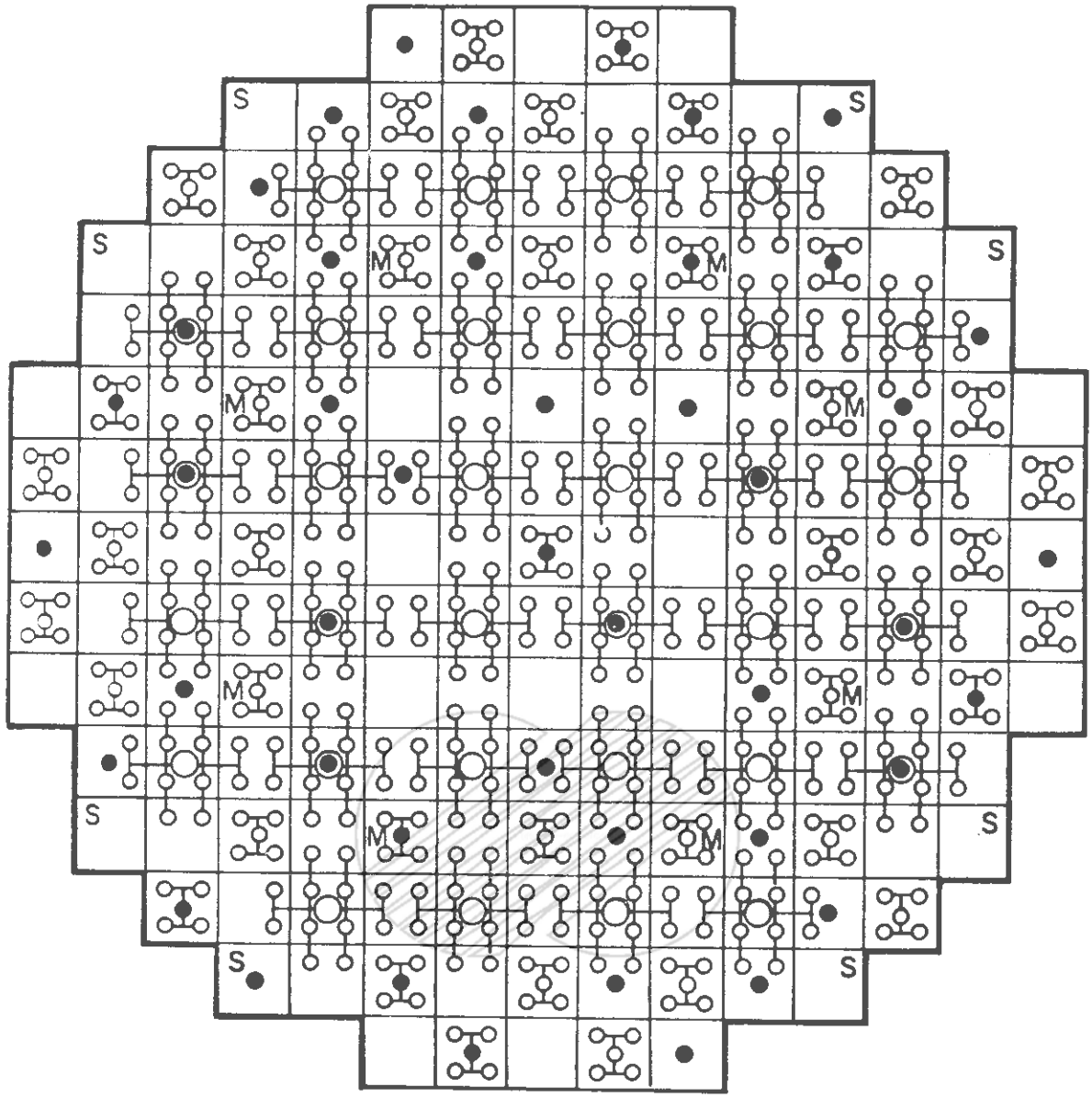

177 FUEL ASSEMBLIES
73 CEA's AND CEDM's
8 MANEUVERING CEA's (M)
8 ADDITIONAL LOCATIONS FOR SHUTDOWN CEA's (S)
45 FIXED RHODIUM IN-CORE NEUTRON DETECTOR STRINGS (●)

KOREA ELECTRIC POWER CORPORATION
YONGGWANG 3 & 4
FSAR

CONTROL ELEMENT ASSEMBLY AND DRIVE LOCATIONS AND INCORE INSTRUMENT LOCATIONS

Figure 4.3-50

5 - LEAD REGULATING BANK
4 - SECOND REGULATING BANK
3 - THIRD REGULATING BANK
2 - FOURTH REGULATING BANK
1 - LAST REGULATING BANK
B - SHUTDOWN BANK B
A - SHUTDOWN BANK A
P - PSR GROUP
S - SPARE CEA LOCATIONS

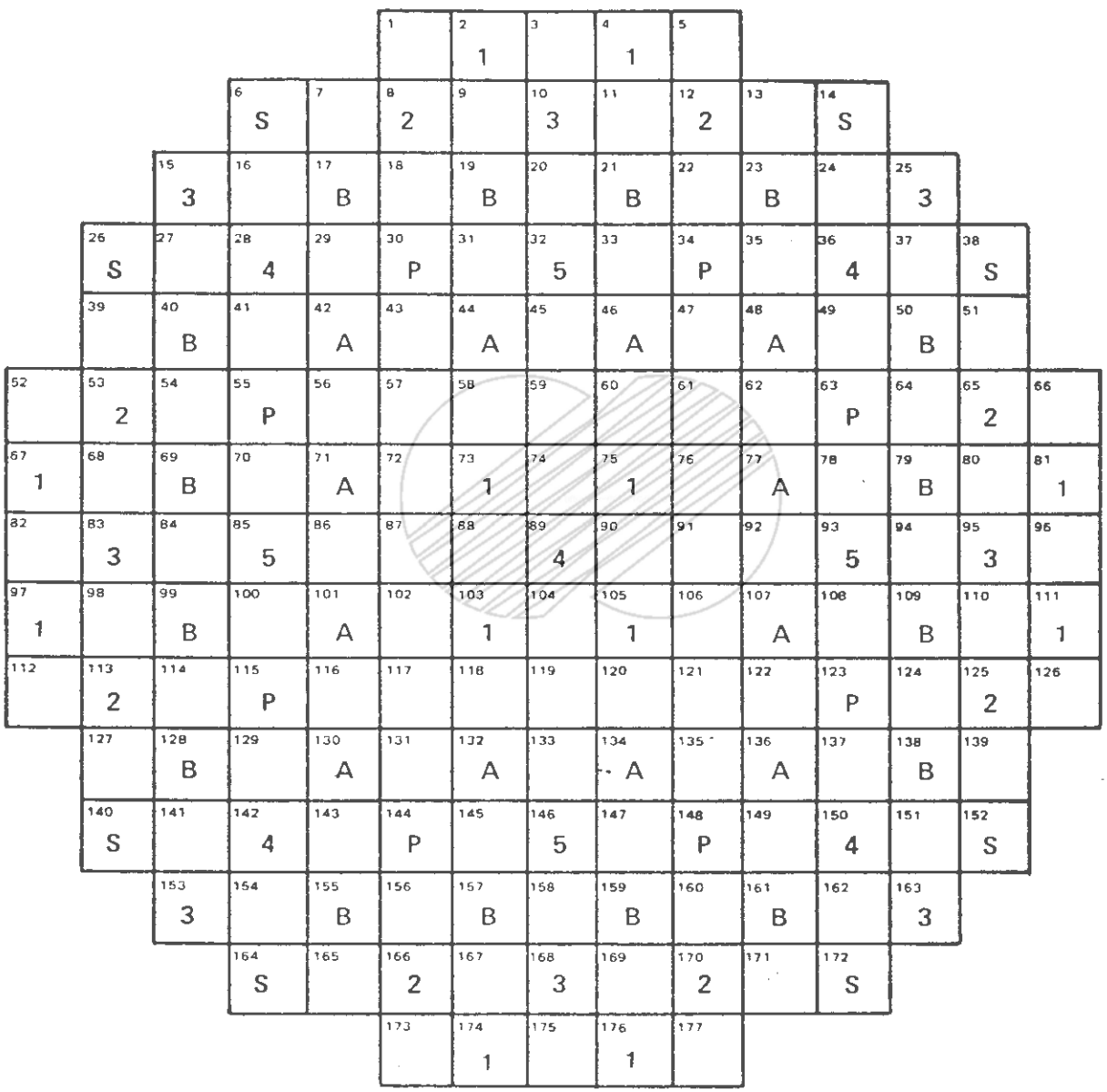

KOREA ELECTRIC POWER CORPORATION
YONGGWANG 3 & 4
FSAR

CEA BANK IDENTIFICATION

Figure 4.3-51

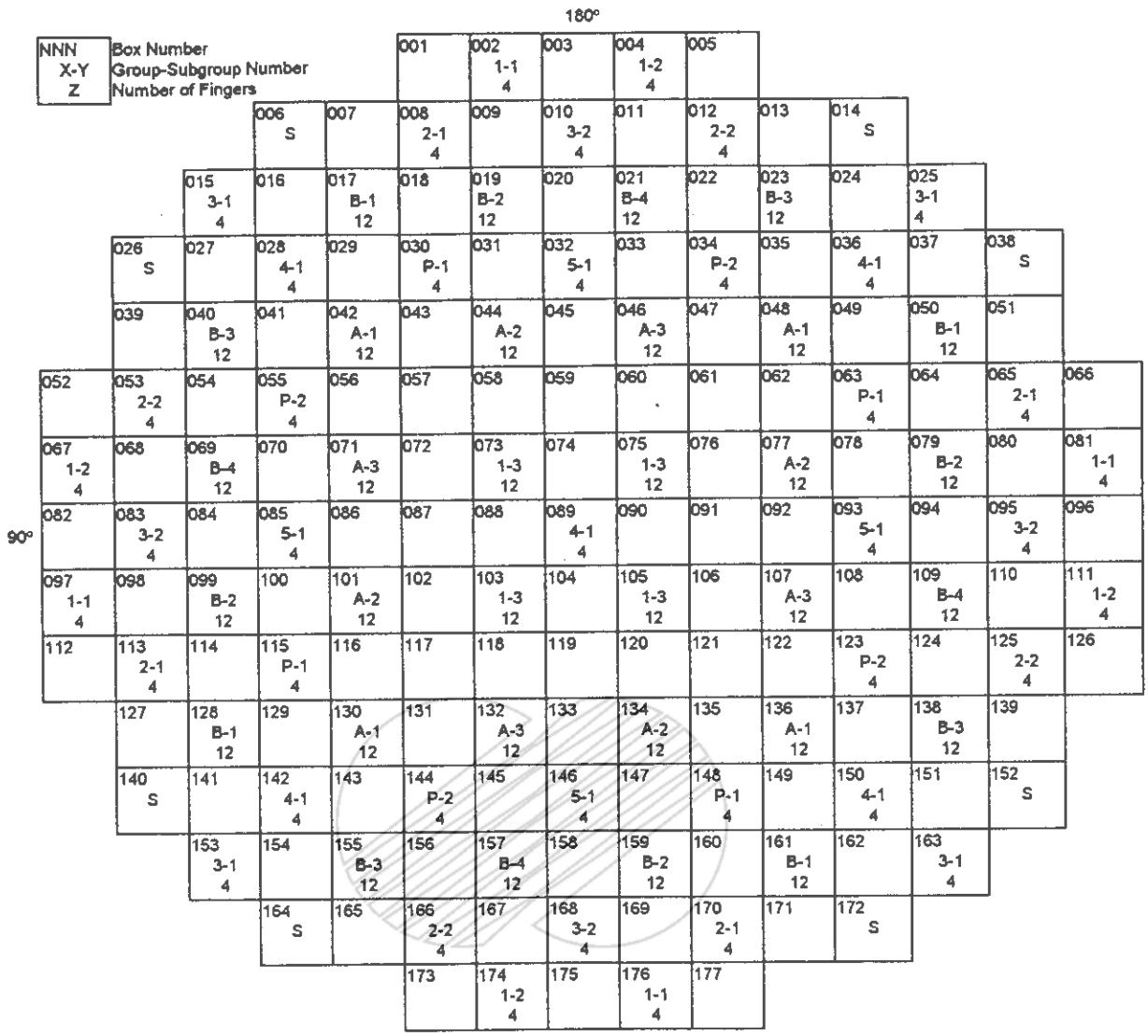

5 - Lead Regulating Bank
4 - Second Regulating Bank
3 - Third Regulating Bank
2 - Fourth Regulating Bank
1 - Last Regulating Bank
B - Shutdown Bank B
A - Shutdown Bank A
P - PSCEA Group
S - Spare CEA Location

KOREA ELECTRIC POWER CORPORATION
YONGGWANG 3 & 4 FSAR

CEA GROUP ARRANGEMENT AND
NUMBER OF FINGERS

FIGURE 4.3-51a

Amendment 85
1998. 9. 22

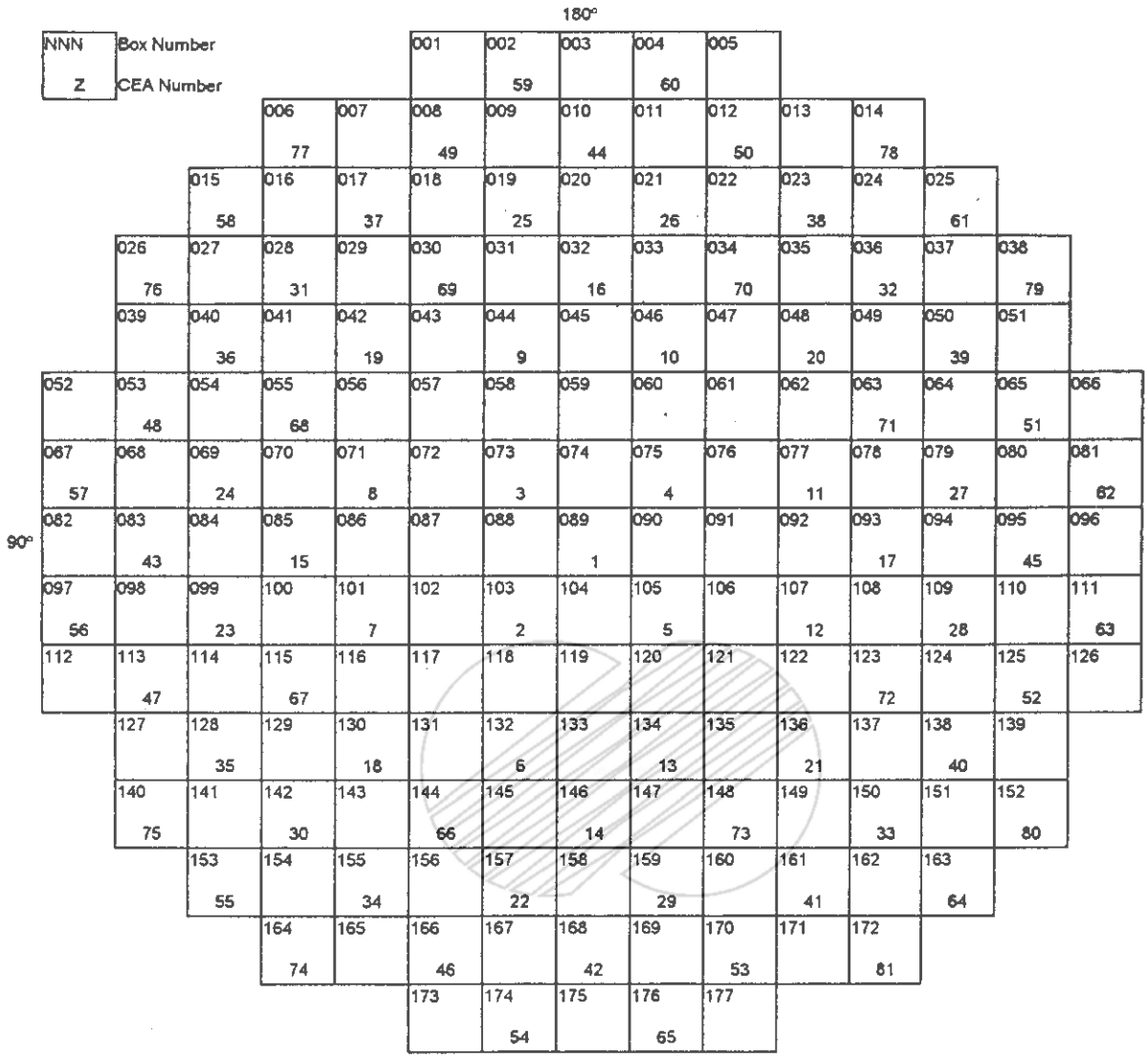

KOREA ELECTRIC POWER CORPORATION
YONGGWANG 3 & 4 FSAR

CEA NUMBER

FIGURE 4.3-51b

Amendment 85
1998. 9. 22

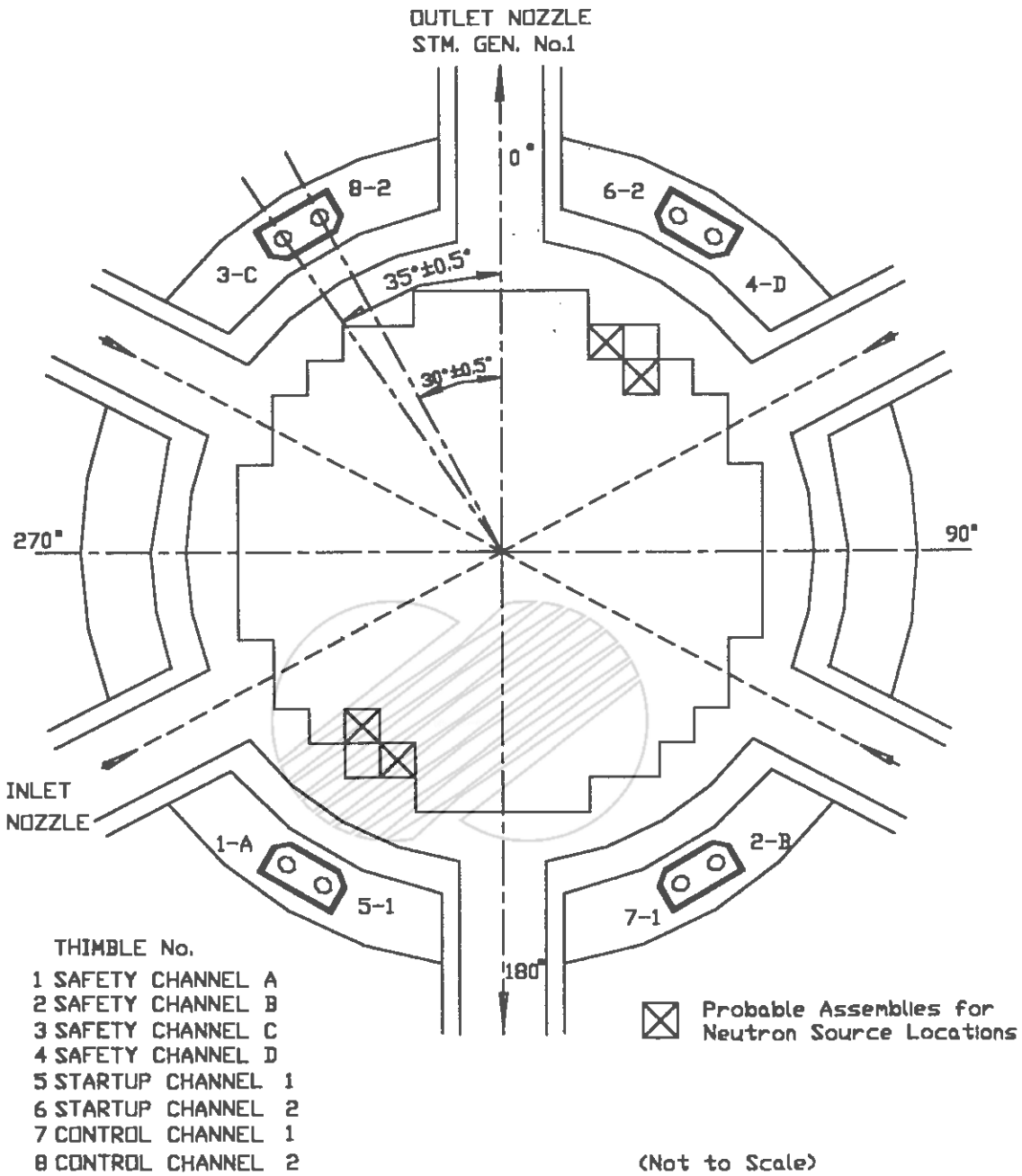

KOREA ELECTRIC POWER CORPORATION
YONGGWANG 3 & 4 FSAR

EXCORE DETECTOR LOCATION

FIGURE 4.3-51c

Amendment 85
1998. 9. 22

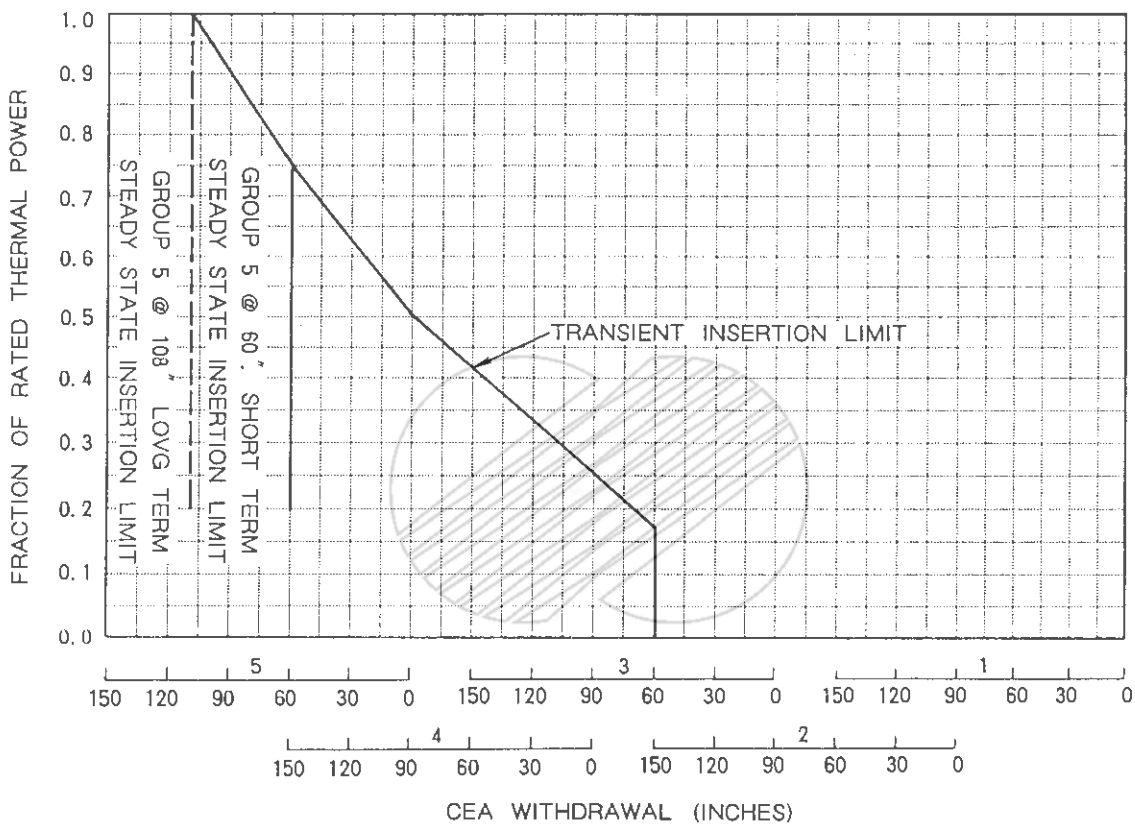

KOREA ELECTRIC POWER CORPORATION
YONGGWANG 3 & 4
FSAR

TYPICAL POWER-DEPENDENT CEA INSERTION LIMIT

Figure 4.3-52

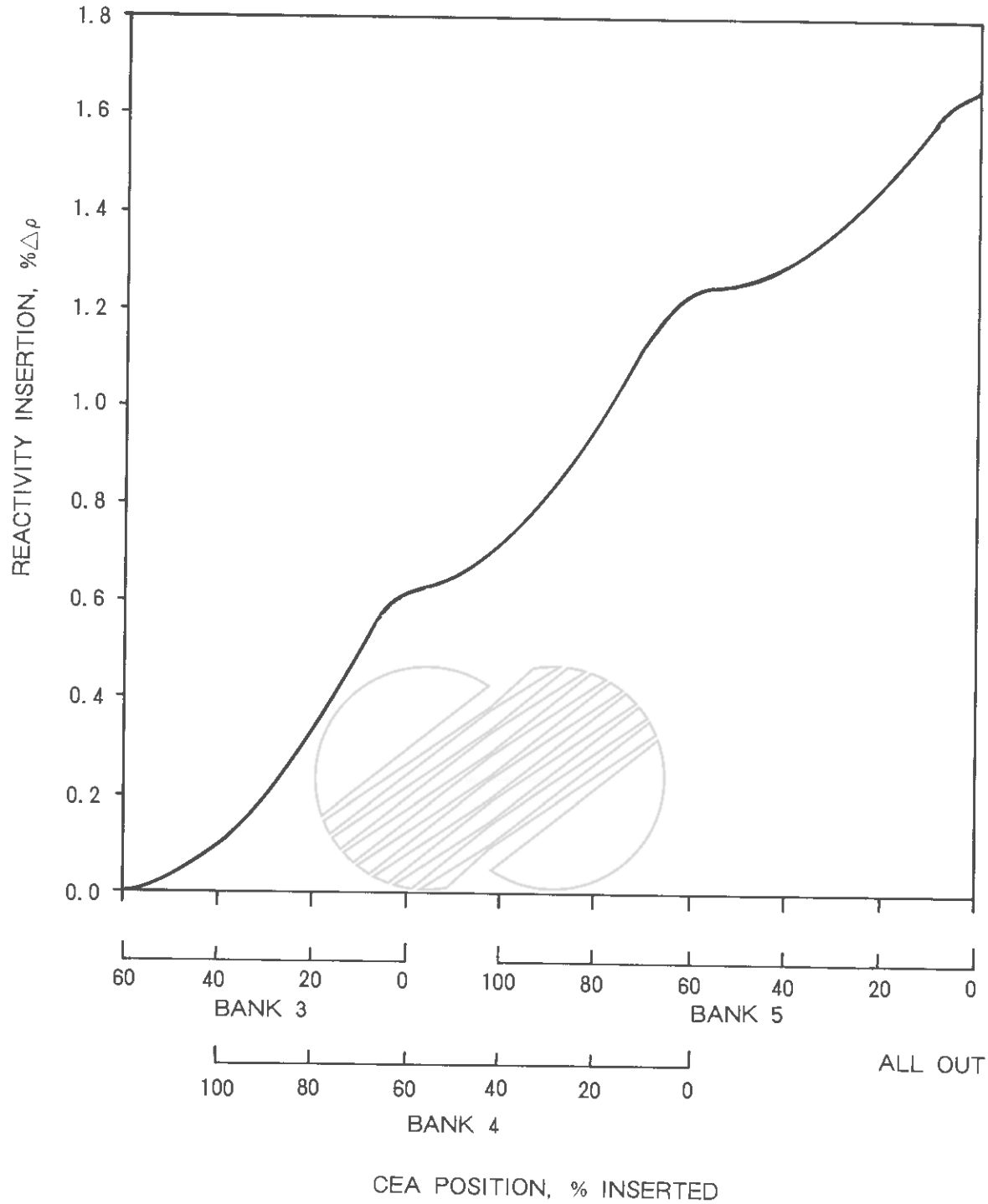

KOREA ELECTRIC POWER CORPORATION
YONGGWANG 3 & 4
FSAR

TYPICAL INTEGRAL WORTH VS.
WITHDRAWAL AT ZERO POWER,
EOC 1 CONDITIONS

Figure 4.3-53

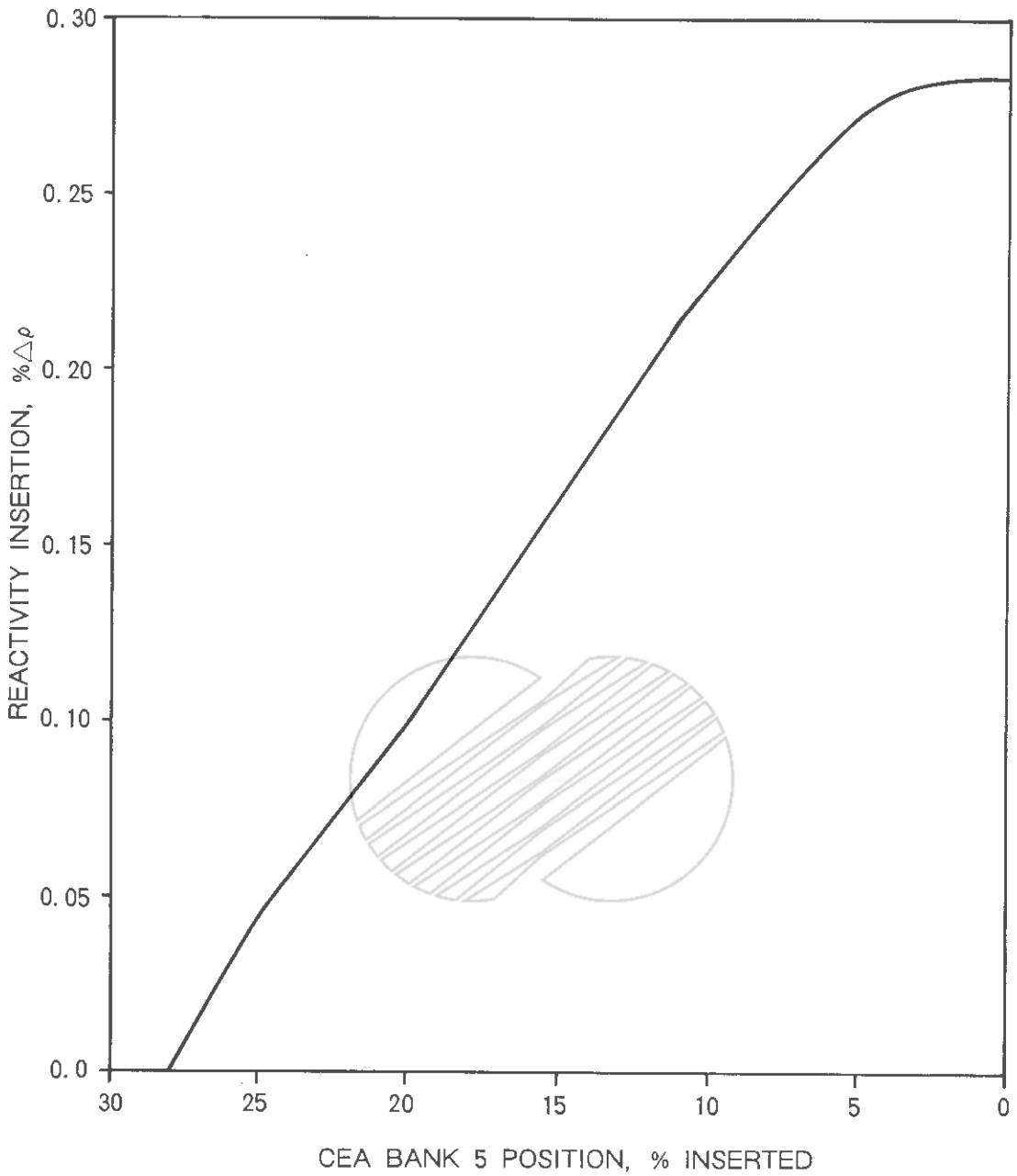

KOREA ELECTRIC POWER CORPORATION
YONGGWANG 3 & 4
FSAR

TYPICAL INTEGRAL WORTH VS.
WITHDRAWAL AT HOT FULL POWER,
EOC 1 EQUILIBRIUM
XENON CONDITIONS
Figure 4.3-54

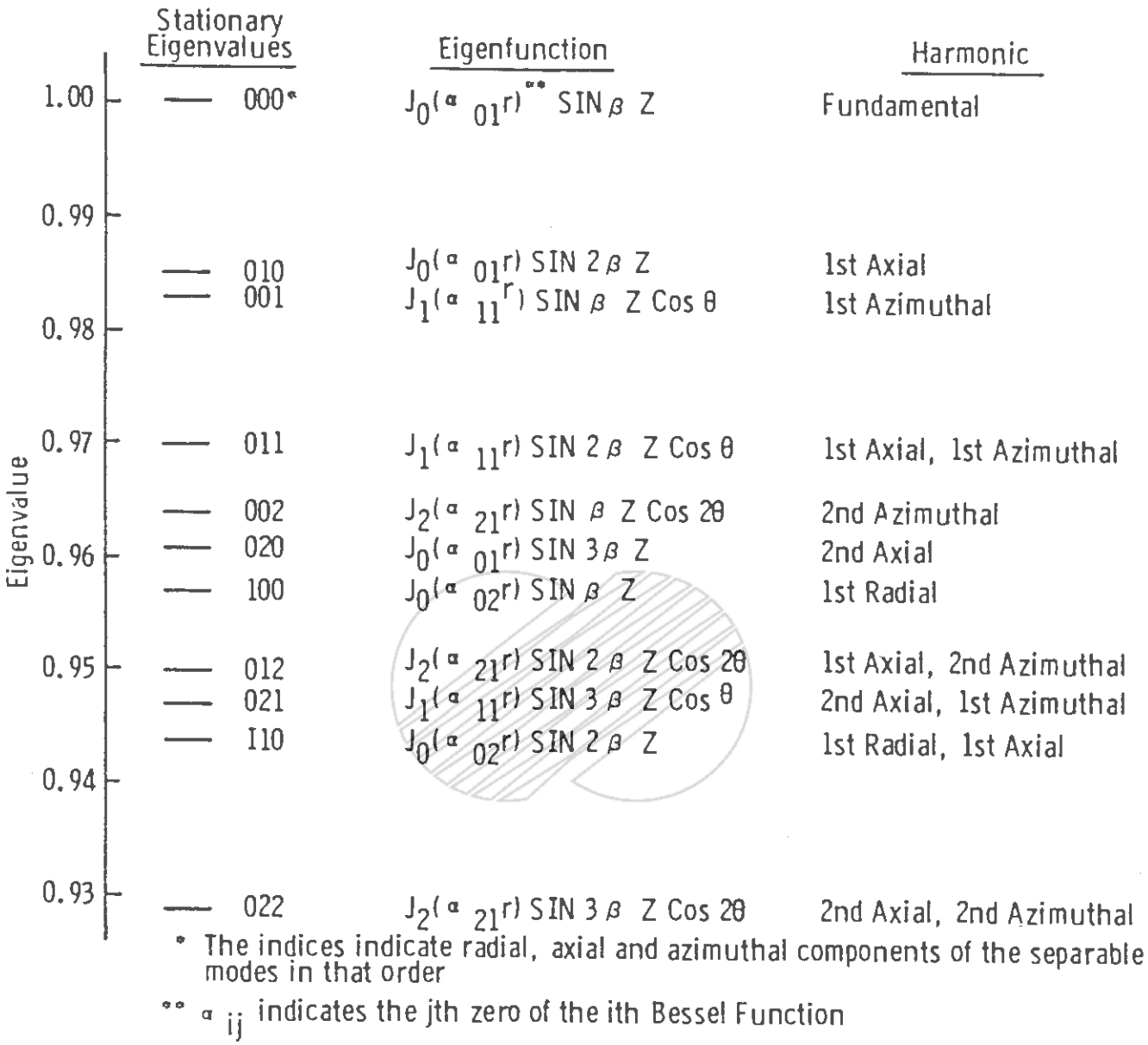

* The indices indicate radial, axial and azimuthal components of the separable modes in that order

** α_{ij} indicates the jth zero of the ith Bessel Function

KOREA ELECTRIC POWER CORPORATION
YONGGWANG 3 & 4
FSAR

REACTIVITY DIFFERENCE BETWEEN FUNDAMENTAL AND EXCITED STATES OF A BARE CYLINDRICAL REACTOR

Figure 4.3-55

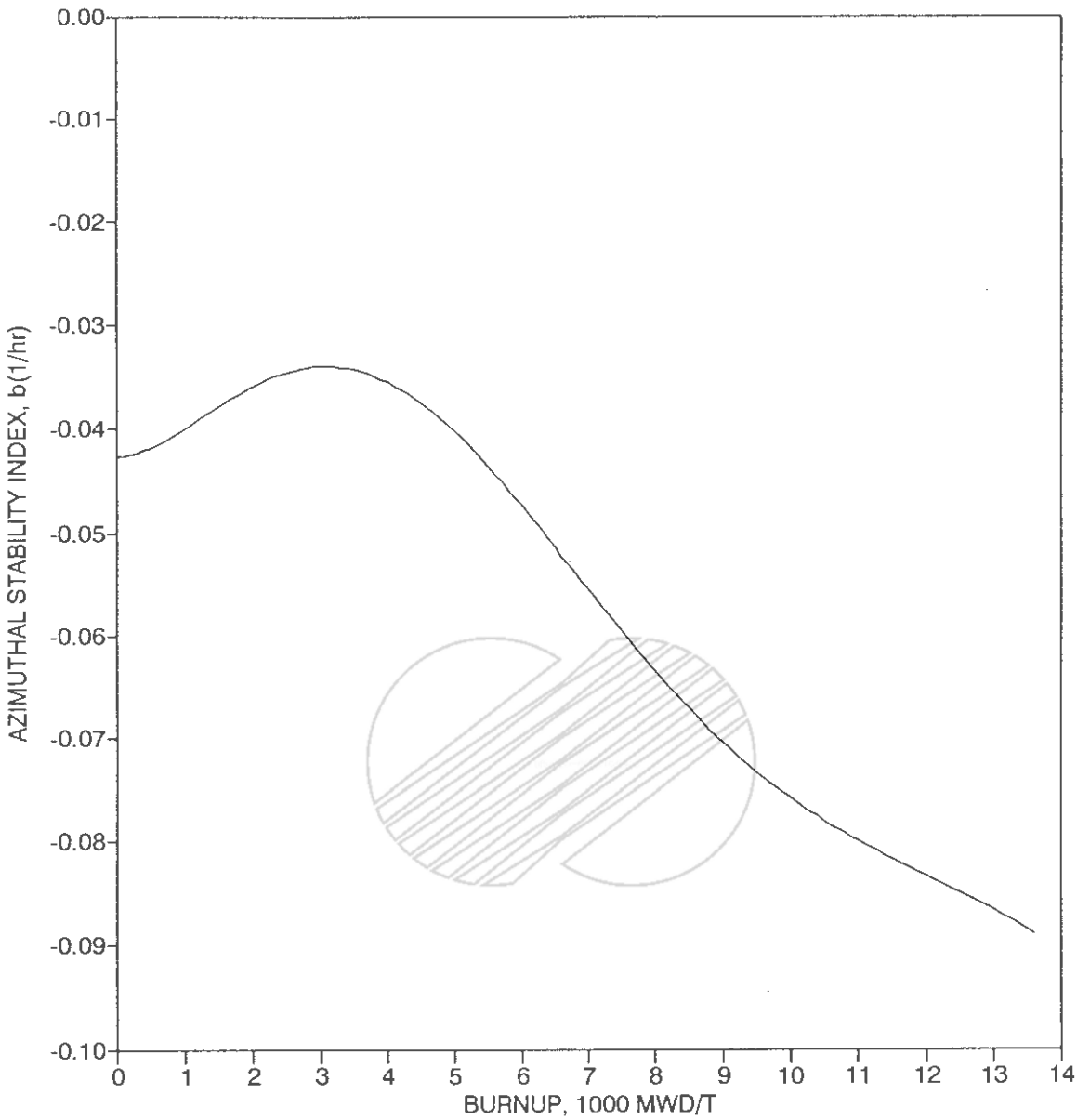

KOREA ELECTRIC POWER CORPORATION
YONGGWANG 3 & 4
FSAR

EXPECTED VARIATION OF THE
AZIMUTHAL STABILITY INDEX,
HOT FULL POWER, NO CEAs

Figure 4.3-56

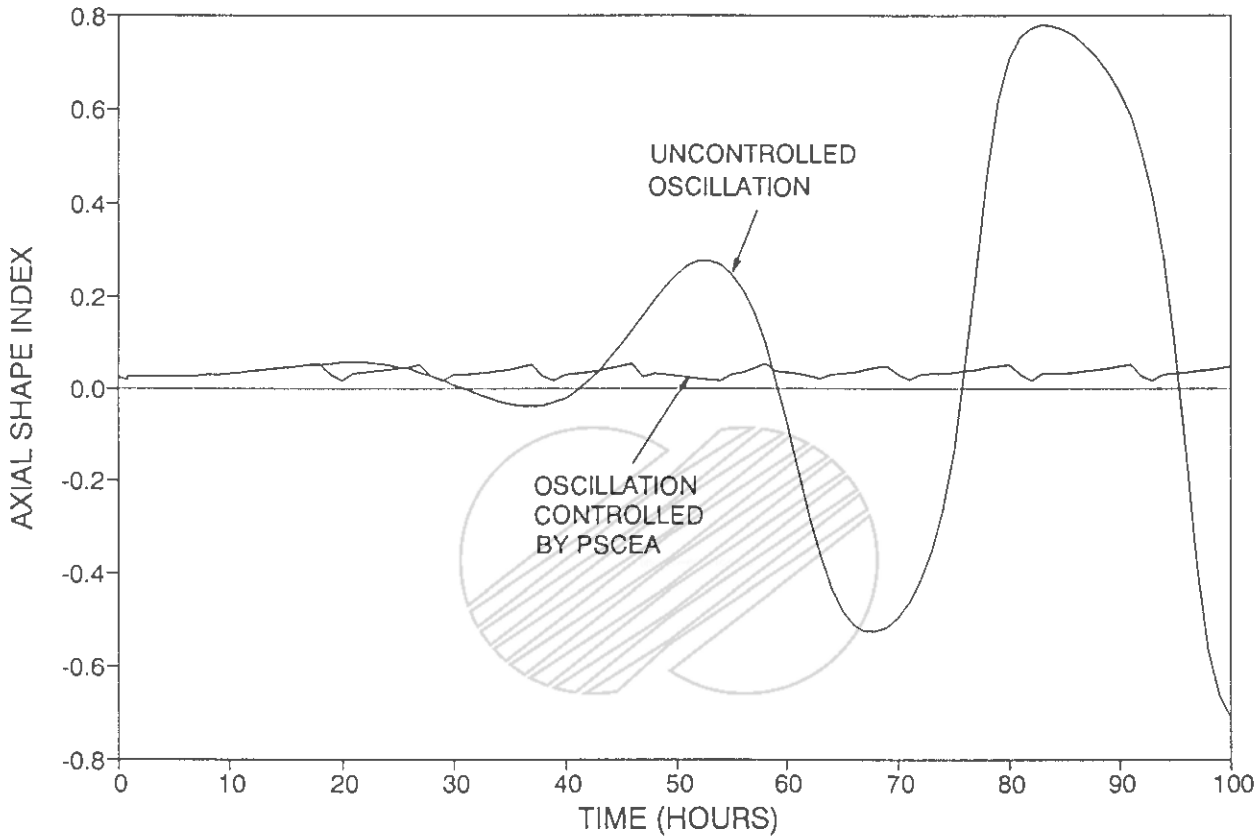

KOREA ELECTRIC POWER CORPORATION
YONGGWANG 3 & 4
FSAR

PSCEA CONTROLLED AND
UNCONTROLLED OSCILLATION

Figure 4.3-57

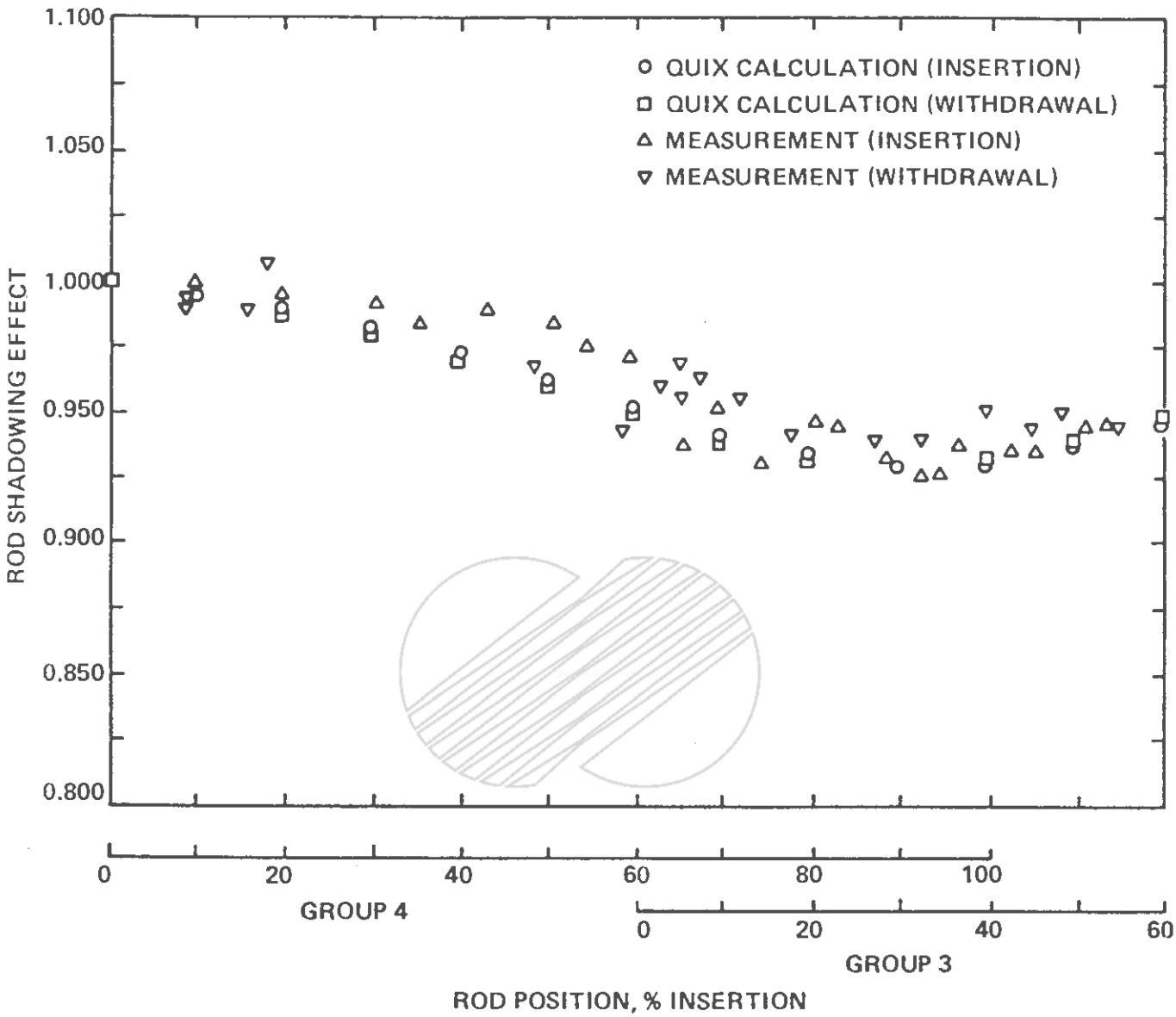

KOREA ELECTRIC POWER CORPORATION
YONGGWANG 3 & 4
FSAR

ROD SHADOWING EFFECT VS. ROD POSITION FOR ROD INSERTION AND WITHDRAWAL TRANSIENT AT PALISADES

Figure 4.3-58

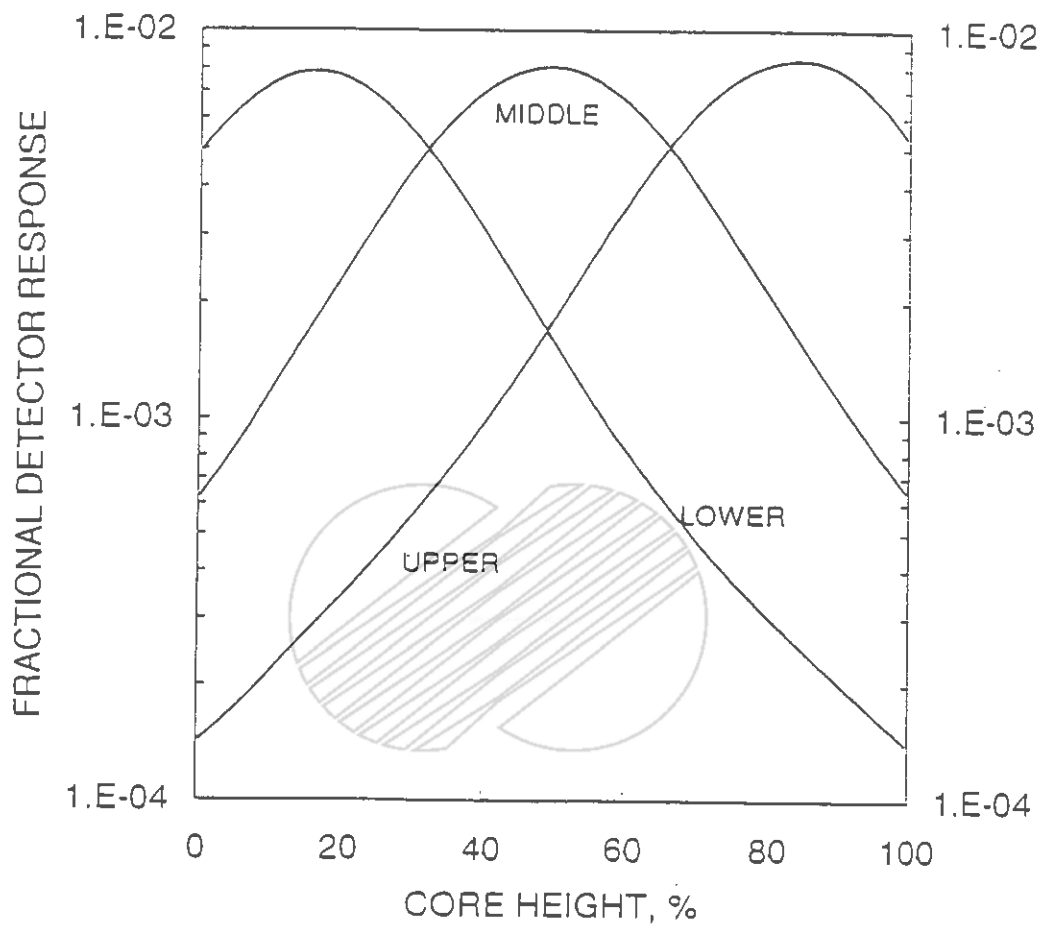

164

KOREA ELECTRIC POWER CORPORATION
YONGGWANG 3 & 4
FSAR

TYPICAL THREE SUBCHANNEL ANNEALING

Figure 4.3-59

Amendment 164
2000. 11. 20

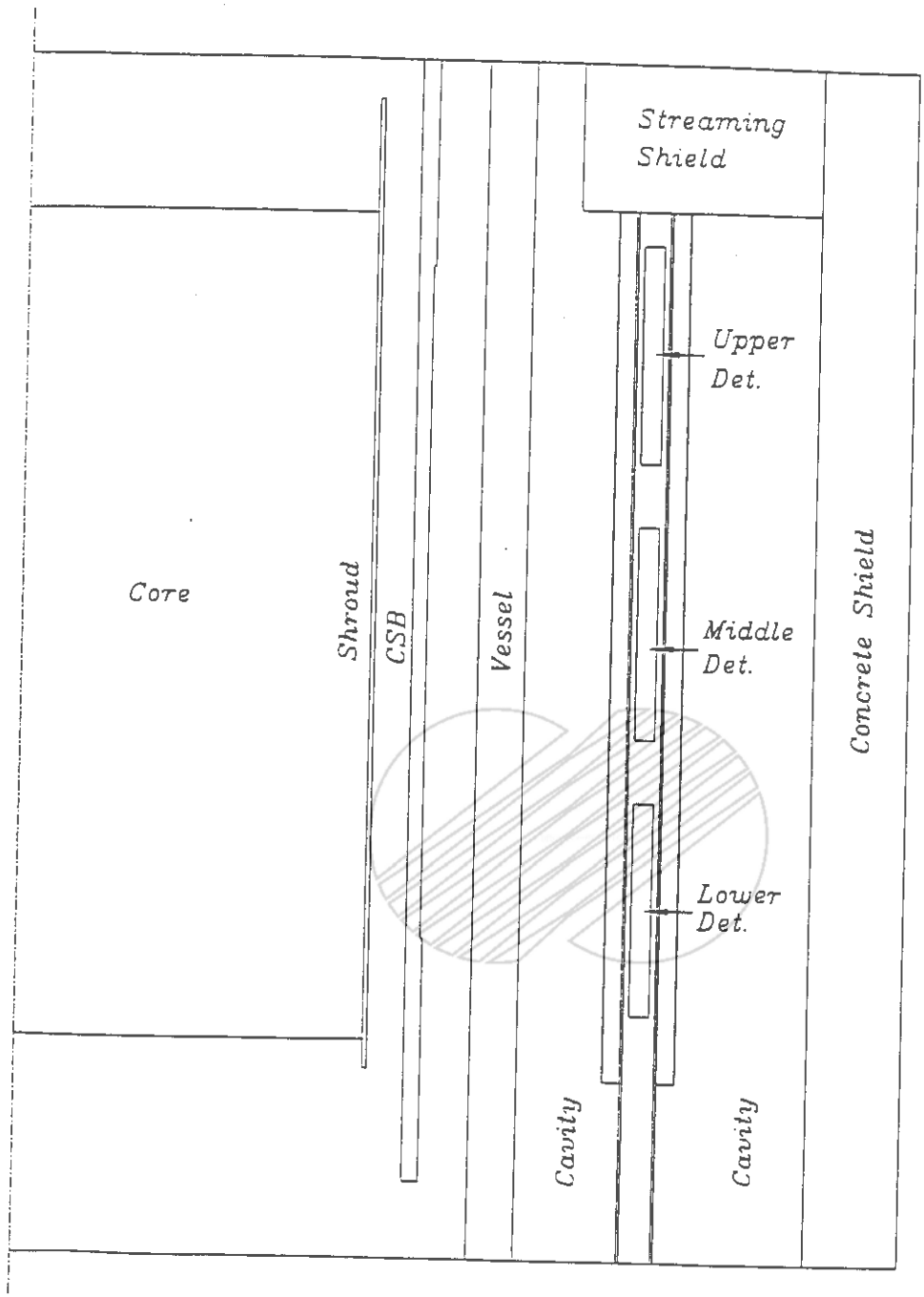

164

KOREA ELECTRIC POWER CORPORATION
YONGGWANG 3 & 4
FSAR

GEOMETRY LAYOUT

Figure 4.3-60

Amendment 164
2000. 11. 20

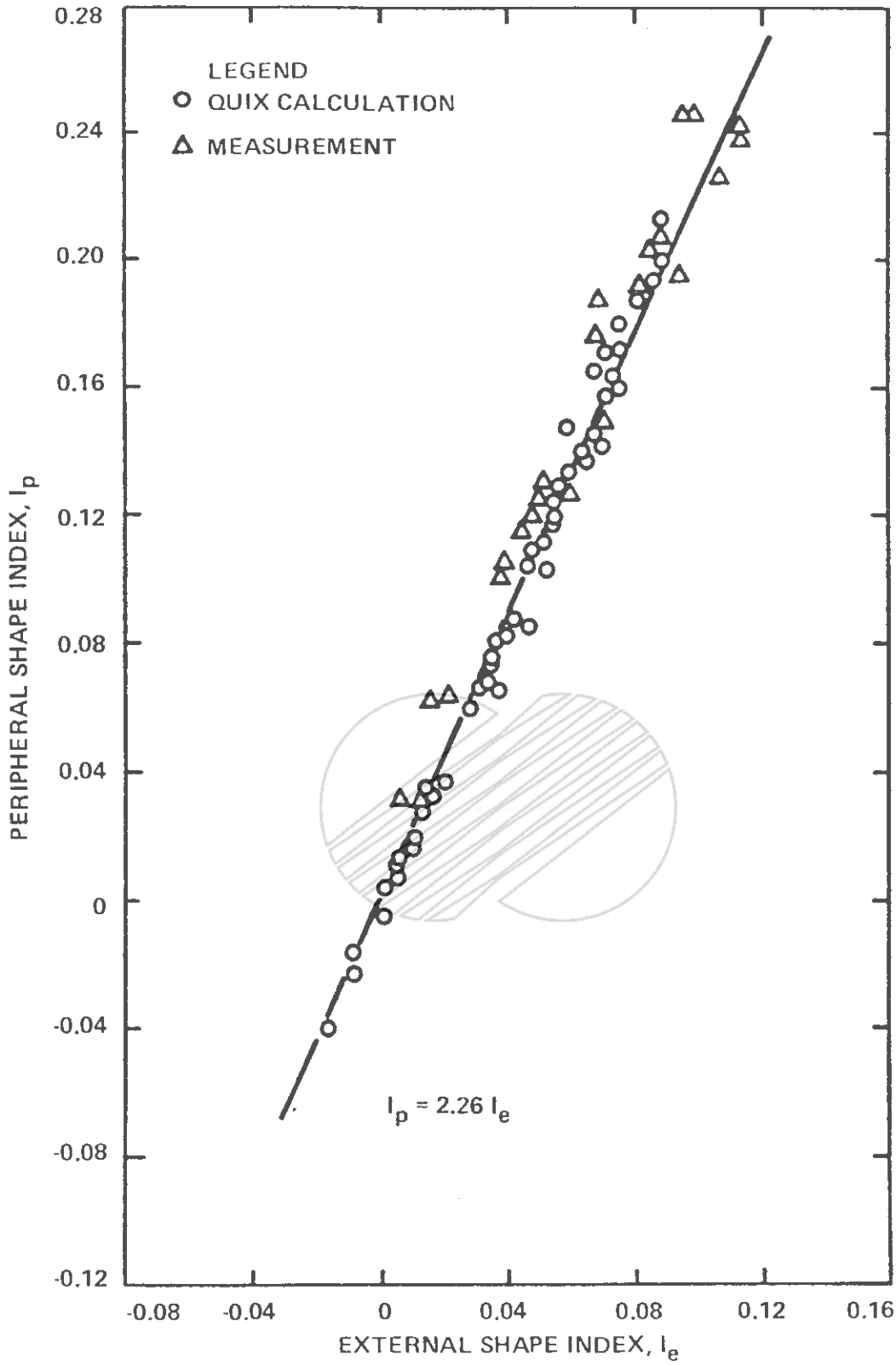

KOREA ELECTRIC POWER CORPORATION
YONGGWANG 3 & 4
FSAR

COMPARISON OF MEASURED AND CALCULATED SHAPE-ANNEALING CORRELATION FOR PALISADES

Figure 4.3-61

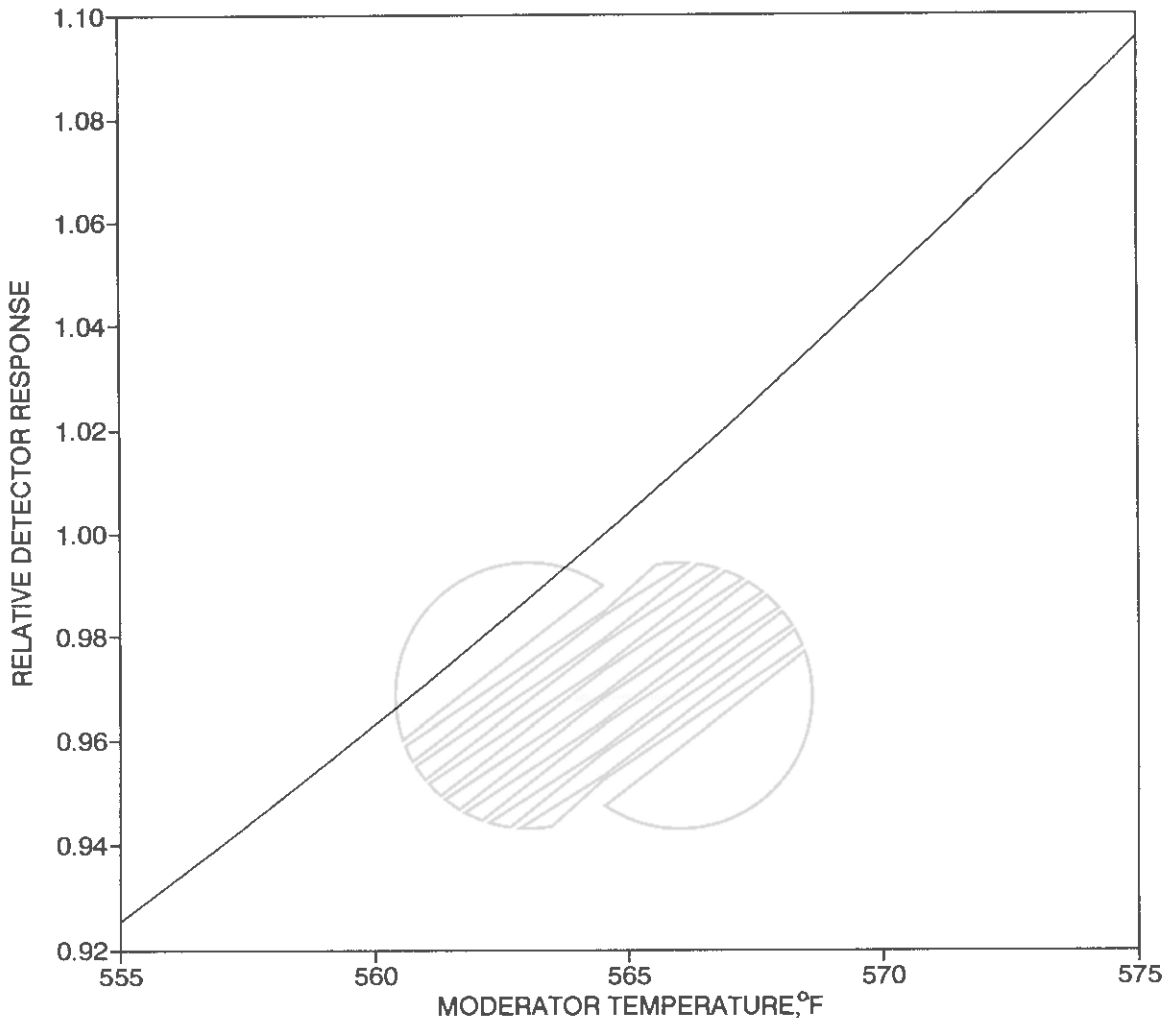

KOREA ELECTRIC POWER CORPORATION
YONGGWANG 3 & 4
FSAR

RELATIVE DETECTOR RESPONSE VS.
REACTOR INLET TEMPERATURE

Figure 4.3-62

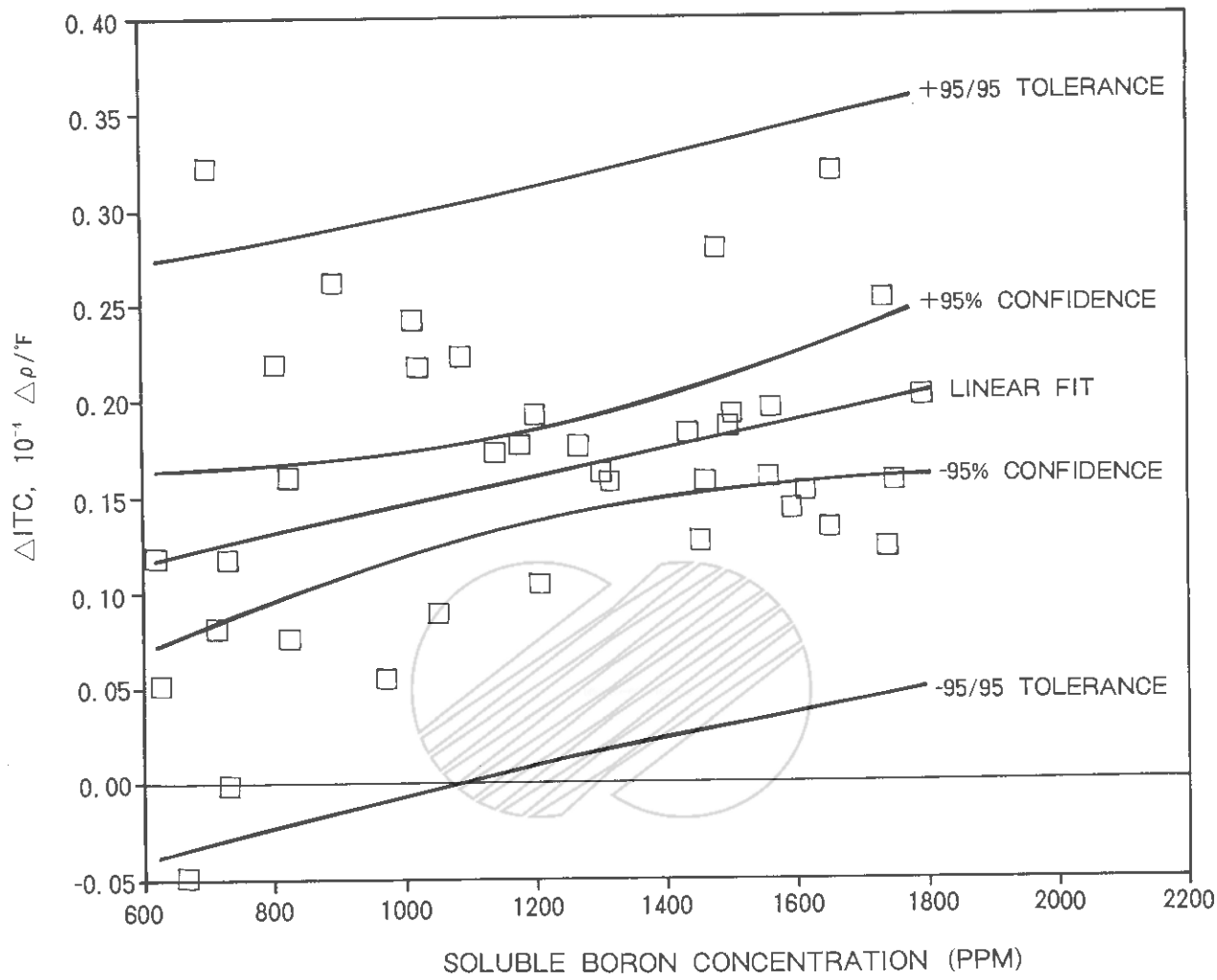

KOREA ELECTRIC POWER CORPORATION
YONGGWANG 3 & 4
FSAR

CALCULATION-MEASUREMENT ITC
DIFFERENCE VS. SOLUBLE BORON
3D ROCS (DIT)

Figure 4.3-63

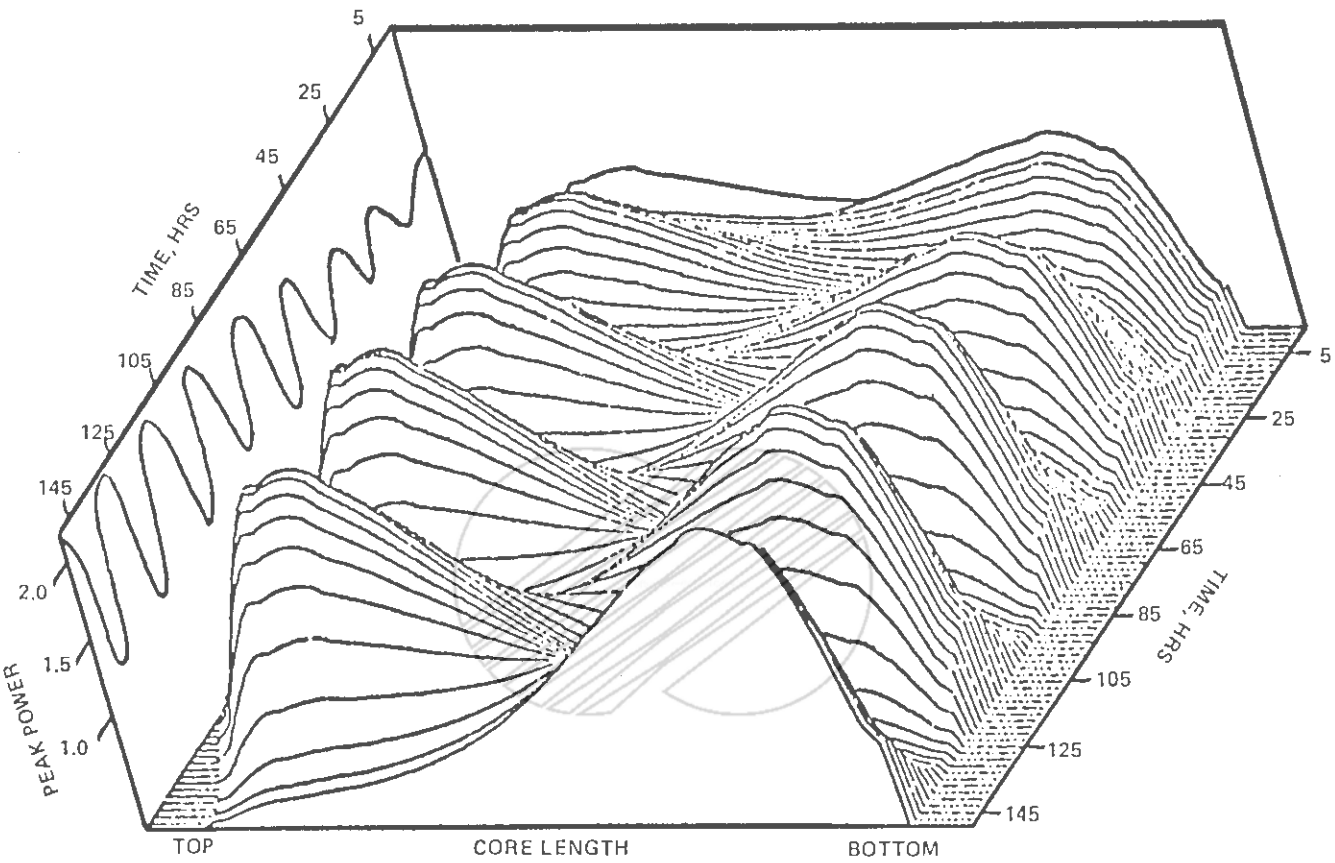

KOREA ELECTRIC POWER CORPORATION
YONGGWANG 3 & 4
FSAR

A DIVERGENT AXIAL OSCILLATION
IN AN EOC CORE WITH REDUCED
POWER FEEDBACK

Figure 4.3-64

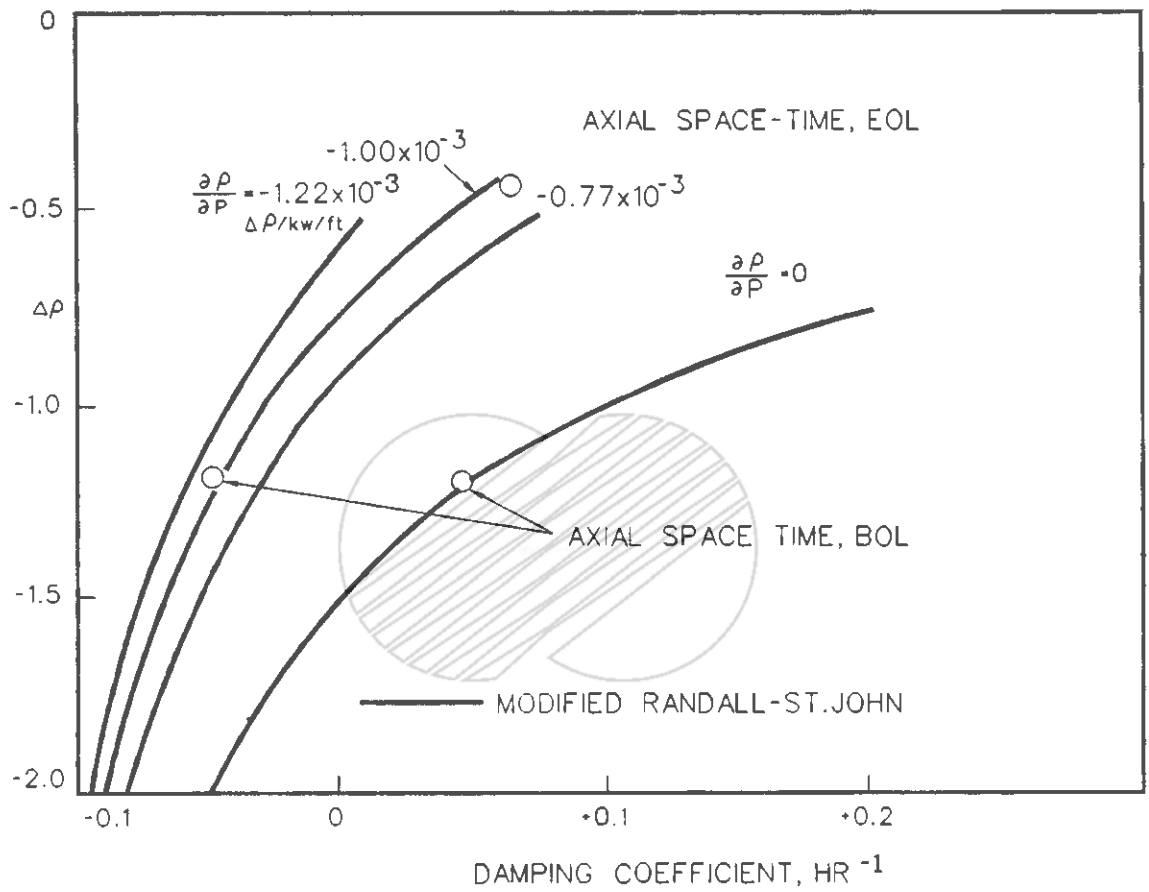

KOREA ELECTRIC POWER CORPORATION
YONGGWANG 3 & 4
FSAR

REACTIVITY DIFFERENCE BETWEEN
FUNDAMENTAL AND EXCITED STATE
VS. DAMPING COEFFICIENT

Figure 4.3-65

4.4 THERMAL AND HYDRAULIC DESIGN

This section presents the steady-state thermal and hydraulic analysis of the reactor core, the analytical methods, and the experimental work done to support the analytical techniques. Discussions of the analyses of anticipated operational occurrences and accidents are presented in Chapter 15. The prime objective of the thermal and hydraulic design of the reactor is to ensure that the core can meet steady-state and transient performance requirements without violating the design bases.

4.4.1 Design Bases

Avoidance of thermally or hydraulically induced fuel damage during normal steady-state operation and during anticipated operational occurrences is the principal thermal hydraulic design basis. The design bases for accidents are specified in Chapter 15. In order to satisfy the design basis for steady-state operation and anticipated operational occurrences, the following design limits are established, but violation of these will not necessarily result in fuel damage. The reactor protection system (RPS) provides for automatic reactor trip or other corrective action before these design limits are violated.

4.4.1.1 Minimum Departure from Nucleate Boiling Ratio

The minimum departure from nucleate boiling ratio (DNBR) shall be such as to provide at least a 95% probability with 95% confidence that departure from nucleate boiling (DNB) does not occur on a fuel rod having that minimum DNBR during steady-state operation and anticipated transients of moderate frequency. A value of 1.21 using the KCE-1 correlation coupled with the CETOP code provides at least this probability and confidence.

4.4.1.1 Hydraulic Stability

Operating conditions shall not lead to flow instability during steady-state operation or anticipated operational occurrences.

4.4.1.3 Fuel Design Bases

The peak temperature of the fuel shall be less than the melting point (refer to Subsections 4.2.1.2.4.4.c and 4.2.1.3.3.) during steady-state operation and anticipated occurrences of moderate frequency.

The fuel design bases for fuel clad integrity and fuel assembly integrity are given in Subsection 4.2.1. Thermal and hydraulic parameters that influence the fuel integrity include maximum linear heat rate, core coolant velocity, coolant temperature, clad temperature, fuel-to-clad gap conductance, fuel burnup, and UO_2 temperature. Other than the design limits already specified, no limits need to be applied to these parameters directly. Conformance with the design limits specified here and conformance with the design bases specified in Subsection 4.2.1 are sufficient to ensure fuel clad integrity, fuel assembly integrity, and the avoidance of thermally or hydraulically induced fuel damage for steady-state operation and anticipated occurrences of moderate frequency.

4.4.1.4 Coolant Flow, Velocity, and Void Fraction

The primary coolant flow with all four pumps in operation shall be neither less than the design minimum nor greater than the design maximum. The design minimum RCS flow rate is equal to 95% of the nominal RCS flow rate. The nominal RCS flow rate means the 100% design flow rate. The value of the design minimum RCS flow rate is shown in Table 4.4-1. A percentage of the flow rate entering the reactor vessel is not effective for cooling the core. This percentage is called the core bypass flow rate. The core bypass flow rate has the characteristics to be proportional with the total amount of the primary coolant flow rate. The design minimum core flow rate is obtained by subtracting the design maximum core bypass flow rate from the design minimum RCS flow rate. The nominal core flow rate is obtained by subtracting the design maximum core bypass flow rate from the nominal RCS flow rate. The design maximum core bypass flow rate is shown in Table 4.4-1. In thermal margin analyses, the design minimum 563

core flow rate is used. The design maximum RCS flow rate for use in core design at full-power conditions is equal to 113.1% of the nominal RCS flow rate. 563

Design of the reactor internals provides that the coolant flow is distributed to the core such that the core is adequately cooled during steady-state operation and anticipated operational occurrences. Therefore, no specific orifice configuration is used.

Although the coolant velocity, its distribution, and the coolant voids affect the thermal margin, design limits need not be applied to these parameters because they are not in themselves limiting. These parameters are included in the thermal margin analyses and thus affect the thermal margin to the design limits.

4.4.2 Description of Thermal and Hydraulic Design of the Reactor Core

4.4.2.1 Summary Comparison

The thermal and hydraulic parameters for the reactor are listed in Table 4.4-1. A comparison of these parameters with those for the Arkansas Nuclear One Unit 2 (Docket No. 50-368) and System 80 CESSAR (Docket STN-50-470F) are included in this table.

4.4.2.2 Critical Heat Flux Ratios

4.4.2.2.1 Departure from Nucleate Boiling Ratio

The margin to DNB in the core is expressed in terms of the DNBR. The DNBR is defined as the ratio of the heat flux required to produce departure from nucleate boiling at the calculated local coolant conditions to the actual local heat flux.

While the DNB correlation used for design of the core loaded with 16X16 standard (HID-1B or HID-1L) or Guardian™ fuels is the CE-1 correlation (References 1 and 2), the DNB correlation used for design of the core loaded with 16X16 PLUS7™ fuels is the KCE-1 correlation (Reference 3). Based on the statistical evaluation of the CE-1 and KCE-1 correlations and relevant data, it is concluded that the appropriate minimum DNBR is 1.20 (References 2 & 4) and 1.124 (References 3), respectively. The design minimum DNBR has increased with the application of statistical combination of uncertainties (SCU) methods (Reference 5). Engineering enthalpy rise factor, engineering heat flux factor, systematic variation of the rod pitch and clad diameter, and core inlet flow factor uncertainties are combined with other uncertainty factors at the 95/95 confidence/probability level, and this combination is expected to yield a higher design limit of 1.21 on KCE-1 minimum DNBR. This limit is then used in conjunction with a CETOP model based on nominal dimensions (see Subsection 4.4.2.9.5). Table 4.4-1 gives the value of minimum DNBR for the coolant conditions and engineering factors in the table, for the radial power distributions in Figures 4.4-1 and 4.4-2, and for the 1.26 peaked axial power distribution in Figure 4.4-3. Values of minimum DNBR or maximum fuel temperature at the design overpower cannot be provided with any meaning. The concept of a design overpower is not applicable for the YGN 3&4 cores since the reactor protection system prevents the design basis limits from being exceeded.

A comparison of the minimum DNBRs computed using different correlations for the same power, design minimum RCS flow, coolant temperature and pressure, and power distribution is presented in Table 4.4-2. The minimum DNBR values in both the limiting matrix subchannel and the limiting subchannel next to the guide tube are presented. The correlations compared are the KCE-1 correlation and the CE-1 correlation. 563

The TORC and the CETOP computer codes (References 6 and 7) are used to compute the local coolant conditions in the core and thereby the minimum DNBR. A discussion of the KCE-1 DNB correlation and the analytical methods is presented in Subsections 4.4.4.1 and 4.4.4.5.2, respectively.

4.4.2.2.2 Application of Power Distribution and Engineering Factors

Distribution of power in the core is expressed in terms of factors that define the local power (per unit length produced by the fuel) relative to the core average power (per unit length produced by the fuel). The method used to compute these factors, which describe the core power distribution, is discussed in Section 4.3. The energy produced in the fuel is absorbed by the fuel pellets, fuel cladding, and the moderator and results in the generation of heat in those places. The fraction of energy deposited in the fuel pellet and cladding is called the fuel rod energy deposition fraction. Accordingly, the core average heat flux from the fuel rods is determined by multiplying the core power by the average fuel rod energy deposition fraction and then dividing by the total heat transfer area. The energy deposition fractions

used for DNB analyses for the average and the hot fuel rods are given in Table 4.4-1.

The effects on local heat flux and subchannel enthalpy rise of deviations from nominal dimensions and specifications within tolerance are included in thermal margin analyses by certain factors called engineering factors. These factors are applied to increase the local heat flux at the location of minimum DNBR and to increase the enthalpy rise in the subchannel adjacent to the rod with the minimum DNBR. Diversion crossflow and turbulent interchange mixing are not input as factors on subchannel enthalpy rise but are explicitly treated in the TORC and CETOP codes analytical models.

Uncertainties in the power distribution factors are discussed in Subsection 4.4.2.9.4.

SCU methods were used to statistically combine the uncertainties associated with the thermal hydraulic code system input parameters. In this methodology the plant specific data for YGN 3&4 has been statistically combined with KCE-1 CHF correlation statistics at 95/95 confidence/probability level to yield a design DNBR limit. This design DNBR limit is 1.21 when the following uncertainties are combined:

a. Uncertainty in the inlet flow distribution
b. Systematic variation on fuel rod pitch
c. Systematic variation on fuel clad OD
d. Engineering enthalpy rise factor
e. Engineering heat flux factor
f. Penalty on DNBR (minimum) due to fuel rod bowing
g. Statistics associated with the KINS approved 1.124 DNBR limit (Reference 3)
h. Penalty on code uncertainty imposed by NRC.

"Delete"

The 1.21 DNBR limit is used in safety analysis, core protection calculators (CPC) trip setpoints and COLSS power operating limit calculations in conjunction with a CETOP model based on a nominal geometry.

4.4.2.2.2.1 Power Distribution Factors

Power distribution factors account for variations in rod radial power, axial power, nuclear power, total heat flux, and fuel pellet augmentation effects. Values for these factors are listed in Table 4.4-1.

a. Rod Radial Power Factor

The rod radial power factor is the ratio of the average power per unit length produced by a particular fuel rod to the average power per unit length produced by the average-powered fuel rod in the core. The maximum rod radial power factor is the ratio of the average power per unit length produced by the highest-powered rod in the core to the average power per unit length produced by the average-powered fuel rod in the core. Radial power distributions are dependent upon a variety of parameters (control rod insertion, power level, fuel exposure, etc.). The core-wide and hot-assembly radial power distributions used for a typical DNB analysis are shown in Figures 4.4-1 and 4.4-2. The maximum rod radial power factor for those figures is selected as 1.60 for comparison with Arkansas Nuclear One Unit 2 and CESSAR. The actual maximum rod radial power factor in the core will normally be lower; but it is not limited to a maximum value of 1.60. The only limits are those specified in Subsection 4.4.1. The protection system in conjunction with the reactor operator utilizing the core operating

limit supervisory system (COLSS) ensures that those design limits are not violated.

b. Axial Power Factor

The axial power factor is the ratio of the local power per unit length produced by a fuel rod to the average power per unit length produced by the same fuel rod. The maximum axial power factor is the ratio of the maximum local power per unit length produced by a rod to the average power per unit length produced by the same fuel rod. The axial power distribution directly affects the DNBR.

Typically, the farther the location of the peak heat flux is from the core inlet, the lower the value of the peak heat flux needed to reach the DNBR limit. However, fuel temperature is almost independent of the location of the peak heat flux and is principally dependent on the value of the peak heat flux or linear heat rate. The axial power distribution and the maximum rod radial power factor are continuously determined and processed through the COLSS and the RPS such that the design basis limits are not exceeded. Section 4.3 describes the power distribution and its control. Figure 4.4-3 shows several axial power distributions used for this analysis. The minimum DNBR in Table 4.4-1 is determined using the 1.26 peaked axial power distribution whereas the maximum heat fluxes are determined using the 1.47 peaked axial power distribution.

c. Nuclear Power Factor

The nuclear power factor is the ratio of the maximum local power per unit length produced in the core to the average power per unit length produced by the average-powered fuel rod in the core. It is conservatively calculated as the product of the maximum axial and radial

power factors. For comparison with Arkansas Nuclear One Unit 2 and CESSAR, a value of 2.35 is selected for computing maximum heat fluxes. The actual value of the nuclear power factor is normally lower throughout the cycle, but is not limited to a maximum value of 2.35. The design limits are those specified in Subsection 4.4.1. The protection and supervisory systems assure that those design limits are not violated.

d. Total Heat Flux Factor

The total heat flux factor is the ratio of the local fuel rod heat flux to the core average fuel rod heat flux, excluding the effects of fuel densification. The total heat flux factor is the product of the nuclear power factor, the engineering heat flux factor, and the ratio of the hot to the average rod energy deposition fractions.

e. Augmentation Factor

Fuel densification may lead to axial gaps in the fuel pellet stacks and can cause increased localized power peaking. An augmentation factor is applied to the total heat flux factor to determine the maximum local heat flux.

The augmentation factor, defined as the ratio of the local heat flux to the unperturbed heat flux, accounts for the effects of gaps occurring between the fuel rod pellets caused by fuel densification. The axial length over which the localized power perturbation is considered to occur is called the gap length. However, the densification of modern fuel is insufficient to cause the formation of significant axial gaps. Therefore, the augmentation factor is 1.0. The effect of this factor on DNBR is discussed in Subsection 4.4.2.2.3.

4.4.2.2.2.2 Engineering Factors

Engineering factors account for local variations in heat flux, linear heat rate, enthalpy rise, and subchannel pitch and bow effects. Values for these engineering factors are listed in Table 4.4-1.

a. Engineering Heat Flux Factor

The effect on local heat flux due to normal manufacturing deviations from nominal dimensions and specifications is accounted for by the engineering heat flux factor. Design variables that contribute to this engineering factor are initial pellet density, pellet enrichment, pellet diameter, and clad outside diameter.

These variables are combined statistically to obtain the engineering heat flux factor. The design value used for the engineering heat flux factor is based on drawing and specification tolerance limits for the YGN 3&4 fuel. The engineering heat flux factor is applied to the rod with the minimum DNBR and increases the heat flux when calculating DNBR. It does not affect the enthalpy rise in the subchannel; the effect on the enthalpy rise in the subchannel due to normal manufacturing deviations from normal design dimensions and specifications is accounted for by the engineering enthalpy rise factor.

b. Engineering Factor on Linear Heat Rate

The effect of deviations from nominal fuel rod design dimensions and specifications on fuel temperature is accounted for by the engineering factor on linear heat rate. The method used to calculate this factor is described in Appendix B of Reference 8. Since the final value is less than 1.03, using the value 1.03 is conservative.

c. Engineering Enthalpy Rise Factor

The engineering enthalpy rise factor accounts for the effects of normal manufacturing deviations in fuel fabrication from nominal dimensions and specifications on the enthalpy rise in subchannel adjacent to the rod with the minimum DNBR. Tolerance deviations (average over the length of the fuel rods that adjoin the subchannel) for fuel pellet density, enrichment, and diameter contribute to this factor. The design value used for the engineering enthalpy rise factor is based on drawing and specification tolerance limits for the YGN 3&4 fuel.

The engineering enthalpy rise factor is applied by multiplying it by the rod radial power factor of each of the fuel rods adjacent to the subchannel adjoining the rod with the minimum DNBR. This increases the enthalpy rise in the subchannels that adjoin the same fuel rods.

d. Pitch and Bow Factor

The pitch and bow factor is an allowance for the effect of enthalpy rise or the possible decreased flow rate in the subchannel resulting from a smaller than nominal subchannel flow area.

Uncertainties in fuel rod pitch and clad diameter are explicitly treated in the SCU analysis (refer to Subsection 4.4.2.2.2) to arrive at an increased DNBR limit. Hence, the pitch and bow factor is no longer used in design analyses.

4.4.2.2.3 Fuel Densification Effect on DNBR

The perturbation in local heat flux due to fuel densification is given in Table 4.4-1. Local heat flux variations much larger than the perturbation in

local heat flux due to fuel densification have no significant adverse effect on DNBR in 16 x 16 fuel assemblies. Therefore, no specific allowance is made or required for the effect on DNBR of local heat flux variations due to densification of the fuel. This effect on critical heat flux is discussed in Subsection 4.4.4.1 and reported in CENPD-207 (Reference 2).

4.4.2.3 Linear Heat Generation Rate

The core average and maximum fuel rod linear heat generation rates are given in Table 4.4-1. The maximum fuel rod linear heat generation rate is determined by multiplying the core average fuel rod linear heat generation rate by the product of the nuclear power factor, the engineering factor on linear heat rate, and the ratio of the hot to the average fuel rod energy deposition fractions. The effects of fuel densification are not included in the maximum fuel rod linear hheat generation rate presented in Table 4.4-1; although to determine the maximum local linear heat generation rate, including the effect of gaps occurring between the fuel pellets, the augmentation factor is applied.

4.4.2.4 Void Fraction Distribution

The core average void fraction and the maximum void fraction are calculated using the Maurer method (Reference 9). The void fractions discussed below are values for the reactor operating conditions and engineering factors given in Table 4.4-1 for the radial power distribution in Figures 4.4-1 and 4.4-2, and for the 1.26 peaked axial power distribution in Figure 4.4-3. For these conditions, only subcooled boiling occurs in the core.

The core average void fraction is essentially zero. The local maximum void fraction is 12.1% and occurs at the exit of the matrix subchaanel. The average exit void fractions and qualities in different regions of the core are shown in Figure 4.4-4 for the core radial power distribution shown in Figure 4.4-1. 812

The axial distribution of void fraction and quality in the matrix subchannel is shown in Figure 4.4-5. The average void fraction in that subchannel is 1.3%. 812

4.4.2.5 Core Coolant Flow Distribution

The core inlet flow distribution is required as input to the TORC thermal margin code (refer to Subsection 4.4.4.5.2). The four-loop inlet flow distribution used in the TORC analysis is based on the results obtained from the YGN 3&4 reactor flow model test program. A description of the model test is given in Section 4.4.4.2.1.

4.4.2.6 Core Pressure Drops and Hydraulic Loads

4.4.2.6.1 Reactor Vessel Flow Distribution

563

The main coolant flow path in the reactor vessel is down the annulus between the reactor vessel and the core support barrel, through the flow skirt, up through the core support region and the reactor core, through the fuel alignment plate, and out through the two reactor vessel outlet nozzles. A portion of this flow leaves the main flow path as shown schematically in Figure 4.4-6. Part of the bypass flow is used to cool the reactor internals in the areas not in the main coolant flow path and to cool the CEAs. Table 4.4-3 lists the bypass flow paths and the percent of the total vessel flow rate that flows through these paths.

563

The thermal margin calculations conservatively use the design maximum core bypass flow rate of 3% the total vessel flow rate.

4.4.2.6.2 Reactor Vessel and Core Pressure Drops

The irrecoverable pressure losses from the inlet to the outlet nozzles are calculated using standard loss coefficient methods and information obtained from YGN 3&4 flow model tests.

Pressure losses at 100% power, the nominal RCS flow rate, and an operating pressure of 2250 lb/in^2 (158 kg/cm^2) are listed in Table 4.4-4 together with the coolant temperature used to calculate each pressure loss. The calculated pressure losses include both geometric and Reynolds number dependent effects. 563

4.4.2.6.3 Hydraulic Loads on Internal Components

The significant steady state hydraulic loads that act on the reactor internals during postcore steady-state operation are listed in Table 4.4-5. These loads are determined from analytical methods and from results of reactor flow model and components test programs (refer to Subsections 4.4.4.2.1 and 4.4.4.2.2, respectively). The design hydraulic loads consist of steady-state drag and impingement loads, and the fluctuating loads induced by pump-induced pressure pulsations, vortex shedding, and turbulence. The design hydraulic loads for the reactor internals are evaluated conservatively at design maximum RCS flow rates equal to 123% and 114.1% of nominal RCS flow rate for the pre-core and post-core conditions. 563

For determining the design hydraulic loads on the vessel internals, the effects of uncertainties in the input, such as force coefficients and dimensional tolerances, are included. The effect of a 6-psi (0.42-kg/cm^2) increase in core ΔP due to crudding is added where appropriate to arrive at the final design hydraulic loads. These effects, as well as the flow rate uncertainty, are included in the fuel assembly design hydraulic uplift force.

In evaluating the design hydraulic loads, consideration is given to the particular pump operating configuration and coolant temperature that maximizes the hydraulic load for a given internal component.

All hydraulic loads in Table 4.4-5 are based on the design maximum RCS flow rate and a coolant temperature of 500°F (260°C), which is the minimum temperature to allow four-pump operation. When other coolant conditions result in more limiting loading for individual components, the loads in Table 4.4-5 are adjusted in the detailed design analysis. 563

Hydraulic loads for postulated accident conditions are discussed in Subsection 3.9.2.5.

4.4.2.7 Correlations and Physical Data

4.4.2.7.1 Heat Transfer Coefficients

The correlations used to determine cladding temperatures for nonboiling forced convection and nucleate boiling are discussed here. The surface temperature of the cladding is dependent on the axial and radial power distributions, the temperature of the coolant, and the surface heat transfer coefficient.

The surface heat transfer coefficient for nonboiling forced convection is obtained from the Dittus-Boelter correlation (Reference 10) where fluid properties are evaluated at the bulk condition.

$$h_{db}=\frac{0.023k}{D_e}(N_R)^{0.8}(N_{Pr})^{0.4} \qquad (4.4\text{-}1)$$

where:

h_{db} = heat transfer coefficient, Btu/hr-ft^2 -^{o}F

k = thermal conductivity, Btu/hr-ft-^{o}F

D_e = equivalent diameter = $4A/P_W$, ft

N_R = Reynolds number, based on the equivalent diameter and coolant properties evaluated at the local bulk coolant temperature

N_{pr} = Prandtl number, based on coolant properties evaluated at the local bulk coolant temperature

A = cross-sectional area of flow subchannel, ft^2

P_W = wetted perimeter of flow subchannel, ft

No specific allowance is made or considered necessary for the uncertainties associated with the Dittus-Boelter correlation because the Dittus-Boelter correlation is not used directly in computing thermal margin, but rather plays a part in determining pressure drop and cladding temperature. The validity of the overall scheme for predicting pressure drop is shown by the excellent agreement between predicted and experimental values obtained during the DNB test program and described in CENPD-161 (Reference 6). The uncertainty associated with the cladding temperatures calculated for single-phase heat transfer is not a major concern because the limiting fuel and cladding temperatures occur where the cladding-to-coolant heat transfer is by nucleate boiling.

The temperature drop across the surface film is calculated from the following equation:

$$\Delta T_{film} = q''/h_{db} \qquad (4.4\text{-}2)$$

where:

q'' = fuel rod surface heat flux, Btu/hr-ft^2

The maximum fuel rod heat flux is the product of the core average fuel rod heat flux and the total heat flux factor (refer to Table 4.4-1 and Subsection 4.4.2.2.2). Nucleate boiling may occur on the clad surface. In the nucleate boiling regime, the surface temperature of the cladding is determined from the Jens and Lottes correlation (Reference 11):

$$T_{wall} = T_{sat} + 60\ (q'' \times 10^{-6})^{0.25}\ \ [\exp\ (-P/900)] \qquad (4.4\text{-}3)$$

where:

P = pressure, psia
T_{sat} = saturation temperature, °F

Nucleate boiling is assumed to exist if T_{wall} is less than the sum of $T_{coolant}$ plus ΔT_{film}.

The cladding surface temperature is calculated by summing the temperature of the coolant at the particular location and the temperature drop across the surface film; if nucleate boiling occur. It is calculated directly from the Jens and Lottes correlation.

4.4.2.7.2 Core Irrecoverable Pressure Drop Loss Coefficients

Irrecoverable pressure losses through the core result from friction and geometric changes. The pressure losses through the lower and upper end fittings were initially calculated using the standard loss coefficient method and then verified by test (refer to Subsection 4.4.4.2.2). The correlations used to determine frictional and geometric losses in the core are presented in Subsection 4.4.4.2.3.

4.4.2.7.3 Void Fraction Correlations

Three separate void regions are considered in flow boiling. Region 1 is highly subcooled where a single layer of bubbles develops on heated surface and remains attached to the surface. Region 2 is a transition region from highly subcooled to bulk boiling where the steam bubbles detach from the heated surface. Region 3 is the bulk boiling regime.

The void fraction in Regions 1 and 2 is predicted using the Maurer Method (Reference 9). The calculation of the void fraction in the bulk boiling regime is discussed in Subsection 4.4.4.2.3.

4.4.2.8 Thermal Effects of Operational Transients

Design-basis limits on DNBR and fuel temperature are established so that thermally induced fuel damage will not occur during steady-state operation or during anticipated operational occurrences. The COLSS provides information to the operator so he can assure that proper steady-state conditions exist. The RPS ensures that the design limits are not violated. The COLSS provides the reactor operator with a comparison of the actual core operating power to the licensed power and to the limiting power based on DNBR and linear heat rate. An alarm is sounded if the operating power reaches one of the limiting powers. The limits are maintained by LCO using COLSS (or CPC when COLSS is out of service) to provide sufficient margin not to exceed the design-basis limits in the event that the most limiting anticipated operational occurrence occurs simultaneously with the operating power being at the limiting power in steady state.

The COLSS thermal margin algorithm is an analytical approximation to the standard thermal margin design methods described in Subsection 4.4.4.5.2.

4.4.2.9 Uncertainties in Estimates

4.4.2.9.1 Pressure Drop Uncertainties

The reactor vessel pressure losses in Table 4.4-4 are the best estimate values calculated for nominal RCS flow rate with standard loss coefficient methods. 563
The uncertainties in the correlations for the loss coefficients and the dimensional uncertainties on the reactor vessel and internals are considered when determining maximum and minimum vessel hydraulic resistance. The uncertainties at the 2σ level are estimated to be equivalent to approximately ± 10% of the best estimate vessel pressure loss.

4.4.2.9.2 Hydraulic Load Uncertainties

The effects of uncertainties in the input values are considered when determining the design hydraulic loads for normal operation (refer to Subsection 4.4.2.6.3). The uncertainties in flow rate, force and pressure coefficients, and dimensional tolerances are evaluated at the 2σ level.

4.4.2.9.3 Fuel and Clad Temperature Uncertainty

Uncertainty in the ability to predict the maximum fuel temperature is a function of gap conductance, thermal conductivities, peak linear heat rate, and heat generation distribution. Uncertainties in gap conductance and thermal conductivity are taken into account in the analytical model. Uncertainties in the peak linear heat rate are included in estimating the total nuclear peak. Uncertainties in fuel pellet density, enrichment, pellet diameter, and clad diameters are contained in the engineering factor on linear heat rate (Subsection 4.4.2.2.2).

Uncertainty in predicting the cladding temperature at the location of maximum heat flux is the uncertainty in the film temperature drop, which is minimal at

this location where nucleate boiling occurs.

4.4.2.9.4 DNBR Calculation Uncertainties

a. The uncertainty in the calculation of minimum DNBR is the result of the following uncertainties:

1. The uncertainty in the input to the core analytical model, the TORC code. This includes the core geometry, power distribution, inlet flow and temperature distribution, exit pressure distribution, single-phase friction factor constants, spacer grid loss coefficients, diversion crossflow resistance and momentum parameters, turbulent interchange constants, and hot fuel rod energy deposition fraction.

2. The uncertainty in the analytical model used to compute the actual distribution of flow and the local subchannel coolant conditions.

3. The uncertainty in the KCE-1 correlation to predict DNB.

b. The following paragraphs discuss the above uncertainties and the allowances for them, if needed, in the thermal margin analysis of the core.

1. Uncertainty in the Input to the Core Analytical Model

a) Uncertainty in core geometry, as manifested by manufacturing variations within tolerances, is considered by the inclusion of engineering factors in the DNBR analyses; see Subsection 4.4.2.2.2 for discussion of the method used to compute conservative values.

b) Uncertainties on the power distribution factors are applied in the COLSS and RPS (see Subsection 7.7).

c) The core inlet flow distribution is obtained from flow model testing discussed in Subsection 4.4.4.2. Uncertainties in the core flow distribution are included in the design method for TORC analyses.

d) Uncertainties in the core inlet temperature distribution and core exit pressure distribution are addressed in the design method for TORC analyses.

e) The Blasius single-phase friction factor equation for smooth rods is given and shown to be valid in Subsection 4.4.4.2.3. The spacer grid loss coefficient is obtained from pressure drop data discussed in Subsection 4.4.4.2.3.

f) The value of minimum DNBR is relatively insensitive to cross flow resistance and momentum parameters (Reference 6).

g) Subsection 4.4.4.1 describes the testing to determine the inverse Peclet number, which is indicative of the turbulent flow interchange between subchannels. The inverse Peclet number is input to the TORC code and is used to determine the effect of turbulent interchange on the enthalpy rise in adjacent subchannels. The selection of inverse Peclet number 0.0101 for PLUS7™ fuel is based on justification provided based on the similarity of geometric parameters with other Westinghouse fuel mixing vane grid designs for which inverse Peclet numbers have been previously addressed.

h) The same fuel rod energy deposition fraction is used for the hot rod as for the average rod. The hotter the rod, the lower the actual value of energy deposition fraction with respect to

that for the average rod. A lower energy deposition fraction reduces the hot rod heat flux and thereby increases its DNBR. The use of the average rod energy deposition fraction for the hot rod is therefore conservative. See Section 4.3 for a discussion of the calculation of the energy deposition fractions.

2. Uncertainty in the Analytical Model

The ability of the TORC code to accurately predict subchannel local conditions in rod bundles is described in CENPD-161 (Reference 6). The ability of the code to accurately predict the core wide coolant conditions is described in CENPD-206 (Reference 13). However, an allowance for TORC code uncertainty is included in the SCU analysis as discussed in Subsection 4.4.2.9.5.

3. Uncertainty in the DNB Correlation

The uncertainty in the DNB correlation is determined by a statistical analysis of DNB test data.

"Delete"

4.4.2.9.5 Statistical Combination of Uncertainty

Use of a 1.21 minimum DNBR limit with a best estimate design CETOP-D model ensures, with at least 95% probability and 95% confidence, that the hot rod will not experience a departure from nucleate boiling. The 1.21 minimum DNBR limit includes explicit allowances for system parameter uncertainties, CHF correlation uncertainty, rod bow penalty, and the NRC penalty for the TORC code uncertainty.

Several conservatisms are included in the SCU methodology (Reference 5). The significant conservatisms include the following:

a. Combination of system parameter probability density functions (PDFs) at the 95% confidence level to yield a resultant minimum DNBR limit at 95% confidence level.

b. Use of pessimistic system parameter PDFs.

c. Derivation of the new minimum DNBR limit such that it applies to both four-pump and three-pump operation.

d. Use of single most adverse set of state parameters to generate the response surface.

e. Application of NRC imposed code uncertainty penalty.

"Delete"

"Delete"

4.4.2.10 Flux Tilt Considerations

An allowance for degradation in the power distribution in the x-y plane (commonly referred to as flux tilt) is provided in the protection limit setpoints even though little, if any, tilt in the x-y plane is expected.

The tilt, along with other pertinent core parameters, is continually monitored during operation by the COLSS (described in Section 7.7). If the core margins are not maintained, the COLSS actuates an alarm to signal the operator to take corrective action. The CPCs actuate a trip if limiting safety system settings are reached.

The thermal margin calculations used in designing the reactor core are performed using the TORC and CETOP codes. The TORC and CETOP codes described in Subsection 4.4.4.5.2, are based on an open-core analytical method for performing such calculations and treat the entire core on a three-dimensional basis. Thus, any asymmetry or tilt in the power distribution is analyzed by providing the corresponding power distribution in the TORC and CETOP input.

4.4.3 Description of the Thermal and Hydraulic Design of the Reactor Coolant System (RCS)

A summary description of the RCS is given in Section 5.1.

4.4.3.1 Plant Configuration Data

4.4.3.1.1 Configuration of the RCS

An isometric view of the RCS is given in Figure 4.4-7. Dimensions are shown on the general arrangement drawings, Figures 5.1-1 and 5.1-2. Table 4.4-6 lists the valves and pipe fittings which form part of the RCS.

Table 4.4-7 lists nominal RCS flow rate and the design minimum RCS flow rate through each flow path in the RCS. 563

Table 4.4-8 provides the volume, minimum flow area, flow path length, height, and liquid level of each volume, and bottom elevation for each component within the RCS.

Components of the ECCS are to be located so as to meet the criteria for net positive suction head discussed in Section 6.3. Line lengths and sizes for the safety injection system are to be determined so as not to violate the fluid delivery rates assumed in the safety analyses described in Chapter 15 the total head losses throughout the injection lines are to be determined not to exceed the head losses deduced from the fluid delivery rate.

Table 5.1-1 provides a steady-state pressure, temperature, and flow distribution through the RCS.

4.4.3.2 Operating Restrictions on Pumps

The minimum RCS pressure at any given temperature is limited by the required net positive suction head (NPSH) for the reactor coolant pumps during portions of plant heatup and cooldown. To ensure that the pump NPSH requirements are met under all possible operating conditions, an operating curve is used which gives permissible RCS pressure as a function of temperature.

The reactor coolant pump NPSH restriction on this curve is determined by using the NPSH requirement for one-pump operation (maximum flow; hence, maximum required NPSH) and correcting it for pressure and temperature instrument errors and pressure measurement location. The NPSH required versus pump flow is supplied by the pump vendor. Plant operation below this curve is prohibited. At low reactor coolant temperature and pressure, other considerations require that the minimum pressure versus temperature curve be above the NPSH curve.

4.4.3.3 Power Flow Operating Map (BWR)

This subsection is not applicable to PWR FSAR.

4.4.3.4 Temperature-Power Operating Map (PWR)

A typical temperature-power operating map(temperature control program) is described in Subsection 5.4.10 and depicted in Figure 5.4-7. This program is based on best estimate expected RCS flow. Actual RCS flow can range between a minimum expected to maximum expected fiow as described in subsection 4.4.4.5. Since actual flow can be different from best estimate as determined during initial startup, or change based on cycle or time in cycle, an optimum temperature control program for existing conditions any time in core or plant life can be determined and programmed into appropriate control systems. The optimum program determination should include such factors as : SG efficiency, TG efficiency, maintenance of Tc within the allowable Technical Specification limits, and SG outlet steam pressure must be maintained greater than 75.2kg/cm^2 a (1070psia) at 100% rated thermal power. 17

The adequacy of natural circulation for decay heat removal after reactor shutdown has been verified analytically and by tests on the Palisades reactor (Docket No. 50-255) and Calvert Cliffs 1 (Docket No. 50-317). The core ΔT in the analysis has been shown to be lower than the normal full power ΔT; thus the thermal and mechanical loads on the core structure are less severe than normal design conditions. In addition, St. Lucie Unit 1 (Docket No. 50-335) successfully performed a cooldown from full power conditions using only natural circulation cooling following a reactor trip.

Heat removed from the core during natural circulation may be rejected either by dumping steam to the main condenser or to the atmosphere; the rate of heat removal may be controlled to maintain core ΔT within allowable limits.

4.4.3.5 Load-Following Characteristics

The design features of the RCS influence its load following and transient response. The RCS is capable of following the normal transients identified in Subsection 3.9.1.1. These requirements are considered when designing the pressurizer spray and heater systems, charging/letdown system, reactor regulating system (RRS), and feedwater control system. Finally, these transients are included in the equipment specification for each RCS component to ensure the structural integrity of the system.

When load changes are initiated, the RRS senses a change in the turbine power and positions CEAs to attain the programmed coolant average temperature. RCS boron concentration can also be adjusted to attain the appropriate coolant temperature. The feedwater system employs a controller that senses changes in steam flow, feedwater flow, and water level and acts to maintain steam-generator level at the desired point. The pressurizer pressure and level control systems respond to deviations from preselected setpoints caused by the expansion or contraction of the reactor coolant and actuate the spray or heaters and the charging or letdown systems as necessary to maintain pressurizer pressure and level.

4.4.3.6 Thermal and Hydraulic Characteristics Table

Principal thermal and hydraulic characteristics of the RCS components are listed in Table 4.4-9.

4.4.4 Evaluation

4.4.4.1 Critical Heat Flux

The margin to critical heat flux (CHF) or DNB is expressed in terms of the DNBR. The DNBR is defined as the ratio of the heat flux required to produce

DNB at the calculated local coolant conditions to the actual heat flux.

The KCE-1 correlation (Reference 3) is used with the TORC computer code (Reference 6) and the CETOP computer code (Reference 7) to determine DNBR values for normal operation and anticipated operational occurrences. The KCE-1 correlation was developed in conjunction with the TORC code specifically for DNB margin predictions for fuel assemblies with the PLUS7™ mixing vane spacer grids. Topical Report KNF-TR-SGH-04001/N/A (Reference 3) provides detailed information on the KCE-1 correlation and source data. In brief, the correlation is based on data from tests conducted for PLUS7™ fuel development at the Chemical Engineering Research Laboratories of Columbia University. Those tests used electrically heated 6 x 6 array rod bundles corresponding dimensionally to a portion of a 16 x 16 assembly with the mixing vane spacer grids.

The KCE-1 correlation (Reference 3) was developed from DNB data for 2 test sections with the following characteristics:

Fuel Assembly Geometry	No. Heated Rods	Lateral Power Distribution	Heated Length ft (m)	Axial Grid Spacing in (cm)
16 x 16	32	Non-Uniform	12.5(3.81)	15.72(39.93)
16 x 16	36	Non-Uniform	12.5(3.81)	15.72(39.93)

"Delete"

Local coolant conditions at the DNB location were determined by using the TORC code in a manner consistent with the use of the code for reactor thermal margin calculations. The local coolant properties for the non-uniform axial power distribution were assumed to be those for the uniform axial power distribution. The assumption is conservative since the critical heat flux for the uniform axial heat flux distribution is higher than that for the non-uniform axial heat flux distribution in general. The KCE-1 correlation was developed based on the conservative assumption and the same functional form of CE-1 correlation. The KCE-1 correlation predicted the 225 source data with a mean and standard deviation of the ratio of measured and predicted DNB heat fluxes of 0.9866 and 0.05304, respectively, which support the use of a 1.124 DNBR limit. The applicable parameter ranges of KCE-1 correlation are as follows:

Pressure	1395 to 2415 psia (98.1 to 169.8 kg/cm^{2}A)
Local Coolant Quality	-0.150 to 0.275
Local Mass Flux	0.85 x 10^6 to 3.15 x 10^6 lbm/hr-ft^2) (4.15 x 10^6 to 15.4 x 10^6 kg/hr-m^2)

One important factor in the prediction of DNB and local coolant conditions is the treatment of coolant mixing or turbulent interchange. The effect of turbulent interchange on enthalpy rise in the subchannels of 16 x 16 fuel assemblies with mixing vane spacer grids is calculated in the TORC code by the following equation:

"Delete"

$$\hat{P}e = \frac{w}{G\overline{D_e}} \qquad (4.4\text{-}4)$$ 812

where:

$\hat{P}e$ = inverse Peclet number
w = turbulent interchange between adjacent subchannels, lb/hr-ft
$\overline{D_e}$ = average equivalent diameter of the adjacent subchannels, ft
$\overline{G}$ = average mass velocity of the adjacent subchannels, $lb/hr\text{-}ft^2$

The inverse Peclet number, which is mainly affected by spacer grid span, increases when the spacer grid span decreases and the number decreases when the span increases. Westinghouse has used the inverse Peclet number of 0.0101 for the 26 inches mixing vane grid span fuels (Reference 12). The inverse Peclet number of 0.0101 for the PLUS7™ fuel with the 15.72 inches mixing vane grid span was determined based on the justification (Reference 12).

The design basis requires that the minimum DNBR for normal operation and anticipated operational occurrences be chosen to provide a 95% probability at the 95% confidence level that DNB will not occur on a fuel rod having that minimum DNVR. Statistical evaluation of the KCE-1 correlation and relevant data shows that the appropriate minimum DNBR is 1.124 (References 3). This limit has been increased to 1.21 for YGN 3&4 as a result of the SCU analysis (see Subsection 4.4.2.9.5).

"Delete"

4.4.4.2 Reactor Hydraulics

4.4.4.2.1 Reactor Flow Model Tests

A scale flow model test has been conducted for the YGN 3&4 reactor design as part of the NSSS system design. Reactor flow model tests have been conducted by CE in the past for several different classes of reactor design, including the System 80 reactor design. An open-core design approach was used for the model core to obtain test data for confirmation of input for the CE open core thermal margin analysis methods. Details of the YGN 3&4 reactor flow model test program are presented in Appendix 4A.

Hydraulic design parameters derived from reactor flow model test results include the core inlet flow distribution and core exit pressure distribution and pressure drops in the reactor vessel.

a. Core Inlet Flow and Core Exit Pressure Distributions

The core inlet flow and the core exit pressure distributions are required as input to the TORC code for core thermal margin analysis (refer to Subsection 4.4.4.5.2).

The core inlet flow distributions and core exit pressure distributions (for four-loop and three-loop operations) used in TORC analysis are based on the results obtained from the YGN 3&4 reactor flow model test program as described in Appendix 4A.

b. Reactor Pressure Losses

Reactor vessel pressure drop predictions other than for the core region have been verified by flow model test results. Where appropriate, corrections have been made to flow model test results to account for differences in Reynolds number and surface relative roughness between model and reactor. Reactor pressure drop predictions for the core region are based on data from CE 16 x 16 fuel assembly components tests (see Subsection 4.4.4.2.2). YGN 3&4 reactor vessel pressure drop predictions based on those test results are given in Table 4.4-4 (see Subsection 4.4.2.6.2).

4.4.4.2.2 Components Testing

Components test programs have been conducted in support of all WEC reactors. The tests subject a full-size reactor core module comprising one to five fuel assemblies, control element assembly and extension shaft, control element drive mechanism, and reactor internals to reactor conditions of water chemistry, flow velocity, temperature, and pressure under the most adverse operating conditions allowed by design. Two objectives of the programs are to confirm the basic hydraulic characteristics of the components and to verify that fretting and wear will not be excessive during the components' lifetime. When the reactor design is revised, a new program embodying the important aspects of the latest design is conducted.

Thus, components tests have been run on the Palisades design, the cruciform control elements, on the Fort Calhoun with CEAs and rack-and-pinion control element drive mechanisms (CEDMs), on the Maine Yankee design with a dual CEA and a magnetic jack CEDM, and on the Arkansas design with a 16 x 16 fuel assembly, a CEA, and magnetic jack CEDM.

During the course of the tests for PLUS7 fuel assembly components, information is obtained on fuel rod fretting and on fuel assembly uplift and pressure drop. The first subject is discussed in Section 4.2. The second is discussed below.

As part of the assessment of fuel assembly margin to uplift in the reactor, measurements are made of the flow rate required to produce fuel assembly lift-off. To obtain the desired information, the point of fuel assembly lift-off is determined from accelerometer signals.

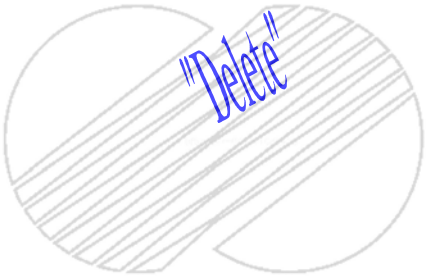

Data reduction involves the calculation of an uplift coefficient, describing the hydraulic uplift force acting on the assembly; the coefficient is defined as follows:

$$K_{up} = W_o / (\gamma V^2 A / 2g) \qquad (4.4\text{-}5)$$

where:

W_o = wet weight of assembly, lbf
V = flow velocity in assembly at the point of liftoff, ft/sec
A = envelope area of assembly, ft^2
γ = water specific weight, lbf/ft^3
g = gravitational constant, ft/sec^2

A plot of the Kup data shows that they can be fitted by the relation:

$$Kup = \alpha N_R^{-\beta} \qquad (4.4\text{-}6)$$

where α and β are peculiar to the particular components test being run and the standard error of estimate is typically 4%, including replication and instrument error.

The uplift coefficient and its associated uncertainty are employed in the analysis of the uplift forces on the fuel assemblies in the reactor. The force is determined for the most adverse assembly location for startup and normal operating conditions. Additional input to the calculation includes analytical corrections to the coefficient for the absence of the CEA, for crud formation, and for small geometrical differences among the fuel assemblies for the different reactor designs all nominally describable by the same components test.

Pressure measurements are also made during the components test to verify the accuracy of the calculated loss coefficients for various fuel assembly components. Direct reduction of the pressure drop data yields the loss coefficients for the lower and upper end fitting region, while the spacer grid loss coefficient is evaluated by subtracting a calculated fuel rod friction loss from the measured pressure drop across the fuel rod region.

Experience has shown that the experimental end fitting loss coefficients are essentially independent of Reynolds Number and, with their sample standard deviations, are in reasonable agreement with the predicted values used in the calculation of core pressure drop (Subsection 4.4.2.6). The design value for the 16 x 16 PLUS7 fuel assembly spacer grid is based upon experimental results from the 16 x 16 fuel assembly design components test program.

As described in Section 4.2, a components test was performed on the System 80 reactor design. The test hardware consists of five fuel assemblies, core support structure, CEA shroud, control element assembly, and drive mechanism.

"Delete"

4.4.4.2.3 Core Pressure Drop Correlations

The total pressure drop along the fuel rod region of the core is computed as the sum of the individual losses resulting from friction, acceleration of the fluid, the change in elevation of the fluid, and spacer grids. The individual losses are computed using the momentum equation and the consistent set of empirical correlations presented in the TORC code (Reference 65).

In the following paragraphs, the correlations used are summarized and the validity of the scheme is demonstrated with a comparison of measured and predicted pressure drops for single-phase and two-phase flow in fuel assembly with CEA-type geometry.

For isothermal, single-phase flow, the pressure drop due to friction for flow along the bare rods is based on the equivalent diameter of the bare fuel assembly and the Blasius friction factor:

$$f = 0.184\ N_R^{-0.2} \qquad (4.4\text{-}7)$$

The pressure drop associated with the spacer grids is computed using a grid loss coefficient (K_{SG}) given by a correlation that has the following form:

$$K_{SG} = D_1 + D_2\ N_R^{D3} \pm \text{Standard Error of Estimate} \qquad (4.4\text{-}8)$$

The constants, D_n, are determined from pressure drop data obtained for a wide range of Reynolds Numbers for isothermal flow through a big guide tube-type fuel assembly fitted with the mixing vane spacer grids. The data come from a components test program on a 16 x 16 fuel assembly design (Subsection 4.4.4.2.2). The standard error of estimate associated with the loss coefficient relation includes replication and instrument error.

To compute pressure drop either for heating without boiling or for subcooled boiling, the friction factor given above for isothermal flow is modified through the use of the multipliers given by Pyle (Reference 14). The multipliers were developed to incorporate the effects of subcooled voids on the acceleration and elevation components of the pressure drop as well as the effect on the friction losses. Consequently, it is not necessary to compute specifically either a void fraction for subcooled boiling or the individual effects of subcooled boiling on the friction, acceleration, or elevation components of the total pressure drop.

The effect of bulk boiling on the friction pressure drop is computed using a curve fit to the Martinelli-Nelson data (Reference 15) above 2000 psia (140.6 kg/cm^2A) or the Martinelli-Nelson correlation (Reference 15) with the modification given by Pyle (Reference 14) below 2000 psia (140.6 kg/cm^2A). The acceleration component of the pressure drop for bulk boiling conditions is computed in the usual manner for the case of two-phase flow where there may be a nonunity slip ratio (Reference 16). The elevation and spacer grid pressure drops for bulk-boiling are computed as for single-phase flow except that the bulk coolant density ($\bar{\rho}$) is used, where:

$$\bar{\rho} = \alpha \rho_V + (1-\alpha)\rho_L \qquad (4.4\text{-}9)$$

and where:

α = bulk boiling void fraction
ρ_V = density of saturated vapor, lb/ft^3
ρ_L = density of saturated liquid, lb/ft^3

The bulk boiling void fraction used in computing the elevation, acceleration, and spacer grid losses is calculated by assuming a slip ratio of unity if the pressure is greater than 1850 psia (130 kg/cm^{2}A) or by using the Martinelli-Nelson void fraction correlation (Reference 15) with the modifications presented by Pyle (Reference 14) if the pressure is below 1850 psia (130 kg/cm^{2}A).

To verify that the scheme described above accurately predicts pressure drop for single-phase and two-phase flow through the 16 x 16 assembly, geometry comparisons have been made of measured pressure drop and the pressure drop predicted by TORC (Reference 6) for the rod bundles used in the DNB test program at Columbia University (refer to Subsection 4.4.4.1). Figure 6.7 of CENPD-161 (Reference 6) shows some typical results for a 21-rod fuel assembly of the 16 x 16 fuel assembly geometry (5 x 5 assembly with four rods replaced by a control element guide tube). The excellent agreement demonstrates the validity of the methods described above.

4.4.4.3 Influence of Power Distributions

The reactor operator, utilizing the COLSS, will restrict operation of the plant such that power distributions that are permitted to occur will have an adequate margin to satisfy the design bases during anticipated operational occurrences. A discussion of the methods of controlling the power distributions is given in Subsection 4.3.2.4.2. A discussion of the expected power distributions is given in Subsection 4.3.2.2.3, and typical planar rod radial power factors and axial shapes are given in Figures 4.3-3 through 4.3-23. The

full power maximum rod radial power factor is taken as 1.60 and is used in the calculations of the core thermal margins that are given here in Section 4.4. Comparison with expected power distributions, discussed in Section 4.3, shows that this integrated rod radial power factor is at least 3% higher than all the calculated values and, therefore, is a meaningful value for thermal margin analyses.

If CEAs or PSCEAs are inserted in the core, the same planar radial power distribution does not exist at each axial elevation of the core, nor does the same axial power distribution exist at each radial location in the core. From the analysis of many three-dimensional power distributions, the important parameters that establish the thermal margin in the core are the maximum rod power and its axial power distribution (Reference 13). Examination of many axial power distributions shows that 1.26 peaked axial power distribution in Figure 4.4-3 to be among those giving the lowest DNBRs. The combination of that axial shape and the maximum rod radial power factor of 1.60 is therefore a meaningful combination for DNB analyses. The maximum linear heat rate at a given power is determined directly from the core average fuel rod linear heat rate and the nuclear power factor. The value of 2.35 for the nuclear power factor is selected and corresponds to the 1.60 rod radial power factor combined with the 1.47 peaked axial shape shown in Figure 4.4-3. As stated before, the supervisory and protection systems measure the maximum rod radial power factor and the axial power distribution in the core and ensure that the design limits specified in Subsection 4.4.1 are not violated.

4.4.4.4 Core Thermal Response

Steady-state core parameters are summarized in Table 4.4-1 for normal four-pump operation. Figure 4.4-8 shows the sensitivity of the minimum DNBR to small changes in pressure, inlet temperature and flow from the conditions specified in Table 4.4-1. The same 1.26 peaked axial power distribution and 1.60 maximum rod radial power factor are used.

The response of the core to anticipated operational occurrences is discussed in Chapter 15. The response of the core at the design overpower cannot be presented with any meaning. The concept of a design overpower is not applicable to YGN 3&4 cores since the RPS prevents the design basis limits from being exceeded.

The supervisory and protection systems ensure that the design bases in Subsection 4.4.1 are not violated for any steady-state operating condition of inlet temperature, pressure, flow, power, and core power distributions or for the anticipated operational occurrences discussed in Chapter 15.

4.4.4.5 Analytical Methods

4.4.4.5.1 Reactor Coolant System Flow Determination

The design minimum RCS flow rate to be provided by the reactor coolant pumps is established by the required mass flow rate to result in no violation of the design limits in Subsection 4.4.1 during steady-state operation and anticipated operational occurrences. This design minimum RCS flow rate is specified in Table 4.4-1. 563

The reactor coolant pumps are sized to produce a flow rate greater than or equal to the design minimum RCS flow rate for the maximum expected system flow resistance. The maximum system flow resistance is determined by adding an allowance for uncertainty to the best estimate system flow resistance. From this maximum system flow resistance, the required minimum reactor coolant pump head is determined.

Upon completion of the manufacturing and testing of the pumps, the characteristic pump head or performance curve is established. The expected maximum, best estimate, and minimum reactor coolant system flow rates are determined as follows:

a. Best Estimate Expected Flow

The best estimate expected RCS flow is determined by equating the head loss around the reactor coolant flow path to the head rise supplied by the reactor coolant pumps (Subsection 5.4.1 has a description of the pumps).

b. Maximum Expected Flow

The maximum expected flow is determined in a manner analogous to the best estimate expected flow except that statistical techniques are employed. A pump performance curve probability distribution for each pump is calculated by statistically combining measurement uncertainties in flow and head. The uncertainties are based on performance and acceptance testing done at the pump vendor's facility. The system head loss uncertainty distributions are evaluated by statistically combining the uncertainties in the correlations for loss coefficients and normal manufacturing tolerances about nominal dimensions. The expected flow rate probability distribution is determined from the statistical combination of the respective pump curve probability distributions and the probability distributions for the system resistances. This probability distribution for the expected flow rate is used in turn to define the maximum and minimum expected flow rates. The maximum expected flow rate is defined by the upper flow rate limit on the expected flow rate probability distribution above which the actual flow rate has only a 5% probability of existing. This maximum expected flow rate will be equal to or less than the design maximum flow.

c. Minimum Expected Flow

The minimum expected flow is also determined by using the expected

flow rate probability distribution discussed above. The minimum expected flow rate is defined as the lower flow rate limit on the expected flow rate probability distribution below which the actual flow rate has only a 5% chance of existing. This minimum expected flow rate will be equal to or greater than the design minimum flow.

Upon installation of the pumps in the reactor coolant system, the operating flow is determined by one or more of the following flow measurement techniques:

a. Pump casing differential pressure method, using a correlation between pump casing differential pressure and flow rate

b. Calorimetric methods (may be a heat balance performed on either the primary or secondary coolant)

c. Other nonintrusive flow measurement methods such as ultrasonic flow meters

The uncertainties included in the calculation of the operating flow are those uncertainties associated with the measurement technique or techniques used above. These uncertainties are statistically combined to give the overall uncertainty in primary coolant flow as determined from onsite tests. The best estimate flow reduced for uncertainties shall be greater than the design minimum flow.

Any significant formation of crud buildup is detected by continuous monitoring of the reactor coolant system flow. A significant buildup of crud is not anticipated, however, due to the design of the water chemistry.

4.4.4.5.2 Thermal Margin Analysis

Thermal margin analyses of the reactor core are performed using the TORC code which is an open core analytical method based on the COBRA-III C code (Reference 17) and the CETOP code. A complete description of the TORC code and application of the code for detailed core thermal margin analyses is contained in CENPD-161 (Reference 6). A simplified procedure used to apply the TORC code for design thermal margin calculations is described in detail in CENPD-206 (Reference 13). The CETOP code, derived from the same theoretical bases as TORC, is streamlined for use in the thermal margin analyses. A complete description of CETOP is provided in CEN-214(A) (Reference 7). A brief description of the codes and their use is given here.

The COBRA-III C code solves the conservation equations for mass, axial and lateral momentum, and energy for a collection of parallel flow channels that are hydraulically open to each other. Since the size of a channel in design varies from the size of fuel assembly or more to the size of a subchannel within a fuel assembly, certain modifications were necessary to enable a realistic analysis of thermal-hydraulic conditions in both geometries. The principal revisions to arrive at the TORC code, which leave the basic structure of COBRA-III C unaltered, are in the following areas:

a. Modification of the lateral momentum equation for core wide calculations where the smallest channel size is typically that of a fuel assembly.

b. Addition of the capability for handling nonzero lateral boundary conditions on the periphery of a collection of parallel flow channels. This capability is particularly important when analyzing the group of subchannels within the hot fuel assembly.

c. Addition of the capability to handle nonuniform core exit pressure distributions.

d. Insertion of standard WEC empirical correlations and the ASME fluid property relationships.

Details of the lateral momentum equations and the empirical correlations used in the TORC code are given in CENPD-161 (Reference 6).

The application of the TORC code for detailed core thermal margin calculations typically involves two or three stages. The first stage consists of calculating coolant conditions throughout the core on the coarse mesh basis. The core is modeled such that the smallest unit represented by a flow channel is a single fuel assembly. The three-dimensional power distribution in the core is superimposed on the core coolant inlet flow and temperature distributions. The core inlet flow and core exit static pressure distribution are obtained from flow model tests discussed in Subsection 4.4.4.2, and the inlet temperature for normal four loop operation is assumed uniform. The axial distributions of flow and enthalpy in each fuel assembly are then calculated on the basis that the fuel assemblies are hydraulically open to each other. Also determined during this stage are the transport quantities of mass, momentum, and energy that cross the lateral boundaries of each flow channel.

In the second stage, typically the hot assembly and adjoining fuel assemblies are modeled with a coarse mesh. The hot assembly is typically divided into four to five partial assembly regions. One of these regions is centered on the subchannels adjacent to the rod having the minimum DNBR. The three-dimensional power distribution is superimposed on the core coolant inlet flow and temperature distributions. The lateral transport of mass, momentum, and energy from the stage-one calculations is imposed on the peripheral boundary enclosing the hot assembly and the neighboring assemblies. The axial distributions of flow and enthalpy in each channel are calculated as well as the

transport quantities of mass, momentum, and energy that cross the lateral boundary of each flow channel. In some cases, the hot assembly detail normally included in the second stage is included in the first stage, thereby eliminating the need for the intermediate stage. In these cases, the second stage is the subchannel model discussed below.

The third stage involves a fine mesh modeling of the partial assembly region that centers on the subchannels adjacent to the rod having the minimum DNBR. All of the flow channels used in this stage are hydraulically open to their neighbors. The output from the stage-two calculations, in terms of the lateral transport of mass, momentum, and energy, is imposed on the lateral boundaries of the stage three partial assembly region. Engineering factors are applied to the minimum DNBR rod and subchannel to account for uncertainties on the enthalpy rise and heat flux due to manufacturing tolerances. The local coolant conditions are calculated for each flow channel. These coolant conditions are then input to the DNB correlation and the minimum value of DNBR in the core is determined.

A more detailed description of this procedure with example is contained in CENPD-161 (Reference 6). This procedure is used to analyze in detail any specific three-dimensional power distribution superimposed on an explicit core inlet flow distribution. The detailed core thermal margin calculations are used primarily to develop and to support the simplified design core thermal margin calculational scheme discussed below.

The method used for design calculations is discussed in detail in CENPD-206 (Reference 13). In summary, the method is to use one limiting hot assembly radial power distribution for all analyses, to raise or lower the hot assembly power to provide the proper maximum rod radial power factor, and to use the core average mass velocity in all fuel assemblies except the hot assembly. The appropriate reduction for the hot assembly mass velocity is determined based upon the results of the YGN 3&4 flow model tests (see Subsection

4.4.4.2.1). This methodology is used in the thermal margin analyses of the YGN 3&4 reactors.

The CETOP code (Reference 7), a variant of the TORC code, is used as a design code for YGN 3&4 thermal margin analyses. CETOP has the same theoretical bases as TORC, but has been improved to reduce execution time. The CETOP code uses the transport coefficients to obtain accurate determination of diversion crossflow and turbulent mixing between adjoining channels with a less detailed calculational model. Furthermore, a prediction-correction method is used to solve the conservation equations, replacing the iterative method used in the TORC code, and thereby reducing execution time. The conservatism of CETOP relative to TORC is assured by benchmarking analyses which demonstrate that CETOP yields accurate or conservative DNBR results relative to TORC.

4.4.4.5.3 Hydraulic Instability Analysis

Flow instabilities leading to flow excursions or flow oscillations have been observed in some boiling flow systems containing one or more closed, heated channels. Flow instability phenomena are a concern primarily because they may lead to a reduction in the DNB heat flux relative to that observed during a steady flow condition. Flow instabilities are not, however, expected to reduce thermal margin in WEC PWRs during normal operation or anticipated operational occurrences. This conclusion is based upon available literature, experimental evidence, and the results of core flow stability analyses.

Review of the available information on boiling systems has resulted in the following qualitative observations. Flow instabilities that have been observed have occurred almost exclusively in closed-channel systems operating at low pressures relative to PWR operating pressures. Increasing pressure has been found to have a stabilizing influence in many cases where flow instabilities have been observed (Reference 18), and the high operating pressure characteristic of PWRs minimizes the potential for flow instability. For PWR

operating pressures, experimental results (Reference 19) have shown that, even with closed channel systems, operating limits due to the occurrence of critical heat flux (CHF) are encountered before the flow stability threshold is reached. It would be expected that the low resistance to coolant crossflow among subchannels of WEC PWR fuel assemblies would have a stabilizing effect, and that expectation is confirmed by experimental results (References 20, 21, and 22), which show that flow stability in parallel heated channels is enhanced by cross connections between the channels.

Experimental evidence that flow instabilities will not adversely affect thermal margin is provided by the data from the rod bundle DNB tests conducted by WEC (References 1 and 2); many rod bundles have been tested over wide ranges of operating conditions with no evidence of premature DNB or of inconsistent data that might be indicative of flow instabilities in the rod bundle.

Analytical support for the conclusion that flow instabilities will not reduce the thermal margin of WEC PWRs is provided in Reference 23. That document presents an assessment of core flow stability for a typical WEC PWR. The assessment was made using the CE-HYDNA code, the WEC version of HYDNA flow stability code presented in Reference 24. In addition to the WEC PWR flow stability assessment, Reference 23 contains the following information:

a. A description of the CE-HYDNA flow stability code

b. A user's manual and FORTRAN listing of the CE-HYDNA code

c. Results of sensitivity studies and of code verification through comparison with experimental data

The CE-HYDNA code provides the fundamental analytical tool for the assessment of flow stability in WEC PWRs. The code has the capability of analyzing transient one-dimensional flow phenomena in several groups of laterally closed

channels with common entrance and exit plenums. The use of CE-HYDNA for analysis of open-array WEC PWR cores is conservative because the stabilizing effects of interchannel communication (References 20, 21, and 22) are neglected.

The results presented in Reference 23 are for a WEC 3450 MWt class reactor but those results are representative of all WEC PWRs. It was found that, for nominal coolant conditions, the flow is stable throughout the range of reactor power levels examined (100% - 250% rated power). Additional calculations were performed covering a wide range of operating conditions. These calculations showed that, even under severely adverse operating conditions, the flow is stable at greater than 100% of rated power. The results provide additional evidence that flow instabilities will not adversely affect core thermal margin during normal operation or anticipated operational occurrences.

4.4.5 Testing and Verification

Data descriptive of thermal and hydraulic conditions within the reactor vessel will be obtained as part of the startup program.

4.4.6 Instrumentation Requirements

The incore instrumentation system will be used to confirm core power distributions and assist in the calibration of the excore flux measurement system. Further descriptions are contained in Section 7.7.

4.4.7 References

1. "Critical Heat Flux Correlation for C-E Fuel Assemblies with Standard Spacer Grids, Part 1, Uniform Axial Power Distribution," September 1976, CENPD-162-P-A (Proprietary), CENPD-162-A (Non-Proprietary).

2. "Critical Heat Flux Correlation for C-E Fuel Assemblies with Standard Spacer Grids, Part 2, Non-Uniform Axial Power Distributions," December 1984, CENPD-207-P-A (Proprietary), CENPD-207 (Non-Proprietary).

3. "KCE-1 임계열속 상관식(KCE-1 Critical Heat Flux Correlation)", KNF-TR-SGH-04001/N/A, October 2004.

4. Safety Evaluation by the Office of Nuclear Reactor Regulation Related to the Operation San Onofre Units 2 and 3, Supplement 4, Docket No. 5D-361 and 5D-362.

5. "Modified Statistical Combination of Uncertainties", CEN-356(V)-P-A, Revision 1-P-A, Combustion Engineering, May 1988.

6. "TORC Code: A Computer Code for Determining the Thermal Margin of a Reactor Core," July 1975, CENPD-161-P-A (Proprietary), CENPD-161 (Non-Proprietary).

7. "CETOP-D Code Structure and Modeling Methods for Arkansas Nuclear One Unit 2," Combustion Engineering Topical Report CEN-214(A)-P, July 1982.

8. "C-E Fuel Evaluation Model Topical Report," Combustion Engineering, Inc., CENPD-139 (Proprietary), CENPD-139 Rev. 01 (Non-Proprietary), CENPD-139 Supplement 1 (Proprietary), CENPD-139 Supplement 1, Rev. 01 (Non-Proprietary), July 1974.

9. G. W. Maurer,"A Method of Predicting Steady State Boiling Vapor Fractions in Reactor Coolant Channels," Bettis Technical Review, WAPD-BT-19, Reactor Technology, June 1960.

10. F. W. Dittus and L. M. K. Boelter, "Heat Transfer in Automobile Radiators of the Tubular Type," University of California Publication in Engineer Vol. 2, No. 13, pp. 443-461, 1930.

11. W. H. Jens and P. A. Lottes,"Analysis of Heat Transfer, Burnout, Pressure Drop, and Density Data for High Pressure Water," ANL-4627, May 1,1951.

12. "TDC(Thermal Diffusion Coefficient) for KAFD Fuel", CN-KAFD-01-1, 2001.

13. "TORC Code Verification and Simplified Modeling Methods," CENPD-206-P-A, (Proprietary), CENPD-206-A (Non-Proprietary), June 1981.

14. R. S. Pyle, "A Program for the Thermal Analysis of a Pressurized Water Nuclear Reactor During Steady-State Operation, STDY-3," WAPD-TM-213, June 1960.

15. R. C. Martinelli and D. B. Nelson, "Prediction of Pressure Drop During Forced Circulation Boiling of Water," ASME Transactions, August 1948.

16. O. J. Mendler et al.,"Natural Circulation Tests with Water at 800 to 2000 psia Under Non-Boiling, Local Boiling, and Bulk Boiling Conditions," Journal of Heat Transfer, August 1961.

17. D. S. Rowe, "COBRA-IIIC: A Digital Computer Program for Steady-State and Transient Thermal-Hydraulic Analysis of Rod Bundle Nuclear Fuel Elements," BNWL-1695, March 1973.

18. J. A. Boure, A. E. Bergles, and L. S. Tong, "Review of Two-Phase Flow Instability," ASME Paper 71-HT-42, August 1971.

19. H. S. Kao, C. D. Morgan, and M. B. Parker,"Prediction of Flow Oscillation in Reactor Core Channel," ANS Transactions, Vol. 16, p. 212, 1973.

20. T. N. Veziroglu and S. C. Lee, "Boiling-Flow Instabilities in a Cross-Connected Parallel-Channel Upflow System," ASME Paper 71-HT-12, August 1971.

21. S. Kakac et al., "Transient Boiling Flow Instabilities in a Four Parallel Channel Upflow System," Proceedings of Condensed Papers of the Two-Phase Flow and Heat Transfer Symposium-Workshop, October 18-20, 1976, pp.175-181.

22. RESAR-3S, Volume 2, Section 4.4.3.5, July 1975.

23. Letter to J. F. Stolz, USNRC, from D. H. Williams, Arkansas Power & Light Co., January 16, 1978, and enclosure, "Assessment of Core Flow Stability for C-E PWRs," CEN-64(A)-P (Proprietary) and CEN-64(A) (Non-Proprietary), July 1977.

24. H. B. Currin, et al., "HYDNA-Digital Computer Program for Hydrodynamic Transients in a Pressure Tube Reactor or a Closed Channel Core," Report CVNA-77, 1961.

"Delete"

TABLE 4.4-1 (Sh. 1 of 4)

THERMAL AND HYDRAULIC PARAMETERS

REACTOR PARAMETERS	YGN 3&4 (PLUS7)	SYSTEM 80 CESSAR-F (DOCKET-STN-50-470F)	ARKANSAS NUCLEAR ONE UNIT 2 (DOCKET NO.50-368)	
Core Average Characteristics at Full Power:				563
Total core heat output, MWt	2815	3,800	2,815	
Total core heat output, million Btu/h (million Kcal/hr)	9608 (2421)	12,970	9,608	
Average fuel rod energy deposition fraction	0.975	0.975	0.975	
Hot fuel rod energy deposition fraction	0.975	0.975	0.975	
Primary system pressure psia (kg/cm^2)	2,250 (158)	2,250	2,250	
Reactor inlet coolant temperature, °F (°C)	564.5 (296)	565	553	
Reactor outlet coolant temperature, °F (°C)	624 (329)	621	612	812
Core exit average coolant temperature, °F (°C)	625 (330)	624	614	
Average core enthalpy rise, Btu/lbm (kcal/kg)	85.8 (47.7)	82	82.7	

TABLE 4.4-1 (Sh. 2 of 4)

REACTOR PARAMETERS	YGN 3&4 (PLUS7)	SYSTEM 80 CESSAR-F (DOCKET-STN-50-470F)	ARKANSAS NUCLEAR ONE UNIT 2 (DOCKET NO.50-368)
Design minimum RCS flow rate, gal/min (L/min)	313,500 (1.187×10^6)	445,600	322,000
Design maximum core bypass flow rate, % of RCS flow rate	3.0	3.0	3.5
Design minimum core flow rate, gal/min (L/min)	304,000 (1.151×10^6)	432,000	310,700
Hydraulic diameter of nominal subchannel, in. (cm^2)	0.498 (1.264)	0.471	0.471
Core flow area, ft^2 (m^2)	46.21 (4.293)	60.8	44.7
Core avg mass velocity, million lbm/hr-ft^2 (million kg/hr-m^2)	2.42 (11.82)	2.61	2.60
Core avg coolant velocity, ft/sec (m/sec)	15.4 (4.69)	16.6	16.4
Core avg fuel rod heat flux, Btu/hr-ft^2 (kcal/hr-m^2)	183,545 (497,859)	184,400	185,000
Total heat transfer area, ft^2 (m^2)	51,023 (4,740)	68,600	51,000
Average fuel rod linear heat rate kW/ft (W/cm)	5.26 (172.6)	5.40	5.41

TABLE 4.4-1 (Sh. 3 of 4)

REACTOR PARAMETERS	YGN 3&4 (PLUS7)	SYSTEM 80 CESSAR-F (DOCKET-STN-50-470F)	ARKANSAS NUCLEAR ONE UNIT 2 (DOCKET NO. 50-368)
Power density, kW/L	96.6	95.6	96.6
No. of active fuel rods	41,772	54,956	40,644
Power Distribution Factors:			
Rod radial power factor	1.60	1.55	1.55
Nuclear power factor	2.35	2.28	2.28
Total heat flux factor	2.42	2.35	2.35
Maximum augmentation factor	1.00	1.00	1.00
Engineering Factors:			
Engineering heat flux factor	1.03	1.03	1.03
Engineering factor on linear heat rate	1.03	1.03	1.03
Engineering enthalpy rise factor	1.03	1.03	1.03
Maximum fuel rod heat flux, Btu/hr-ft^2 (kcal/hr-m^2)	444,648 (1.206×10^6)	433,000	433,800

TABLE 4.4-1 (Sh. 4 of 4)

REACTOR PARAMETERS	YGN 3&4 (PLUS7)	SYSTEM 80 CESSAR-F (DOCKET-STN-50-470F)	ARKANSAS NUCLEAR ONE UNIT 2 (DOCKET NO.50-368)
Maximum fuel rod linear heat rate, kW/ft (W/cm)	12.7 (417.8)	12.7	12.7
UO2 maximum steady state temperature, °F (°C)	3,137 (1,725)	3,200	3,420
Characteristics of Channel with Minimum DNBR:			
Outlet temperature, °F (°C)	653 (345)	652	652.6
Outlet enthalpy, Btu/lbm (kcal/kg)	706 (392)	699	704
Minimum DNBR at nominal condition (CHF correlation)	2.16(KCE-1)	1.79(CE-1)	2.14(W-3 correlation)

TABLE 4.4-2

COMPARISON OF THE DEPARTURE FROM NUCLEATE BOILING RATIONS COMPUTED WITH DIFFERENT CORRELATIONS

	DNBRs FOR NOMINAL REACTOR CONDITIONS		DNBRs FOR REACTOR CONDITIONS GIVING A 1.21 KCE-1 MINIMUM DNBR	
CORRELATION	MATRIC SUBCHANNEL	SUBCHANNEL NEXT TO GUIDE TUBE	MATRIX SUBCHANNEL	SUBCHANNEL NEXT TO GUIDE TUBE
KCE-1	2.270	2.186	1.238	1.233
CE-1	2.025	1.724	0.923	0.823

TABLE 4.4-3

DESIGN REACTOR COOLANT FLOWS IN BYPASS CHANNELS

BYPASS ROUTE	PATHS *	PERCENT OF TOTAL VESSEL FLOW
Outlet nozzle clearances	1	1.30
Alignment keyways	6	0.60
Core shroud annulus	3	0.39
Instrumented center guide tubes	2	0.07
Non-instrumented center guide tubes	4	0.20
Corner guide tubes	5	0.45
Total bypass	All	3.00

* See Figure 4.4-6

TABLE 4.4-4

REACTOR VESSEL BEST ESTIMATE PRESSURE LOSSES AND COOLANT TEMPERATURES AT NOMINAL RCS FLOW RATE 563

COMPONENT	PRESSURE LOSS (lb/in^2)	PRESSURE LOSS (kg/cm^2)	TEMPERATURE (°F)	TEMPERATURE (°C)
Inlet nozzle and 90° turn	6.4	0.45	564.5	296
Downcomer, lower plenum, and support structure	11.6	0.82	564.5	296
Fuel assembly	20.3	1.43	594.0	312
Fuel assembly outlet to outlet nozzle	17.5	1.23	623.6	329
Total pressure loss	55.8	3.93		

TABLE 4.4-5 (Sh. 1 of 2)

DESIGN STEADY-STATE HYDRAULIC LOADS
ON VESSEL INTERNALS AND FUEL ASSEMBLIES
(Postcore Load Values at 500°F)

COMPONENT	STEADY-STATE LOAD DESCRIPTION	LOAD VALUE
1. Core support barrel	Radial pressure differential directed inward opposite inlet duct	96.8 lb/in^2 (6.81 kg/㎠)
	Uplift load	1.11 x 10^6 lb (5.0 x 10^5 kg)
	Lateral load	0.17 x 10^6 lb (7.7 x 10^4 kg)
2. Upper guide structure	Uplift load	0.62 x 10^6 lb (2.8 x 10^5 kg)
	Lateral load	290 x 10^3 lb (132.0x10^3kg)
3. Flow skirt	Radial pressure differential directed inward	43 max. psi (3.02 kg/㎠) 19 avg. psi (1.34 kg/㎠)
	Axial load directed downward	2348 max. lb/ft of circ. (3494 kg/m) 1072 avg. lb/ft of circ. (1595 kg/m)
4. Instrumentation plate supports	Lateral drag load directed inward	14.9 psi max. support (1.05 kg/㎠)
5. Instrumentation support plate	Uplift load	964 lb (437 kg)
6. Instrumentation tube	Lateral drag load directed inward	2244 lb max./tube (1018 kg)
7. Bottom plate	Drag load directed upward	58,600 lb (26,581 kg)

TABLE 4.4-5 (Sh. 2 of 2)

COMPONENT	STEADY-STATE LOAD DESCRIPTION	LOAD VALUE	
8. Lower support structure beams	Drag load directed inward	954 lb (433 kg)	
	Lateral assembly load	4620 lb (2096 kg)	
9. Fuel assembly	Uplift load	2550 lb (1157 kg)	1
10. Core shroud	Radial pressure differential	30.3 lb/in^2 bottom (2.13 kg/cm^2)	
	directed outward	0.0 lb/in^2 top (0.0 kg/cm^2)	
11. Fuel alignment plate	Drag load directed upward	257,800 lb (116,938 kg)	
12. CEA guide tube	Lateral drag load	1043 lb, max./tube (473 kg)	1
13. Upper guide plate	Load directed downward	22,200 lb (10,070 kg)	
14. Guide structure support system	Axial and radial pressure differentials	0.1 lb/in^2(0.007 kg/cm^2)	1

TABLE 4.4-6 (Sh. 1 of 3)

RCS VALVES AND PIPE FITTINGS

PRESSURE BOUNDARY VALVES

VALVE	VALVE NO.	SIZE (inch) (mm)	QUANTITY
Reactor vessel vent	RC-212	3/4 (19)	1
Refueling level indicator	RC-214, RC-358	3/4 (19)	2
RCS drains	RC-215, 216, 232, 332, 233, 333, 234, 334, 235, 335	2 (51)	10
Reactor coolant pump (RCP)	RC-248, 249, 252, 253, 256, 257, 260, 261	3/4 (19)	8
Pressurizer level indicator	RC-206, 207, 208, 209	3/4 (19)	4
Pressurizer pressure indicator	RC-204, 205	3/4 (19)	2
Pressurizer safety	RC-200, 201, 202	6x8 (152x203)	3
Pressurizer spray line	RC-240, 241, 242, 243, 236, 237	3 (76) 3/4 (19)	4 2
Pressurizer spray line control	RC-100E, 100F	3 (76)	2
Pressurizer spray line check	RC-244	4 (102)	1
Sample system	RC-210, 213, 238	3/4 (19)	3
Reactor vessel closure head leakoff	RC-211, RC-403	3/4 (19)	2
RCS pressure differential	RC-292, 293, 294, 295, 296, 297, 298, 299	3/4 (19)	8
Steam Generator Drain (primary side)	RC-350, 351, 352, 353 354, 355, 356, 357	3/4 (19)	8

TABLE 4.4-6 (Sh. 2 of 3)

VALVE	VALVE NO.	SIZE (inch)	(mm)	QUANTITY
RCP seal housing drain	RC-752, 753, 754, 755	3/4	(19)	4
RCP Vent	RC-712, 713, 714, 715	3/4	(19)	4
RCP HP cooler	RC-446, 447, 448, 449, 450, 451, 452, 453	1	(25)	8
RCP filter drain	RC-868, 869, 870, 871, 700, 701, 702, 703	1	(25)	8
RCP seal cooler pressure	RC-724, 725, 726, 727, 736, 737, 738, 739	1	(25)	8
RCP controlled bleedoff	RC-430, 431, 432, 433,	1	(25)	4
	344, 345, 346, 347	3/4	(19)	4
RCP vapor seal pressure indicator	RC-380, 381, 382, 383	1	(25)	4
RCP pressure differential	RC-248, 249, 252, 253 256, 257, 260, 261	3/4	(19)	8
RV leakoff line pressure indicator	RC-217	3/4	(19)	1
Steam generator pressure differential (primary side)	RC-270, 271, 272, 273 274, 275, 276, 277 278, 279, 280, 281 282, 283, 284, 285	3/4	(19)	16
RCP oil drain	RC-756, 757, 758, 759 790, 791, 792, 793	2	(51)	8
RCP motor drain	RC-761, 762, 763, 764	3/4	(19)	4
RCP oil reservoir	RC-800, 801, 802, 803 796, 797, 798, 799 320, 321, 322, 323 719, 718, 717, 716	1/2	(13)	16
RCP oil reservoir Drain	RC-112, 113, 114, 115	1/2	(13)	4

TABLE 4.4-6 (Sh. 3 of 3)

RCS PIPE FITTINGS

ELBOWS	SIZE (inch)	SIZE (mm)	RADIUS (inch)	RADIUS (mm)	QUANTITY
35°	42	(1067)	63	(1600)	2
45°	30	(762)	45	(1143)	4
90°	30	(762)	45	(1143)	8
44°9′	30	(762)	45	(1143)	4

TABLE 4.4-7

NOMINAL AND DESIGN MINIMUM RCS FLOW RATES

	Nominal RCS Flow Rate		Design Minimum RCS Flow Rate	
FLOW PATH	lbm/hr	kg/hr	lbm/hr	kg/hr
Total RCS flow	121.5×10^6	55.1×10^6	115.42×10^6	52.35×10^6
Core bypass flow	3.65×10^6	1.65×10^6	3.46×10^6	1.57×10^6
Core flow	117.85×10^6	53.46×10^6	111.96×10^6	50.78×10^6
Hot leg flow	60.75×10^6	27.56×10^6	57.71×10^6	26.18×10^6
Cold leg flow	30.38×10^6	13.78×10^6	28.86×10^6	13.09×10^6

TABLE 4.4-8 (Sh. 1 of 2)

REACTOR COOLANT SYSTEM GEOMETRY

COMPONENT	FLOW PATH LENGTH ft(m)	TOP (d) ELEVATION ft(m)	BOTTOM (d) ELEVATION ft(m)	MINIMUM FLOW AREA ft^2 (m^2)	VOLUME ft^3(m^3)
Hot Leg	14.36 (4.38)	2.40 (0.731)	-1.75 (-0.53)	9.62 (0.89)	138.15 (3.91)
Reactor Coolant Pump					
Suction Leg	24.68 (7.52)1.04 (0.32)-9.96		(-3.04)4.91(0.46)	122.53 (3.40)	
Discharge Leg	19.29 (5.88)	1.25 (0.38)	-1.25 (-0.38)	4.91 (0.46)	95.65 (2.71)
Pressurizer					1815 (51.40)
Liquid Level @ Full Power	---	31/58 (9.62)	---	50.07 (4.65)(a)	900 (25.48)
Surge Line	---	max. 25(7.62) min. 18.87(5.75)	3.89 (1.18)	0.56 (0.052)	max.49 (1.39)(e) min.40 (1.13)
Steam Generator(b)					
Inlet Nozzle	2.72 (0.83)	7.21 (2.20)	4.11 (1.25)	9.62 (0.89)	26.17 (0.74)
Inlet Plenum	3.38 (1.03)	9.04 (2.76)	3.35 (1.02)	66.79 (6.20)	225.76 (6.39)
Outlet Plenum	4.43 (1.35)	9.04 (2.76)	3.35 (1.02)	50.96 (4.73)	225.76 (6.39)
Outlet Nozzle	2.0 (0.61)	5.63 (1.72)	3.86 (1.18)	4.91 (0.46)	9.81 (0.28)
Tubes(Active & Inactive)	67.12 (20.46)	45.7 (12.93)	9.04 (2.76)	2.4E-3 (2.2E-4)(c)	1334.88 (37.80)
Reactor Vessel					
Inlet Nozzle	4.2 (1.28)	1.47 (0.45)	-1.47 (-0.45)	4.91 (0.46)	20.50 (0.58)
Down Comer	19.9 (6.07)	11.7 (3.57)	-19.8 (-6.04)	25.28 (2.35)	1066.42 (30.20)
Lower Plenum	5.8 (1.77)	-19.8 (6.04)	-25.3 (-7.71)	32.01 (2.97)	301.77 (8.55)
Lower Support Structure & Inactive Core	2.9 (0.88)	-18.2 (-5.55)	-20.6 (-6.28)	23.62 (2.19)	199.5 (5.65)
Active Core	12.5 (3.81)	-5.19 (-1.58)	-17.7 (-5.39)	46.21 (4.29)	599.9 (16.99)
Upper Inactive Core	2.6 (0.79)	-3.47 (-1.06)	-5.19 (-1.58)	34.19 (3.18)	163.5 (4.63)
Outlet Plenum	7.3 ((2.23)	1.95 (0.59)	-2.2 (-0.67)	14.65 (1.36)	380.22 (10.77)
Core Shroud Bypass	16.4 (5.00)	-3.6 (-1.10)	-18.2 (-5.55)	0.07 (0.01)	228.9 (6.48)
CEA Shroud Assembly & Tie Tubes	19.4 (5.91)	15.4 (4.69)	-5.19 (-1.58)	0.29 (0.03)	1037.2 (29.37)
Ugs. CEA Shroud Annulus	10.6 (3.23)	12.9 (3.93)	2.3 (7.01)	1.15 (0.11)	179.8 (5.09)
Top Head	3.2 (0.96)	19.1 (5.82)	12.7 (3.87)	5.61 (0.52)	302.7 (8.57)
Outlet Nozzle	3.27 (1.00)	1.87 (0.57)	-1.87(-0.57)	9.62 (0.89)	41.5 (1.18)

NOTES:

a. For the cylinder.

b. Top and bottom elevations are referenced to base of SG

c. Flow path area per tube.

d. Reactor vessel nozzle centerline is the reference elevation. It has an elevation of 0.0ft.

e. Including hot leg, PZR nozzles.

f. Depends on individual plant surge line height.

TABLE 4.4-9 (Sh. 1 of 2)

REACTOR COOLANT SYSTEM COMPONENT

THERMAL AND HYDRAULIC DATA

ITEM	VALUE
Reactor Vessel	
Reactor core thermal power, MWt	2815
Design pressure, psia (kg/cm^2A)	2500 (175.8)
Operating pressure, psia (kg/cm^2A)	2250 (158.2)
Coolant outlet temperature, °F (°C)	621 (327)
Coolant inlet temperature, °F (°C)	564.5 (296)
Coolant outlet state	Subcooled
Total coolant flow, 10^6 lb/hr (kg/hr)	121.5 (55.1)
Average coolant enthalpy	
Inlet, Btu/lb (kcal/kg)	565 (313.9)
Outlet, Btu/lb (kcal/kg)	645 (358.3)
Average coolant density	
Inlet, lb/ft^3 (g/cm^3)	45.9 (0.735)
Outlet, lb/ft^3 (g/cm^3)	41.2 (0.660)
Steam Generators	
Number of units	2
Primary Side (or tube sides)	
Design pressure/temperature, psia/°F (kg/cm^2A/°C)	2500/600 (175.8/343.3)
Operating pressure, psia (kg/cm^2A)	2250 (158.2)
Inlet temperature, °F (°C)	621 (327)
Outlet temperature, °F (°C)	564.5 (296)
Secondary (or shell side)	
Design pressure/temperature, psia/°F (kg/cm^2A/°C)	1270/575 (89.3/301.7)
Full load steam pressure/temperature, psia/°F (kg/cm^2A/°C)	1070/552.9 (75.2/289.4)
Zero load steam pressure, psia (kg/cm^2A)	1170 (82.3)
Total steam flow per gen., lb/hr (kg/hr)	6.36×10^6 (2.88×10^6)
Full load steam quality, %	99.75
Feedwater temperature, full power, °F (°C)	450 (232.2)

NOTE: Values for full power and nominal RCS flow rate conditions | 563

TABLE 4.4-9 (sh. 2 of 2)

ITEM	VALUE
Pressurizer	
Design pressure, psia (kg/cm^2A)	2500 (175.8)
Design temperature, °F (°C)	700 (371.1)
Operating pressure, psia (kg/cm^2A)	2250 (158.2)
Operating temperature, °F (°C)	653 (345)
Internal volume (ft^3) (m^3)	1800 (50.97)
Heaters	
Type and rating of heaters, kW	Immersion/50
Installed heater capacity, kW	1800
Reactor Coolant Pumps	
Number of units	4
Type	Vertical-centrifugal
Rated flowrate (gal/min) (L/min)	85400 (323264)
Design pressure/temperature, psia/°F (kg/cm^2A/°C)	2500/650 (175.8/343.3)
Suction operating pressure, psia (kg/cm^2A)	2220 (156.1)
Type drive motor	Squirrel-cage induction
Rated head, ft (m)	345 (105.1)
Rating and power requirements, hp, hot (kW)	6325 (4717)
Pump speed, r/min	1190
Total head input to RCS, MWt	10
Reactor Coolant Piping	
Flow per loop, 10^6 lb/hr (10^6 kg/hr)	
Hot leg	60.75 (27.56)
Cold leg	30.38 (13.78)
Pipe size (inside dia.), in. (mm)	
Hot leg	42 (1067)
Cold leg	
Suction leg	30 (762)
Discharge leg	30 (762)
Pipe design press./temp., psia/°F (kg/cm^2A/°C)	2500/650 (175.8/343.3)
Pipe operating press./temp., psia/°F (kg/cm^2A/°C)	
Hot leg	2250/621 (158.2/327)
Cold leg	2250/564.5 (158.2/295.8)

Amendment 339
2007.01.09

ASSEMBLY NUMBER AVERAGE ROD RADIAL POWER FACTOR MAXIMUM ROD RADIAL POWER FACTOR					1 0.533 0.950	2 0.645 0.996	3 0.474 0.714
			4 0.334 0.657	5 0.912 1.247	6 1.132 1.386	7 1.072 1.218	8 1.233 1.447
		9 0.347 0.641	10 0.898 1.164	11 0.973 1.096	12 1.119 1.248	13 1.392 1.524	14 1.197 1.273
	15 0.334 0.655	16 0.898 1.165	17 1.154 1.291	18 0.922 1.070	19 1.480 1.600	20 1.152 1.225	21 1.139 1.238
	22 0.912 1.248	23 0.972 1.093	24 0.922 1.074	25 1.327 1.431	26 1.097 1.172	27 1.315 1.466	28 0.953 1.016
29 0.533 0.952	30 1.132 1.384	31 1.119 1.252	32 1.392 1.519	33 1.099 1.172	34 0.883 0.944	35 1.071 1.179	36 1.294 1.416
37 0.645 0.994	38 1.072 1.220	39 1.392 1.510	40 1.153 1.228	41 1.318 1.470	42 1.073 1.180	43 1.071 1.156	44 1.054 1.191
45 0.474 0.714	46 1.233 1.447	47 1.197 1.273	48 1.139 1.238	49 0.953 1.016	50 1.294 1.416	51 1.054 1.191	52 0.799 0.830

KOREA HYDRO & NUCLEAR POWER COMPANY
YONGGWANG 3 & 4
FSAR

CORE-WIDE PLANAR POWER
DISTRIBUTION FOR SAMPLE
DNB ANALYSIS

Figure 4.4-1

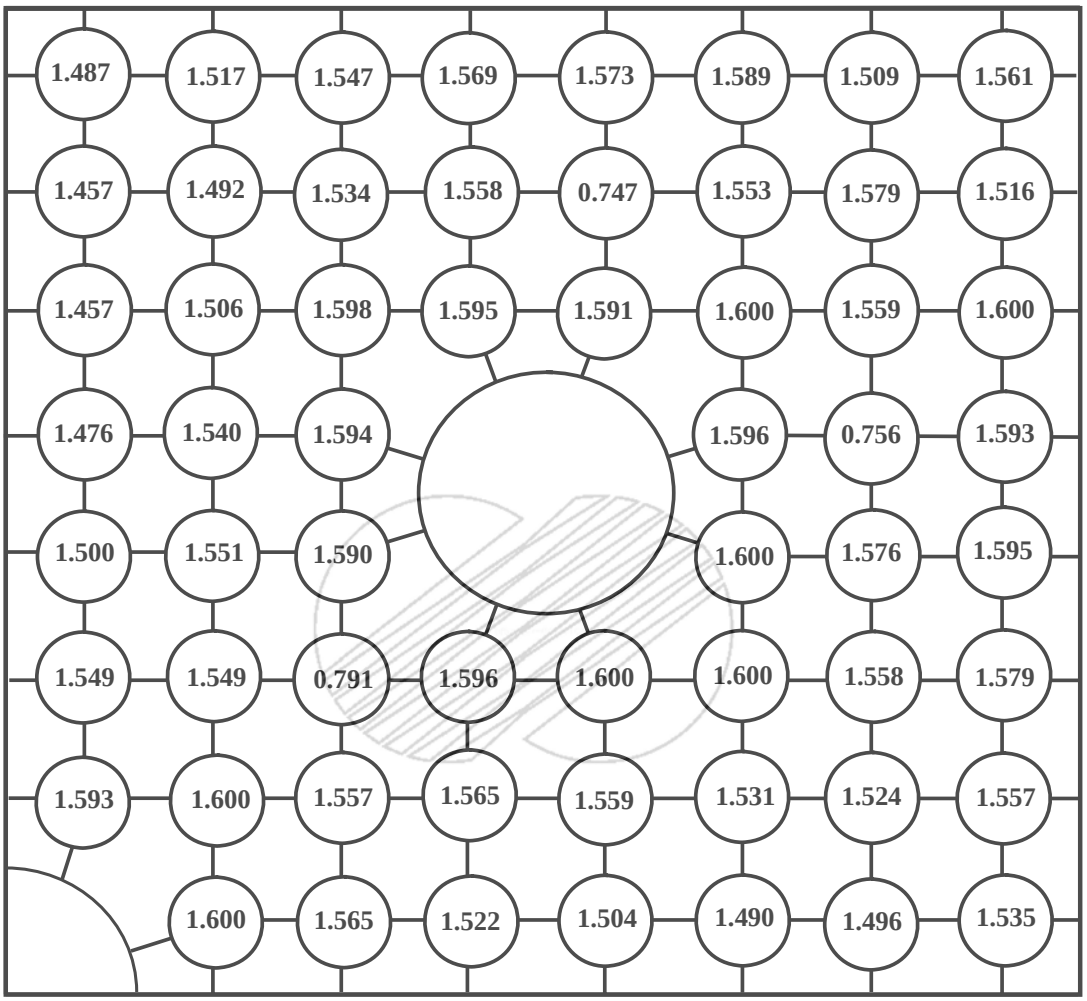

KOREA HYDRO & NUCLEAR POWER COMPANY
YONGGWANG 3 & 4
FSAR

ROD RADIAL POWER FACTORS IN
HOT ASSEMBLY FOR SAMPLE
DNB ANALYSIS

Figure 4.4-2

Amendment 339
2007.01.09

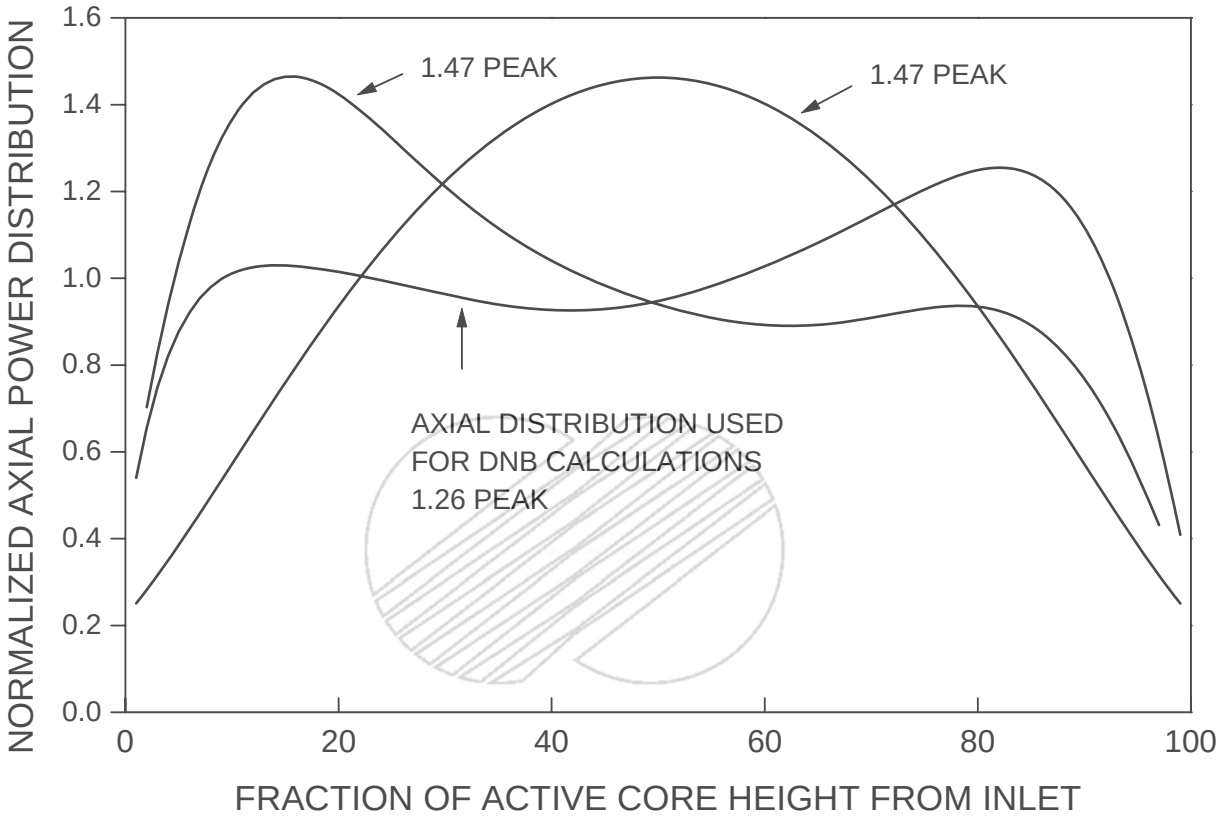

KOREA HYDRO & NUCLEAR POWER COMPANY
YONGGWANG 3 & 4
FSAR

TYPICAL AXIAL POWER DISTRIBUTIONS

Figure 4.4-3

EXIT VOID FRACTION (%) EXIT QUALITY (%)							
					0 -22	0 -20	0 -23
			0 -26	0 -14	0 -9	0 -10	0 -7
		0 -26	0 -14	0 -12	0 -9	0 -3	0 -7
	0 -25	0 -14	0 -8	0 -13	0 -1	0 -8	0 -8
	0 -14	0 -12	0 -13	0 -5	0 -9	0 -5	0 -12
0 -22	0 -8	0 -9	0 -3	0 -9	0 -14	0 -10	0 -5
0 -19	0 -10	0 -3	0 -8	0 -5	0 -10	0 -10	0 -10
0 -23	0 -7	0 -7	0 -8	0 -12	0 -5	0 -10	0 -16

KOREA HYDRO & NUCLEAR POWER COMPANY
YONGGWANG 3 & 4
FSAR

AVERAGE VOID FRACTIONS AND QUALITIES
AT THE EXIT OF DIFFERENT CORE REGIONS

Figure 4.4-4

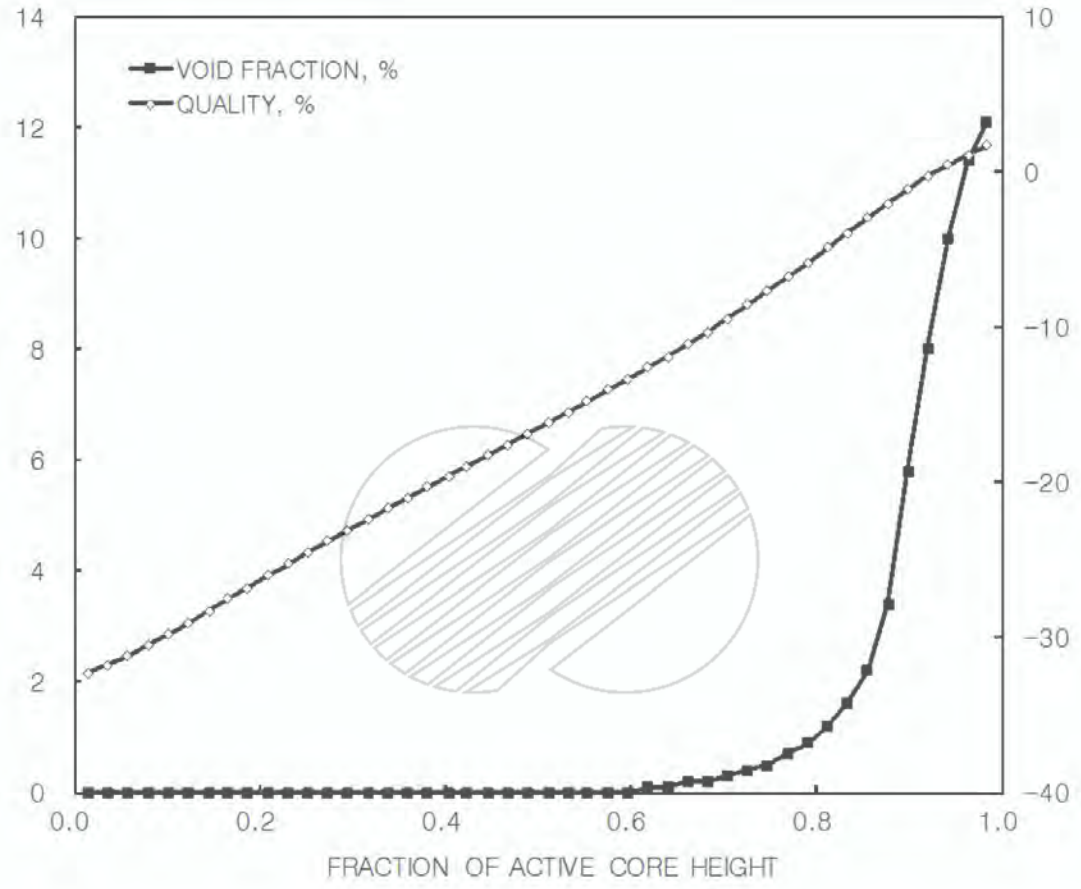

KOREA HYDRO & NUCLEAR POWER COMPANY
YONGGWANG 3 & 4
FSAR

AXIAL DISTRIBUTION OF VOID FRACTION AND QUALITY OF THE SUBCHANNEL WITH THE MAXIMUM VOID FRACTION IN THE LIMITING ASSEMBLY

Figure 4.4-5

Amendment 1
October 1994

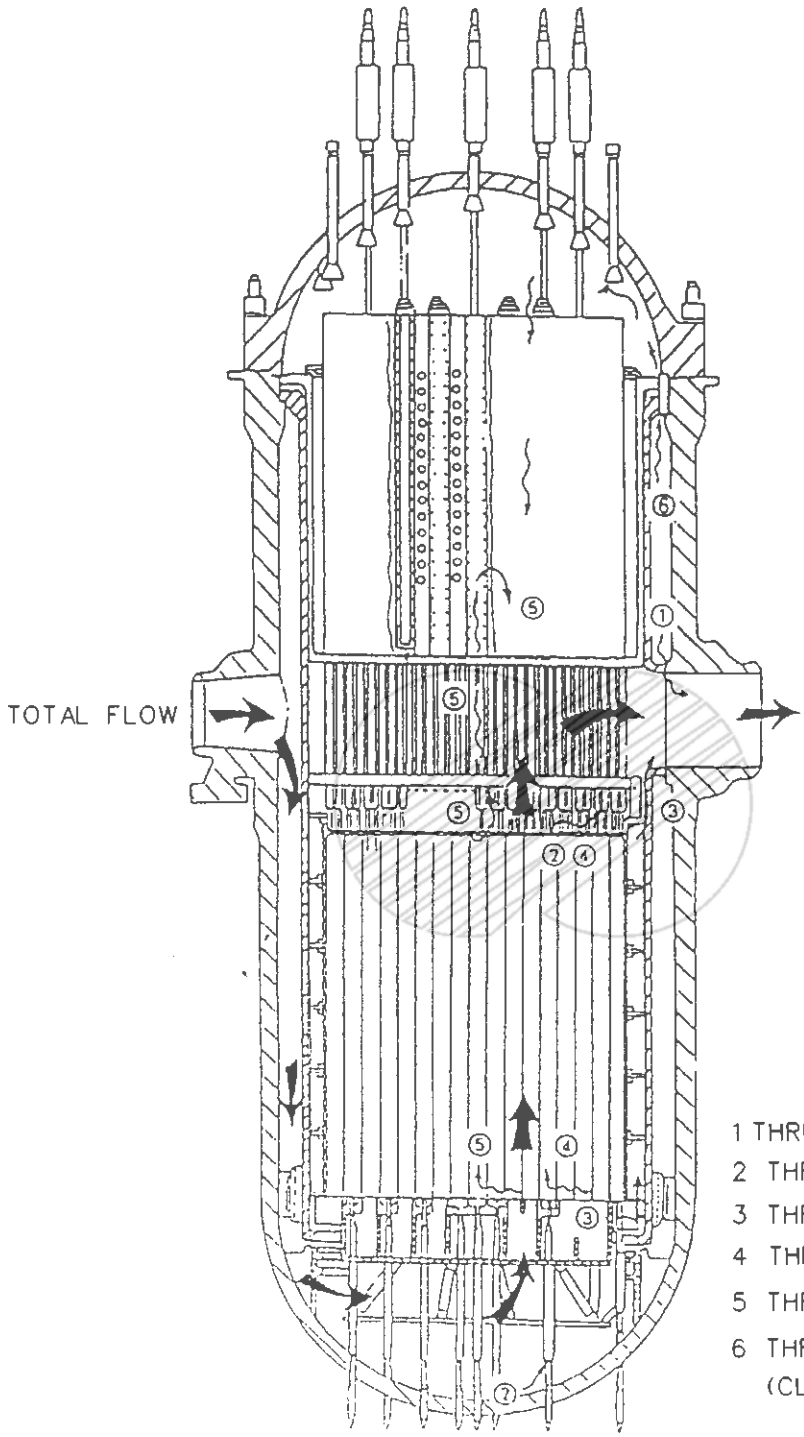

KOREA ELECTRIC POWER CORPORATION
YONGGWANG 3 & 4
FSAR

REACTOR FLOW PATHS

Figure 4.4-6

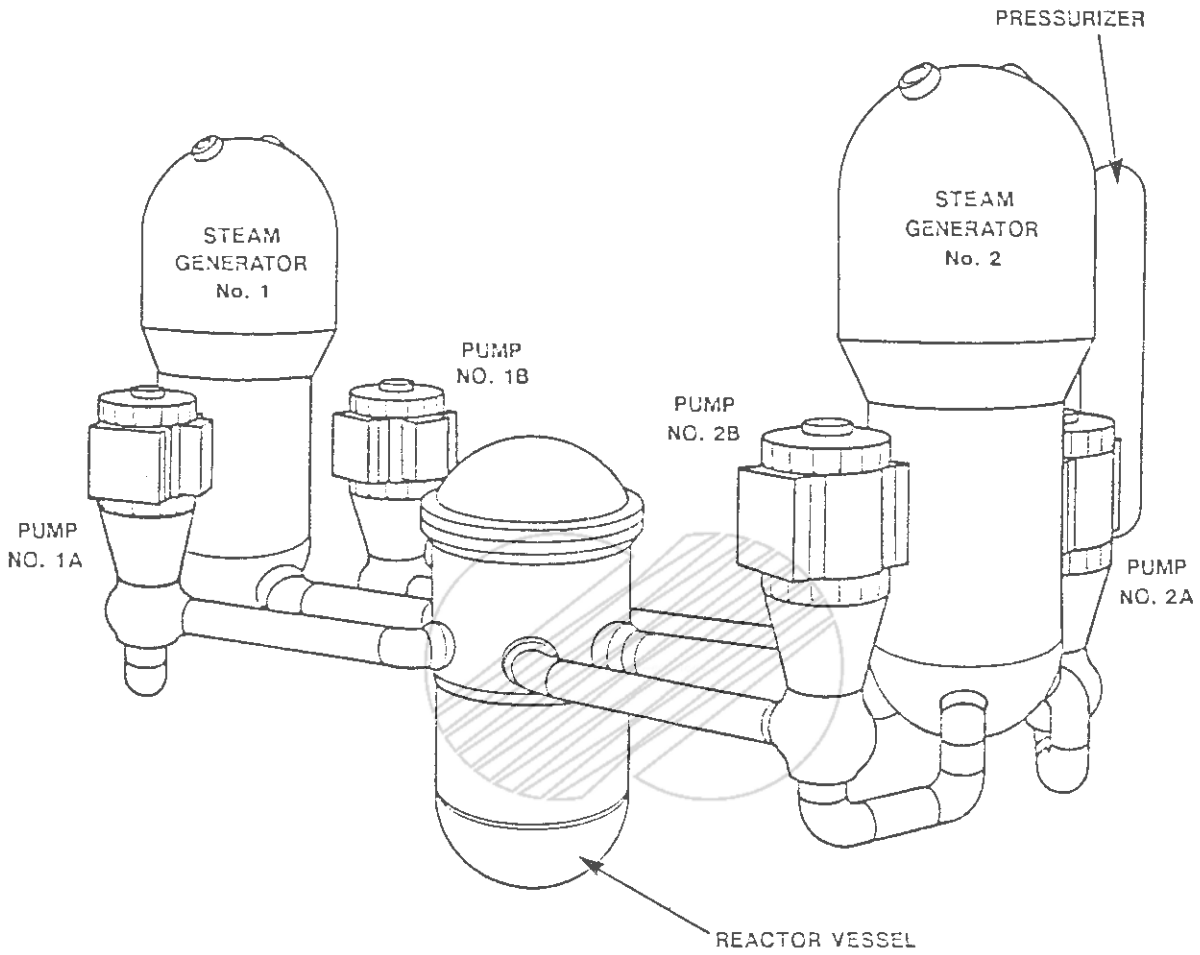

KOREA ELECTRIC POWER CORPORATION
YONGGWANG 3 & 4
FSAR

ISOMETRIC VIEW OF THE REACTOR COOLANT SYSTEM

Figure 4.4-7

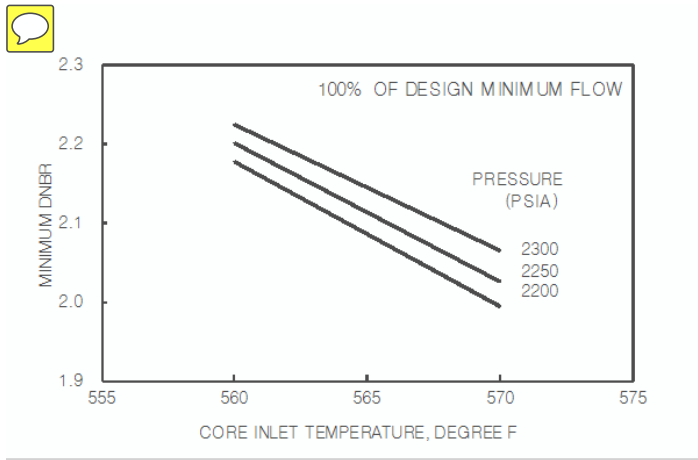

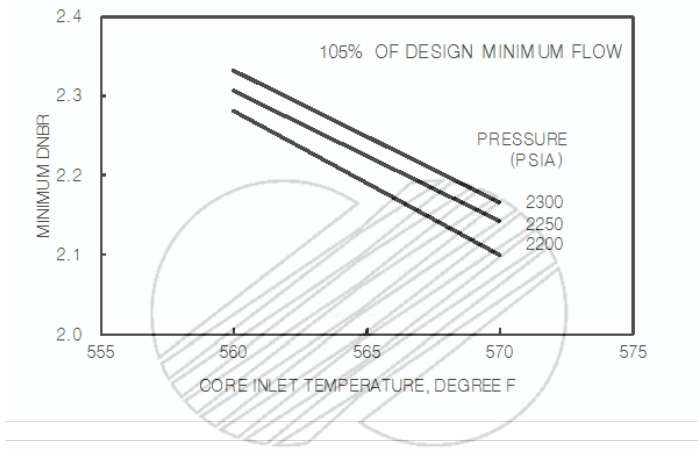

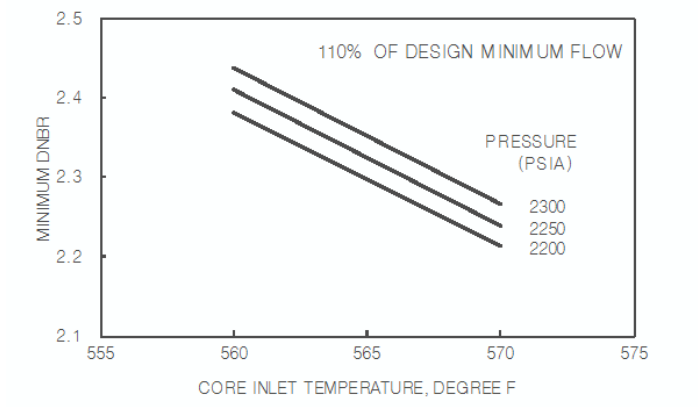

KOREA HYDRO & NUCLEAR POWER COMPANY
YONGGWANG 3 & 4
FSAR

SENSITIVITY OF MINIMUM DNBR TO SMALL CHANGES IN REACTOR COOLANT CONDITIONS

Figure 4.4-8

4.5 REACTOR MATERIALS

4.5.1 Control Element Drive Structural Materials

4.5.1.1 Material Specifications

a. The materials used in the control element drive mechanism (CEDM) reactor coolant pressure boundary components are as follows:

1. Motor housing assembly
   SA 182, Type 347 (austenitic stainless steel)
   ASME Code Case N-4-11 (modified Type 403 martensitic stainless steel), and additional requirements of ASME SA-182.
   SB 166 (nickel-chromium-iron alloy)

2. Upper pressure housing
   SA 213, Type 316 (austenitic stainless steel)
   SA 479, Type 316 (austenitic stainless steel)
   ASTM A276, Type 440C (martensitic stainless steel with yield strength greater than 90 ksi [6,327 kg/cm^2])

The above listed materials, with the exception of the ASTM A276, Type 440C material, are also listed in Section III of the ASME Boiler and Pressure Vessel Code. In addition, the materials comply with Sections II and IX of the ASME Boiler and Pressure Vessel Code.

The functions of the above listed components are described in Subsection 3.9.4.1.

b. The materials in contact with the reactor coolant used in the CEDM motor assembly components are as follows:

1. Latch guide tubes

2. Magnet and spacer

3. Latch and magnet housing

4. Spacer

5. Alignment tab

6. Spring

7. Pin

8. Dowel pin

9. Adjusting Nut

10. Stop

11. Latch and pin

12. Locking cup and screws

The functions of the CEDM motor assembly components are described in Subsection 3.9.4.1.

c. The materials in contact with the reactor coolant used in the extension shafts are listed below:

1. Shafts, rod, and plunger

2. Gripper

3. Spring

4. Pin

The functions of the extension shaft components are described in Subsection 3.9.4.1.

d. The weld rod filler materials used with the above listed components are Type 308 stainless steel, Type 316 stainless steel, and Inconel 82.

All of the material listed above, a through d, were used in an extensively tested CEDM assembly that exceeded lifetime requirements, as described in Subsection 3.9.4.4.1. Also, all of the materials have performed satisfactorily in service in the Maine Yankee (Docket 50-309), Millstone 2 (Docket 50-236), and Calvert Cliffs (Docket 50-317), in addition to other designed reactors. Material purchased to code editions and addenda earlier than the one specified in the contract is used as permitted when the requirements of Section III, Subsection NCA-1140, paragraph (e) are satisfied.

4.5.1.2 Control of the Use of 90 ksi Yield Strength Material

The only control element drive structural material identified in Subsection 3.1.1 that has a yield strength greater than 90 ksi (6,327 kg/cm^2) is ASTM A276, Type 440C, martensitic stainless steel. Its usage is limited to the steel ball in the vent valve on the top of the CEDM and bearing inserts in the motor assembly. The ball is used as a seal and is not a primary load-bearing member of the pressure boundary; the inserts, which are Type 440C for surface hardness, see little stress and are not part of the safety release mechanism in the motor assembly. This material was tested and exceeded lifetime requirements. Also, this material is presently being used in operating reactors, such as Maine Yankee (Docket 50-209), Calvert Cliffs (Docket 50-317), and St. Lucie Unit 1 (Docket 50-335), and has performed satisfactorily for the same application.

4.5.1.3 Control of the Use of Sensitized Austenitic Stainless Steel

Control of the use of sensitized austenitic stainless steel is consistent with the recommendations of Regulatory Guide 1.44, as described in Subsections 4.5.1.3.1 through 4.5.1.3.3, except for the criterion used to demonstrate freedom from sensitization. The ASTM A708 Strauss Test is used in lieu of the ASTM A262 Method E, Modified Strauss Test, to demonstrate freedom from sensitization in fabricated unstabilized austenitic stainless steel. The

former test has shown, through experimentation, excellent correlation with the type of corrosion observed in severely sensitized austenitic stainless steel.

4.5.1.3.1 Solution Heat Treatment Requirements

All raw austenitic stainless steel, both wrought and cast, employed in the fabrication of the control element drive mechanism structural components is supplied in the solution annealed condition, as described in Subsection 4.5.2.3.1.1.

4.5.1.3.2 Material Inspection Program

Extensive testing on stainless steel mockups, fabricated using production techniques, has been conducted to determine the effect of various welding procedures on the susceptibility of unstabilized Type 300 series stainless steels to sensitization-induced intergranular corrosion. Only those procedures and practices demonstrated not to produce a sensitized structure are used in the fabrication of control element drive mechanism structural components. The ASTM Standard A708 (Strauss Test) is the criterion used to determine susceptibility to intergranular corrosion. This test has shown excellent correlation with a form of localized corrosion peculiar to sensitized stainless steels. As such, ASTM A708 is utilized as a go/no-go standard for acceptability.

4.5.1.3.3 Avoidance of Sensitization

Homogeneous or localized heat treatment of unstabilized austenitic stainless steel in the temperature range 800° to 1500°F (426.7° - 815.6°) is prohibited.

Weld heat-affected zone-sensitized austenitic stainless steel (which will fail in the Strauss Test, ASTM A708) is avoided in control element drive mechanism structural components by careful control of the following conditions:

a. Weld heat input to less than 60 kJ/in.
b. Interpass temperature to 350°F(176.7°C) maximum
c. Carbon content to $\leq$ 0.065%

4.5.1.4 Control of Delta Ferrite in Austenitic Stainless Steel Welds

The austenitic stainless steel, primary pressure-retaining, welds in the control element drive mechanism structural components are consistent with the recommendations of Regulatory Guide 1.31 as follows:

"The delta ferrite content of A-No. 8 (Table QW-442 of the ASME Code, Section IX) austenitic stainless steel welding materials is controlled to 5FN-20FN.

"The delta ferrite determination is carried out using methods specified in the ASME Code, Section III, for each heat, lot or heat/lot combination of weld filler material. For submerged arc process, the delta ferrite determination for each wire/flux combination may be made on a production or simulated (qualification) production weld."

4.5.1.5 Cleaning and Contamination Protection Procedures

The procedure and practices followed for cleaning and contamination protection of the control element drive mechanism structural components are in compliance with the recommendations of Regulatory Guide 1.37 and are described in the following paragraphs.

Specific requirements for cleanliness and contamination protection are included in the equipment specifications for components fabricated with austenitic stainless steel. The provisions described below indicate the type of procedures utilized for components to provide contamination control during fabrication, shipment, and storage.

Contamination of Type 300 austenitic stainless steels by compounds that can alter the physical or metallurgical structure and/or the properties of the material is avoided during all stages of fabrication. Painting of Type 300 series stainless steels is prohibited. Grinding is accomplished with resin or rubber-bonded aluminum oxide or silicon carbide wheels that have not previously been used on materials other than Type 300 series stainless alloys.

Internal surfaces of completed components are cleaned to the extent that grit, scale, corrosion products, grease, oil, wax, gum, adhered or embedded dirt, or extraneous material are not visible to the unaided eye.

Cleaning is effected by either solvents (acetone or isopropyl alcohol) or inhibited water (100-300 ppm hydrazine). Water conforms to the following requirements:

Halides	
Chloride, ppm	< 0.60
Fluoride, ppm	< 0.40
Conductivity, mhos/cm	< 5.0
pH	6.0 - 8.0
Visual clarity	No turbidity, oil or sediment

To prevent halide-induced intergranular corrosion that could occur in an aqueous environment with significant quantities of dissolved oxygen, flushing water is inhibited via additions of hydrazine. Experiments have proven these inhibitors to be effective. Operational chemistry specifications preclude halides and oxygen (both prerequisites of intergranular attacks) and are shown in Subsection 9.3.4.

4.5.2 Reactor Core Support and Internals Structure Materials

4.5.2.1 Material Specifications

The material used in fabrication of the reactor core support and internal structures is primarily Type 304 stainless steel. The flow skirt is fabricated from Inconel. Welded connections are used where feasible; however, in locations where mechanical connections are required, structural fasteners are used which are designed to remain captured in the event of a single failure. Structural fastener material is typically a high-strength austenitic stainless steel; however, in less critical applications Type 316 stainless steel is employed. Hardfacing of Stellite material is used at wear points. The effect of irradiation of the properties of the materials is considered in the design of the reactor core support and internal structures. Work hardening properties of austenitic stainless steels are not used.

The following is a list of the major components of the reactor core support and internals structures together with their material specifications:

a. Core support barrel assembly

1. Type 304 austenitic stainless steel to the following specification:

   - SA 182
   - SA 240
   - SA 479

2. Precipitation hardening stainless steel to the following specifications:

- SA 453, Grade 660
- SA 638, Grade 660

b. Upper guide structure assembly

1. Type 304 austenitic stainless steel to the following specifications:

   - SA 182
   - SA 240
   - SA 213
   - SA 479

2. Precipitation hardening stainless steel to the following specifications:

   - SA 638, Grade 660

3. Type 347 austenitic stainless steel to the following specifications:

   - SA 479
   - SA 312

c. Core shroud assembly

1. Type 304 austenitic stainless steel to the following specifications:

   - SA 182
   - SA 240

d. Holddown ring

SA 182, modified to ASME Code Case N-124

e. Bolt and pin material

SA 453 and SA 638, Grade 660 material (trade name A-286) is used for bolting and pin applications. This alloy is heat-treated to a minimum yield strength of 85,000 lb/in^2 (5976 kg/cm^2). Its corrosion properties are similar to those of the Type 300 series austenitic stainless steels. It is austenitic in all conditions of fabrication and heat treatment. This alloy was used for bolting in previous reactor systems and test facilities in contact with primary coolant and has proven completely satisfactory.

f. Chrome plating and hardfacing

Chrome plating or hardfacing is employed on reactor core support and internals structure components or portions thereof where required by function. Chrome plating complies with Federal Specification No. QQ-C-320b. The hardfacing material employed is Stellite 25.

g. Special purpose material

SA 479 S21800 (Trade name Nitronic 60) is used for special applications (e.g., snubbers and lift bolt inserts) where anti-galling properties are desired.

All of the materials employed in the reactor core support and internal structures and incore instrument support system have performed satisfactorily in operating reactors such as Palisades (DOCKET-50-255), Fort Calhoun (DOCKET-50-285), and Maine Yankee (DOCKET-50-309).

4.5.2.2 Welding Acceptance Standards

Welds employed on reactor internals and core support structures meet the acceptance standards delineated in Article NG-5000, Section III, Division I, and control of welding is performed in accordance with Section III, Division I, and Section IX of the ASME Code. In addition, consistency with the recommendations of Regulatory Guides 1.31 and 1.44 is described in Subsection 4.5.2.3.

4.5.2.3 Fabrication and Processing of Austenitic Stainless Steel

The following information applies to unstabilized austenitic stainless steel as used in the reactor core support and internal structures.

4.5.2.3.1 Control of the Use of Sensitized Austenitic Stainless Steel

The recommendations of Regulatory Guide 1.44, as described in Subsections 4.5.2.3.1.1 through 4.5.2.3.1.5, are followed except for the criterion used to demonstrate freedom from sensitization. The ASTM A708 Strauss test is used in lieu of the ASTM A262 Method E, Modified Strauss Test, to demonstrate freedom from sensitization in fabricated unstabilized austenitic stainless steel, since the former test has shown, through experimentation, excellent correlation with the type of corrosion observed in severely sensitized austenitic stainless steel.

4.5.2.3.1.1 Solution Heat Treatment Requirements

All raw austenitic stainless steel material, both wrought and cast, employed in the fabrication of the reactor internals is supplied in the solution-annealed condition, as specified in the pertinent ASME B&PV Code material specification; viz, 1900° to 2050°F (1037.8° - 1121.1°C) for 1/2 to 1 hr/in.

of thickness and rapidly cooled to below 700°F (371.1°C). The time at temperature is determined by the size and the type of component.

Solution heat treatment is not performed on completed or partially fabricated safety-related components. Rather, the extent of chromium carbide precipitation is controlled during all stages of fabrication as described in Subsection 4.5.2.3.1.4.

4.5.2.3.1.2 Material Inspection Program

Extensive testing of stainless steel mockups, fabricated using production techniques, was conducted to determine the effect of various welding procedures on the susceptibility of unstabilized Type 300 series stainless steels to sensitization-induced intergranular corrosion. Only those procedures and practices demonstrated not to produce a sensitized structure are used in the fabrication of reactor internals' components. The ASTM Standard A708 (Strauss Test) is the criterion used to determine susceptibility to intergranular corrosion. This test has shown excellent correlation with a form of localized corrosion peculiar to sensitized stainless steel. As such, ASTM A708 is utilized as a go/no-go standard for acceptibility.

As a result of the above tests, a relationship was established between the carbon content of Type 304 stainless steel and weld heat input. This relationship is used to avoid weld heat-affected zone sensitization as described in Subsection 4.5.2.3.1.4.

4.5.2.3.1.3 Unstabilized Austenitic Stainless Steels

The unstabilized grade of austenitic stainless steel with a carbon content greater than 0.03% used for components of the reactor internals is Type 304.

This material is furnished in the solution-annealed condition. The acceptance criterion used for this material, as furnished from the steel supplier, is ASTM A262, Method E.

Exposure of completed or partially fabricated components to temperatures ranging from 800° to 1500°F (426.7° - 815.6°C) is prohibited except as described in Subsection 4.5.2.3.1.5.

Duplex, austenitic stainless steels containing more than 5 FN delta ferrite (weld metal, cast metal, weld deposit overlay) are not considered unstabilized since these alloys do not sensitize, i.e., form a continuous network of chromium-iron carbides. Specifically, the following alloys are in this category:

CF8M, CF8 : Cast stainless steel (delta ferrite controlled to 5FN-33FN)

Type 308, 309, 312, 316 : Single and combined stainless steel weld filler metals (delta ferrite controlled to 5FN-20FN as deposited)

In duplex austenitic/ferritic alloys, chromium-iron carbides are precipitated preferentially at the ferrite/austenite interfaces during exposure to temperatures ranging from 800° to 1500°F (426.7° - 815.6°C). This precipitate morphology precludes intergranular penetrations associated with sensitized Type 300 series stainless steels exposed to oxygenated or otherwise faulted environments.

4.5.2.3.1.4 Avoidance of Sensitization

Exposure of unstabilized austenitic 300 Series stainless steels to temperatures ranging from 800° to 1500°F (426.7° - 815.6°C) will result in carbide

precipitation. The degree of carbide precipitation or sensitization depends on the temperature, the time at that temperature, and the carbon content. Severe sensitization is defined as a continuous grain boundary chromium-iron carbide network. This condition induces susceptibility to intergranular corrosion in oxygenated aqueous environments, as well as those containing halides. Such a metallurgical structure will readily fail the Strauss Test, ASTM A708. Discontinuous precipitates (i.e., an intermittent grain boundary carbide network) are not susceptible to intergranular corrosion in a PWR environment.

Weld-heat-affected zone-sensitized austenitic stainless steels are avoided (which will fail the Strauss Test, ASTM A708) by careful control of the following conditions:

a. Weld heat input to less than 60 kJ/in.
b. Interpass temperature to 350°F (176.7°C) maximum
c. Carbon content ≤ 0.065%

A weld heat input of less than 60 kJ/in. is used during most fabrication stages of the Type 304 stainless steel core support structure. Higher heat inputs are used in some heavy section weld joints. Freedom from weld-heat-affected zone sensitization in those higher heat input weldments is demonstrated with weld runoff samples produced at the time of component welding in material having a carbon content equal to or greater than the highest carbon content of those heats of steel being fabricated. Specimens so provided are subjected to the Strauss Test, ASTM A708.

4.5.2.3.1.5 Retesting Unstabilized Austenitic Stainless Steels Exposed to Sensitizing Temperature

Sensitization, which may be susceptible to intergranular corrosion, is avoided during welding, as described in Subsection 4.5.2.3.1.4. Homogeneous or localized heat treatment of unstabilized stainless steels in the temperature range

of 800° to 1500°F (426.7° - 815.6°C) is avoided. Complex substructures may be thermally stabilized after fabrication and before final machining. Such treatment produces only minor, discontinuous precipitates. In addition to thermocouple records during this heat treatment, a sample of Type 304 stainless steel, having a carbon content equal to or greater than the highest carbon heat of material present in the structure, is included as a monitor sample. After heat treatment, the monitor sample is subjected to the Strauss Test, ASTM A708, as well as to a metallographic examination to verify freedom from sensitization.

4.5.2.3.2 Nonmetallic Thermal Insulation

Nonmetallic thermal insulation is not used on the reactor core support and internal structures.

4.5.2.3.3 Control of Delta Ferrite in Welds

The recommendations of Regulatory Guide 1.31 are followed, as described in Subsection 4.5.1.4.

4.5.2.3.4 Control of Electroslag Weld Properties

The electroslag process, Regulatory Guide 1.34, is not utilized to fabricate reactor internal components.

4.5.2.3.5 Welder Qualification for Areas of Limited Accessibility

The specific recommendations of Regulatory Guide 1.71 were not followed. However, performance qualifications for personnel welding under conditions of limited accessibility are conducted and maintained in accordance with the requirements of ASME Code, Sections III and IX. A requalification is required when

a. any of the essential variables of Section IX are changed or

b. when authorized personnel have reason to question the ability of the welder to satisfactorily perform to the applicable requirements.

Production welding is monitored for compliance with the procedure parameters, and welding qualification requirements are certified in accordance with Sections III and IX. Further assurance of acceptable welds of limited accessibility is afforded by the welding supervisor assigning only the most highly skilled personnel to these tasks. Finally, weld quality, regardless of accessibility, is verified by the performance of the required nondestructive examination.

4.5.2.4 Contamination Protection and Cleaning of Austenitic Stainless Steel

Compliance with the recommendations of Regulatory Guide 1.37, "Quality Assurance Requirements for Cleaning of Fluid Systems and Associated Components of Water Cooled Nuclear Power Plants," is accomplished by conformance to "Quality Assurance Requirements for Nuclear Facility Applications," ANSI/ASME NQA-2.

4.6 FUNCTIONAL DESIGN OF REACTIVITY CONTROL SYSTEMS

YGN 3&4 includes the following reactivity control systems: the control element drive mechanisms (CEDMs), the safety injection system (SIS), and the chemical and volume control system (CVCS). The pertinent information, evaluations, and testing of the CEDMs are treated in Subsections 4.6.1, 4.6.2, and 4.6.3, respectively. The combined performance of the CEDMs and other reactivity control systems are discussed in Subsections 4.6.4 and 4.6.5.

4.6.1 Information for CEDMs

Component diagrams, description, and characteristics of the CEDMs are presented in Subsection 3.9.4.

4.6.2 Evaluation of CEDMs

The safety function of the CEDMs is to drop CEAs into the reactor core when the motive power is removed from the CEDM power bus. The active interface between the RPS and the CEDMs is at the trip circuit breakers located in the reactor trip switchgear (RTSG).

4.6.2.1 Single Failure

A failure mode and effects analysis of the RPS (including the RTSG) is presented in Section 7.2, which demonstrates compliance with IEEE Standard 279-1971 and shows that no single failure in the RPS can prevent the removal of electrical motive power from the CEDMs. For the trip function, the CEDMs are essentially passive devices. When power is removed from the CEDM coils, the armature springs automatically cause the latches to be disengaged from the CEDM drive shafts, allowing insertion of the CEAs by gravity. For the execution of the trip function, all the CEDMs are independent of one another. In other words, the failure of one CEDM to trip does not affect the operability

of any other CEDM. Sufficient shutdown margin is always maintained to ensure that the shutdown capability can be retained in the event of a failure of any CEDM. Therefore, no single failure can prevent the CEDMs from providing sufficient scram reactivity to achieve a shutdown.

4.6.2.2 Isolation of the CEDMs from Other Equipment

The interface between the CEDMs and the CEDM control system is at the CEDM control system power switches, which provide the isolation of the motive power from the low-voltage logic control signal. The interface between the CEDMs and the CEAs involves no nonessential elements. Therefore, no isolation is required.

4.6.2.3 Protection from Common Mode Failure

Protection of essential systems from the consequences of a postulated pipe rupture is provided by separation via physical plant layout, pipe restraints, protective structures and compartments, watertight barriers, isolation capability or other suitable means described in Section 3.6. In addition, each RTSG is separated from other areas of the plant by rated fire barriers (refer to Subsection 9.5.1).

4.6.3 Testing and Verification of the CEDMs

The precore and postcore CEDM performance test is described in Chapter 14, which verifies the proper operation and sequencing of the CEDMs.

4.6.4 Information for Combined Performance of the Reactivity Control Systems

Plan and elevation layout drawings showing the reactivity control systems are presented in Section 1.2.

Table 4.6-1 lists all the postulated accidents analyzed in Chapter 15 that take credit for two or more reactivity control systems for preventing or mitigating each accident. The related reactivity systems are also tabulated.

4.6.5 Evaluation of Combined Performance

The CEDMs, CVCS, and SIS are separated (see Section 1.2) and totally diverse in design and operation. In addition, since the CEDMs, the SIS, and the CVCS are protected from missiles, pipe breaks, and their effects (as delineated in Section 6.3 and Subsection 9.3.4), there are no credible potential common mode failures that could cause the combination of the CEDMs, SIS, and CVCS to fail to provide sufficient reactivity insertion to achieve a shutdown under design conditions.

TABLE 4.6-1

POSTULATED ACCIDENTS

EVENT	CEDMs	SIS	CVCS
Feedwater line break	A	B	B
Steam line break	A	A	B
LOCA	A	A	B
Letdown line break	A	A	B
Steam generator tube rupture	A	A	B
CEA ejection	A	A	B
Boron dilution	A	C	B
Uncontrolled CEA withdrawal	A	B	C
CEA drop	A	B	C
Inadvertent opening of atmospheric dump valve or main steam safety valve	A	B	B
Loss of normal feedwater flow or loss of condenser vacuum	A	B	C
Reactor coolant pump shaft seizure, shaft break, or total loss of reactor coolant flow	A	B	C
Pressurizer level control system malfunction	A	B	C

NOTES: A = Use expected and required
B = Use expected but not required
C = Use not expected and not required

APPENDIX 4A

YGN 3&4 REACTOR FLOW MODEL TEST PROGRAM

APPENDIX 4A

TABLE OF CONTENTS

LIST OF TABLES

LIST OF FIGURES

APPENDIX A - YGN 3&4 REACTOR FLOW MODEL TEST PROGRAM

1.0 INTRODUCTION

A series of flow model tests has been conducted to determine the hydraulic characteristics of the YGN 3&4 reactors.

The first test objective was to determine the core inlet flow field and pressure fields at the inlet and exit of the model core to provide input information required by the open core thermal margin code, TORC. The second objective was to measure the nozzle-to-nozzle pressure losses inside the vessel to verify values calculated by CE standard pressure loss methods.

2.0 DESCRIPTION OF FLOW MODEL

2.1 PRESSURE VESSEL AND CORE SUPPORT STRUCTURES

A cross-sectional view of the flow model is presented in Figure 4A-1. Geometric similarity to the reactor main flow paths was maintained, with a scaling factor of 0.199 except in the model core. Relatively stagnant regions at the top of the downcomer and in the upper guide structure and closure head volume were truncated for ease and economy of model assembly.

2.2 MODEL CORE

The model core consisted of an array of 177 square tubes, each representing one fuel assembly. Six levels of flow resistor plates match the axial flow resistance of reactor fuel assemblies, and approximately match the axial distribution of axial flow resistance over the length of the assembly. Aligned round holes through adjoining tube walls match the resistance to cross-flow between reactor fuel assemblies. Model and reactor fuel assemblies are compared in Figure 4A-2. The model core design and associated "open-core" flow model testing technique follow the methodology of flow model tests for the

ABB-CE 3400 Series reactors, as described in CENPD-206-P (Reference 1).

2.3 MODEL INSTRUMENTATION

Model instrumentation consisted of wall static pressure taps in the inlet and outlet ducts, at the top and bottom of the downcomer, and in the inlet and outlet of each core tube. These taps provide for assessment of the breakdown of reactor vessel pressure drop and for measurement of both core inlet flow distribution and core inlet and core outlet pressure boundary conditions. A detailed summary of pressure tap locations is provided in Figure 4A-3.

3.0 DESCRIPTION OF TEST FACILITY

3.1 TEST FACILITY AND OPERATING CONDITIONS

Testing was conducted in the ABB-CE Large Scale Hydraulic Test Facility, TF-15. For the configuration representing full flow with four operating reactor coolant pumps, model flow was set at 10,500 gpm (39,745 L/min). All tests were conducted at approximately 80°F (27°C) fluid temperature. At these conditions, flow in the model is fully turbulent, with an outlet duct Reynolds number of 2.5×10^6. The corresponding reactor Reynolds number at full power is 1.5×10^7. It is expected that nondimensionalized pressure drops and flow distributions do not change at the higher reactor Reynolds numbers.

3.2 TEST LOOP

The TF-15 flow model test loop is depicted in Figure 4A-4. Three circulating pumps are required to provide the 10,500 gpm (39,745 L/min) model flow rate. Individual inlet and outlet duct flow settings are established with flow control valves and calibrated flowmeters. Flowmeter signals are continuously fed to the data acquisition system to verify constancy of flow settings.

3.3 DATA ACQUISITION SYSTEM

The data logger system consists of analog to digital input channels, digital pulsed output channels, a CPU, software, disk based data storage, a CRT display, and printers. The CPU is a personal computer (PC) that is expanded with a data acquisition board. The PC has the basic input/output devices of keyboard, CRT, disk drives, and printer ports. The data acquisition board added the ability to communicate with instruments and controls. Schematic outlines of the data logger and the instrument system are depicted in Figure 4A-5.

The software performs the functions of obtaining transmitter performance data, of analyzing the performance data to generate equations to convert input instrument voltages into engineering units, of controlling the selection of solenoid valves to open, of logging the identification of valves to disk storage, and of printing a temporary record of the data.

3.4 CALIBRATION STANDARDS

Calibration of the pressure differential transmitters was performed using controlled standards. Standard pressure signals were applied to each transmitter and the output voltage was recorded on the data logger system. The data was used to establish a relationship between the standard engineering units and the transmitter output voltage. Linear curve fits were used to relate voltage to engineering units.

The pressure differential transmitters were calibrated before the start of testing, at an intermediate point during the test program, and after the last tests. Zero-shift checks were made before the start of each test day. The test loop thermocouple calibration was checked before testing.
The inlet flow meters were calibrated before the start of the test program by an independent outside testing laboratory. The outlet flow meters were

calibrated against the inlet flow meters.

4.0 DATA ANALYSIS

4.1 MODEL INPUT PRESSURES

Model point pressures were converted to Euler numbers of one of several forms.

a. For the planar pressure distributions at the core inlet and core exit, P_{in} and P_{out}:

(4A-1)

(4A-2)

b. For point-to-point pressure differentials:

(4A-3)

Euler numbers are readily coverted to desired pressure-drop loss coefficient forms, considering averaged data from repeat runs.

4.2 CORE INLET FLOW DISTRIBUTION

The four-pump core inlet flow distribution was determined from a computer code simulation of the model core. The measured core inlet and exit planar pressure distributions and the measured flow rate from the reactor flow model tests were used as input to the HERMITE code, Reference 2. The code calculated the core inlet flow distribution for each test run.

The distribution was expressed in nondimensional form as the fraction of average core mass velocity at each fuel assembly location. This core inlet

flow distribution is used to verify the design value for the hot assembly inlet mass velocity factor used in thermal margin analyses.

The core inlet flow distribution for three operating reactor coolant pumps was also determined for use in analyzing the seized rotor accident.

4.3 CORE EXIT PRESSURE DISTRIBUTION

The core exit pressure distribution was determined with the flow model for an elevation downstream of the upper end fitting resistance. This pressure distribution is converted to the following nondimensional form for application in reactor TORC thermal/hydraulic analysis:

[redacted] (4A-4)

where pressures are at the elevation of the upper ends of fuel rods and

P_{out_i} = exit static pressure at assembly location i,

$\bar{P}_{out}$ = core average exit static pressure,

$\bar{P}_{in}$ = core average inlet static pressure.

The reactor core exit pressure distribution in this nondimensional form was provided for the normal condition with four operating reactor coolant pumps, and for three operating pumps (seized rotor accident).

4.4 REACTOR VESSEL PRESSURE DROP

Reactor vessel irreversible pressure drops are calculated with incremental loss coefficients derived from flow model test data as follows:

(4A-5)

For reactor pressure drop calculations, model K_i values are analytically adjusted to accommodate any model scaling approximations and are applied considering local fluid density variation at power.

(4A-6)

5.0 DISCUSSION OF TEST RESULTS

An overview of the flow model test results are provided here.

5.1 CORE INLET FLOW DISTRIBUTION

The core inlet flow distribution was determined for 4-pump and 3-pump configurations. Some non-uniformity in the flow distributions was observed, caused by the effects of local hardware in the lower plenum. The core inlet flow distributions for 4-pump and 3-pump configurations are shown in Figures 4A-6 and 4A-7. The measured core inlet flow distributions were determined to be acceptable.

5.2 CORE EXIT PRESSURE DISTRIBUTION

Core exit pressure distribution was determined for 4-pump and 3-pump configurations. The results are shown here in Figures 4A-8 and 4A-9. The pressure distributions are relatively uniform, and were determined to be acceptable.

5.3 REACTOR VESSEL PRESSURE LOSS COEFFICIENTS

The reactor vessel pressure loss coefficients were measured for 4-pump operation. The values are given in Table 4A-1. These loss coefficient values were determined to be acceptable.

5.4 OVERALL ASSESSMENT OF TEST RESULTS

The flow model test program produced valves for the hydraulic parameters, which were determined to yield acceptable reactor thermal-hydraulic performance. Therefore, the flow model test program was successful.

6.0 REFERENCES

1. "TORC Code Verification and Simplified Modeling Methods," CENPD-206-P-A (Proprietary), CENPD-206-A (Non-Proprietary), June 1981.

2. "Users Manual for HERMITE Space-Time Neutronics and Thermal Hydraulics Code," CE-CES-91, Rev 0-P (Proprietary); CE-CES-91, Rev. 0 (Non-Proprietary), March 1988.

TABLE 4A-1

SUMMARY OF LOSS COEFFICIENTS FOR THE REACTOR VESSEL

Test Config.	Vessel Flow Path Segment	Loss Coefficient K_i
4-loop Balanced	Inlet nozzle to core inlet	2.59
	Core	2.70
	Core exit to outlet nozzle	2.25

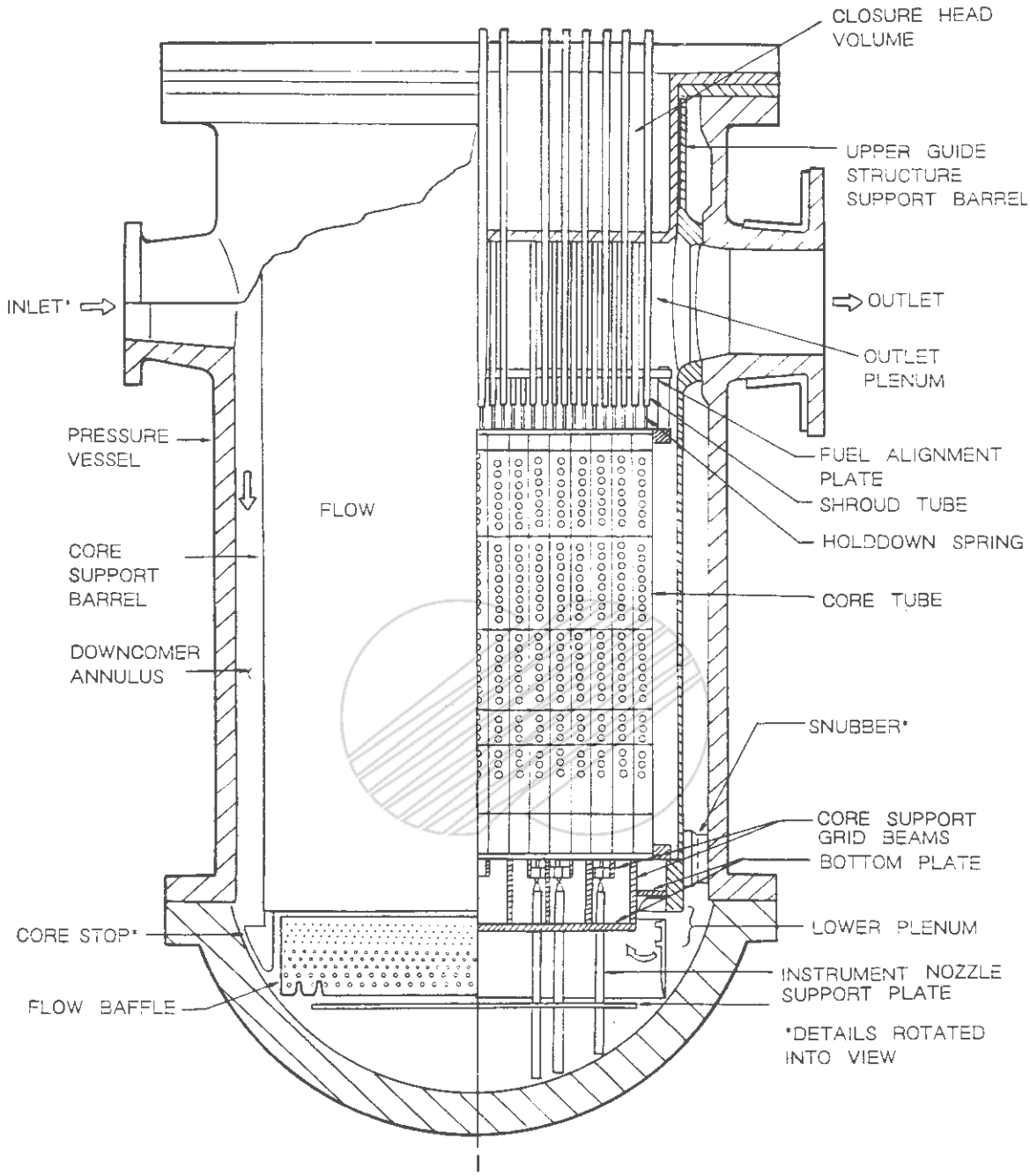

KOREA ELECTRIC POWER CORPORATION
YONGGWANG 3 & 4
FSAR

REACTOR FLOW MODEL

Figure 4A-1

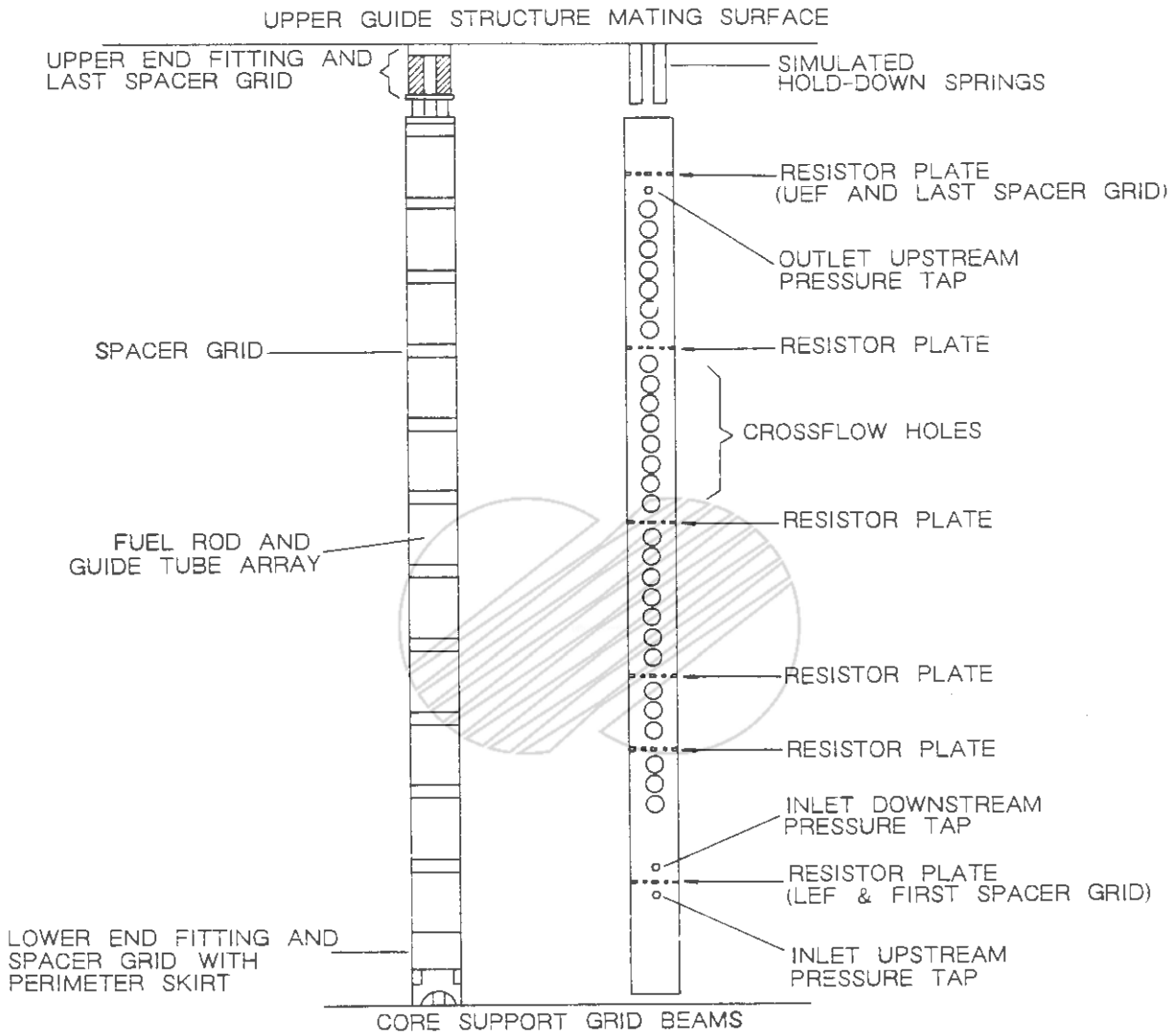

KOREA ELECTRIC POWER CORPORATION
YONGGWANG 3 & 4
FSAR

COMPARISON OF REACTOR AND MODEL FUEL ASSEMBLY LAYOUT

Figure 4A-2

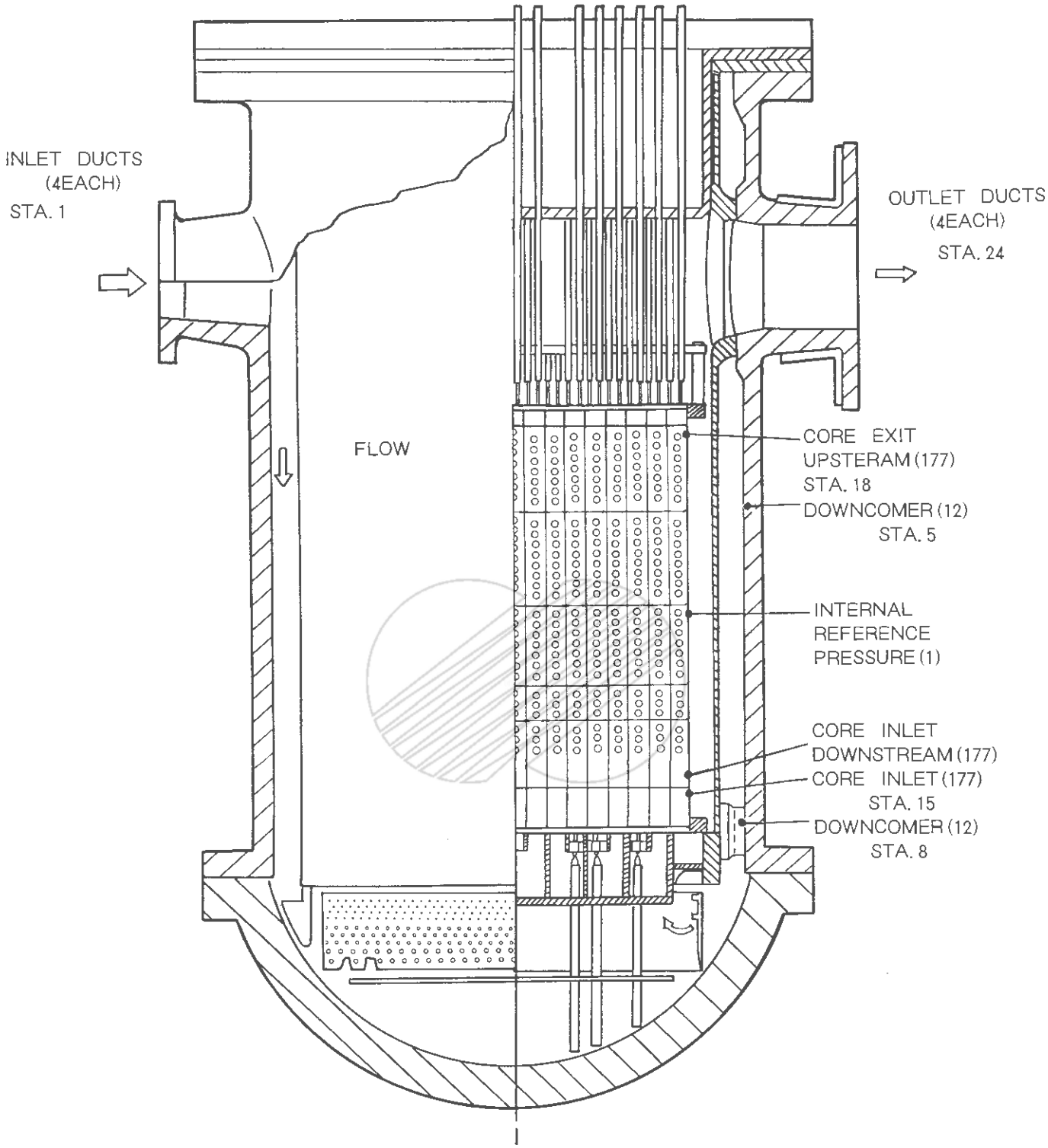

KOREA ELECTRIC POWER CORPORATION
YONGGWANG 3 & 4
FSAR

PRESSURE TAP LOCATIONS IN THE
REACTOR FLOW MODEL

Figure 4A-3

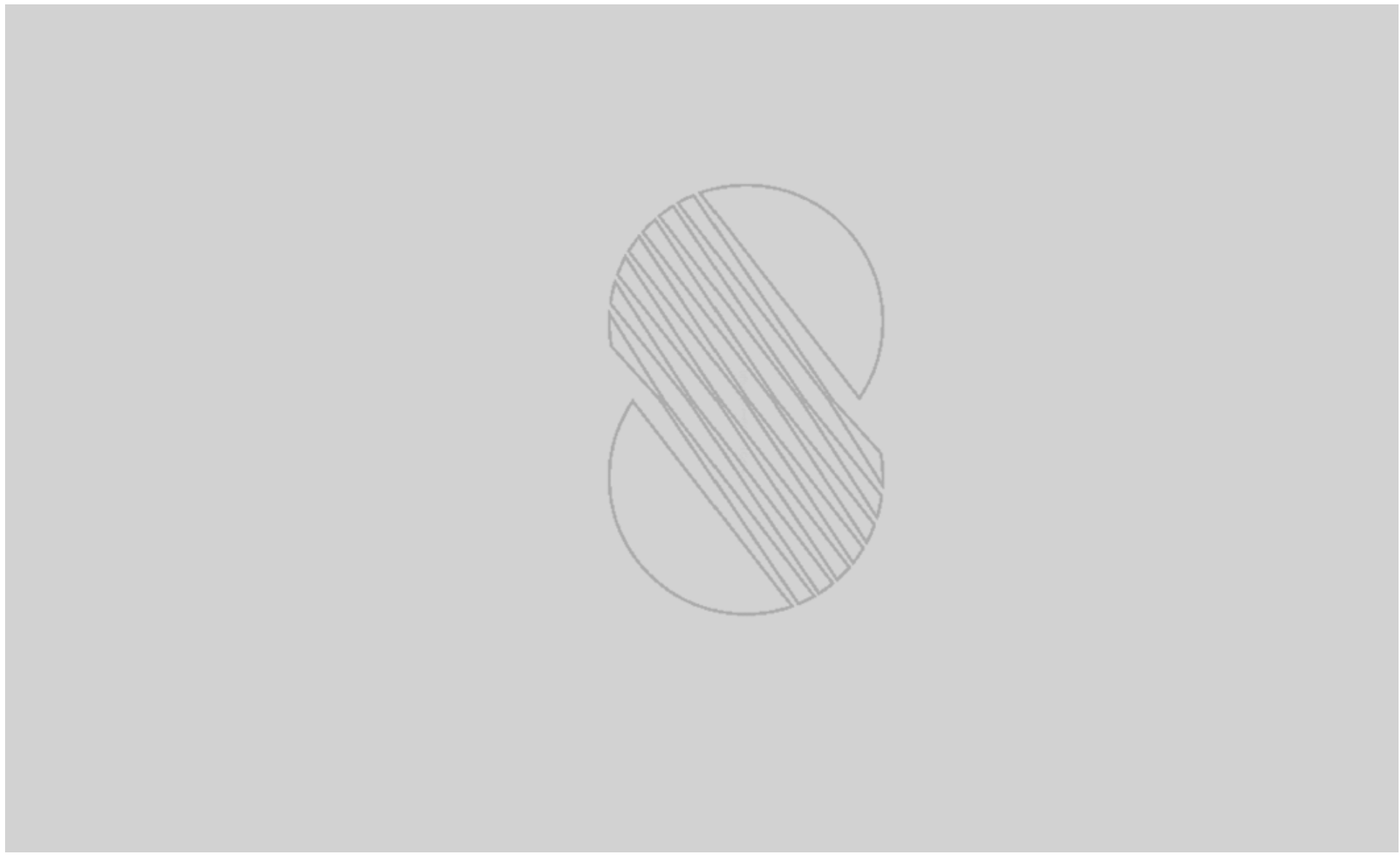

KOREA ELECTRIC POWER CORPORATION
YONGGWANG 3 & 4
FSAR

TEST LOOP SCHEMATIC

Figure 4A-4

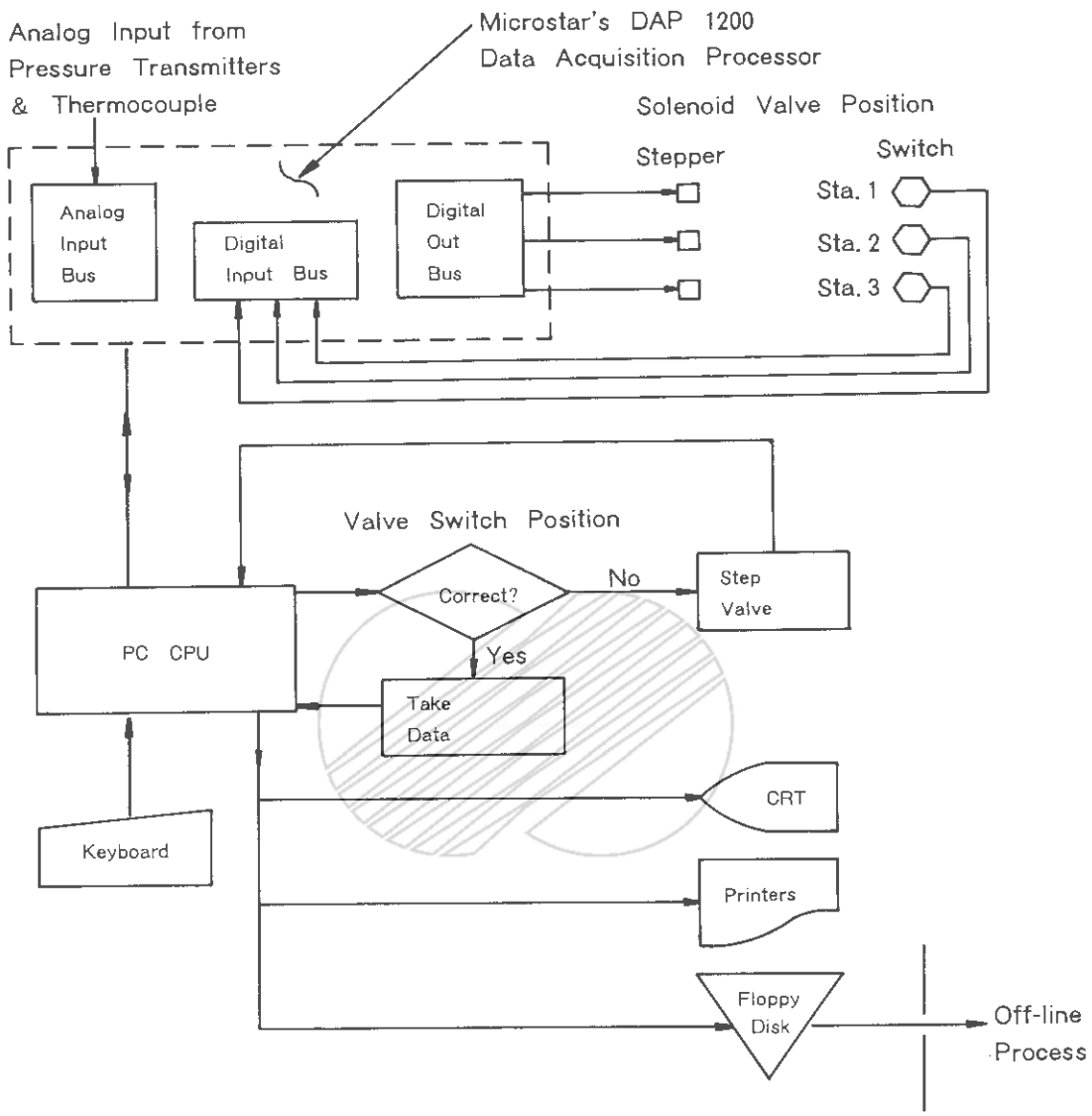

KOREA ELECTRIC POWER CORPORATION
YONGGWANG 3 & 4
FSAR

SCHEMATIC OF DATA LOGGER
INTERFACES

Figure 4A-5

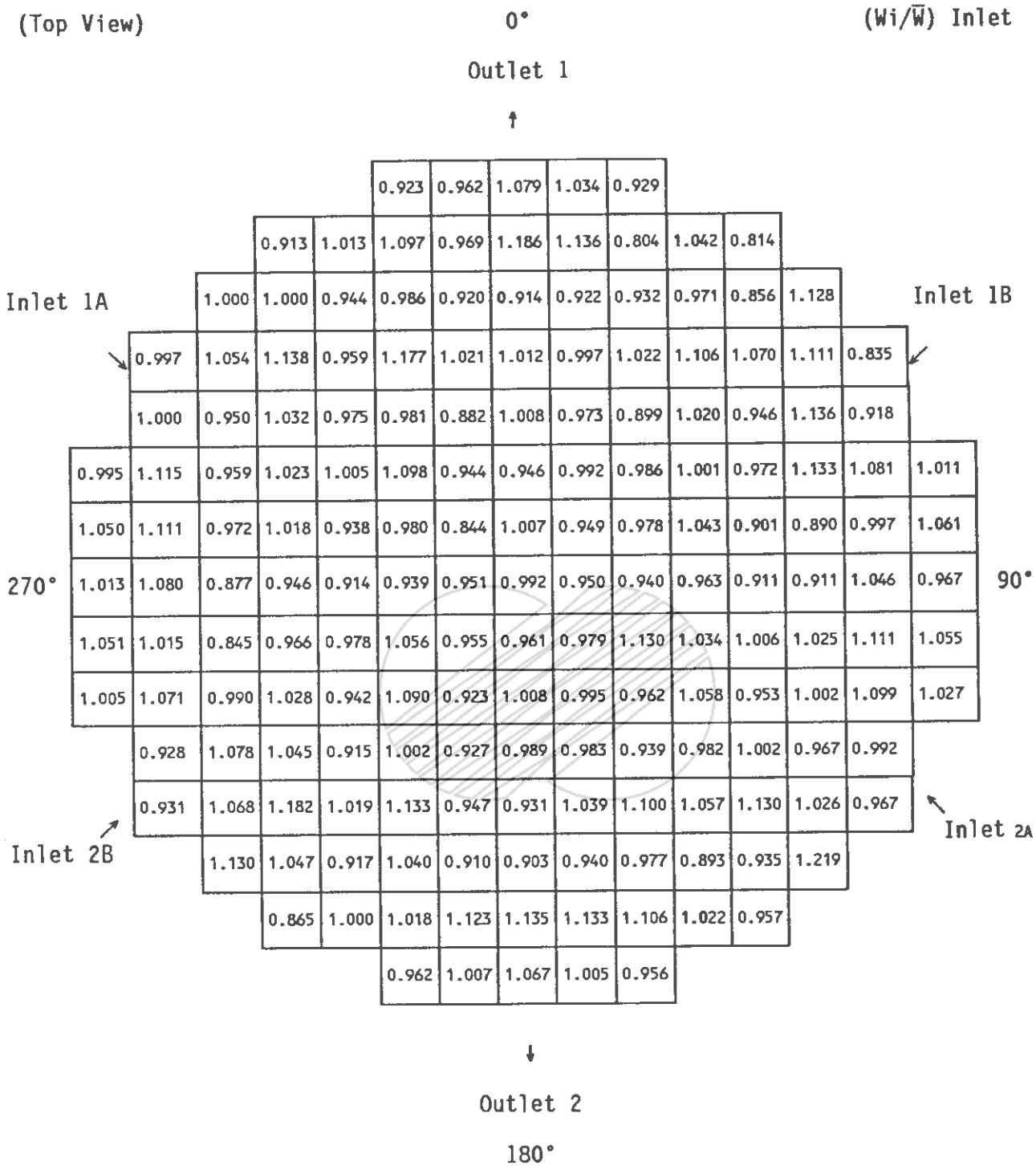

KOREA ELECTRIC POWER CORPORATION
YONGGWANG 3 & 4
FSAR

4-PUMP CORE INLET FLOW DISTRIBUTION

Figure 4A-6

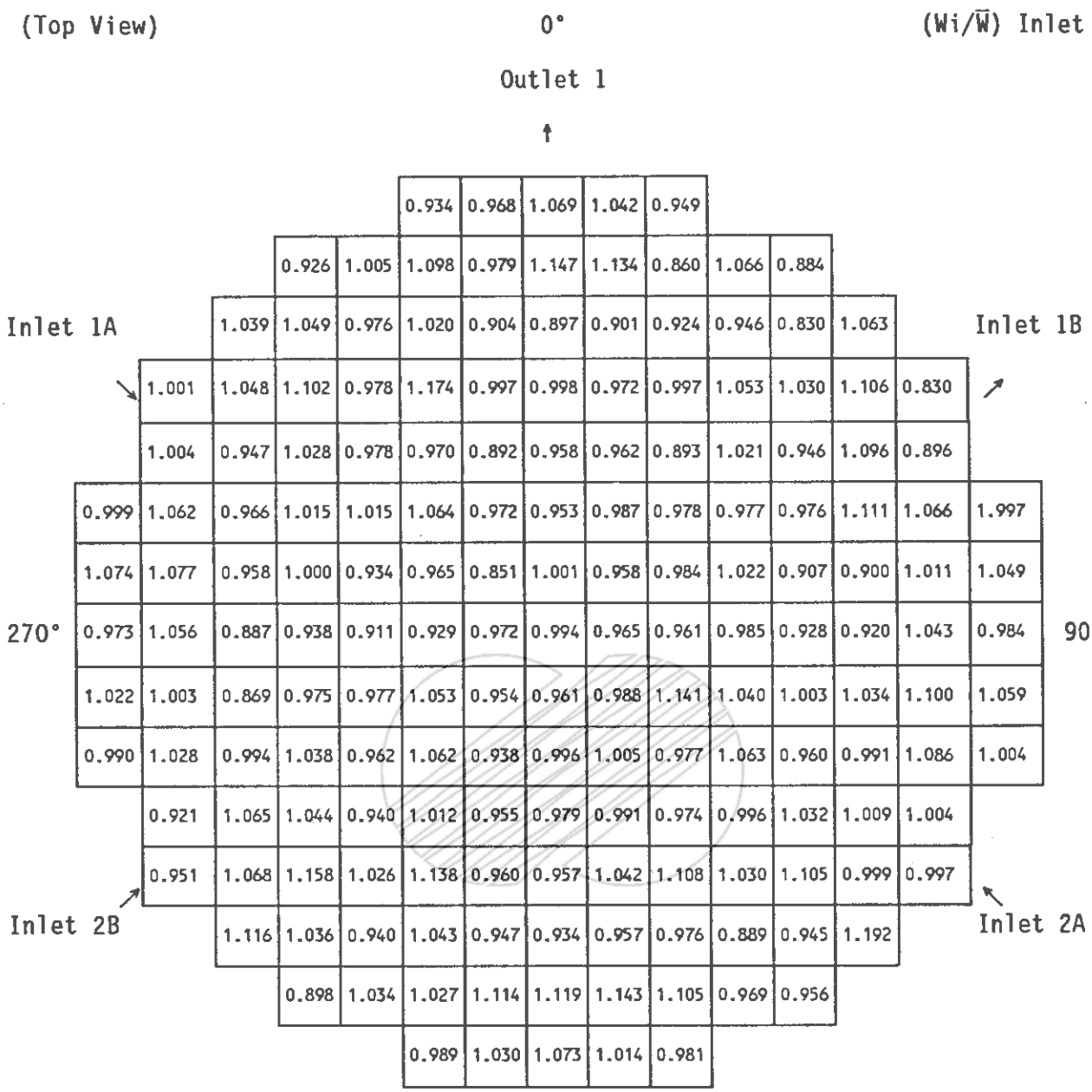

KOREA ELECTRIC POWER CORPORATION
YONGGWANG 3 & 4
FSAR

3-PUMP CORE INLET FLOW DISTRIBUTION

Figure 4A-7

$$\frac{P_{OUTi} - \overline{P}_{OUT}}{\overline{P}_{IN} - \overline{P}_{OUT}} = E_{OUTi}$$

(Top View)

0°
Outlet 1

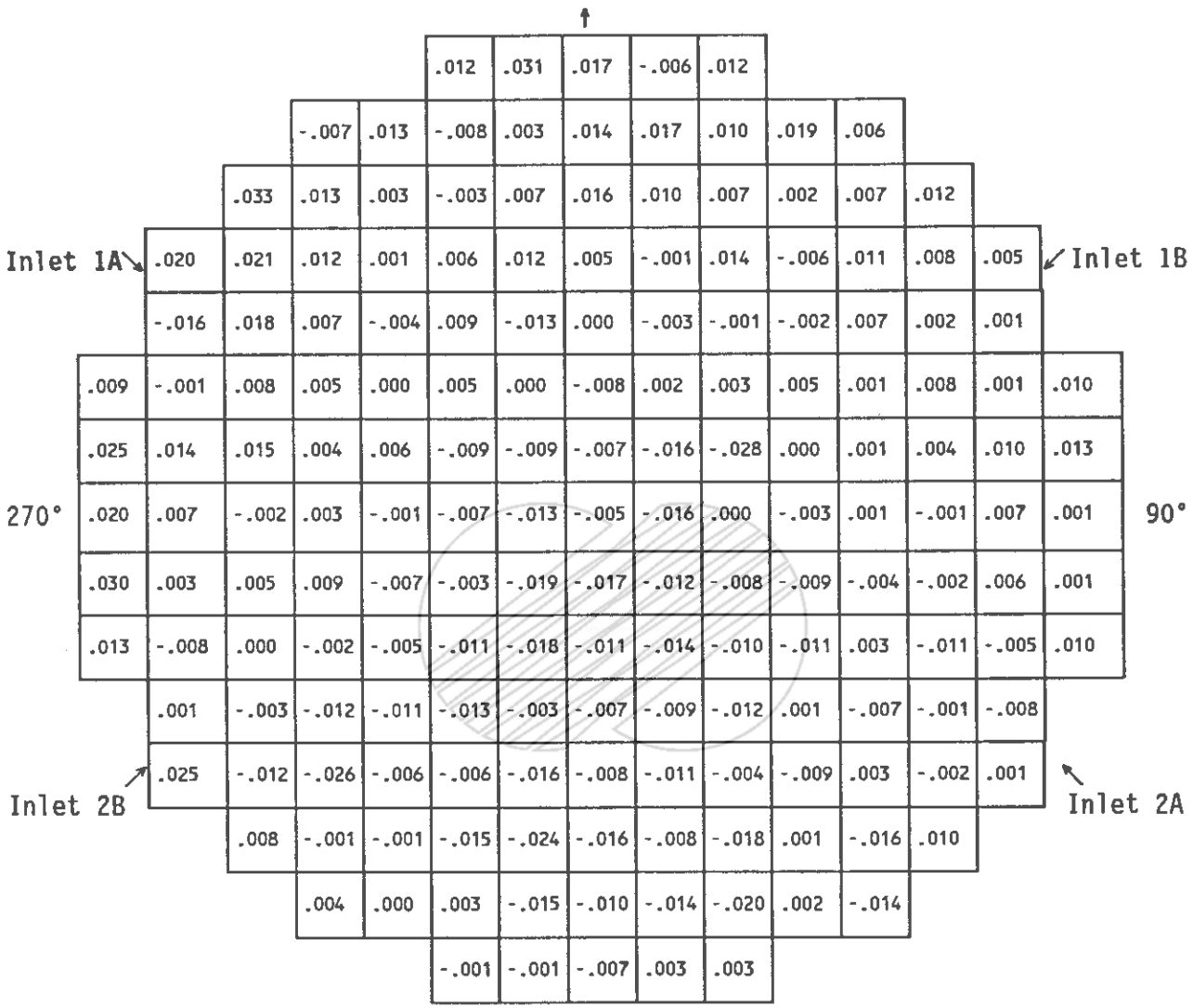

Outlet 2

180°

KOREA ELECTRIC POWER CORPORATION
YONGGWANG 3 & 4
FSAR

4-PUMP CORE EXIT PRESSURE DISTRIBUTION

Figure 4A-8

Amendment 339
2007.01.09

APPENDIX 4B1

HOT LOOP FLOW TESTING OF

WEC SYSTEM 80 FUEL AND CEA COMPONENTS

APPENDIX 4B1

TABLE OF CONTENTS

LIST OF FIGURES

1.0 SUMMARY

Hot loop flow testing for WEC System 80 was completed during 1980 and 1981. Test components included an array of five fuel assemblies, a 12-rod control element assembly (CEA) and supporting structures. Pressure drops and CEA scram times were measured for a range of temperature and flow rate settings. Results were nearly as predicted based on analyses and the results of hot loop tests preceding those for WEC System 80. A 1300-hour wear test was run, finding no fretting wear on fuel rods and no other wear on fuel exterior surfaces. Some wear occurred inside rodded CEA guide tubes, but at acceptable rates. The YGN fuel assemblies, CEA, and supporting structures are identical to WEC System 80. Therefore, the following test facility description and test results are applicable to YGN 3&4.

2.0 TEST FACILITY DESCRIPTION

Tests were performed in the 36 in. (91.4 cm) ID main section of the WEC TF-2 hot loop. The piping arrangement in this loop is shown in Figure 4B1-1.

The loop includes systems that maintain steady temperature and pressure and normal reactor water chemistry.

3.0 TEST COMPONENTS

3.1 Stackup

The test component stackup is shown in Figure 4B1-2. The support structures were bolted to lugs and a support ring bolted at the bottom of the test vessel. The fuel assemblies and CEA were enclosed within lower and upper support structures, which were joined by bolts at the fuel alignment plate.

3.2 Fuel Assemblies

3.2.1 Details of Design

Fuel assemblies closely matched the production reactor fuel design, as described in Subsection 4.2.2, with the following differences:

a. Fuel Rod Loading

46% of the fuel rods (544) were of prototype construction, with depleted UO2 pellets. 54% (636) were dummy rods of solid stainless steel. Prototype rods were used in all positions of concern with respect to fretting wear.

b. Lower End Fitting Leg Braces

Braces are deleted between legs of the lower end fitting. The test design, with braces, is considered less favorable with respect to fretting wear.

c. Inside Dimension of Guide Tubes and Upper End Fitting (UEF) Posts

The ID in upper ends of guide tubes and in UEF posts for production fuel are enlarged relative to the test fuel slightly as a precaution, allowing use of wear sleeves if needed. The tube enlargement has little effect on guide tube wear tendency, and speeds CEA scrams very slightly.

3.2.2 Spacer Grip Spring Settings

All spacer grip springs were set for the minimum restraint of fuel rods expected during the fuel lifetime.

3.2.3 Fuel Array in Test

The array of five fuel assemblies is shown in Figure 4B-3, with relationships to the fuel shroud and CEA.

3.3 Control Element Assembly

WEC System 80 reactors utilize both 4-rod and 12-rod control element assemblies. The 12-rod CEA was chosen for hot loop tests because it has a lower weight per rod ratio (hence slower scrams) and is a more complex structure. The test CEA was functionally identical to that shown in Figure 4.2-4.

3.4 Support Structures

The support structures were prototypical sections of a WEC System 80 reactor and provided support and alignment of the fuel assemblies and CEA. The lower ends of the fuel assemblies engage alignment pins on an open grid beam array. The fuel shroud cross section is noted in Figure 4B-3. All possible corner shapes and fuel-to-shroud clearances were included. Shroud tubes in the upper guide structure were held by the upper guide structure support plate (UGSSP) and fuel alignment plate (FAP), and engaged the four posts of each fuel upper end fitting. The region between the FAP and the UGSSP is an outlet plenum, where flow passes up around the shroud tubes and exits the outlet nozzle. Effects of a pressure gradient across the reactor outlet plenum were included in tests. The gradient causes flow circulation through small holes in the UGSSP upward near the reactor centerline and downward near the outlet nozzles. In TF-2 the flow circulation was driven through external piping, employing a CEA shroud and seal assembly above the UGSSP.

4.0 TEST RESULTS

4.1 Scram Time vs. Acceptance Curve

Hot loop tests previewed the scram performance checks that will be required for every reactor CEA during startup tests. Measured scram times to the 90% insertion point for reactor scrams must be less than or equal to the maximum allowable value of 4 seconds(including delay time) which is used in the safety analyses. The reactor scram tests are run at approximately 525°F (274℃) with all pumps running. The TF-2 scram for this condition is plotted in Figure 4B1-4, along with the acceptance curve.

4.2 Pressure Drops in Fuel

Fuel assembly pressure drops were measured over a range of flow Reynolds numbers. Results are in good agreement with measurements for similar fuel in prior TF-2 tests. The test results support the flow resistances used in design analyses for WEC System 80 and based on the prior measurements. Those analyses include fuel holddown spring design requirements, support structure hydraulic loadings, and the prediction of system flow rate.

4.3 Fuel Rod Fretting

The test for fuel rod fretting ran 1300 hours, [redacted] The setting was based on worst-case reactor conditions at full power, with 116% design flow. Test fluid velocities exceeded those expected in any WEC System 80 reactor. No fretting was found on any of the fuel rod surfaces.

4.4 Guide Tube Wear

In view of observed CEA motion dependence on upper guide structure flow, a sequence of different flow conditions was set during the wear test. With each

change of flow conditions, the CEA was raised to a new position. Conditions included the maximum pressure differences expected across the reactor UGSSP, both upward and downward, and an intermediate equalized condition. Following the tests, all CEA guide tubes were inspected with an eddy current probe. The four tubes which gave the largest indications were removed and sectioned longitudinally (clamshelled) for precise inspection. Greatest wear occurred for the UGSSP upflow condition, at points of CEA rod tip contact in guide tubes. Guide tube wear at the highest rate observed in tests will not contribute to violation of stress limits in Subsection 4.2.3.

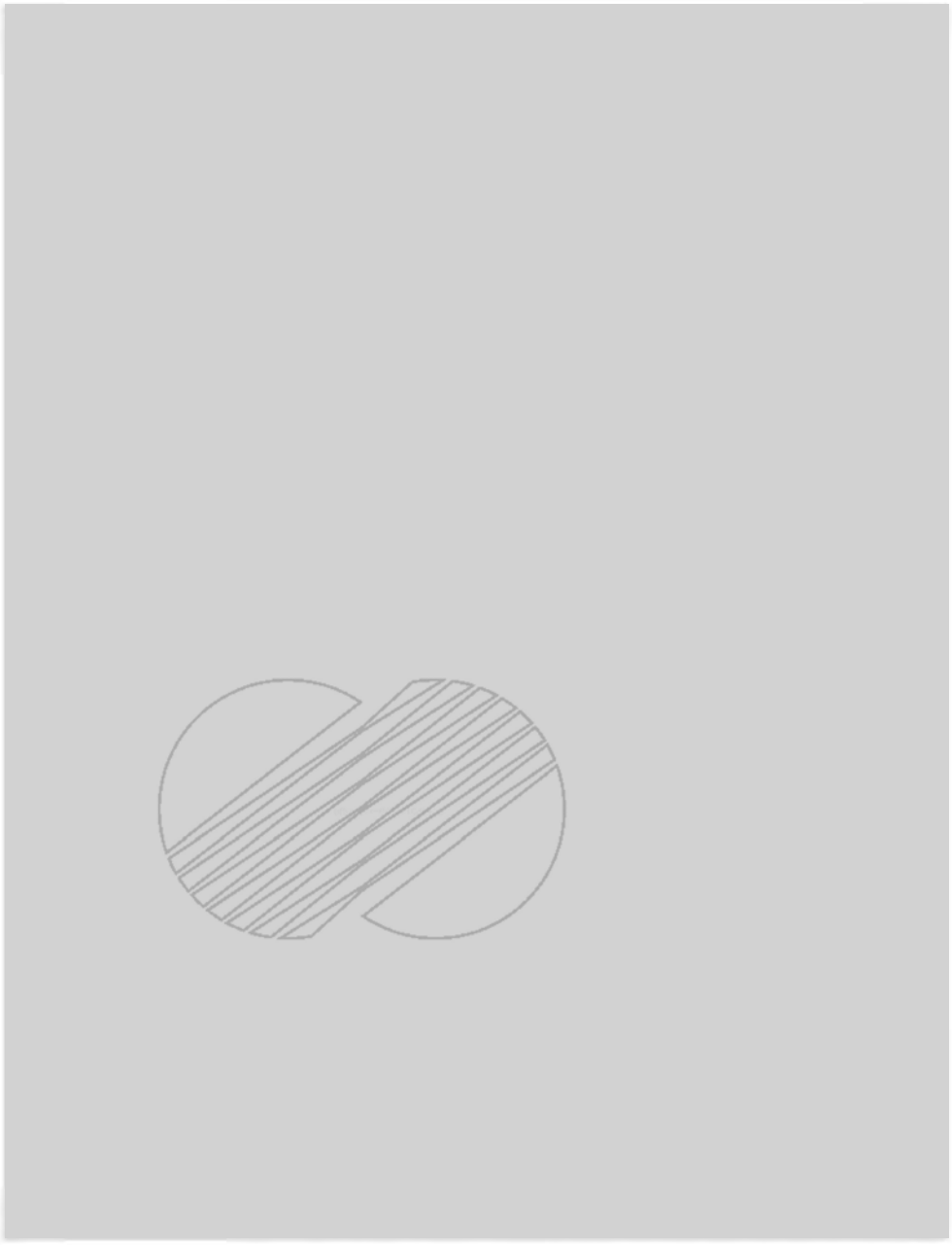

KOREA HYDRO & NUCLEAR POWER COMPANY
YONGGWANG 3 & 4
FSAR

WEC TF-2 HOT LOOP PIPING
ISOMETRIC

Figure 4B1-1

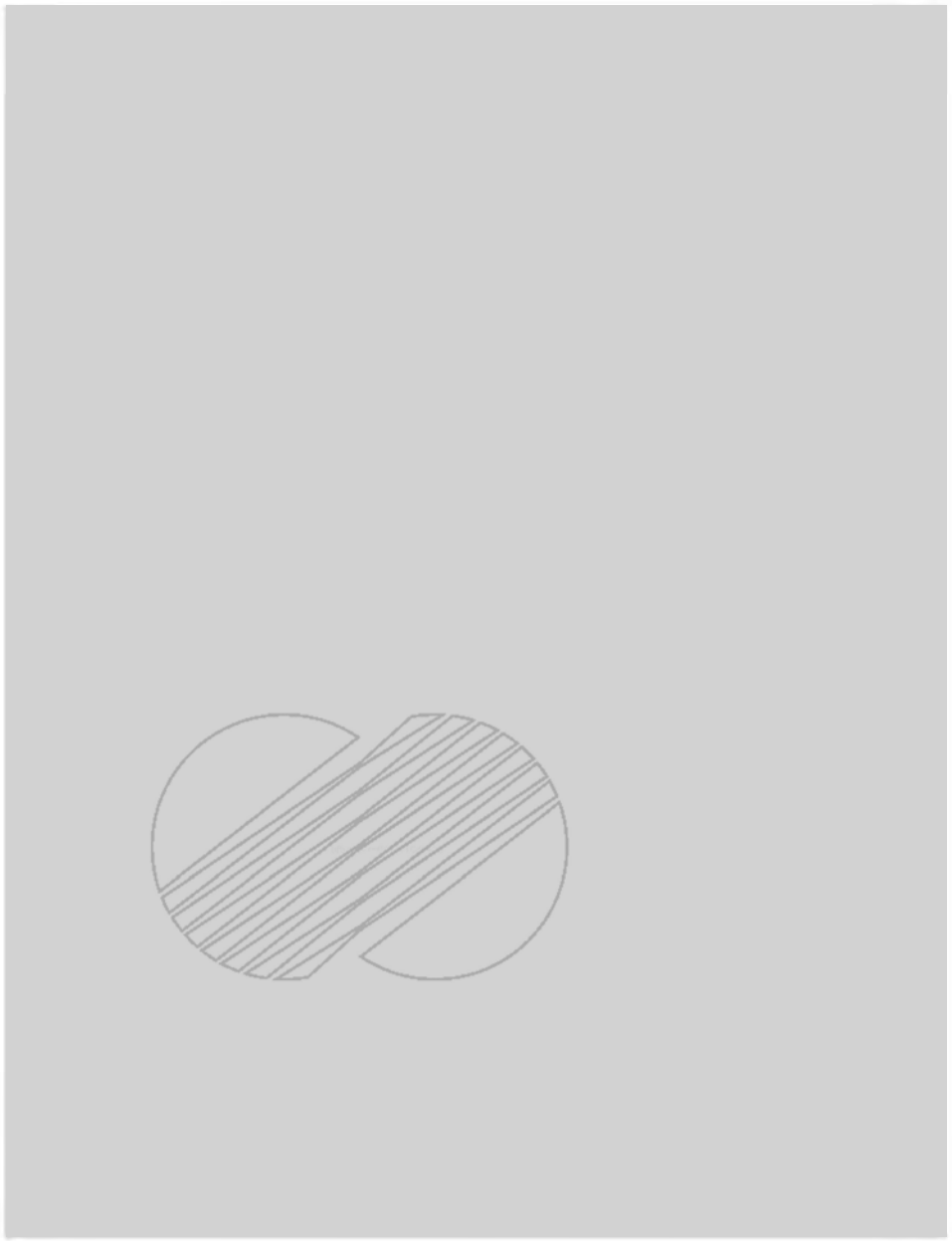

KOREA HYDRO & NUCLEAR POWER COMPANY
YONGGWANG 3 & 4
FSAR

WEC STSTEM 80 FUEL HOT LOOP TESTS,
COMPONENTS STACKUP IN TF-2

Figure 4B1-2

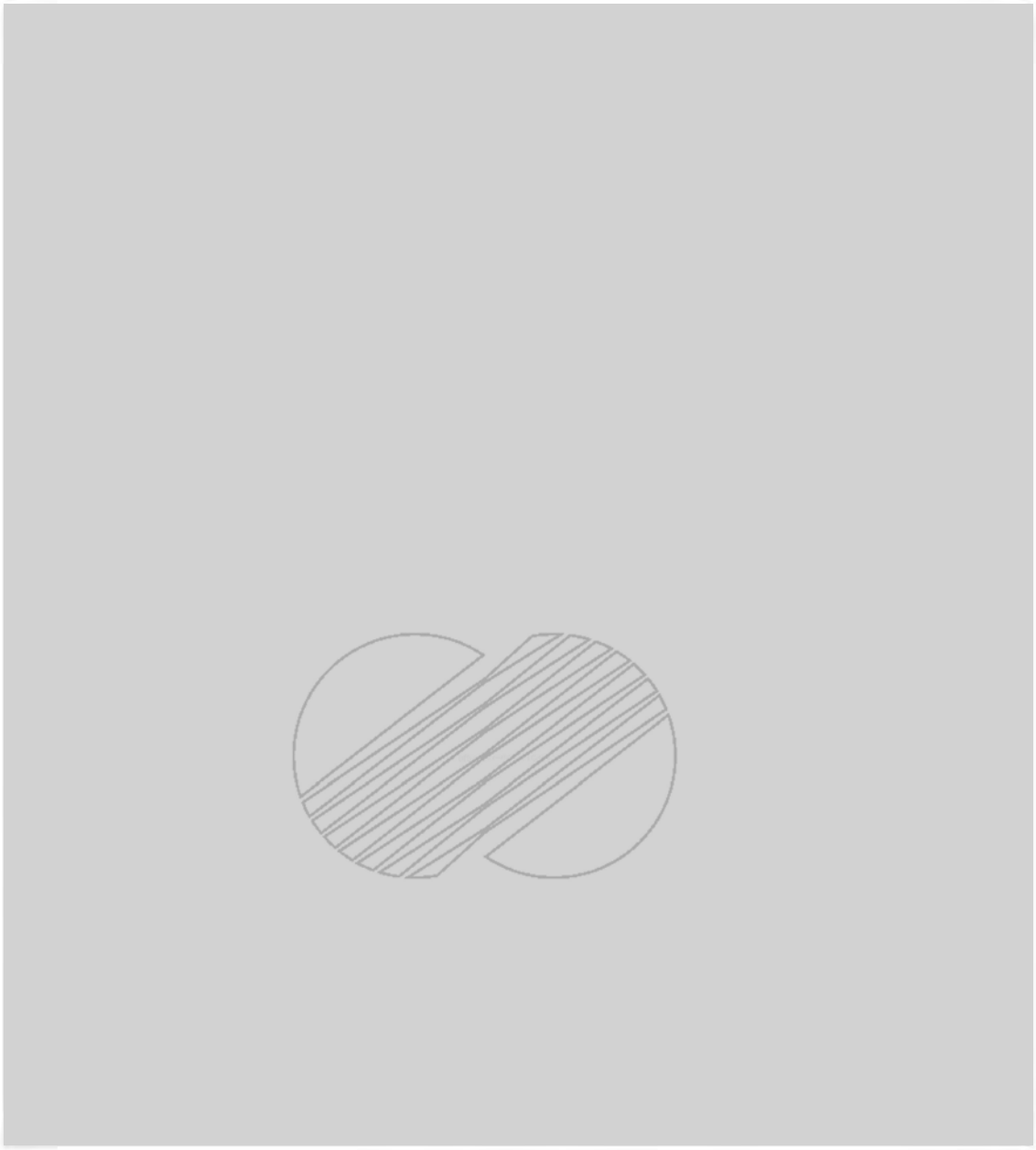

KOREA HYDRO & NUCLEAR POWER COMPANY
YONGGWANG 3 & 4
FSAR

CROSS SECTION THROUGH FUEL
SHROUD AND FUEL ARRAY
TF-2 TESTS

Figure 4B1-3

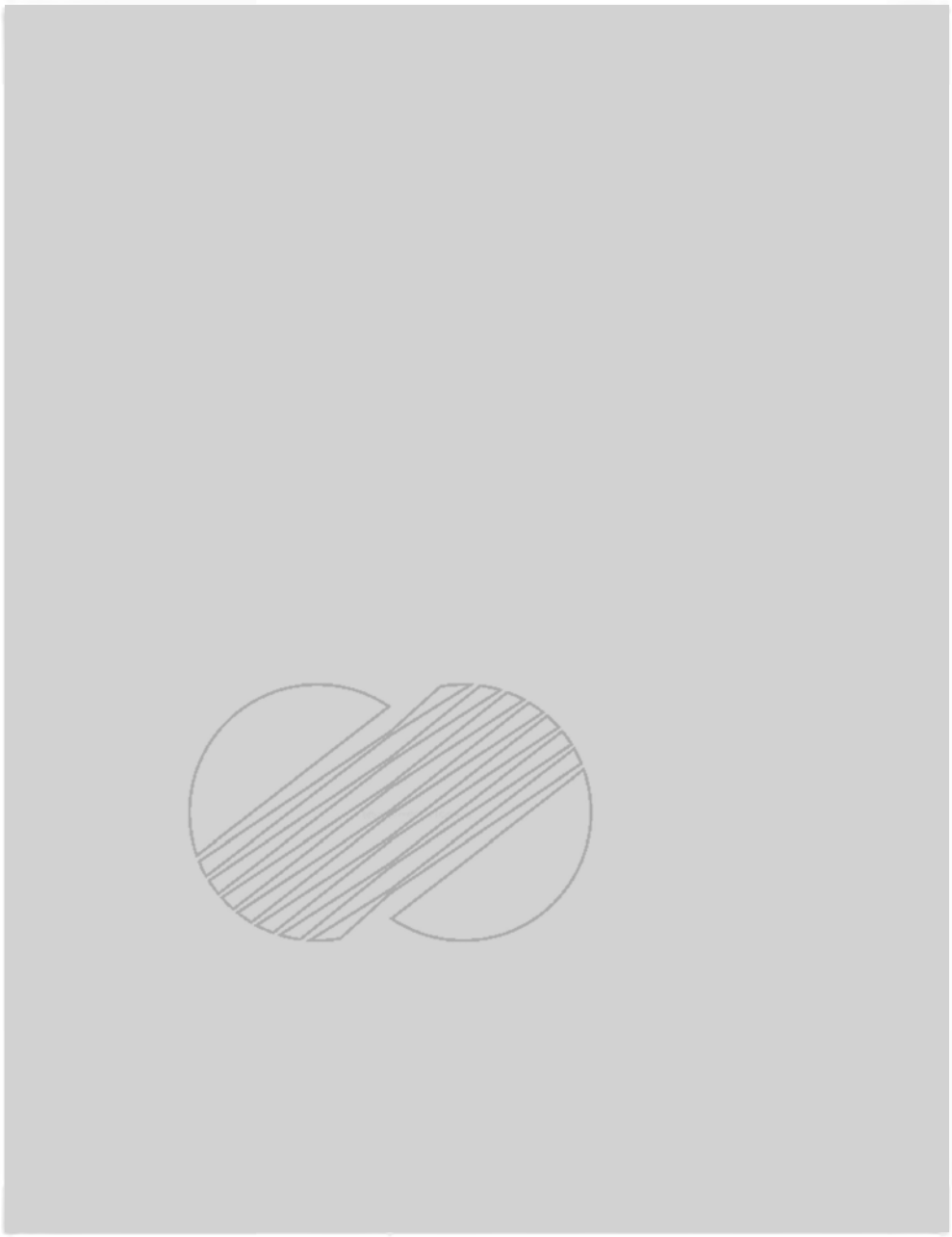

KOREA HYDRO & NUCLEAR POWER COMPANY
YONGGWANG 3 & 4
FSAR

TEST SCRAM VS. ACCEPTANCE CURVE,
525°F FOUR-PUMP FLOW
SETTING IN TF-2

Figure 4B1-4

APPENDIX 4B2

HOT LOOP FLOW TESTING OF FLUS7 FUEL

APPENDIX 4B2 - HOT LOOP FLOW TESTING OF PLUS7 FUEL

TABLE OF CONTENTS

LIST OF FIGURES

1.0 SUMMARY

Hot loop flow testing for PLUS7 fuel was completed during 2000 and 2001. the fuel assembly pressure drop, uplift force and vibration test were performed in the FACTS(Fuel Assembly Compatibility Test System) and the fuel assembly long term wear test and vibration test were performed in the VIPER(Vibration Investigation and Pressure Drop Experimental Research). the test results confirm that there was no abnormal flow-induced vibration response and no measurable wears affecting the fuel rod integrity on fuel exterior surface.

2.0 TEST FACILITY DESCRIPTION

The piping arrangement in FACTS loop is shown in Figure 4B2-1.

VIPER loop test include an array of two fuel assemblies to perform flow test and the piping arrangement in this loop is shown in the Figure 4B2-2.

3.0 TEST COMPONENTS

3.1 Test Vessel

The test vessels of FACTS와 VIPER were shown in the Figure 4B2-3, 4B2-4 respectively. The fuel assembly was located in the housing of vessel and enclosed within lower and upper support structure.

3.2 Fuel Assemblies

3.2.1 Details of Design

3.2.1.1 Fuel Assembly in FACTS Loop Test

The fuel assembly used in the FACTS loop test closed matched the production reactor PLUS7 fuel design as described in Subsection 4.2.2, except for using depleted UO2 pellets instead of enriched UO2 pellets in the fuel rod.

3.2.1.2 Fuel Assemblies in VIPER Loop Test

The fuel assemblies used in the VIPER Loop Test closed matched production reactor GUARDIAN and PLUS7 fuel design as described in Subsection 4.2.2, except for using depleted UO2 pellets instead of enriched UO2 pellets in the fuel rod.

3.2.2 Spacer Grid Settings

All spacer grid springs in FACTS loop test were set for as-built grid cell size and spacer grid springs in the VIPER loop test were set for the minimum restraint of fuel rods expected during the fuel lifetime.

3.2.3 Fuel Array in Test

The array of two fuel assemblies in VIPER loop test is shown in Fogure 4B2-5, with relationships to the fuel shroud.

4.0 TEST RESULTS

4.1 Pressure Drop in Fuel

Fuel assembly pressure drops were measured over a range of flow reynolds numbers. Results are in good agreement with measurements for similar fuel in prior test. The test results support the flow resistance used in design analyses and based on the prior measurements. Those analyses include fuel holddown spring design requirements, support structure hydraulic loadings, and prediction of system flow rate.

4.2 Fuel Rod Fretting

The test for fuel rod fretting ran 500 hours. Test fluid velocities exceeded those expected in YGN 3,4 Reactor. No fretting was found on any of the fuel rod surface.

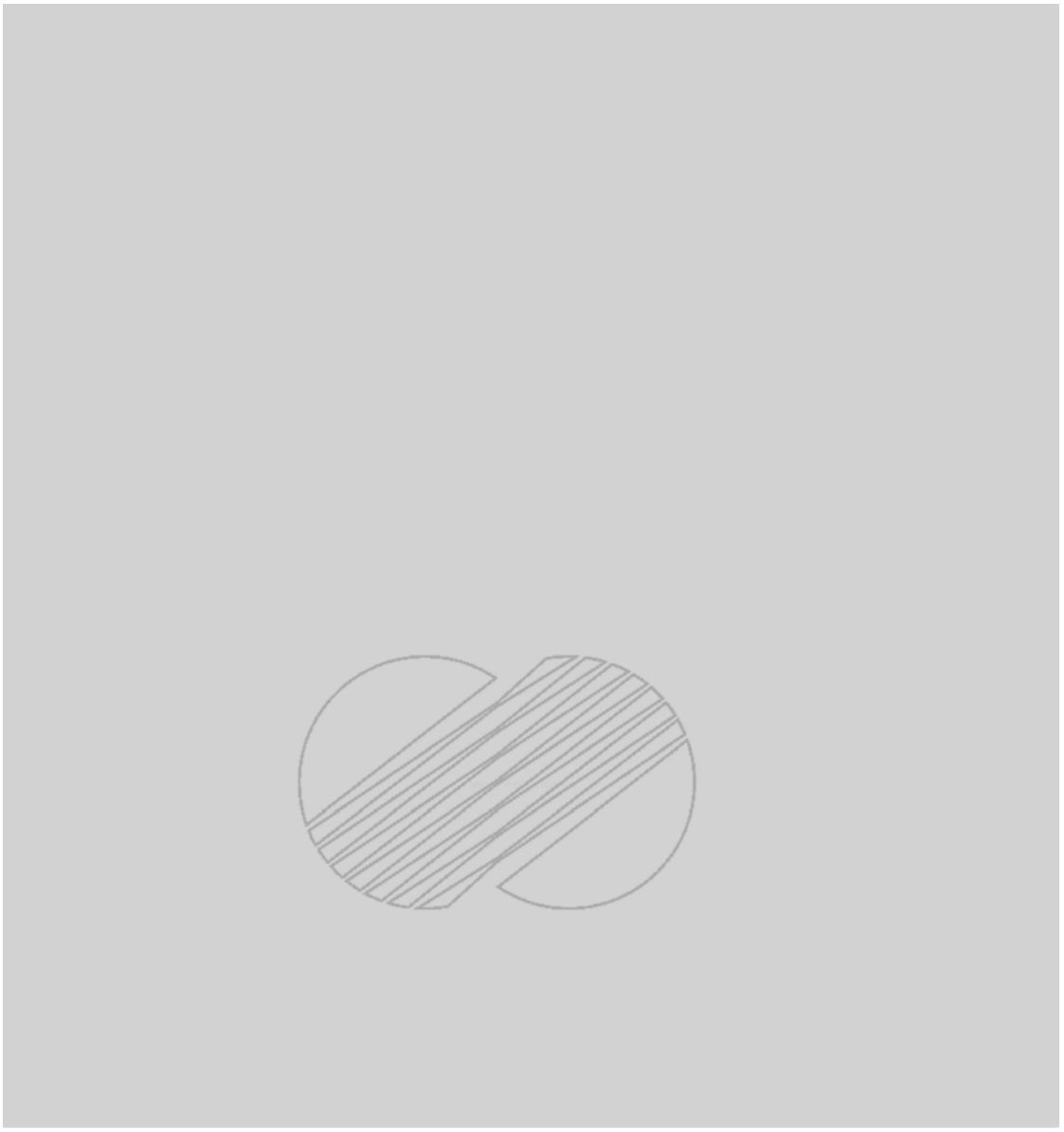

KOREA HYDRO & NUCLEAR POWER COMPANY
YONGGWANG 3 & 4
FSAR

FACTS HOT LOOP PIPING
ISOMETRIC

Figure 4B2-1

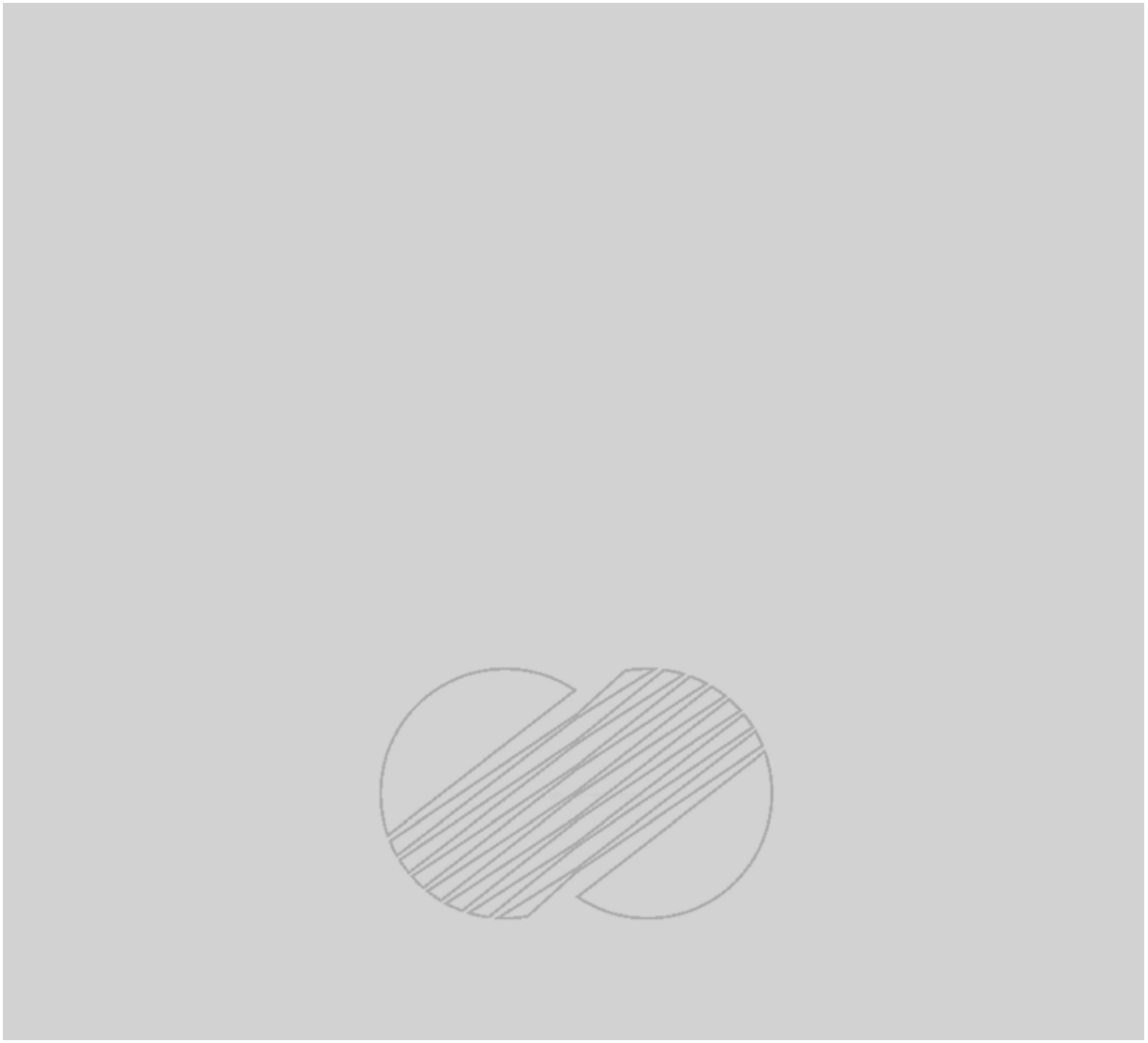

KOREA HYDRO & NUCLEAR POWER COMPANY
YONGGWANG 3 & 4
FSAR

VIPER HOT LOOP PIPING
ISOMETRIC

Figure 4B2-2

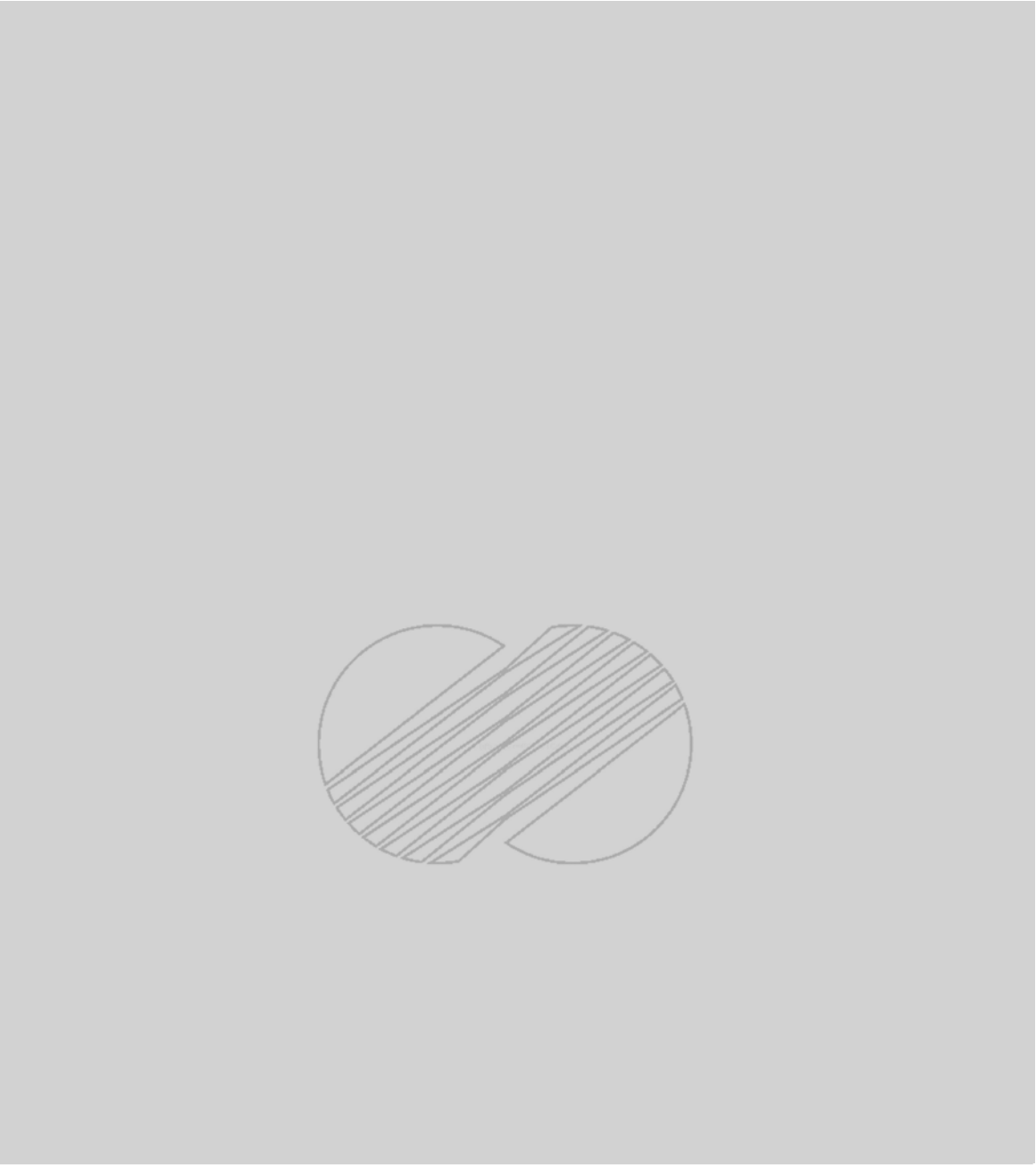

KOREA HYDRO & NUCLEAR POWER COMPANY
YONGGWANG 3 & 4
FSAR

FACTS HOT LOOP TEST VESSEL

Figure 4B2-3

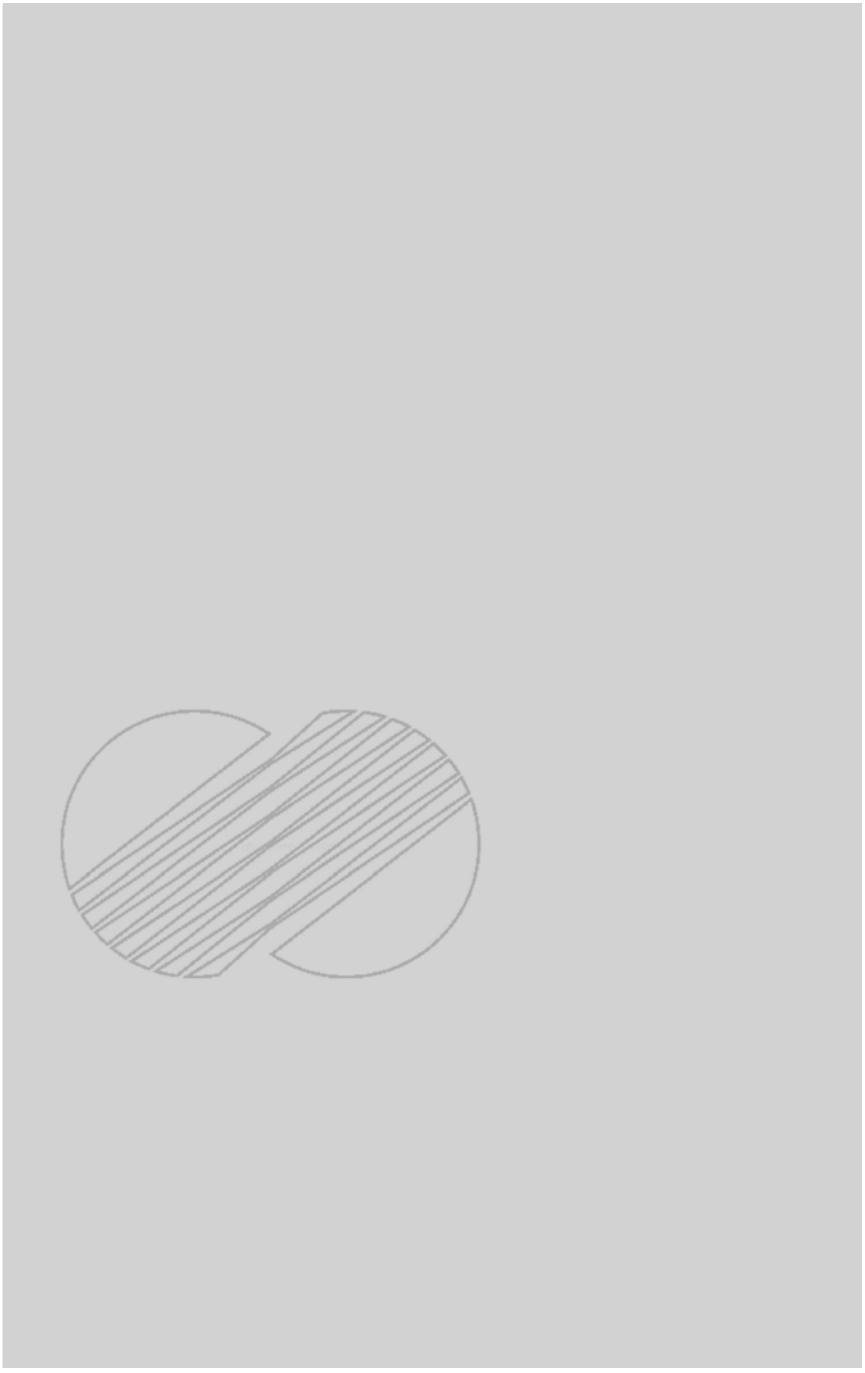

KOREA HYDRO & NUCLEAR POWER COMPANY
YONGGWANG 3 & 4
FSAR

VIPER HOT LOOP TEST VESSEL

Figure 4B2-4

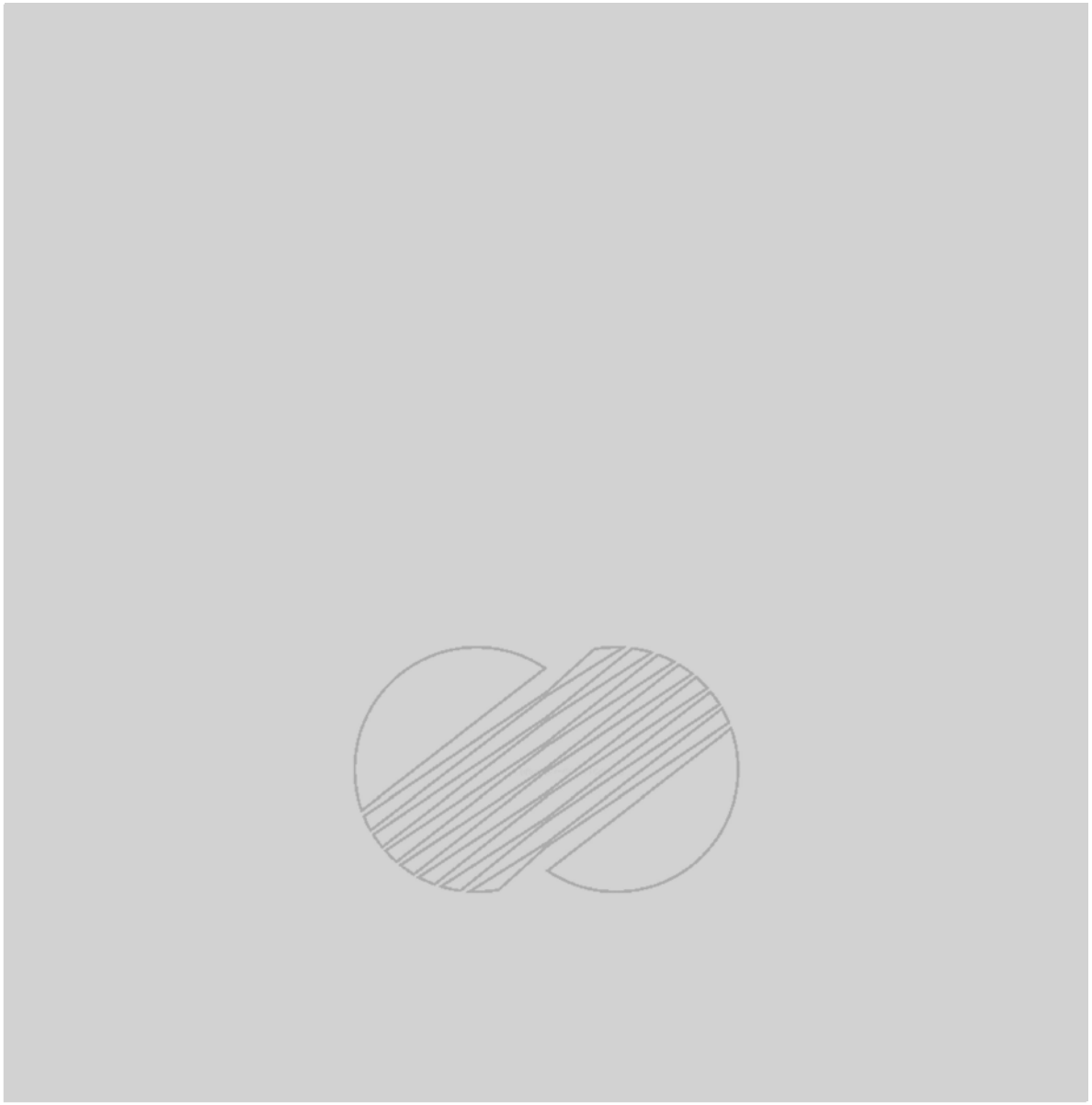

KOREA HYDRO & NUCLEAR POWER COMPANY
YONGGWANG 3 & 4
FSAR

CROSS SECTION THROUGH FUEL
SHROUD AND FUEL ARRAY
VIPER TEST

Figure 4B2-5